OKLAHOMA STATE UNIVERSITY

NIBLACK RESEARCH SCHOLARS

2021-22

FINAL REPORTS

NIBLACK RESEARCH SCHOLARS

PREFACE

Oklahoma State University is pleased to present the enclosed reports of the 2021-22 Niblack Research Scholars.

Thanks to the continued support of OSU alumnus and retired Pfizer executive Dr. John Niblack, the Niblack Research Scholars program affords OSU students the unique opportunity to conduct real scientific research as undergraduates. Dr. Niblack himself participated in research at OSU during his undergraduate experience and believes it impacted his decision to pursue science as a career. His vision and passion to inspire a new generation of scientists lives on in this program.

Dr. John and Heidi Niblack with the 2021-22 Niblack Research Scholars.

(bottom row, L to R)
Alex Bias, Rio Bonham, Hunter McConnell, Meji Jayaseelan,

(2nd front row from bottom, L to R)
Garrett Thornton, Carson Wright, Carson Raper, Seth Robbins,

(2nd front row from top, L to R)
Andre Abit, Manoj Jagadeesh, Jillian Gore, Karley White

(top row, L to R)
Heidi Niblack, Dr. John Niblack, OSU V.P. for Research Dr. Kenneth Sewell, Andrew Thomas

SESSION ONE:

Hunter McConnell

"The Effect of Dietary Fatty Acid Source on Gene Expression in the Rumen of Cattle"
Research Area: Animal and Food Sciences
Faculty Sponsor: Dr. Andew Foote
Graduate Student Mentor: Mindy King

Andre Abit

"Effect of Overexpression of Sulfate Transporter Gene AST68 on Arsenic Tolerance in *Arabidopsis thaliana*"
Research Area: Biochemistry and Molecular Biology
Faculty Sponsor: Dr. Ramanjulu Sunkar
Graduate Student Mentor: Pei Jia Ng

Carson Raper

"Comparing Ageing Structures for Striped Bass"
Research Area: Natural Resource Ecology and Management
Faculty Sponsor: Dr. Daniel Shoup
Graduate Student Mentor: Alex Vaisvil

Rio Bonham

"Effectiveness of Soil Moisture Sensors to Improve Irrigation Management"
Research Area: Biosystems and Agricultural Engineering
Faculty Sponsor: Dr. Saleh Taghvaeian
Graduate Student Mentor: Mukesh Mehata

The Effect of Dietary Fatty Acid Source on Gene Expression in the Rumen of Cattle

Hunter McConnell

Department of Animal and Food Sciences
Faculty Sponsor: Dr. Andrew Foote
Graduate Student Mentor: Mindy King

ABSTRACT

The objective of this experiment was to ascertain how different fatty acid sources impacted gene expression in the rumen epithelium. The study utilized rumen cannulated Holstein steers (n = 8) in a crossover design with two 16-d periods with a 20-d washout between periods. The diets contained (DM-basis) dry-rolled corn (57%), Sweet Bran (25%), chopped prairie hay (8%), vitamin-mineral supplement (5%), and 5% of either high oleic soybean oil (Oleic) or 5% commodity soybean oil diet containing predominantly linoleic acid (Linoleic). The diets were provided ad libitum and refusals were collected and subsampled. Water access was unrestricted. Rumen papillae biopsies were taken on d-16 of each period and flash-frozen using dry ice and alcohol. RNA was extracted and sequenced using short read sequencing. Differential gene expression (DEG) was analyzed using edgeR. Data were analyzed within periods to determine differences between treatments. In period 1, there were 25 DEGs (False Discovery Rate (FDR) < 0.05) with 13 downregulated and 12 upregulated in the Oleic treatment. In period 2, there were 35 DEGs (FDR < 0.05) with 12 downregulated and 23 upregulated in the Oleic treatment. The gene *LILRA6*, which is involved in immune function, was differentially expressed in both periods. Many of the KEGG pathways enriched were related to fatty acid metabolism, chemokine signaling, cytokine-cytokine receptor interactions, and immune function-related pathways. Gene ontology enrichment analysis highlighted inflammatory response, chemokine-mediated signaling, and other immune-related processes. These data indicated that dietary fat composition may impact gut inflammatory and immune function.

1. Introduction

The largest cost associated with beef cattle production is feed (Ahola and Hill, 2012). It is unlikely that feed costs are going to decrease so producers must instead rely on methods to improve feed utilization. The demand for improved feed utilization has led to many studies with the goal of determining biological factors associated with feed efficiency. Despite this, there is still limited information about how the utilization of different nutrients impacts feed efficiency. Reduced average daily gain (ADG), a measure of feed efficiency, has previously been associated with increased expression of inflammatory genes and rumen fatty acid concentrations (Lindholm-Perry et al., 2017, Reynolds et al., 2017). Understanding the relationship between inflammatory gene expression and rumen fatty acid concentrations could allow for a greater understanding of how inflammation impacts nutrient utilization.

Certain fatty acids are more strongly correlated with the inflammatory effect. Linoleic acid specifically has been associated with a reduction in efficiency and increased inflammatory response (Artegoitia et al., 2017, Reynolds et al., 2017). Two mechanisms may cause this inflammatory response. The first mechanism is nutrient and metabolic surplus causing chronic inflammation (Hotamisligil, 2006). Chronic inflammation is characteristic of common metabolic disorders such as obesity and type 2 diabetes and causes abnormal cytokine production, increased acute-phase reactants, and activates a network of inflammatory signaling pathways (Hotamisligil, 2006). The second mechanism is through inflammatory long-chain fatty acid metabolites (Medzhitov, 2008). One common class of these metabolites is eicosanoids which are produced from the metabolism of arachidonic acid (Medzhitov, 2008). Linoleic acid is a precursor to arachidonic acid (Medzhitov, 2008).

This inflammatory effect is not limited to ruminant animals. In the United States, 6% of all energy in a human diet is derived from linoleic acid (Choque et al., 2014). Linoleic acid is an essential fatty acid as it serves as a precursor to the n-6 family of fatty acids, however, the exact requirement of linoleic acid is still unknown (Choque et al., 2014). It is generally concluded that current diets well exceed any requirement (Choque et al., 2014). Linoleic acid even at this concentration is unlikely to cause inflammation in humans because the efficiency of the conversion between linoleic and arachidonic acid is only 1% (Choque et al., 2014). Still, in vitro studies indicate that elevated concentrations of linoleic acid will improve the efficiency of this conversion and could lead to inflammation (Choque et al., 2014).

More research is required to extrapolate the impact of fatty acids on rumen inflammation and feed efficiency. The objective of this study was to examine the effect of increased linoleic acid concentrations on inflammatory gene expression. The hypothesis being that there would be an increase in inflammatory gene expression in response to increased linoleic acid.

2. Experimental Details

Animal Management and Experimental Design

This study utilized eight cannulated Holstein steers (average body weight (BW) 856 ± 78.4 (Std Dev)) kg housed in 4.57 x 12.19 m individual pens at the Oklahoma State University Willard Sparks Beef Research Center. Pens were equipped with automatic waterers. The duration of this project was 52 days with two 16-d periods and a 20-d washout between the periods.

Steers were randomly assigned to receive one of two dietary treatments in a crossover design. The base diet included on a dry matter (DM) basis: 57% dry-rolled corn, 25% sweet bran, 8% chopped hay, 5% supplement, and 5% soybean oil (Table 1). The two treatment diets differed in the source of soybean oil. High oleic soybean oil which is predominantly oleic acid was included in the Oleic diet and commodity soybean oil which is predominantly linoleic acid was included in the Linoleic diet. Diets were formulated to meet NASEM requirements (National Academies of Sciences and Medicine, 2016). Both diets were mixed weekly at the Oklahoma State University Willard Sparks Beef Research Center.

A 100 g batch sample was collected the day of mixing and composited by treatment. All batch composites were dried in a 55°C oven for 48 h and then ground through a 1-mm screen. A 1 g sample of each diet composite was then dried at 105°c for 24 h. Lab DM was calculated by the difference in weight. Organic matter (OM) was calculated based on the weight difference after the samples were further dried at 500°c for 6 h. Neutral detergent fiber (NDF) and acid detergent fiber (ADF) were determined using an ankom 2000 (method numbers 13 and 12, respectively; ankom technology, macedon, ny). Acid detergent lignin was determined (method number 8; ankom technology). Ether extract was analyzed using an ankom xt15 with petroleum ether as the solvent (ankom technology). Feed was provided ad libitum and the daily ration was provided in halves (0730 and 1500 hours). Rations were adjusted daily to ensure 0.5 kg of refusals per day, and water access was unrestricted. Refusals were measured and sampled weekly.

Table 1. Diet composition of the treatments fed to the steers. Item percentages are reported on a DM basis. Composition is based on proximate analysis.

Item	Linoleic	Oleic
Dry-rolled corn, %	57	57
Sweet Bran, %	25	25
Chopped Hay, %	8	8
Supplement, %	5	5
Commodity Soybean Oil, %	5	0
High Oleic Soybean Oil, %	0	5
Composition, DM basis		
DM, %	93.0	93.1
OM, %	94.9	94.7
NDF, %	19.9	20.8
ADF, %	7.2	7.1
Fat, %	7.4	7.4

Biological Collections

On d-16 rumen papillae biopsies were collected for RNA sequencing. At 4 hours post feeding, the rumen was manually evacuated and a portion of the ventral sac of the rumen was inverted through the cannula. Rumen papillae were cut from the ventral sac using Iris scissors. Papillae were rinsed with phosphate-buffered saline to remove contaminants. Following processing, papillae were placed in a sterile microcentrifuge tube and flash frozen in a mixture of dry ice and 70% ethanol. Following collections, the papillae were stored at -80°C.

RNA Processing and Sequencing

Total RNA was isolated from the papillae using the RNeasy Mini Kit and QiaShredder columns (Qiagen, Hilden, Germany). Approximately 30 mg of papillae were thoroughly homogenized in 600 uL of RLT Plus buffer with B-mercaptoethanol. The lysate was added to a Qiashredder column and centrifuged for 3 minutes at 21,100 x g Following this step, the manufacturer's instructions were followed for the RNeasy Mini Kit. Total RNA was quantified using a Qbit (Invitrogen; Waltham, MA) and sample integrity was analyzed with a Bioanalyzer (Agilent; Santa Clara, CA). The RNA concentrations were 264-890 ng/mL, and all RNA integrity numbers were ≥ 9.1.

BGI Americas Corporation (Cambridge, MA, USA) performed the cDNA library preparation and RNA sequencing using the DNBSEQ platform. Sequencing generated paired-end reads of 150 bp length. The 16 samples averaged 36 million reads ranging from 34.4 to 36.2 million. An average of 95.95% (94.67-96.88%) of the reads mapped to the ARS-UCD1.2 reference genome.

Hierarchical Clustering

Counts per million-normalized (CPM) read counts were used in combination with the hclust function of base R in order to conduct hierarchical clustering (R Core Team, 2021). Hierarchical clustering analysis was conducted using the dist(method = Euclidean) followed by hclust(method = average) to compute the Euclidean distance between rows and compute the hierarchical clustering of the calculated distance matrix.

Differential Gene Expression

Raw reads were analyzed for differential gene expression using EdgeR v3.32.1 (Robinson et al., 2010). First, raw read data was normalized using the trimmed means of M values (TMM) of EdgeR and RUVseq v1.24.0 was used to remove unwanted variation (Risso et al., 2014). RUVseq identifies genes with constant expression across all samples as in silico negative controls to control variation. Principal component analyses (PCA) were performed

with the plotPCA function of DESeq2 v1.30.1 in order to visualize the similarity of expression among individuals. EDAseq v2.24.0 was used to perform full quartile normalization with the betweenLaneNormalization function prior to differential gene expression analysis. Eight separate differential expression tests were performed: Linoleic vs Oleic, Period 1 vs Period 2, Linoleic vs Oleic within Period 1, Linoleic vs Oleic within Period 2, Period 1 Linoleic vs Period 2 Oleic, and Period 2 Linoleic vs Period 1 Oleic. Differential expression analysis was done with likelihood ratio tests (glmLRT). Genes with a p value and false discovery rate (FDR) ≤ 0.05 were considered significantly differentially expressed.

Functional Annotation

The Database for Annotation, Visualization, and Integrated Discovery (DAVID) was used for Gene Ontology (GO) annotation and Kyoto Encyclopedia of Genes and Genomes (KEGG) pathway analysis was used to determine the biological processes and molecular functions of differentially expressed genes (Huang da et al., 2009, Sherman et al., 2022).

3. Results

Five separate differential expression tests were performed: Linoleic vs Oleic, Linoleic vs Oleic within Period 1, Linoleic vs Oleic within Period 2, Period 1 Linoleic vs Period 2 Oleic, and Period 2 Linoleic vs Period 1 Oleic. This was used to capture all variation between periods, dietary treatments, and animals. Of the five comparisons, four yielded differentially expressed genes. There were no genes differentially expressed in the comparison of all Linoleic vs Oleic samples.

When comparing the Oleic to the Linoleic dietary treatment within Period 1 there were a total of 25 differentially expressed genes (Table 2). Thirteen of these genes were downregulated and 12 were upregulated in the Oleic dietary treatment. Six of these genes are noncoding RNAs (ncRNA). Two upregulated genes, ACSBG1 and CPT1A, are involved in fatty acid metabolism. Within downregulated genes, four are involved in immune function (EBI3, LOC790255, SPINK9, and TRIM40).

The Oleic vs Linoleic comparison within Period 2 yielded 35 DEGs including 12 downregulated and 23 upregulated in the Oleic dietary treatment. Six DEGs are involved in leukocyte immunoglobulin-like receptors, and of those five were upregulated. Nine DEGs are ncRNAs.

The Period 2 Oleic dietary treatment compared to the Period 1 Linoleic dietary treatment yielded 4 DEGs. Two of the DEGs were ncRNAs. Of the remaining DEGs one was upregulated in the Period 1 Linoleic dietary treatment (TAT), and one was downregulated (S100A8).

From the comparison of Period 1 Oleic vs Period 2 Linoleic, there were 35 DEGs. Twenty-five genes were downregulated in the Oleic group and 10 were upregulated. Eight of the DEGs, five downregulated and three upregulated, are ncRNAs. Three upregulated and six downregulated genes relate to immune function.

Table 2. List of significant differentially expressed genes from the RNA-Seq analysis of the rumen epithelium of steers fed two diets with different concentrations of linoleic acid.

Linoleic vs Oleic within Period 1				
Gene Symbol	**$\log_2$CPM[1]**	**$\log_2$FC[2]**	***P*-Value**	**FDR[3]**
LOC112442322	-1.731	-4.320	3.56E-07	1.21E-03
LOC790134	-2.066	-4.039	2.30E-05	3.36E-02
LOC790255	-1.017	-3.557	7.09E-09	4.86E-05
LOC112445644	-0.812	-3.552	8.28E-10	2.54E-05
RPTN	-0.449	-2.853	5.66E-09	4.86E-05
LOC104976640	-1.602	-2.404	2.44E-05	3.40E-02
PRG3_1	-1.127	-2.251	1.84E-06	5.12E-03
SPINK9	-1.075	-2.248	3.49E-05	4.29E-02
TRIM40	5.095	-1.576	1.17E-05	2.00E-02
LOC112448582	2.593	-1.494	3.26E-08	1.25E-04
MYPN	-0.169	-1.480	1.37E-05	2.21E-02
LOC281376	5.447	-1.132	1.14E-05	2.00E-02
EBI3	1.720	-0.987	3.01E-05	4.01E-02
CPT1A	7.038	0.684	4.72E-06	1.11E-02
CDH17	1.715	1.401	7.48E-09	4.86E-05
CHI3L2	2.035	1.415	4.07E-06	1.04E-02
LOC112442313	0.734	1.507	2.95E-08	1.25E-04
LOC100848785	8.500	1.702	1.81E-05	2.78E-02
RNASE13	0.731	1.742	1.42E-08	7.24E-05
ACSBG1	-0.325	2.005	5.77E-07	1.77E-03
LOC100848804	8.261	2.010	8.88E-06	1.75E-02
LOC107132272	4.024	2.238	7.23E-06	1.58E-02
DNAJC6	2.451	2.251	7.93E-09	4.86E-05
LOC100337355	-1.966	2.848	3.38E-05	4.29E-02
LOC112441460	-2.773	5.345	9.13E-06	1.75E-02
Linoleic vs Oleic within Period 2				
Gene Symbol	**$\log_2$CPM[1]**	**$\log_2$FC[2]**	***P*-Value**	**FDR[3]**
PRSS2	-1.482	-7.089	1.99E-13	1.53E-09
OSM	-1.094	-5.880	7.60E-14	1.06E-09
LOC783134	-2.571	-5.206	7.11E-06	1.15E-02
LOC104976076	-2.620	-5.156	1.67E-05	1.99E-02
GTSF1	-1.438	-3.423	1.03E-08	3.97E-05
LOC112445038	-1.138	-2.807	4.56E-07	1.27E-03
ACOD1	-1.821	-2.781	1.26E-05	1.68E-02
NFE2	-1.699	-2.679	1.25E-05	1.68E-02
IL1B	1.708	-2.589	8.19E-06	1.24E-02
PLIN4	0.786	-1.402	2.91E-05	3.19E-02
THBS2	1.709	-1.335	4.86E-06	9.93E-03
ILDR1	0.976	-1.211	3.97E-05	4.20E-02
RIPPLY3	2.694	1.296	1.20E-06	2.83E-03
LOC112444164	0.838	1.536	2.72E-05	3.09E-02
TENM3	-1.110	2.460	8.47E-06	1.24E-02
LOC101907747	-1.333	3.110	1.53E-05	1.96E-02
LOC112447060	-1.951	3.295	4.62E-05	4.57E-02
LOC100848051	4.284	3.650	2.64E-06	5.79E-03
LOC100335780	-2.247	4.647	1.69E-05	1.99E-02
LOC790255	-0.533	5.147	5.25E-05	4.65E-02
LOC112441541	-3.056	6.269	5.30E-05	4.65E-02
LOC112446420	-3.056	6.269	5.30E-05	4.65E-02
LOC785868	-3.056	6.269	5.30E-05	4.65E-02
LOC100852090	-2.986	7.257	6.78E-06	1.15E-02
LOC112444750	-2.986	7.257	6.78E-06	1.15E-02
SHC3	-2.986	7.257	6.78E-06	1.15E-02
LOC100140130	-2.919	7.276	4.40E-05	4.50E-02
LOC101902025	-1.449	8.131	1.03E-13	1.06E-09
HBG	-2.572	8.188	6.23E-07	1.59E-03
ELSPBP1	-2.792	9.989	1.80E-08	6.15E-05
PLD6	-1.711	10.331	5.22E-08	1.60E-04
IFI47	-0.070	10.552	3.62E-14	1.06E-09
LOC112445498	-2.622	12.625	5.66E-11	2.48E-07
LOC790181	-2.622	12.625	5.66E-11	2.48E-07
LOC112445615	-2.518	14.242	1.45E-12	8.92E-09

Continued

GO Analysis

The comparison of Period 1 Linoleic vs Period 2 Oleic did not have enough DEGs to be used in GO analysis. For Linoleic vs Oleic within Period 1, the molecular function SH3 domain binding was identified (Table 3). Linoleic vs Oleic within Period 2 yielded two biological processes: defense response and positive regulation of inflammatory response. GO enrichment of Period 2 Linoleic vs Period 1 Oleic yielded 10 biological processes and three molecular functions.

KEGG Analysis

Similar to the GO analysis there were not enough DEGs present in the comparison of Period 1 Linoleic vs Period 2 Oleic for pathway enrichment analysis. The first analysis completed was Linoleic vs. Oleic within Period 1. Two pathways were identified as

significant (P = 0.034, 0.044). Those two pathways, fatty acid degradation and fatty acid metabolism, only contained the genes CPT1A and ACSBG1 (Table 4). An analysis of Linoleic vs Oleic within Period 2 identified three pathways. These pathways included osteoclast differentiation, malaria, and B cell receptor signaling pathway. All three genes identified in the B cell receptor signaling pathway (LOC100852090, LOC783134, and LOC790255) were also present in the osteoclast differentiation pathway which also included IL1B. There were six overrepresented pathways in the comparison of Period 2 Linoleic vs Period 1 Oleic. All six of these pathways included the genes CXCL5, CXCL2, and CCL20. TNF signaling pathway and Rheumatoid arthritis pathways included only those three genes. The four remaining pathways included the IL-17 signaling pathway, viral protein interaction with cytokine and cytokine receptor, chemokine signaling pathway, and cytokine-cytokine receptor interaction.

Table 2. (cont.)

Period 1 Linoleic vs Period 2 Oleic				
Gene Symbol	**logCPM[1]**	**logFC[2]**	***P*-Value**	**FDR[3]**
LOC104974297	-1.639	3.323	1.99E-07	3.05E-03
LOC112445644	-0.884	-4.994	3.05E-11	9.34E-07
S100A8	7.685	-1.177	5.99E-06	4.98E-02
TAT	1.876	2.190	6.49E-06	4.98E-02
Period 2 Linoleic vs Period 1 Oleic				
Gene Symbol	**logCPM[1]**	**logFC[2]**	***P*-Value**	**FDR[3]**
ACP7	0.616	-2.029	3.46E-06	4.08E-03
ARL4D	1.563	-1.278	1.00E-07	1.80E-04
C11H2orf40	-0.610	-2.038	3.18E-06	4.01E-03
CCL20	2.523	-1.960	6.13E-09	1.57E-05
CDH17	1.614	-1.555	3.85E-07	5.91E-04
CHI3L2	1.782	-2.152	9.20E-11	4.70E-07
CTNNA2	-0.710	-2.501	3.13E-06	4.01E-03
CXCL2	3.174	-1.765	3.27E-06	4.01E-03
CXCL5	-0.150	-2.180	1.43E-09	4.89E-06
CXCR1	-0.374	1.911	3.31E-07	5.35E-04
DACT2	-0.642	2.579	8.36E-08	1.60E-04
DNAJC6	2.390	-2.298	2.90E-08	6.85E-05
EDN3	2.912	-1.037	9.87E-06	1.04E-02
KNG1	-0.542	-1.861	1.35E-05	1.33E-02
LOC101905151	2.746	0.949	1.56E-05	1.40E-02
LOC107132272	3.956	-2.894	2.09E-06	2.91E-03
LOC112441824	-1.813	7.159	7.26E-07	1.06E-03
LOC112442269	-1.902	5.378	2.74E-09	8.41E-06
LOC112442313	0.603	-2.234	1.12E-13	1.14E-09
LOC112445527	5.272	-1.604	1.23E-10	5.38E-07
LOC112445528	5.302	-1.849	4.57E-11	2.81E-07
LOC112445645	8.293	-2.019	4.58E-09	1.28E-05
LOC536097	0.379	-1.237	1.41E-05	1.33E-02
LOC790134	-2.273	4.225	5.71E-06	6.26E-03
MAEL	-1.914	-7.814	4.04E-14	6.20E-10
MYPN	-0.050	1.595	4.73E-06	5.37E-03
POSTN	5.708	-1.468	1.59E-05	1.40E-02
RNASE13	0.633	-2.347	3.77E-08	7.71E-05
RSAD2	2.210	1.661	1.36E-05	1.33E-02
S100A8	7.807	-1.209	3.42E-08	7.49E-05
S100A9	6.672	-2.414	2.59E-21	7.95E-17
SMPDL3B	3.945	-1.305	8.89E-10	3.41E-06
SPATA22	-2.157	4.914	1.43E-05	1.33E-02
SPINK6	-1.642	-3.207	2.66E-07	4.53E-04
STAT4	1.323	1.738	4.17E-11	2.81E-07

[1]logCPM = log counts per million mapped reads.
[2]logFC = $\log_2$ fold change
[3]FDR = false discovery rate, the rate at which genes called significant were null.

4. Discussion and Conclusions

The present study identified an increase in the expression of inflammatory genes in response to increased concentrations of linoleic acid. The inflammatory effect is most evident in the upregulation of chemokine receptors and ligands as well as leukocyte immunoglobulin-like receptors in response to the linoleic acid dietary treatment and was further confirmed by GO and KEGG analysis. Enriched KEGG pathways related to fatty acid metabolism, chemokine signaling, cytokine-cytokine receptor interactions, and other pathways involved in overall immune function. The GO enrichment analysis pointed to similar functions including inflammatory response, chemokine-mediated signaling, and receptor binding among other related processes.

These findings are valuable for a pilot study as this effect in ruminants has only been demonstrated previously as correlations (Reynolds et al., 2017). Outside of ruminants, there is compelling evidence of linoleic acid's inflammatory effects. Several studies in rats and mice have identified linoleic acid in the diet as a factor in colitis and inflammatory diseases in the digestive system (Choque et al., 2014, Romagnolo et al., 2019, Tyagi et al., 2012, Xie

et al., 2020). Romagnolo et al. (2019) reported that risk factors for inflammation were increased by linoleic acid. Even though Romagnolo et al. (2019) did not find direct evidence of inflammation, it was concluded that prolonged or increased exposure to linoleic acid would cause epigenetic modifications leading to inflammation and colon cancer (Romagnolo et al., 2019). Xie et al. (2020) found conflicting results. When examining inflammation based on gene expression, they found no evidence of inflammation in the colon or small intestine. However, a diet higher in linoleic acid did cause a significant ($P \leq 0.05$) increase in plasma eicosanoids (Xie et al., 2020). One of the proposed mechanisms for linoleic acid mediated inflammation is conversion to eicosanoids, so this result is in agreement with our hypothesis (Medzhitov, 2008). Finally, Tyagi et al. (2012) explored the relationship between inflammation and the ratio of linoleic acid to α-linolenic acid (an omega-3 fatty acid) while maintaining the same level of total fatty acid supplementation. As the ratio of linoleic acid to α-linolenic acid decreased so did the inflammation in the colon (Tyagi et al., 2012), indicating that either linoleic acid was causing inflammation or α-linolenic acid was reducing inflammation. These studies all concluded that increased concentrations of linoleic acid result in an increased risk for inflammation and related metabolic diseases.

Table 3. Biological processes and molecular functions identified as being divergent between the differentially expressed genes from the two treatment groups. Analyzed by gene ontology (GO) terms using the Database for Annotation, Visualization, and Integrated Discovery (DAVID)[1].

Analysis	Term	Count	*P*-Value	Genes
s Oleic within Period 1 · Function	SH3 domain binding	2	0.047	DNAJC6, MYPN
s Oleic within Period 2 Processes	Defense response	2	0.024	ACOD1, IFI47
	Positive regulation of inflammatory response	2	0.046	IL1B, OSM
Ieic vs Period 2 Linoleic Processes	Neutrophil chemotaxis	6	1.22E-08	CXCR1, CCL20, S100A9, CXCL2, CXCL5, S100A8
	Chemokine-mediated signaling pathway	4	2.79E-05	CXCR1, CCL20, CXCL2, CXCL5
	Inflammatory response	5	2.01E-04	CXCR1, CCL20, CXCL2, CXCL5, KNG1
	Antimicrobial humoral immune response mediated by antimicrobial peptide	3	0.002	S100A9, CXCL2, CXCL5
	Neutrophil aggregation	2	0.003	S100A9, S100A8
	Peptidyl-cysteine S-nitrosylation	2	0.005	S100A9, S100A8
	Leukocyte migration involved in inflammatory response	2	0.007	S100A9, S100A8
	Astrocyte development	2	0.017	S100A9, S100A8
	Synapsis	2	0.029	SPATA22, MAEL
	Positive regulation of intrinsic apoptotic signaling pathway	2	0.039	S100A9, S100A8
Ieic vs Period 2 Linoleic · Function	Chemokine activity	3	0.001	CCL20, CXCL2, CXCL5
	CXCR chemokine receptor binding	2	0.014	CXCL2, CXCL5
	Antioxidant activity	2	0.020	S100A9, S100A8

[1]Laboratory of Immunopathogenesis and Bioinformatics, SAIC-Frederick, Inc. (Frederick, MD)

Dosage of linoleic acid could play a role in the observed inflammatory effect. The inclusion rate of soybean oil in the present study was 5% on a DM basis. While other studies on ruminants have not examined the inflammatory effect of linoleic acid, linoleic acid's effect on the rumen microbiome has been documented (Ivan et al., 2001, Mao et al., 2010, Yang et al., 2009). Linoleic acid appears to be toxic to protozoa and some other microbes including methanogens (Mao et al., 2010). The effect of linoleic acid on protozoa is the most profound, as soybean oil at 3% of DM reduces rumen populations by 52% (Mao et al., 2010). Similar studies have also examined the effect of linoleic acid on rumen fermentation. Bateman II and Jenkins (1998) utilized diets with several different levels of soybean oil and found that 8% on a DM basis was required to impact the concentration of volatile fatty acids,

an indicator of fermentation efficiency. Bateman II and Jenkins (1998) did find though that 2% inclusion limited the digestibility of fatty acids. A reduction of protozoa in the rumen could have several consequences. Rumen protozoa can use metabolic hydrogen to produce methane (Newbold et al., 2015). Methane production accounts for 48% of metabolic hydrogen uses (Mao et al., 2010). When that pathway is limited hydrogen accumulates in the rumen and can limit fermentation due to a buildup of metabolic end-products (Ungerfeld, 2020). It is unclear if hydrogen disposal through biohydrogenation of unsaturated fatty acids in a diet with increased fatty acids could account for the surplus hydrogen (Mao et al., 2010). In this case, the effect of reducing protozoa could lead to a reduction in the efficiency of fermentation (Ungerfeld, 2020).

Table 4. Pathways identified as overrepresented through the Kyoto Encyclopedia of Genes and Genomes (KEGG)1 pathway analysis of differentially expressed genes in the rumen epithelium of steers between the two treatment groups.

Analysis	Term	Count	*P*-Value	Genes
Linoleic vs Oleic within Period 1	bta00071:Fatty acid degradation	2	0.034	CPT1A, ACSBG1
	bta01212:Fatty acid metabolism	2	0.044	CPT1A, ACSBG1
Linoleic vs Oleic within Period 2	bta04380:Osteoclast differentiation	4	0.001	LOC100852090, LOC783134, IL1B, LOC790255
	bta05144:Malaria	3	0.002	IL1B, HBG, THBS2
	bta04662:B cell receptor signaling pathway	3	0.005	LOC100852090, LOC783134, LOC790255
Period 1 Oleic vs Period 2 Linoleic	bta04657:IL-17 signaling pathway	5	7.40E-06	CCL20, S100A9, CXCL2, CXCL5, S100A8
	bta04061:Viral protein interaction with cytokine and cytokine receptor	4	3.01E-04	CXCR1, CCL20, CXCL2, CXCL5
	bta04062:Chemokine signaling pathway	4	0.002	CXCR1, CCL20, CXCL2, CXCL5
	bta05323:Rheumatoid arthritis	3	0.010	CCL20, CXCL2, CXCL5
	bta04060:Cytokine-cytokine receptor interaction	4	0.011	CXCR1, CCL20, CXCL2, CXCL5
	bta04668:TNF signaling pathway	3	0.013	CCL20, CXCL2, CXCL5

[1]http://www.kegg.jp; accessed through the Database for Annotation, Visualization, and Integrated Discovery (DAVID, Laboratory of Immunopathogenesis and Bioinformatics, SAIC-Frederick, Inc., Frederick, MD

In conclusion, the present study supports the hypothesis that increased linoleic acid in the rumen increases the expression of inflammatory genes and pathways in the rumen epithelium. These results are consistent with previous correlations as well as studies in other species. More research is required to confirm the results predicted by gene expression and to decipher the precise mechanism that caused this to occur.

5. Summary

Linoleic acid is thought to cause an inflammatory response in the gastrointestinal tract. While fatty acids can cause inflammation due to energy surplus, the metabolism of linoleic acid to arachidonic acid can produce eicosanoids. Eicosanoids are prominent mediators of inflammation. This experiment examined the role of linoleic acid on inflammatory gene expression in the rumen epithelium. The two treatments each included 5%, on a DM basis, of one variety of soybean oil. Commodity soybean oil, included in the linoleic diet, has a high concentration of linoleic acid. High oleic soybean oil, included in the oleic diet has a reduced concentration of linoleic acid and elevated oleic acid. RNA-sequencing was used to assess gene expression in the rumen epithelium tissue of steers. Analysis of differentially expressed genes indicated that an increased ruminal concentration of linoleic acid increased the expression of inflammatory genes. This conclusion was supported by the pathway analysis as

well as gene ontology biological processes and molecular functions. Future research should confirm if this effect translates into a functional change and how this impacts overall rumen function.

6. Appendices

6a. Acknowledgements

The authors would like to thank Dr. and Mrs. Niblack for their support of the Niblack Undergraduate Research Scholars Program. Without their support, this project and the experience gained from it would not have been possible. They would also like to thank Dr. Foote for his continuous support of this project and all career aspirations, Dr. Hagen for assisting with analysis and funding, Anna Goldkamp and Carlee Salisbury for help with analysis, and all other students who assisted with this study. This work is supported by Hatch accession number 1019668 from the USDA National Institute of Food and Agriculture.

6b. Papers Published

McConnell, H.L., A.K. Goldkamp, M. King, C.M Salisbury, D. Montgomery, J. Moore, D.E. Hagen, A.P. Foote. 2022. The effect of dietary fatty acid source on gene expression in the rumen of cattle. J. Anim.Sci. 100 (Suppl., in press).

"The effect of dietary fatty acid source on gene expression in the rumen of cattle" American Society of Animal Science National Meeting: June 2022

"The effect of dietary fatty acid source on gene expression in the rumen of cattle" Oklahoma State University Summer Research Expo: July 2022

6c. Literature Cited

Ahola, J. K. & Hill, R. A. 2012. Input factors affecting profitability: a changing paradigm and a challenging time. Feed efficiency in the beef industry, 7-19.

Artegoitia, V. M., Foote, A. P., Lewis, R. M. & Freetly, H. C. 2017. Rumen fluid metabolomics analysis associated with feed efficiency on crossbred steers. Scientific reports, 7, 1-14.

Bateman Ii, H. & Jenkins, T. 1998. Influence of soybean oil in high fiber diets fed to nonlactating cows on ruminal unsaturated fatty acids and nutrient digestibility. Journal of Dairy Science, 81, 2451-2458.

Choque, B., Catheline, D., Rioux, V. & Legrand, P. 2014. Linoleic acid: between doubts and certainties. Biochimie, 96, 14-21.

Hotamisligil, G. S. 2006. Inflammation and metabolic disorders. Nature, 444, 860-867.

Huang Da, W., Sherman, B. T. & Lempicki, R. A. 2009. Systematic and integrative analysis of large gene lists using DAVID bioinformatics resources. Nat Protoc, 4, 44-57.

Ivan, M., Mir, P., Koenig, K., Rode, L., Neill, L., Entz, T. & Mir, Z. 2001. Effects of dietary sunflower seed oil on rumen protozoa population and tissue concentration of conjugated linoleic acid in sheep. Small Ruminant Research, 41, 215-227.

Lindholm-Perry, A. K., Artegoitia, V. M., Miles, J. R. & Foote, A. P. 2017. Expression of cytokine genes and receptors in white blood cells associated with divergent body weight gain in beef steers. Agri Gene, 6, 37-39.

Mao, H.-L., Wang, J.-K., Zhou, Y.-Y. & Liu, J.-X. 2010. Effects of addition of tea saponins and soybean oil on methane production, fermentation and microbial population in the rumen of growing lambs. Livestock Science, 129, 56-62.

Medzhitov, R. 2008. Origin and physiological roles of inflammation. Nature, 454, 428-435.

National Academies of Sciences, Engineering & Medicine 2016. Nutrient requirements of beef cattle.

Newbold, C. J., De La Fuente, G., Belanche, A., Ramos-Morales, E. & Mcewan, N. R. 2015. The role of ciliate protozoa in the rumen. Frontiers in microbiology, 6, 1313.

R Core Team 2021. A language and environment for statistical computing. Vienna, Austria: R Foundation for Statistical Computing.

Reynolds, J., Foote, A., Freetly, H., Oliver, W. & Lindholm-Perry, A. 2017. Relationships between inflammation-and immunity-related transcript abundance in the rumen and jejunum of beef steers with divergent average daily gain. Animal genetics, 48, 447-449.

Romagnolo, D. F., Donovan, M. G., Doetschman, T. C. & Selmin, O. I. 2019. n-6 linoleic acid induces epigenetics alterations associated with colonic inflammation and cancer. Nutrients, 11, 171.

Sherman, B. T., Hao, M., Qiu, J., Jiao, X., Baseler, M. W., Lane, H. C., Imamichi, T. & Chang, W. 2022. DAVID: a web server for functional enrichment analysis and functional annotation of gene lists (2021 update). Nucleic Acids Res, 50, W216-21.

Tyagi, A., Kumar, U., Reddy, S., Santosh, V. S., Mohammed, S. B., Ehtesham, N. Z. & Ibrahim, A. 2012. Attenuation of colonic inflammation by partial replacement of

dietary linoleic acid with α-linolenic acid in a rat model of inflammatory bowel disease. British journal of nutrition, 108, 1612-1622.

Ungerfeld, E. M. 2020. Metabolic Hydrogen Flows in Rumen Fermentation: Principles and Possibilities of Interventions. Frontiers in Microbiology, 11.

Xie, M., Yang, J., Zhang, J., Sherman, H. L., Zhang, Z., Minter, L. M., Hammock, B. D., Park, Y. & Zhang, G. 2020. Effects of Linoleic Acid-Rich Diet on Plasma Profiles of Eicosanoids and Development of Colitis in Il-10–/– Mice. Journal of Agricultural and Food Chemistry, 68, 7641-7647.

Yang, S., Bu, D., Wang, J., Hu, Z., Li, D., Wei, H., Zhou, L. & Loor, J. 2009. Soybean oil and linseed oil supplementation affect profiles of ruminal microorganisms in dairy cows. Animal, 3, 1562-1569.

The Effect of Dietary Fatty Acid Source on Gene Expression in the Rumen

Hunter McConnell

Department of Animal and Food Sciences

Faculty Sponsor: Dr. Andrew Foote

Graduate Student Mentor: Mindy King

Background

- Information is limited about how the utilization of different nutrients impacts feed efficiency
- Previous data indicated a correlation between reduced average daily gain, increased expression of inflammatory genes and rumen fatty acid concentration

  (Lindholm-Perry et al., 2017, Reynolds et al., 2017)
- Understanding the relationship between inflammatory gene expression and rumen fatty acid concentrations is important for understanding nutrient utilization

Justification

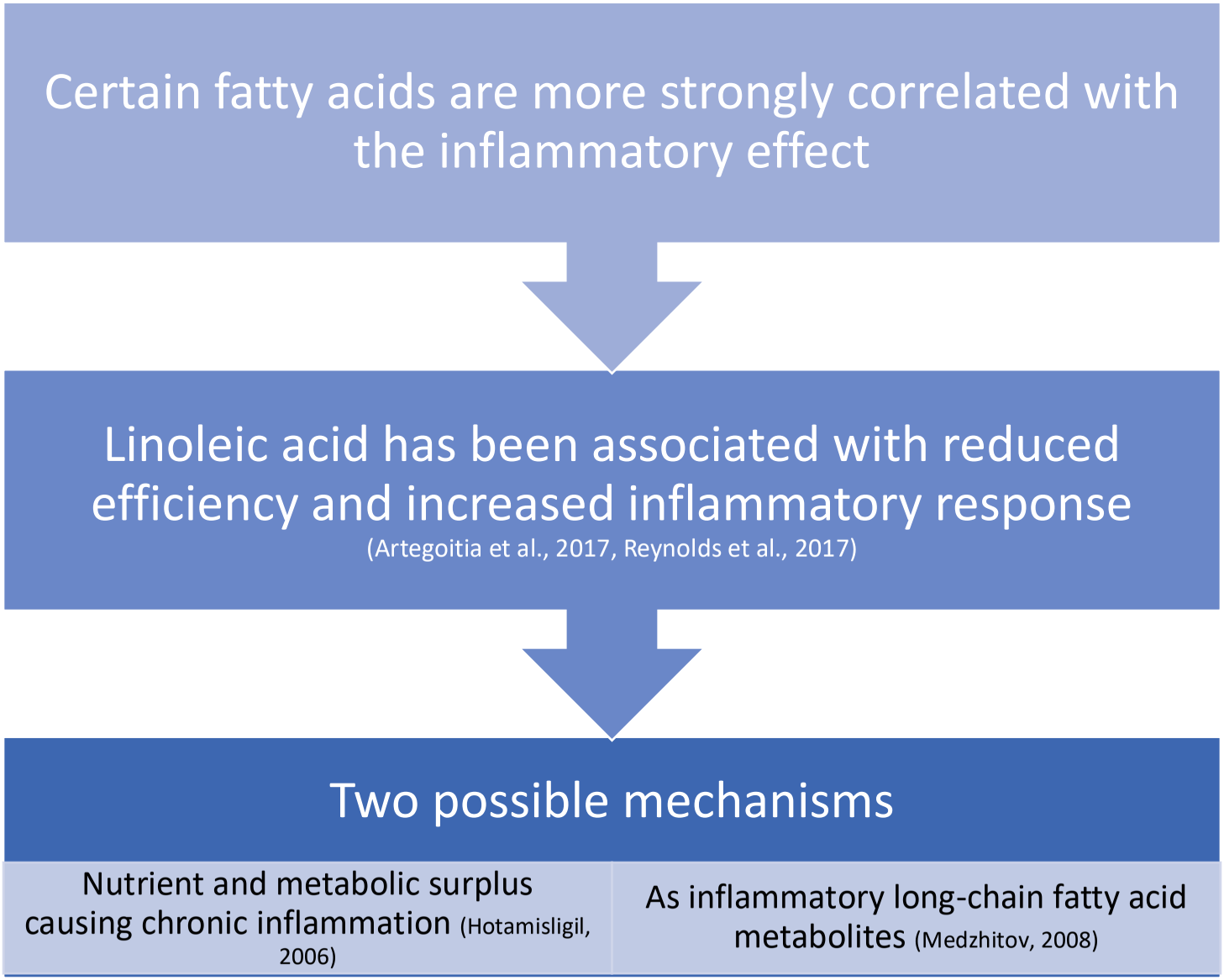

Application to Humans

6% of energy in a US diet is derived from linoleic acid (Choque et al., 2014)

Linoleic acid is an essential fatty acid though current diets likely exceed any requirement (Choque et al., 2014)

It is unlikely that linoleic acid causes inflammation because the conversion of linoleic acid to arachidonic acid is only about 1% (Choque et al., 2014)

In vitro studies indicate that elevated concentrations of linoleic acid will improve the efficiency of the conversion (Choque et al., 2014)

Studies using rodents have identified linoleic acid as a factor in colitis and inflammatory diseases (Choque et al., 2014, Romagnolo et al., 2019, Tyagi et al., 2012, Xie et al., 2020)

Objective: Examine the effect of increased linoleic acid concentrations on inflammatory gene expression

Hypothesis: Increased concentration of linoleic acid will lead to an increase in inflammatory gene expression in the rumen epithelium

Materials and Methods

8 ruminally cannulated Holstein steers (BW 856 ± 78.4 kg)

Crossover design with two 16-d periods and a 20-d washout between the periods

Subsamples of feed were collected on the day feed was batched

Commodity soybean oil was included in the Linoleic diet

High oleic soybean oil was included in the Oleic diet

Item	Linoleic	Oleic
Dry-rolled corn, %	57	57
Sweet Bran, %	25	25
Chopped Hay, %	8	8
Supplement, %	5	5
Commodity Soybean Oil, %	5	0
High Oleic Soybean Oil, %	0	5
Composition, DM basis		
DM, %	93.0	93.1
OM, %	94.9	94.7
NDF, %	19.9	20.8
ADF, %	7.2	7.1
Fat, %	7.4	7.4

Table 1. Diet composition of the treatments fed to the steers. Item percentages are reported on a DM basis. Composition is based on proximate analysis.

Biological Collections and RNA Sequencing

Rumen papillae biopsies were collected on d-16

Rumen papillae were cut from the ventral sac, rinsed with PBS and flash frozen

Total RNA was isolated from the papillae

Sequencing generated paired-end reads of 150 bp length

Data Handling

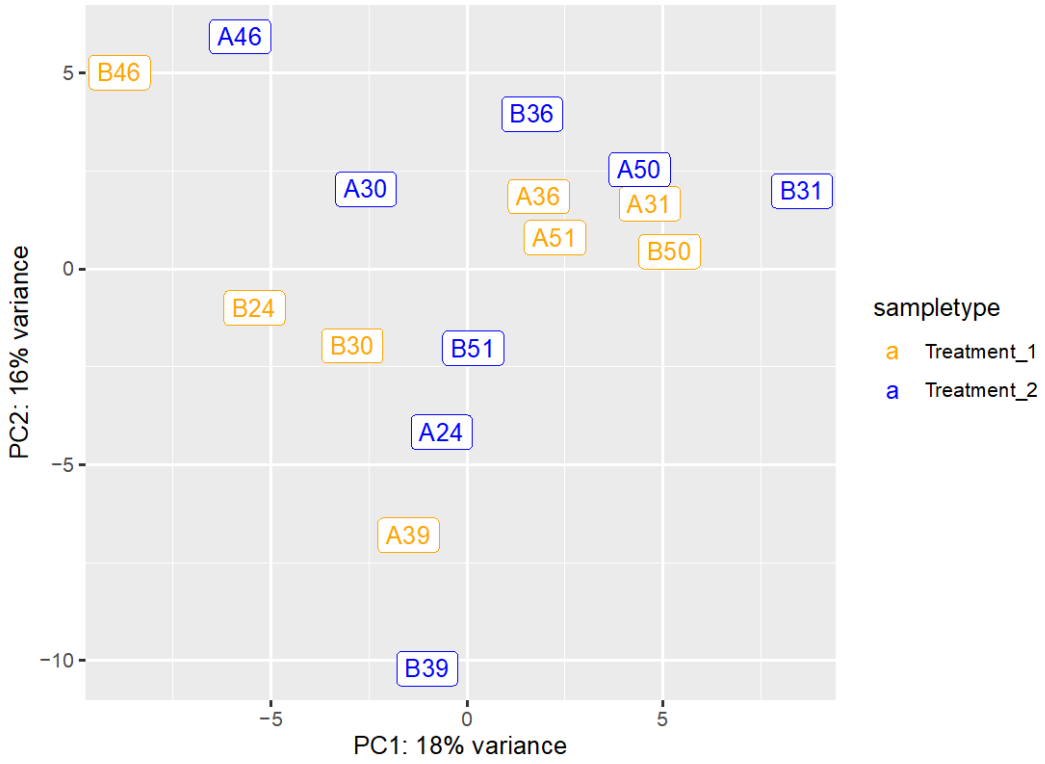

- Raw reads were analyzed for differential gene expression
  - Linoleic vs Oleic
  - Linoleic vs Oleic within Period 1
  - Linoleic vs Oleic within Period 2
  - Period 1 Linoleic vs Period 2 Oleic
  - Period 2 Linoleic vs Period 1 Oleic
- Genes with a p value and false discover rate (FDR) ≤ 0.05 were considered significantly differentially expressed
- Only one test, all Linoleic vs Oleic, yielded no results

Data Handling

Gene Ontology (GO) annotation and Kyoto Encyclopedia of Genes and Genomes (KEGG) pathway analysis were performed using the Database for Annotation, Visualization and Integrated Discovery (DAVID) (Huang da et al., 2009, Sherman et al., 2022)

This identified the biological processes and molecular functions of differentially expressed genes as well as pathways they are involved in

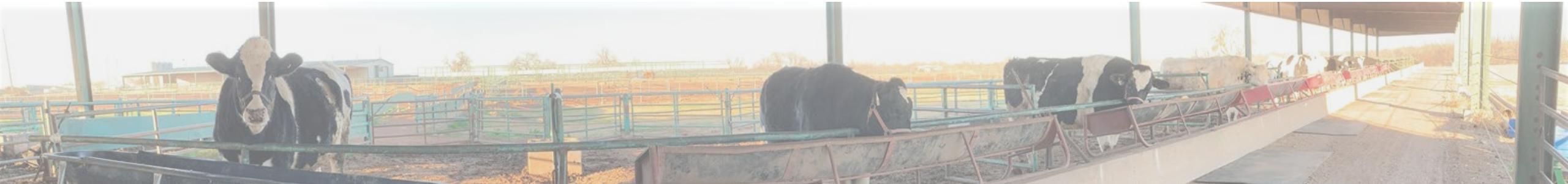

Results

Oleic vs Linoleic treatment within Period 1	Oleic vs Linoleic treatment within Period 2	Period 2 Oleic treatment vs the period 1 Linoleic treatment	Period 1 Oleic Treatment vs Period 2 Linoleic Treatment
• 25 DEGs • 2 upregulated genes involved in fatty acid metabolism • 4 downregulated relate to immune function	• 35 DEGs • 6 involved in leukocyte immunoglobulin-like receptors	• 4 DEGs • TAT was upregulated • S100A8 was downregulated	• 35 DEGs • 3 upregulated and 6 downregulated relate to immune function

Analysis	Term	Count	*P*-Value	Genes
Linoleic vs Oleic within Period 1 Molecular Function	SH3 domain binding	2	0.047	DNAJC6, MYPN
Linoleic vs Oleic within Period 2 Biological Processes	Defense response	2	0.024	ACOD1, IFI47
	Positive regulation of inflammatory response	2	0.046	IL1B, OSM
Period 1 Oleic vs Period 2 Linoleic Biological Processes	Neutrophil chemotaxis	6	1.22E-08	CXCR1, CCL20, S100A9, CXCL2, CXCL5, S100A8
	Chemokine-mediated signaling pathway	4	2.79E-05	CXCR1, CCL20, CXCL2, CXCL5
	Inflammatory response	5	2.01E-04	CXCR1, CCL20, CXCL2, CXCL5, KNG1
	Antimicrobial humoral immune response mediated by antimicrobial peptide	3	0.002	S100A9, CXCL2, CXCL5
	Neutrophil aggregation	2	0.003	S100A9, S100A8
	Peptidyl-cysteine S-nitrosylation	2	0.005	S100A9, S100A8
	Leukocyte migration involved in inflammatory response	2	0.007	S100A9, S100A8
	Astrocyte development	2	0.017	S100A9, S100A8
	Synapsis	2	0.029	SPATA22, MAEL
	Positive regulation of intrinsic apoptotic signaling pathway	2	0.039	S100A9, S100A8
Period 1 Oleic vs Period 2 Linoleic Molecular Function	Chemokine activity	3	0.001	CCL20, CXCL2, CXCL5
	CXCR chemokine receptor binding	2	0.014	CXCL2, CXCL5
	Antioxidant activity	2	0.020	S100A9, S100A8

Table 3. Biological processes and molecular functions identified as being divergent between the differentially expressed genes from the two treatment groups. Analyzed by gene ontology (GO) terms using the Database for Annotation, Visualization, and Integrated Discovery (DAVID)[1].

Analysis	Term	Count	*P*-Value	Genes
Linoleic vs Oleic within Period 1	bta00071:Fatty acid degradation	2	0.034	CPT1A, ACSBG1
	bta01212:Fatty acid metabolism	2	0.044	CPT1A, ACSBG1
Linoleic vs Oleic within Period 2	bta04380:Osteoclast differentiation	4	0.001	LOC100852090, LOC783134, IL1B, LOC790255
	bta05144:Malaria	3	0.002	IL1B, HBG, THBS2
	bta04662:B cell receptor signaling pathway	3	0.005	LOC100852090, LOC783134, LOC790255
Period 1 Oleic vs Period 2 Linoleic	bta04657:IL-17 signaling pathway	5	7.40E-06	CCL20, S100A9, CXCL2, CXCL5, S100A8
	bta04061:Viral protein interaction with cytokine and cytokine receptor	4	3.01E-04	CXCR1, CCL20, CXCL2, CXCL5
	bta04062:Chemokine signaling pathway	4	0.002	CXCR1, CCL20, CXCL2, CXCL5
	bta05323:Rheumatoid arthritis	3	0.010	CCL20, CXCL2, CXCL5
	bta04060:Cytokine-cytokine receptor interaction	4	0.011	CXCR1, CCL20, CXCL2, CXCL5
	bta04668:TNF signaling pathway	3	0.013	CCL20, CXCL2, CXCL5

Table 4. Pathways identified as overrepresented through the Kyoto Encyclopedia of Genes and Genomes (KEGG)1 pathway analysis of differentially expressed genes in the rumen epithelium of steers between the two treatment groups.

Dosage of Linoleic Acid and the Rumen Microbiome

Linoleic acid may be toxic to protozoa and some other microbes in the rumen (Mao et al., 2010)

Soybean oil at 2% of dry matter (DM) was required to limit the digestibility of fatty acids
(Bateman II and Jenkins, 1998)

3% of DM reduced the rumen population of protozoa by 52% (Mao et al., 2010)

8% of DM impacted the concentrations of VFAs
(Bateman II and Jenkins, 1998)

Summary

Fatty acids can cause inflammation due to metabolic surplus

Linoleic acid specifically can be metabolized to arachidonic acid which is a precursor to eicosanoids

Differential gene expression indicated increased expression of inflammatory genes in the rumen epithelium

This was supported by pathway analysis as well as GO biological processes and molecular functions

Future research should be used to confirm the effect on gene expression translates into a functional change

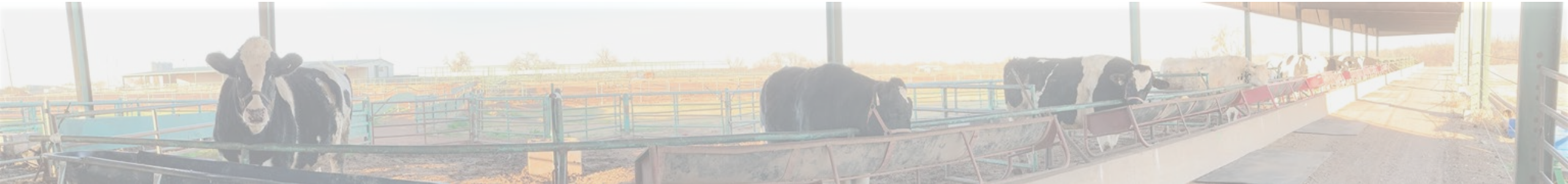

Literature Cited

Ahola, J. K. & Hill, R. A. 2012. Input factors affecting profitability: a changing paradigm and a challenging time. Feed efficiency in the beef industry, 7-19.

Artegoitia, V. M., Foote, A. P., Lewis, R. M. & Freetly, H. C. 2017. Rumen fluid metabolomics analysis associated with feed efficiency on crossbred steers. Scientific reports, 7, 1-14.

Bateman Ii, H. & Jenkins, T. 1998. Influence of soybean oil in high fiber diets fed to nonlactating cows on ruminal unsaturated fatty acids and nutrient digestibility. Journal of Dairy Science, 81, 2451-2458.

Choque, B., Catheline, D., Rioux, V. & Legrand, P. 2014. Linoleic acid: between doubts and certainties. Biochimie, 96, 14-21.

Hotamisligil, G. S. 2006. Inflammation and metabolic disorders. Nature, 444, 860-867.

Huang Da, W., Sherman, B. T. & Lempicki, R. A. 2009. Systematic and integrative analysis of large gene lists using DAVID bioinformatics resources. Nat Protoc, 4, 44-57.

Ivan, M., Mir, P., Koenig, K., Rode, L., Neill, L., Entz, T. & Mir, Z. 2001. Effects of dietary sunflower seed oil on rumen protozoa population and tissue concentration of conjugated linoleic acid in sheep. Small Ruminant Research, 41, 215-227.

Lindholm-Perry, A. K., Artegoitia, V. M., Miles, J. R. & Foote, A. P. 2017. Expression of cytokine genes and receptors in white blood cells associated with divergent body weight gain in beef steers. Agri Gene, 6, 37-39.

Mao, H.-L., Wang, J.-K., Zhou, Y.-Y. & Liu, J.-X. 2010. Effects of addition of tea saponins and soybean oil on methane production, fermentation and microbial population in the rumen of growing lambs. Livestock Science, 129, 56-62.

Medzhitov, R. 2008. Origin and physiological roles of inflammation. Nature, 454, 428-435.

National Academies of Sciences, Engineering & Medicine 2016. Nutrient requirements of beef cattle.

Newbold, C. J., De La Fuente, G., Belanche, A., Ramos-Morales, E. & Mcewan, N. R. 2015. The role of ciliate protozoa in the rumen. Frontiers in microbiology, 6, 1313.

R Core Team 2021. A language and environment for statistical computing. Vienna, Austria: R Foundation for Statistical Computing.

Reynolds, J., Foote, A., Freetly, H., Oliver, W. & Lindholm-Perry, A. 2017. Relationships between inflammation-and immunity-related transcript abundance in the rumen and jejunum of beef steers with divergent average daily gain. Animal genetics, 48, 447-449.

Romagnolo, D. F., Donovan, M. G., Doetschman, T. C. & Selmin, O. I. 2019. n-6 linoleic acid induces epigenetics alterations associated with colonic inflammation and cancer. Nutrients, 11, 171.

Sherman, B. T., Hao, M., Qiu, J., Jiao, X., Baseler, M. W., Lane, H. C., Imamichi, T. & Chang, W. 2022. DAVID: a web server for functional enrichment analysis and functional annotation of gene lists (2021 update). Nucleic Acids Res, 50, W216-21.

Tyagi, A., Kumar, U., Reddy, S., Santosh, V. S., Mohammed, S. B., Ehtesham, N. Z. & Ibrahim, A. 2012. Attenuation of colonic inflammation by partial replacement of dietary linoleic acid with α-linolenic acid in a rat model of inflammatory bowel disease. British journal of nutrition, 108, 1612-1622.

Ungerfeld, E. M. 2020. Metabolic Hydrogen Flows in Rumen Fermentation: Principles and Possibilities of Interventions. Frontiers in Microbiology, 11.

Xie, M., Yang, J., Zhang, J., Sherman, H. L., Zhang, Z., Minter, L. M., Hammock, B. D., Park, Y. & Zhang, G. 2020. Effects of Linoleic Acid-Rich Diet on Plasma Profiles of Eicosanoids and Development of Colitis in Il-10–/– Mice. Journal of Agricultural and Food Chemistry, 68, 7641-7647.

Yang, S., Bu, D., Wang, J., Hu, Z., Li, D., Wei, H., Zhou, L. & Loor, J. 2009. Soybean oil and linseed oil supplementation affect profiles of ruminal microorganisms in dairy cows. Animal, 3, 1562-1569.

Acknowledgements

- Dr. and Mrs. Niblack
- Dr. Andrew Foote
- Dr. Darren Hagen
- Mindy King
- Anna Goldkamp and Carlee Salisbury
- Graduate and Undergraduate Students

Effect of Overexpression of Sulfate Transporter Gene AST68 on Arsenic Tolerance in *Arabidopsis thaliana*

Andre Abit

Department of Biochemistry and Molecular Biology
Faculty Sponsor: Dr. Ramanjulu Sunkar
Graduate Student Mentor: Pei Jia Ng

Abstract

Arsenic (*As*) is the most toxic metalloid, which is widely distributed and abundant in the environment. *As* can accumulate in plant roots to levels that causes physiological and morphological disorders, and plant death. Plants can combat *As* toxicity via detoxification and tolerance mechanisms. Sulfur alleviates arsenic toxicity in plants via detoxification. Global gene expression analysis in response to *As* stress revealed a strong increase in transcripts encoding proteins involved in sulfate transport and assimilation. This led to our hypothesis that enhanced sulfate uptake has a key role in ameliorating *As* toxicity in plants via sulfate-derived antioxidants such as glutathione and phytochelatins. To address this hypothesis, we overexpressed a sulfate transporter gene, AST68, in *Arabidopsis thaliana* ecotype *Columbia* (Col) and evaluated whether or not the transgenic *A. thaliana Col* (OE3 and OE6) will tolerate *As* toxicity compared to the control or wild type *A. thaliana Col* (COL) under different concentrations of Arsenite (0, 20, 30 and 40 microM). Our data supported our initial hypothesis. Under different *As* treatments, there were significant differences between the root lengths of the three *A. thaliana Col* strains. The average root lengths of OE3 and OE6 *A. thaliana Col* were around 17-25% longer than the wild type *A. thaliana Col*, which reveals that transgenic lines are more likely to tolerate *As* stress and grow better under such condition. The overexpression of sulfate transporter gene (AST68) has a significant effect on the *A. thaliana Col* root growth and its ability to tolerate *As* stress.

1. Introduction

Arsenic (*As*) is the most toxic metalloid that is widely distributed and abundant in the environment (Tu and Ma, 2003) and poses toxicity problems to all living organisms including plants and animals (Zhao et al., 2009 and Tripathi et al., 2014). The most common pathway of *As* entering the human body is through consumption of plants for food. Rice, one

of the top three most consumed grains in the world, is affected by *As* toxicity (Hassan et al., 2017). Due to the sessile nature of plants, it is imperative to find ways to help them tolerate *As* stress. In plants, *As* can accumulate in roots that could eventually reach a toxic level. Arsenic toxicity in plants disrupts several physiological and biochemical processes including disruption in photosynthesis and respiration, impairment of nutrient uptake, competition with plant nutrients, shoot and root growth inhibition, and biomass reduction resulting to yield loss and even plant death (Garg and Singla, 2011; Srivastava and D'Souza, 2010). At the biochemical level, plants modulate several pathways that keeps arsenic levels below toxic levels to survive *As* stress. The sulfate assimilation pathway followed by cysteine biosynthetic pathway produces glutathione (GSH) which leads to Phytochelatin (PCs) production (Grill et al., 1987; Hartley-Whitaker et al., 2001; Li et al., 2004; Schmöger et al., 2000; and Zhao et al., 2009). Both detoxification compounds lead to increased arsenic resistance and tolerance in plants. GSH is the central molecule that is derived from sulfate assimilation. GSH has been noted to be a redox regulator and functions as an antioxidant in heavy metal detoxification in plants. PCs also reduce heavy metal toxicity by immobilizing metals throughout the plant (Schmöger et al., 2000).

Several pieces of evidence support a strong connection between sulfate metabolism and arsenic tolerance in several organisms including plants. In yeast, AP1-like transcription factors mediate increased sulfate assimilation leading to production of GSH and regulate the expression of arsenic detoxification genes such ACR2 (arsenate reductase) and ACR3 (arsenite transporter) (Thorsen et al., 2007). Addition of sulfate to the growing media can enhance arsenic accumulation in *As* tolerant plant, *Pteris vittata* (Wei et al., 2009). Furthermore, global gene expression analysis in response to *As* stress in plants revealed a strong increase in transcripts encoding proteins involved in sulfate transport and assimilation (Fu et al., 2014). The positive correlation between sulfate uptake and assimilation to arsenic detoxifying genes has led us to hypothesize that enhanced sulfate uptake has a key role in ameliorating arsenic toxicity in plants, potentially via sulfate-derived antioxidants such as glutathione and phytochelatins. To address this hypothesis, this study aimed to determine the effect of overexpressing AST68 sulfate transporter gene on alleviating *As* toxicity in *Arabidopsis thaliana* ecotype *Columbia (Col)*. The overall objective was to determine the plant stress response to *As* toxicity in wild type *A. thaliana Col* compared to transgenic *A. thaliana Col* with an overexpressed version of the AST68 sulfate transporter gene.

2. Materials and Methods

A. thaliana Col seeds were planted in potted soil to produce enough plants for the transformation stage. After one to two weeks of growth and once the *A. thaliana Col* plants reached the flowering stage, the flowering buds were dipped into a medium containing *Agrobacterium* culture that contain the sulfate transporter gene, AST68. This process would allow the *Agrobacterium* to make physical contact with the cells of the flowering bud. The extra copy of AST68 gene from the agrobacteria would transfer into the cells of the

flowering bud that eventually produced the maturing *A. thaliana Col* seeds. The newly produced *A. thaliana Col* seeds are anticipated to have AST68 gene overexpressed in their genome.

Matured transgenic *A. thaliana Col* seeds were harvested and then planted in round agar plates made from MS Basal Salt Mix, sucrose, and Agar at 5.7-5.8 pH with hygromycin to select for hygromycin resistant plants. After two to three weeks, the plants were inspected, and well-germinated plants were selected. The selected *A. thaliana Col* plants were then transferred to potted soil container and grown to collect more seeds for further trials.

Leaf samples from transgenic plants were obtained at the juvenile stage for DNA extraction to verify if the AST68 gene was successfully overexpressed in the transgenic *A. thaliana Col* plants. DNA extraction was performed for each leaf sample. Cetyltrimethylammonium bromide (CTAB) and chloroform were utilized to separate organic contaminants from the nucleic acids. Isopropanol and ethanol were then used to form the DNA pellet. The DNA samples of the transgenic plants were then used in polymerase chain reaction (PCR) with the proper transgene specific AST68 primers. After the DNA samples of the transgenic plants have undergone PCR, we identified which plants had the highest AST68 expression level. The highest-expressed-transgenic AST68 lines were planted once again to produce more transgenic seeds for the treatment phase.

We selected two transgenic seed lines with the highest AST68 gene expression, OE3 and OE6. Several concentrations of Arsenite: 0, 20, 30 and 40 microM were used in different vertical agar plates that were used to grow wild type and overexpressed AST68 transgenic *A. thaliana* plants. These Arsenite concentrations were selected because the roots of wild type *A. thaliana* were affected at 20 microM or greater (Xu et al., 2015). In each Arsenite concentration, we planted three different *A. thaliana* strains: 1) Control (wild type *A. thaliana Col,* (COL)), 2) Transgenic *A. thaliana Col* with overexpressed AST68 gene (OE3); 3) Transgenic *A. thaliana Col* with overexpressed AST68 gene (OE6). Each treatment plate was divided into three columns where the wild type (control), and *A. thaliana Col* seeds with overexpressed AST68 (OE3 and OE6) were planted, respectively. The vertical agar plates planted with the three different *A. thaliana Col* seeds were placed in a growth chamber where every variable (i.e., light, temperature) was controlled eliminating the confounding variables that could potentially skew our results. Throughout the *A. thaliana's* life cycle, root length was observed and measured to see if there was a change and difference between the treatment groups.

3. Results

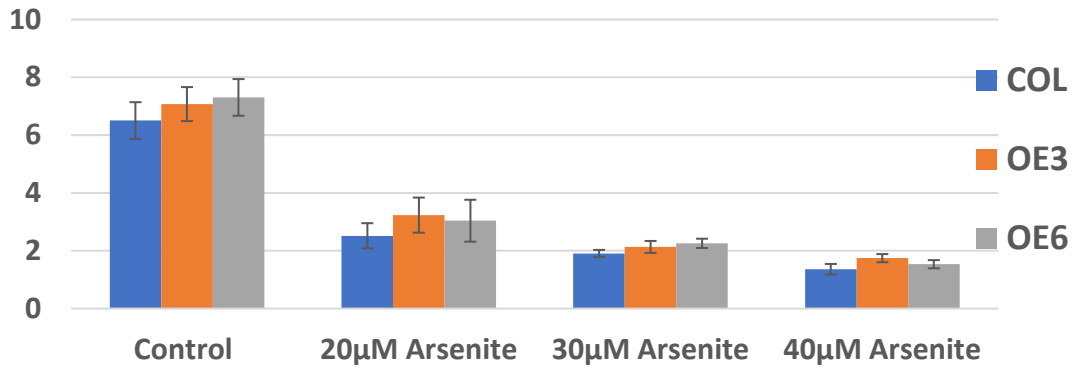

Figure 1. Average root length (cm) for the wild type (COL), overexpressed AST68 (OE3) and overexpressed AST68 (OE6) *A. thaliana Col* in the four arsenic concentrations.

Table 1. Calculated p-values (0.05 level of significance) from the one-way ANOVA test for the three *As* treatment groups.

	20 microliters *As*	30 microliters *As*	40 microliters *As*
Calculated p-value	0.000248	0.039999	0.011316

Root length is a simple phenotypic trait to observe when studying plant health. A healthy plant will express longer roots with moderate root branching. Conversely, unhealthy plants will have much shorter roots that have high root branching close to the soil surface (Jordan et al., 2003). As shown on Figure 1 as well as in Figure 2 in comparison to Figure 3, *A. thaliana* plants that were exposed to *As* stress decreased the average root lengths significantly compared to the control Arsenite concentration. However, despite shorter root lengths under *As* treatment, Figures 1 and 3 show that both the OE3 and OE6 transgenic lines had longer root lengths than wild type *A. thaliana* plants. One-way ANOVA tests with significance levels at 0.05 was used to see if there were statistically significant differences between the different strains of *A. thaliana Col* in each treatment groups. As shown on Table 1, p-values of all three *As* treatment groups were below the 0.05 significance level, revealing that OE3 and OE6 transgenic lines had significantly longer root length and are more likely to tolerate *As* toxicity better than the control plants (COL).

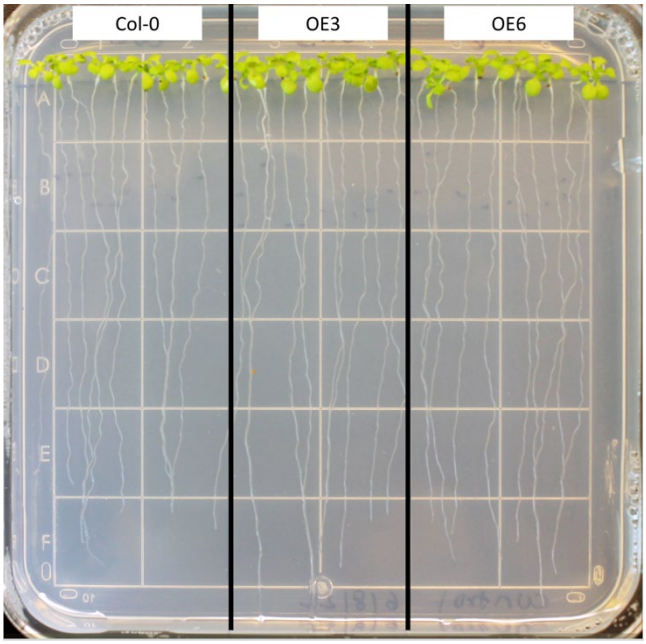

Figure 2. Control vertical plates housing wild type (COL), OE3, and OE6 *A. thaliana Col* at 0 microM of *As*.

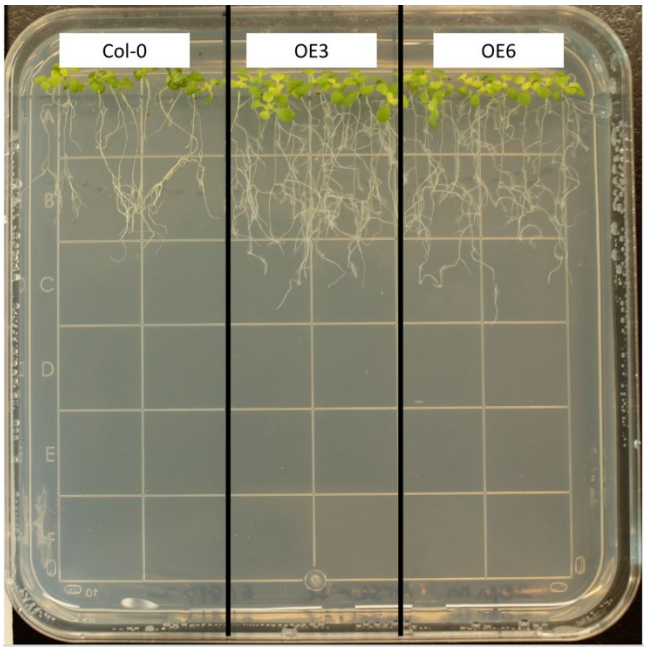

Figure 3. Treatment vertical plates housing wild type (COL), OE3, and OE6 *A. thaliana Col* at 20 microM of *As*.

4. Discussion and Conclusion

Our data supported our initial hypothesis that enhanced sulfate uptake and assimilation have a significant role on a plants ability to tolerate or suppress *As* toxicity. In the different *As* treatments, there was a significant difference between the root lengths of the three *A. thaliana Col* strains. The average root lengths of OE3 and OE6 *A. thaliana Col* were around 17-25% longer than the wild type *A. thaliana Col* (Figure 1)*,* which shows that transgenic plants with an overexpression of AST68 gene are growing better under *As* stress. Such results could potentially be due to an increased amount of sulfate entering the OE3 and OE6 *A. thaliana Col.* When the plant has access to more sulfur, it may have a greater capacity to produce GSH and phytochelatins. Other studies have shown that GSH and phytochelatins are vital in *As* detoxification (Grill et al., 1987 and Hartley-Whitaker, 2001). In a similar study, Li et al. (2004) discovered that increased phytochelatin production would suppress arsenic uptake through complexation with *As*. Similarly, Thorsen et al. (2007) found that the overexpression of phytochelatins in yeast lead to an increased resistance against *As* stress. So, if plants have an overexpressed AST68 sulfate transporter gene, it could tolerate arsenic stress better, potentially via the increased production of sulfate derived compounds such as GSH and phytochelatins.

The results gathered from this study can be applied in other plants that are exposed to *As* stress. Ultimately, our research group is interested on how these genetic changes will help rice, one of the staple crops in the world, better tolerate *As* stress in the field, since *As* threatens major rice growing countries. However, before field trials can be made, we must explore other potential genetic tools to help plants tolerate *As* stress. While our data revealed a significant difference between wild type and transgenic AST68 *A. thaliana,* we only tested the overexpression of one certain gene. For future studies, it would be beneficial to evaluate knockout mutants for the AST68 sulfate transporter gene and study their sensitivity to *As* stress. Different concentrations of *As* should also be evaluated to see which expression levels of the AST68 gene works best at a certain level. Once we understand how to manipulate the expression of the AST68 sulfate transporter gene at various concentrations of *As,* we could then evaluate the expression level of AST68 on rice and other crops exposed to *As* stress.

5. Summary

Based on our findings, the overexpression of sulfate transporter gene, AST68, has a significant effect on the *A. thaliana Col* root growth and on its ability to tolerate arsenic stress compared to control or wild type *A. thaliana Col* (without overexpressed AST68 gene). Through evaluating the overexpression of AST68 gene on *A. thaliana Col* under arsenic stress, we concluded that there is a significant role in which increased sulfate assimilation and metabolism in plants can ameliorate arsenic toxicity. Understanding the relationship between the overexpression of AST68 gene has on a plant's phenotype and its tolerance to *As*

toxicity could potentially create transgenic plants (or crops) that are more stress tolerant to high arsenic levels.

6. Appendices

6a. Acknowledgment

I would like to thank Dr. John Niblack and Mrs. Heidi Niblack for their generosity in providing funding for my Niblack Research Scholarship and be able to conduct this study. I would also like to thank Dr. Ramanjulu Sunkar and Pei Jia Ng for providing me valuable educational and research experiences, and guidance throughout the conduct of this study. I thank Dr. Yofang Li for aiding in the research plans. I also dedicate this work to Dr. William (Bill) Raun† who was my first mentor in research and encouraged me to further develop my research skills.

6b. Literature Cited

Fu, S.F., Chen, P.Y., Nguyen, Q.T., Huang, L-Y., Zeng, G-R., Huang T-L, Lin, C., Huang, H. J. 2014. Transcriptome profiling of genes and pathways associated with arsenic toxicity and tolerance in Arabidopsis. BMC Plant Biol. 14:94.

Garg, N., and Singla, P. 2011. Arsenic toxicity in crop plants: physiological effects and tolerance mechanisms. Environ Chem. Lett 9:303–321.

Grill, E., Winnacker, EL., Zenk, MH. 1987. Phytochelatins, a class of heavy-metal-binding peptides from plants are functionally analogous to metallothioneins. Proceedings of the National Academy of Sciences. USA 84:439-443.

Hartley-Whitaker, Ainsworth, G, Voojis R., Ten Bookum W., Schat, H, Meharg, A. A. 2001. Phytochelatins are involved in differential arsenate tolerance in *Holcus lanatus*. Plant Physiology 126: 299–306.

Hassan, F.E., Niaz, K., Khan, F., Maqbool, F., Abdollahi, M. 2017. The relation between rice consumption, arsenic contamination, and prevalence of diabetes in South Asia. Excli Journal. 16:1132-1143.

Jordan, J.E., White, R.H., Vietor, D.M., Hale, T.C., Thomas, J.C., Engelke, M.C. 2003. Effect of Irrigation Frequency on Turf Quality, Shoot Density, and Root Length Denisty of Five Bentgrass Cultivars. Crop Science. 43(1): 282-287.

Li, Y.J., Dhankher, O.P., Carreira L., Lee. D., Chen. A., Schroeder. J.I., Balish, R.S., Meagher, R. B. 2004. Overexpression of phytochelatin synthase in Arabidopsis leads to enhance arsenic tolerance and cadmium hypersensitivity. Plant and Cell Physiology 45:1787–1797.

Schmöger, M.E.V., Oven. M., Grill, E. 2000. Detoxification of arsenic by phytochelatins in plants. Plant Physiology 122: 793–801.

Srivastava, S. and S.F. D'Souza. 2010. Effect of variable sulfur supply on arsenic tolerance and antioxidant responses in *Hydrilla verticillata* (L.f.) Royle, Ecotoxicology and Environmental Safety 73(6):1314-1322.

Thorsen M, Lagniel G, Kristiansson E, Junot C, Nerman O, Labarre J, Tamás MJ. 2007. Quantitative transcriptome, proteome, and sulfur metabolite profiling of the *Saccharomyces cerevisiae* response to arsenite. Physiol Genomics 30:35–43.

Tripathi D., Singh, V., Chauhan, D., Prasad, S., Dubey, N. 2014. Role of Macronutrients in Plant Growth and Acclimation: Recent Advances and Future Prospective. In: Ahmad P., Wani M., Azooz M., Phan Tran LS. (eds) Improvement of Crops in the Era of Climatic Changes. Springer, New York, NY.

Tu, S., and Ma, L.Q. 2003. Effects of arsenate and phosphate on their accumulation by an arsenic-hyperaccumulator *Pteris vittata* L. Plant Soil 249:373–382.

Wei, S., Ma, L. Q., Sahab, U., Mathews, S., Sundaram, S., Rathinasabapathic, B., Zhou, Q. 2009. Sulfate and glutathione enhanced arsenic accumulation by arsenic hyperaccumulator *Pteris vittata* L. Environmental Pollution. 158:1530-1535.

Xu, W., Dai, W., Yan, H., Shen, H., Chen, Y., Xu, H., Sun, Y., He, Z., Ma, M. 2015. Arabidopsis NIP3;1 Plays an Important Role in Arsenic Uptake and Root-to-Shoot Translocation under Arsenite Stress Conditions. Mol Plant. 8(5):722-33.

Zhao F. J, Ma, J. F., Meharg, A.A., and McGrath S. P. 2009. Arsenic uptake and metabolism in plants-Tansley Review. New Phytologists. 181:777-794.

Effect of Sulfate Transporter Gene Overexpression on Arsenic tolerance in *Arabidopsis thaliana*

Andre Abit
Dr. Ramanjulu Sunkar
Pei Jia Ng

Department of Biochemistry and Molecular Biology

Oklahoma State University

ARSENIC TOXICITY

- Arsenic (*As*) is commonly found in soils that are used in agriculture.
- Arsenic has negative affects on the development of both plants and animals.

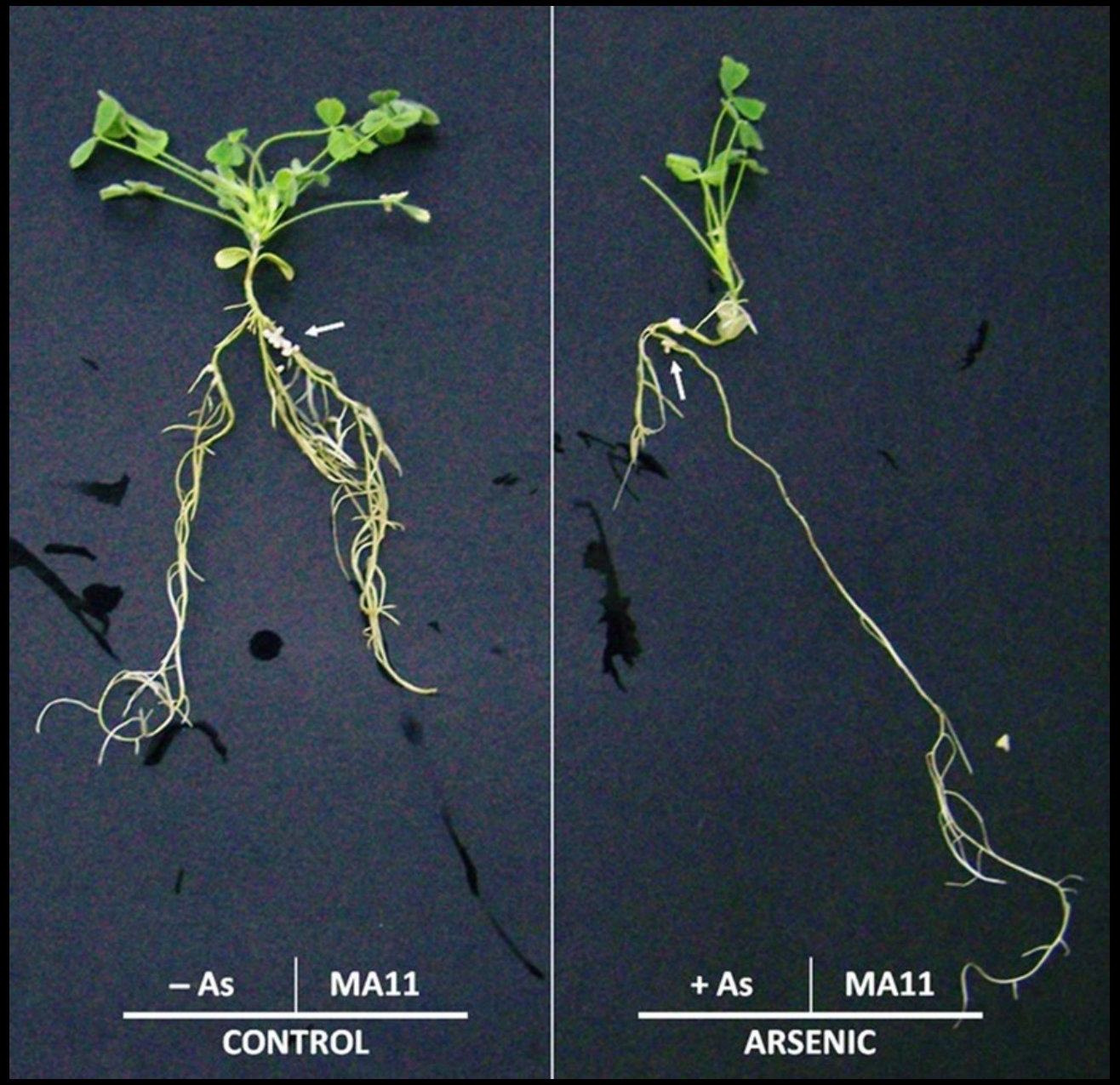

https://doi.org/10.1111/nph.13009

Sulfate Transporter Gene AST68

Glutathione

- Derived from sulfate
- Redox regulator
- Functions as an antioxidant in heavy metal detoxification in plants.

Phytochelatins

- Derived from Glutathione
- Immobilizes heavy metals via complexation

EXPERIMENTAL PROCEDURES

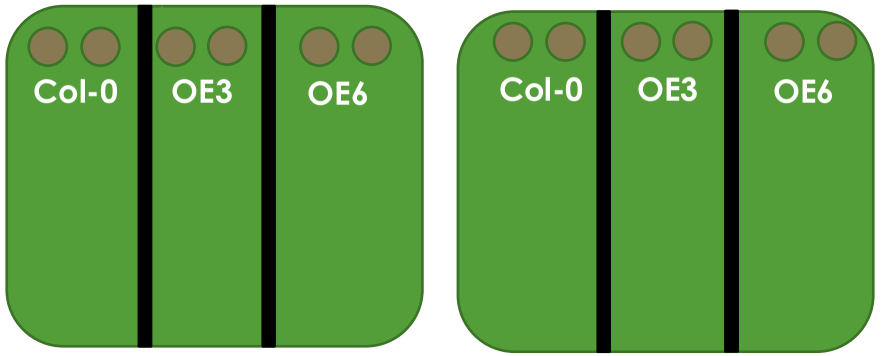

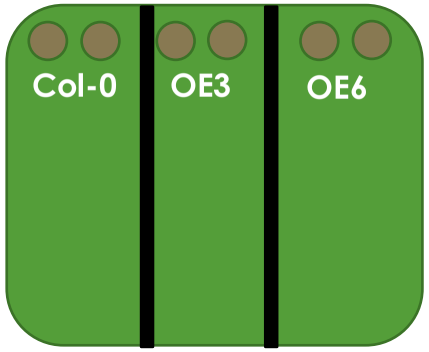

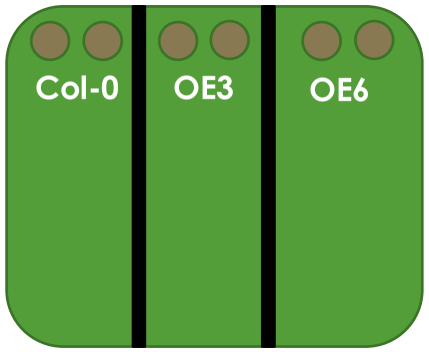

Production of Transgenic Plants

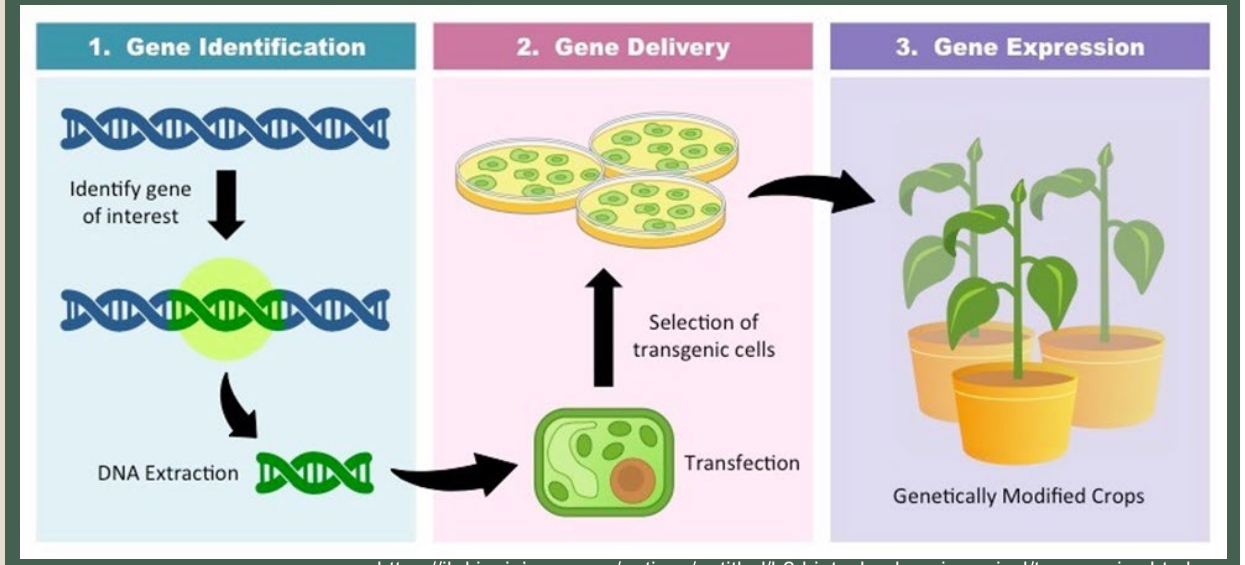

https://ib.bioninja.com.au/options/untitled/b2-biotechnology-in-agricul/transgenics.html

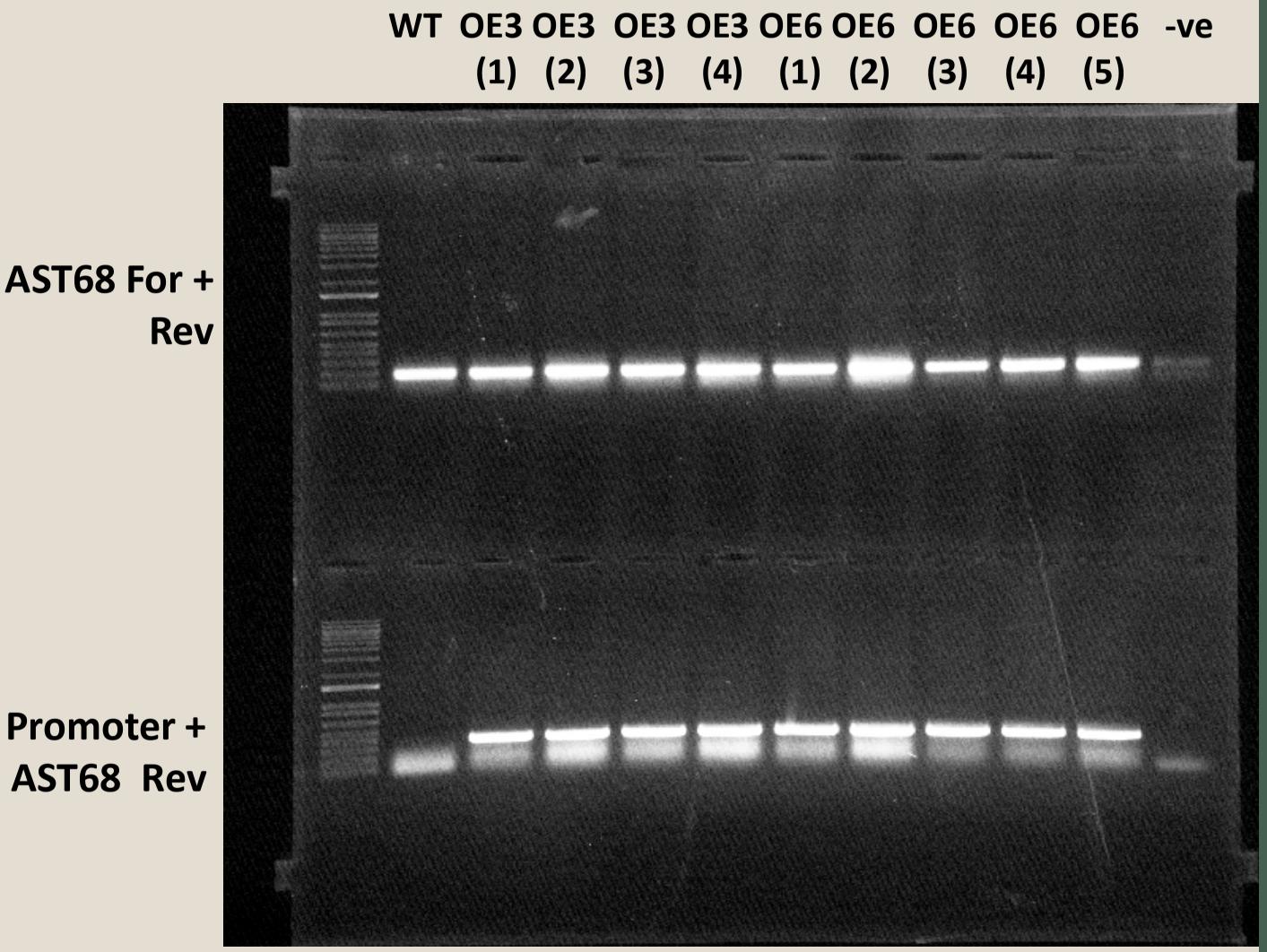

AST68 Sulfate Transporter Gene

RESULTS

Control plate: Wild type (COL), OE3, and OE6 *A. thaliana* at 0 µM of *As*

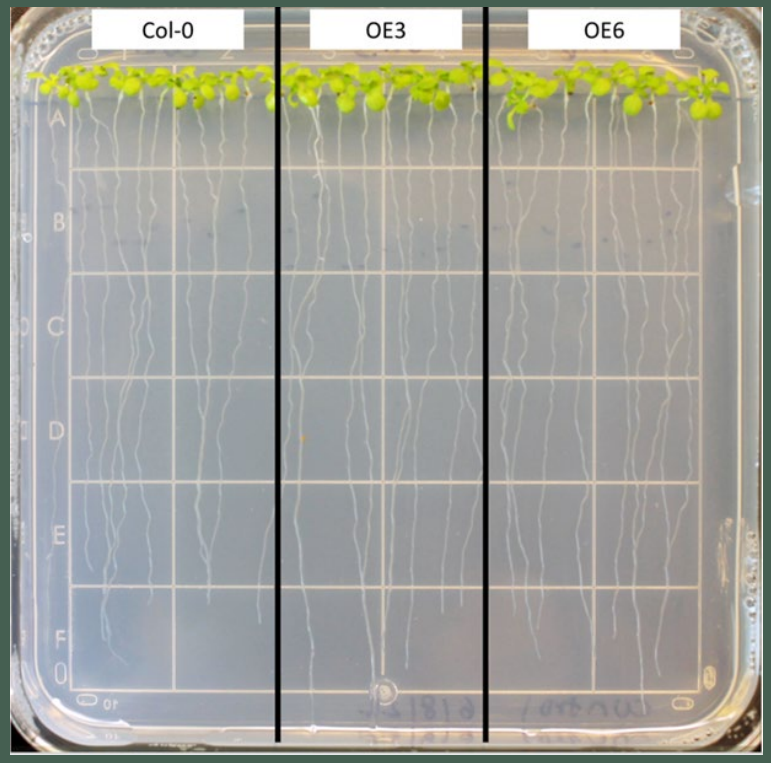

Treatment plate: With wild type (COL), OE3, and OE6 *A. thaliana* at 0 µM of *As*

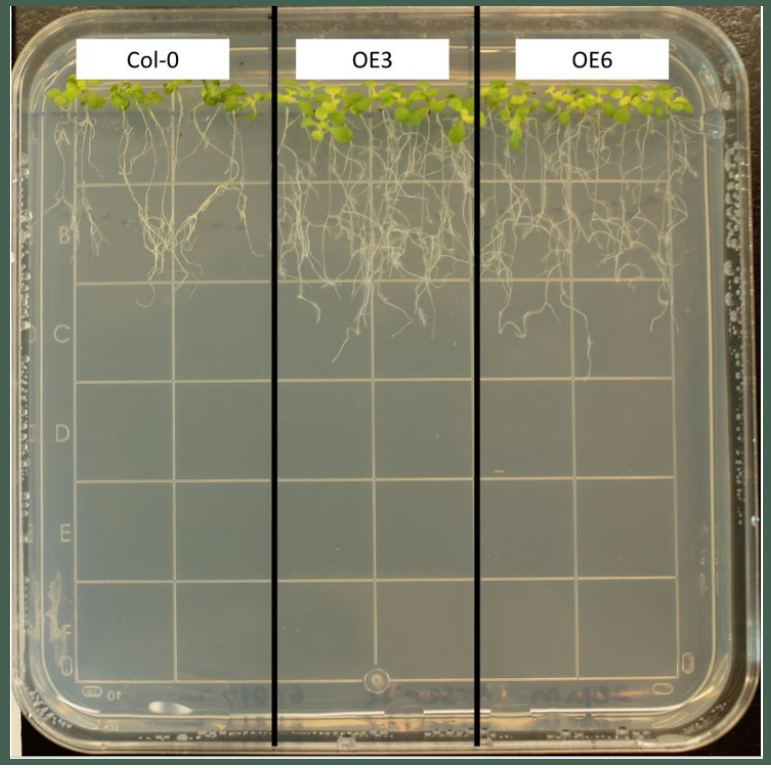

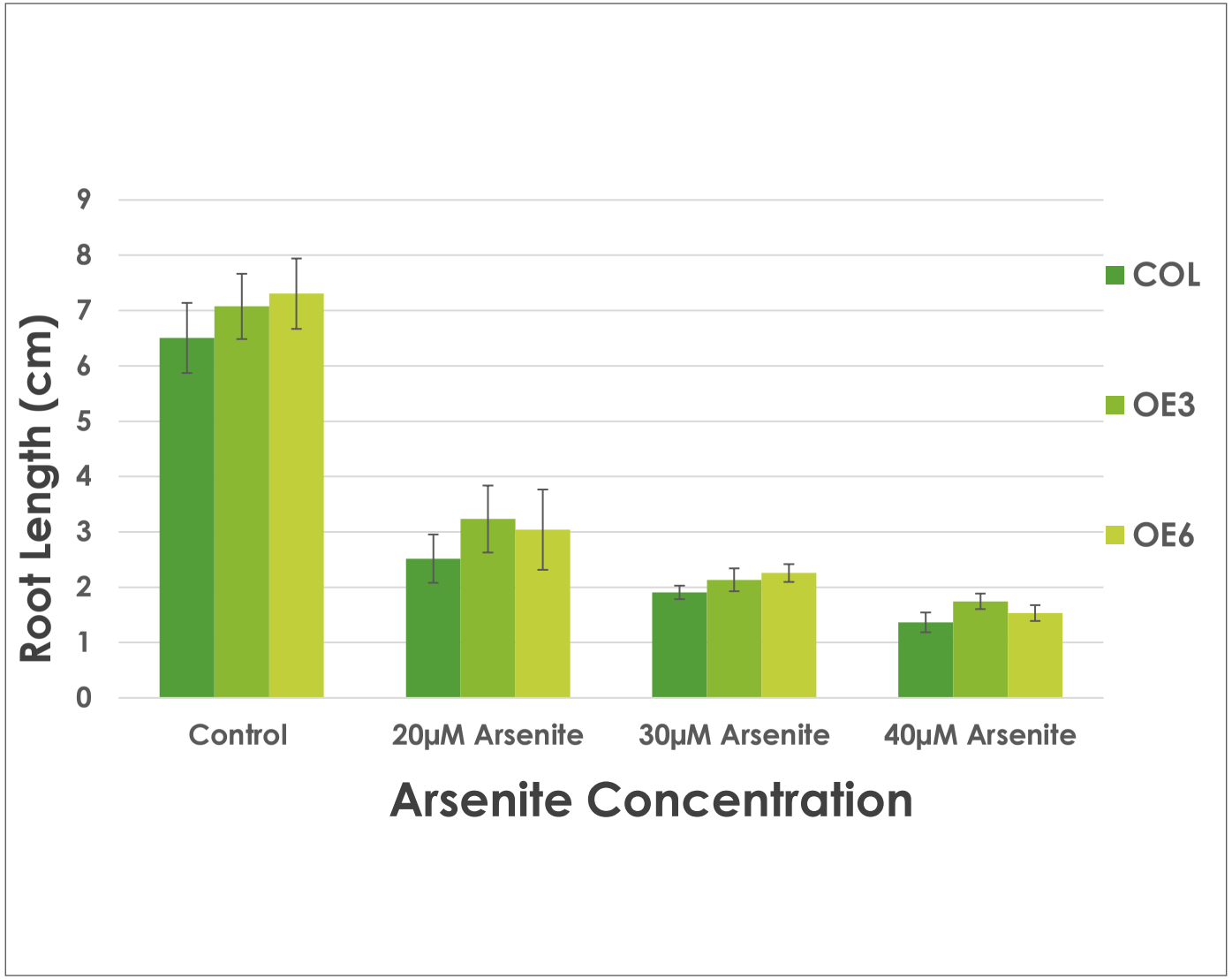
Root Length (cm)
9
8
7
6
5
4
3
2
1
0
COL
OE3
OE6
Control
20μM Arsenite
30μM Arsenite
40μM Arsenite
Arsenite Concentration

RESULTS

CONCLUSIONS

Overexpression of AST68 on *A. thaliana Col* under *As* stress enhanced sulfate uptake and assimilation.

Increased sulfate uptake & assimilation in plants can ameliorate *As* toxicity.

Overexpression (OE)of AST68 aids *A. thaliana's* tolerance to *As* stress.

ACKNOWLEDGEMENTS

- **Dr. John and Mrs. Heidi Niblack**
- **Dr. Ramanjulu Sunkar, Pei Ng and Dr. Yofang Li**
- **Dr. Bill Raun(t)**

Comparing Ageing Structures for Striped Bass

Carson Raper

Department of Natural Resource Ecology
Faculty Sponsor: Dr. Daniel Shoup
Graduate Student Mentor: Alex Vaisvil

ABSTRACT

We compared two structures for ageing striped bass (*Morone saxatilis)*, one that is known to be accurate but is lethal (otoliths) and one that could be a non-lethal approach (dorsal fin spines). One hundred forty-two fish were sampled, and both their otoliths and spines were aged by three readers. Results indicated that among-reader agreement was far higher for the otolith age. The mean dorsal spine age was approximately the same up through age 6. However, beyond this point reader agreement was much more variable. The results suggest that spines are viable as an aging structure until a striped bass reaches age 7 (approximately 850 mm). Beyond this size, lethal ageing practices are more accurate.

1. Introduction

Fish ageing is a common technique researchers and managers use to obtain age and growth data needed to manage fisheries, and it can generate a great deal of information about a population. Fish ages can be determined by looking at growth patterns on several structures, the most common of which are otoliths (hearing bones). Specifically, annuli form during periods of slow growth (i.e., winter), similar to the rings on tree stumps that indicate the passing of seasons. (Schneider, et al. 2000). There are several structures that researchers may choose to use to age fish other than otoliths, such as opercles, dorsal spines, scales, and anal rays (Quist,et al. 2017). Scales and spines or rays may be preferable to other ageing methods because they are external, making them easy to extract and can be removed without euthanizing the fish. However, otoliths are less affected by environmental conditions prevent other structures from getting clear annuli, so sacrificing fish may be necessary to obtain accurate age data (Schneider, et al. 2000).

This study assesses two methods for ageing *Morone saxatilis* (striped bass). Many studies have been conducted across the world assessing the accuracy of ageing samples via otoliths. A case in the Eastern Baltic Sea indicated that even slight changes in the environment or water salinity can cause great variations in age data (Heimbrand, 2020), so the environment may dictate which structure(s) are the best for aging a given species. Scales are both less accurate and less precise than otoliths for ageing striped bass (Liao et al., 2013). Dorsal spines have similar accuracy to otoliths for striped bass in J. Strom Thurmond Reservoir, (Welch et al., 1993), but locations with different growing season length may have different results, so it is not clear if spines can reliably be used to age this species in Oklahoma. This study will determine whether ageing striped bass by spines is as accurate as ageing by otoliths for the Arkansas River basin population, such that spines could be used as a sub-lethal method for aging this species.

2. Experimental Details

One hundred forty-two striped bass were collected at three connected rivers in Oklahoma (Arkansas, lower Illinois, and Canadian rivers). Some fish were collected by electrofishing and others came from angler donations. All fish were taken to the lab and both their otoliths and dorsal fin spines were removed for aging.

Spine removal involves the cutting of a spine as proximal to the body as possible (Quist,et al. 2017). Spines were then placed into an oven at 75 degrees Celsius and left for 24 hours to fully dry. All organic matter was removed, and the spines were sectioned with a low-speed Isomet® saw. The larger proximal end of the spine was cut clean to ensure that the next cut would be an exact 0.76-mm section. Spines that were too small to fit into the Isomet® clamp (~less than 250 mm) were placed upright into clay and then a straw was placed over the spine so embedding epoxy could be poured around the spine. West System 105 Epoxy was paired with West System 205 fast hardener in a separate container and was mixed slowly to avoid air bubbles. The mixed epoxy was poured down the straw to encase the spine and was allowed to sit for 24 hours to cure before being placed into the Isomet® saw and sectioned. Spine cross sections were mounted to a microscope slide with a small amount of Crystal Bond (Electron Microscopy Sciences brand). The mounted sections were then polished with 400 grit and 1000 grit sandpaper until the annuli became clear when viewed with a microscope.

Otoliths were removed from the fish by cutting the scalp using a sawing motion with a scalpel to remove the top of the skull, and the exposed otoliths were then collected using forceps (Quist et al. 2017). After removal, Otoliths were cleaned thoroughly with a medium bristle brush and water before they were placed into a silicone mold anti-sulcus facing up. West System 105 epoxy resin was combined with West System 205 fast hardener in a one-to-one ratio and mixed slowly to avoid bubbles. Mixed epoxy was slowly added to the

silicone mold until it completely submerged the otolith. After a 24-hour period, the otoliths were cross sectioned at the core to remove a slice 0.89-mm thick cross section. Otolith cross sections were then mounted to a microscope slide with a small amount of Crystal Bond (Electron Microscopy Sciences brand) and polished using 400 grit and 1000 grit wet sandpaper until rings were visible under the microscope. Otoliths were then aged by 3 readers counting their visible growth rings, using reflected light, which makes annuli easier to identify than transmitted light (Quist et al. 2017). The otoliths served as the baseline that spines from the same fish were referenced because the accuracy of ages from otoliths are well verified for striped bass (Secor et al., 1995).

Average spine age and its 95% confidence interval was plotted against the average otolith age to assess structure bias using the ageBias() function of the FSA package (Ogle et al. 2022) in R v4.2.0 (R Core Team 2022) with the assumption that where structures differed in estimated age, the otolith was correct. Reader precision for each structure was evaluated as percent reader agreement and the average coefficient of variation of mean ages, which was assessed using the agePrecision() function of the FSA package in R.

3. Results

We found mean dorsal-spine age was approximately the same as mean otolith age up through age 6, but agreement was considerably more variable for ages 7+ and age 9 had significantly lower age from dorsal spines than from otoliths (Figure 1). No fish older than age 7 were ever shorter than 855 mm in length. Reader agreement was considerably higher for otolith ages (50%) than dorsal spines (29%), suggesting that otoliths were more precise (Table 1), but most of the variability occurred for older (7+) ages (Figure 1). Further, the average coefficient of variation in age was lower for otoliths (10% compared with 23% for spines) also indicating better precision from otoliths (Table 1).

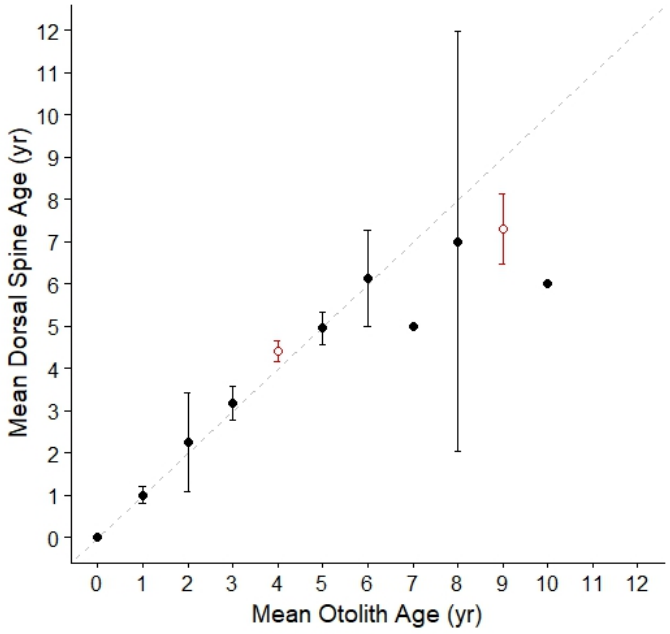

Figure 1. Differences between age estimates derived from otoliths and spines for striped bass in the Arkansas River Basin, Oklahoma

Table 1. Relative accuracy of striped bass age-estimates from otoliths and spines expressed as percent agreement and the coefficient of variation (CV) of age from estimates of three trained agers. All fish were from the Arkansas River Basin, Oklahoma.

Structure Aged	n	Percent Agreement	mean CV
Otoliths	142	50.0	9.97
Spines	142	28.9	23.0

4. Discussion and Conclusions

With reduced reader agreement only for age 7+ fish, our findings suggest that dorsal spines can be used as an acceptable non-lethal method for ageing striped bass when they are ≤ 855-mm in length. Beyond this length, we recommend ageing via otoliths. A similar study using striped bass from J. Strom Thurmond Reservoir, Georgia-South Carolina examined four striped bass structures (including spines and otoliths) and tested both precision and accuracy of their age estimates. This project found that spines were accurate up to 900

millimeters (Welch et al., 1993). Thus, both this study and Welch et al. (1993) indicate that spine age estimates will lack accuracy for older fish. Thus, older fish should still be sacrificed to obtain otoliths for aging unless some other structure can be identified in future studies that is both sub-lethal and accurate for aging striped bass.

5. Summary

We investigated the accuracy of both a lethal (otoliths), and a sublethal (dorsal spines) structure for ageing striped bass. Our results indicated that there was a large deviation in the determined age for the sublethal structure of choice (spines), when compared to the lethal structure (otoliths) for larger fish (>855 mm fish length). Thus, we recommend using sublethal dorsal spines for ageing small fish (< 855), but using otoliths for larger fish to ensure accurate ages.

6. Appendices

6a. Acknowledgements

We would like to thank both Dr. And Mrs. Niblack for making this all possible and additionally I would like to thank my faculty mentor (Dr. Daniel Shoup) as well as the Ph.D. student (Alex Vaisvil) who helped to make this all come together. Allison Salas, Katie Brennan, and Evan Price helped with otolith sectioning and polishing.

6b. Literature Cited

Heimbrand, Y. "Seeking the True Time: Exploring Otolith Chemistry as an Age-determination Tool." *Journal of Fish Biology* 97.2 (2020): 552-65. Web.

Liao, H., Sharov, A. F., Jones, C. M., & Nelson, G. A. (2013). Quantifying the effects of aging bias in Atlantic striped bass stock assessment. *Transactions of the American Fisheries Society*, *142*(1), 193-207. https://doi.org/10.1080/00028487.2012.705255

Ogle, D.H., J.C. Doll, P. Wheeler, and A. Dinno. 2022. FSA: Fisheries Stock Analysis. R package version 0.9.3, https://github.com/fishR-Core-Team/FSA.

Quist, Michael C., and Daniel A. Isermann. *Age and Growth of Fishes: Principles and Techniques*. American Fisheries Society, 2017.

R Core Team. 2022. R: A language and environment for statistical computing. R Foundation for Statistical Computing, Vienna, Austria. URL https://www.R-project.org/

Schneider, James C., P. W. Laarman, and H. Gowing. 2000. Age and growth methods and state averages. Chapter 9 *in* Schneider, James C. (ed.) 2000. Manual of fisheries

survey methods II: with periodic updates. Michigan Department of Natural Resources, Fisheries Special Report 25, Ann Arbor.

Secor, D. H., Trice, T. M., Chesapeake Biological laboratory Center for Estuarine and Environmental Sciences The University of Maryland System, Hornick, H. T., & Maryland Department of Natural Resources. Fisheries Division. (1995). Validation of otolith-based ageing and a comparison of otolith and scale-based ageing in mark recaptured Chesapeake Bay striped bass, Marone saxatilis.Welch, T. J., Van den Avyle, M. J., Betsill, R. K., & Driebe, E. M. (1993). Precision and relative accuracy of striped bass age estimates from otoliths, scales, and anal fin rays and spines. *North American Journal of Fisheries Management*, *13*(3), 616-620. https://doi.org/10.1577/1548-8675(1993)013<0616:paraos>2.3.co;2

Accuracy of Striped Bass age estimates derived from otoliths and spines

Carson Raper, Alex Vaisvil, Dr. Daniel E. Shoup

Department of Natural Resource Ecology
Oklahoma State University

Acknowledgements

- Dr. and Mrs. Niblack
  - Evan Price, Katy Brennan, Allison Salas

The Practice of Ageing Fish

Otoliths

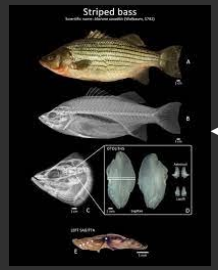

Spines

- Fish are an important resource
- Striped Bass
- Population metrics
  - Growth rate
  - Mortality rate

Is there a better aging method?

- How to get age information?
  - Otoliths (lethal)
  - Other structures (spines, or scales)?

- Objective: Evaluate spines for use as aging structure

Methodology/Processes

Close-up View of Structures

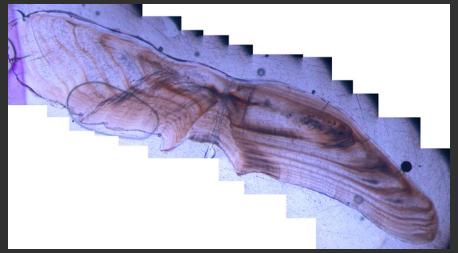

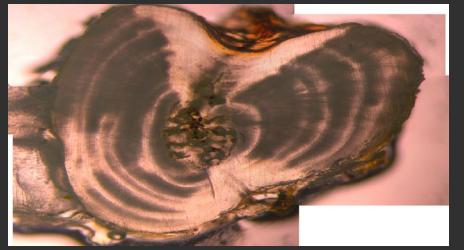

- Removal of Otoliths/Spines
- Prepping of structures
- Reading structure age

Findings & Data Analysis

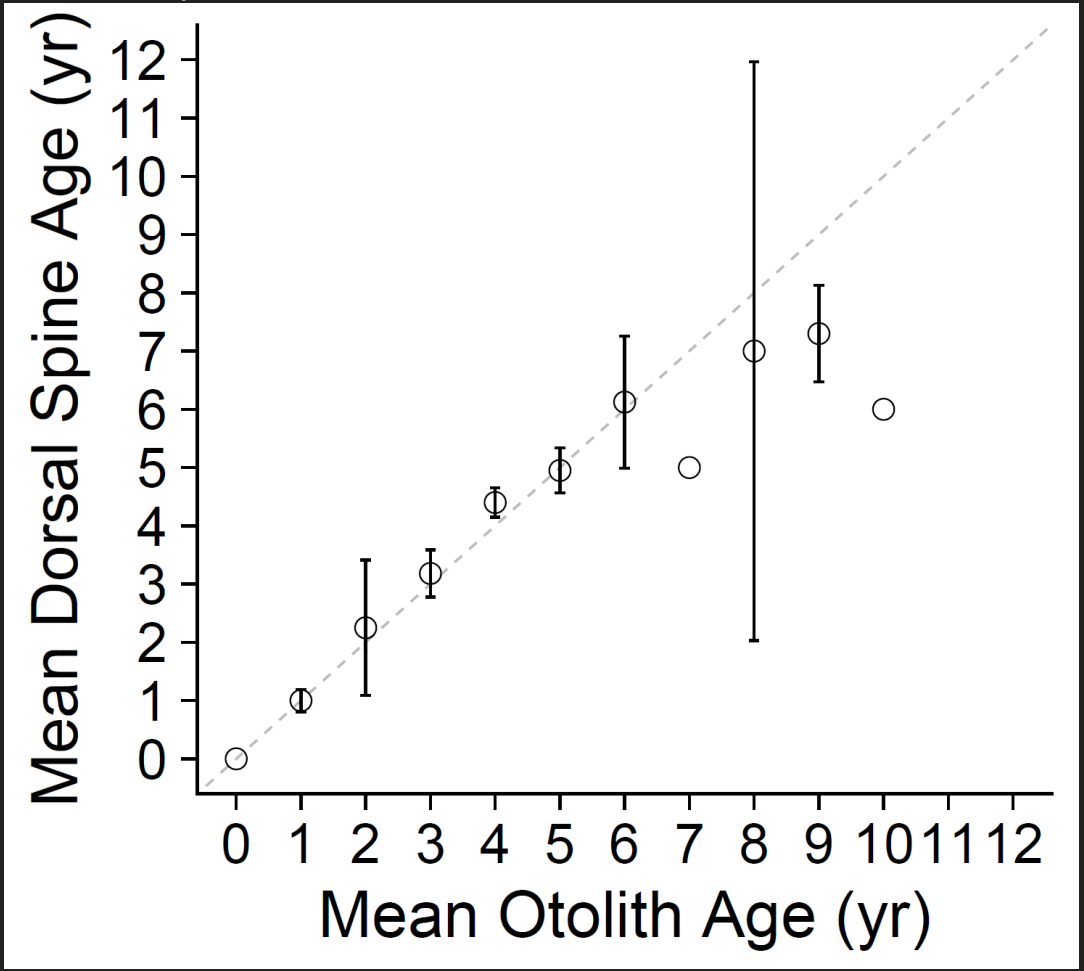

Findings & Data Analysis

Structure Aged	n	Percent Agreement	mean CV
Otoliths	142	50.0	9.97
Spines	142	28.9	23.0

Conclusions

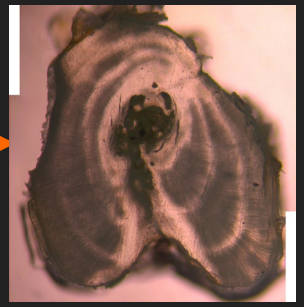

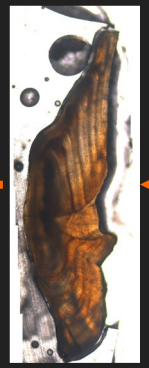

- Spines accurate to ≈ age 6
- Precision of spine ages is poor
- Future directions
  - Other sub-lethal structures better?

Effectiveness of Soil Moisture Sensors to Improve Irrigation Management

Rio Bonham

Department of Biosystems and Agricultural Engineering
Faculty Sponsor: Dr. Saleh Taghvaeian
Graduate Student Mentor: Mukesh Mehata

ABSTRACT

Irrigating agricultural crops is the largest user of freshwater in Oklahoma, with an expected share of 36% of the total water demand by 2060. At the same time, our limited water resources are threatened by frequent droughts and increasing competition among users. It is now more important than ever for agricultural water resources to be conserved at every opportunity possible. One such opportunity is to manage irrigation more precisely using smart technology such as soil moisture sensors. However, smart technology has not been widely adopted. A recent survey reported that only 5% of irrigated land in Oklahoma was managed using soil moisture sensors. The goal of this research project was to investigate how to better implement soil moisture sensors into irrigated operations, particularly at sites with high salinity and clay content which can cause inaccurate readings in commonly used sensors. Commonly used commercial sensors were installed at several experimental fields in each region, varying widely by climate, crop, soil clay content, and salinity. The data provided by the sensors in each field was recorded and analyzed to determine their usefulness in making irrigation decisions. Additionally, soil samples from the fields were collected and analyzed in the lab for soil moisture, salinity, texture, and pH. The results showed that the sensors were generally effective in near real-time monitoring of soil moisture at multiple root zone depths. However, their accuracy degraded rapidly as the clay content and salinity increased, as high as 30% error in these conditions. Almost all the sensors overestimated soil moisture, which could lead to underirrigation and possibly yield-loss. Among the two different calibrations provided by the sensor manufacturer, the texture-adapted combined calibration performed better than the default calibration. The main finding is that these sensors are effective when clay content and salinity are low, but site-specific calibration is required as these two parameters increase.

1. Introduction

Sustainable water resource management is one of the most important issues facing agriculture today. It takes significant amounts of water to provide the global demands of food, fuel, and fiber. This can strain our limited accessible water sources, particularly in times of drought. This phenomenon can be easily seen when considering the drought of 2011-2015 experienced across Oklahoma (Figure 1 and Figure 2).

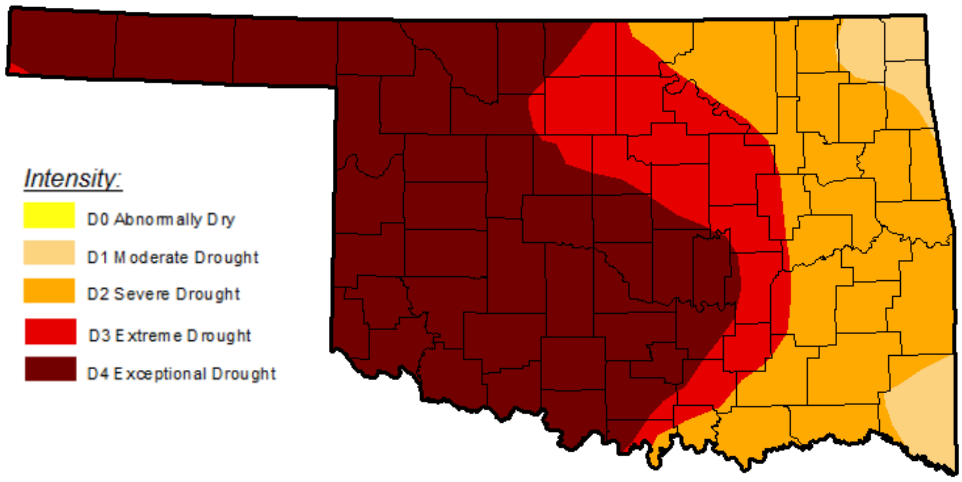

Figure 1. Oklahoma drought map, July 2011. Sourced from the U.S. Drought Monitor (USDM).

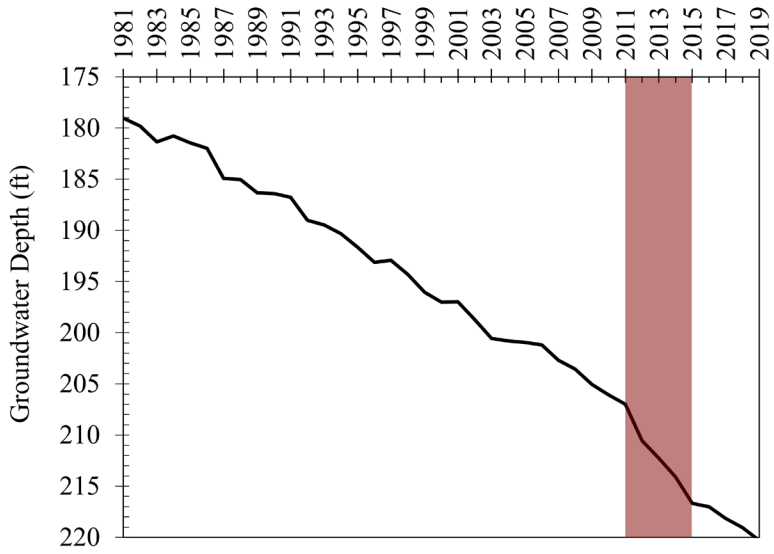

Figure 2. Average depth to water table in Oklahoma Panhandle portion of the Ogallala aquifer. Sourced from Oklahoma Water Resource Board (OWRB) groundwater data.

As seen in Figure 2, the 2011-2015 drought drastically increased the rate of decrease in the already declining Ogallala aquifer. In addition to increasing cost of production, this impact can result in long-term damage to natural resource systems. Similar decreases occurred in countless water sources across the state of Oklahoma, highlighting the need to significantly reduce water consumption. The Oklahoma Water Resources Board (OWRB) projects crop irrigation to lead statewide water demand in 2060 at 36%. In order to effectively reduce total water consumption, there is a need to decrease crop water input while still maintaining profitable yields. One option for accomplishing this is the broadscale adoption of 'smart' irrigation techniques. Smart irrigation techniques involve using sophisticated sensors to precisely measure the amount of water present in the soil. This gives producers a better understanding of when to irrigate than traditional methods, reducing risk of both wasting water and stressing their crops. Despite the advantages of smart irrigation, there is a very low adoption rate of such technologies among Oklahoma producers, as shown in Table 1 (USDA, 2019).

Table 1. State adoption rate of 'smart' irrigation technologies.

State	Adoption Rate (%)
Oklahoma	5%
Texas	10%
Arkansas	11%
Kansas	19%
Nebraska	33%
Nationwide	**12%**

This project sought to address obstacles to adoption of smart irrigation in Oklahoma by evaluating the effectiveness of a common soil moisture sensor and identifying most effective calibrations for problematic soils.

2. Experimental Details

Sentek Drill & Drop soil moisture probes were installed at several fields across western Oklahoma. METER Group rain gauges and infrared thermometers were also installed to provide information regarding irrigation and precipitation (IP) events, as well as crop water stress (Figure 3). The sensors sent data to the cloud at 15-minute to one-hour intervals. Field visits to ensure sensor functionality and to take additional crop data were taken weekly.

Figure 3. Example experimental setup under irrigated cotton at Caddo Research Station (Ft. Cobb, OK).

Sensor collected data were downloaded from the cloud at regular intervals (Figure 4). Soil samples were collected from sensor locations and analyzed for water content, percentage of clay (particle size), salinity, and other parameters. This data was used to compare sensor-measured values to known water content across various soil types. Root mean square error (RMSE) was used to quantify the sensor effectiveness at measuring soil water content.

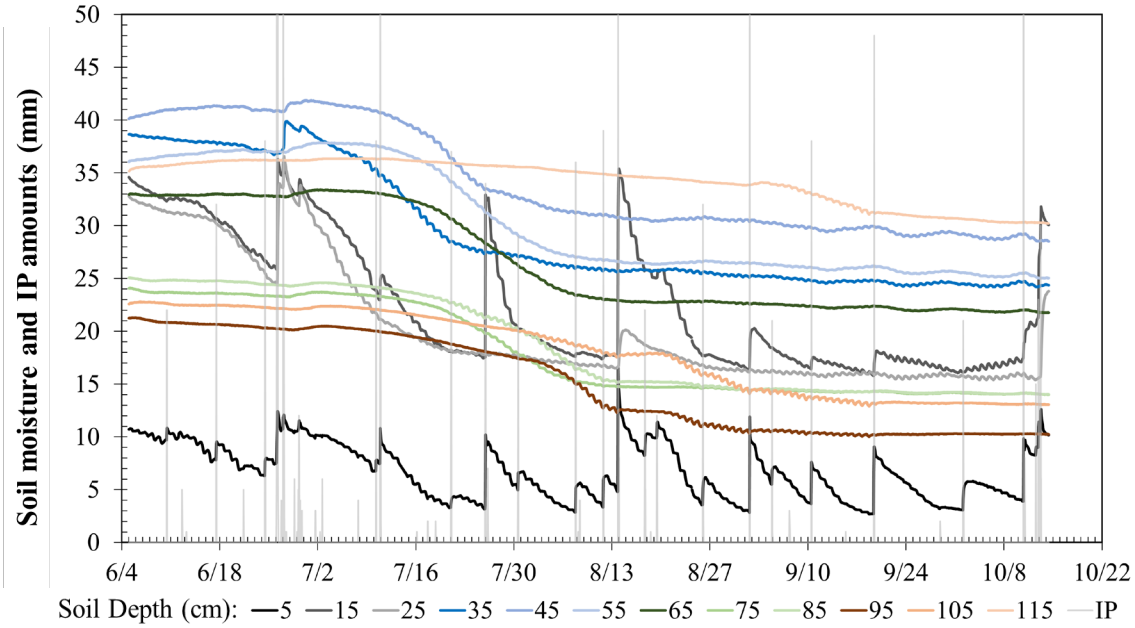

Figure 4. Example of collected sensor data.

3. Results

Sentek provides six different calibrations to be applied to the Drill & Drop probes used in this study based on soil conditions. These calibrations alter how the probe interprets collected data rather than how the data is collected. As such, each calibration's accuracy could be analyzed without the need for six iterations of the experiment. Figure 5 and Figure 6 show the impact of each calibration on sensor accuracy in varying soil conditions using RMSE as the statistical indicator. Figure 7 illustrates how the application of the most accurate calibration (Silty clay loam) increases sensor performance.

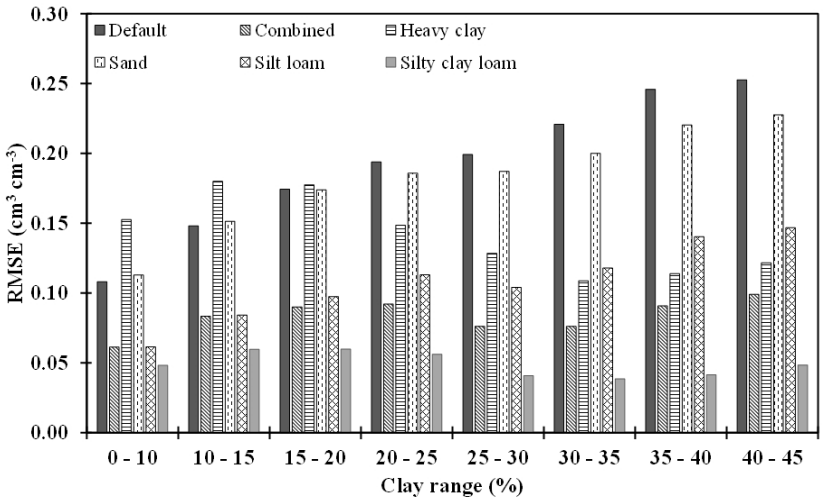

Figure 5. Sensor errors for different calibrations at various ranges of clay content.

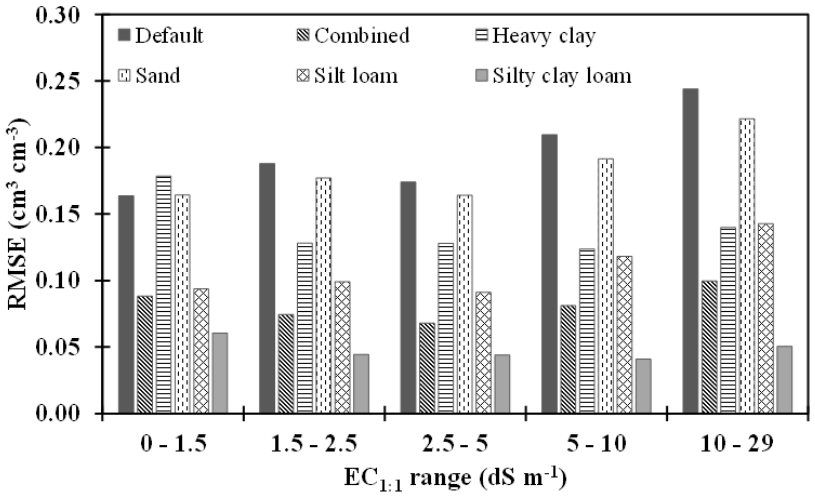

Figure 6. Sensor errors for different calibrations at various ranges of soil electrical conductivity (EC).

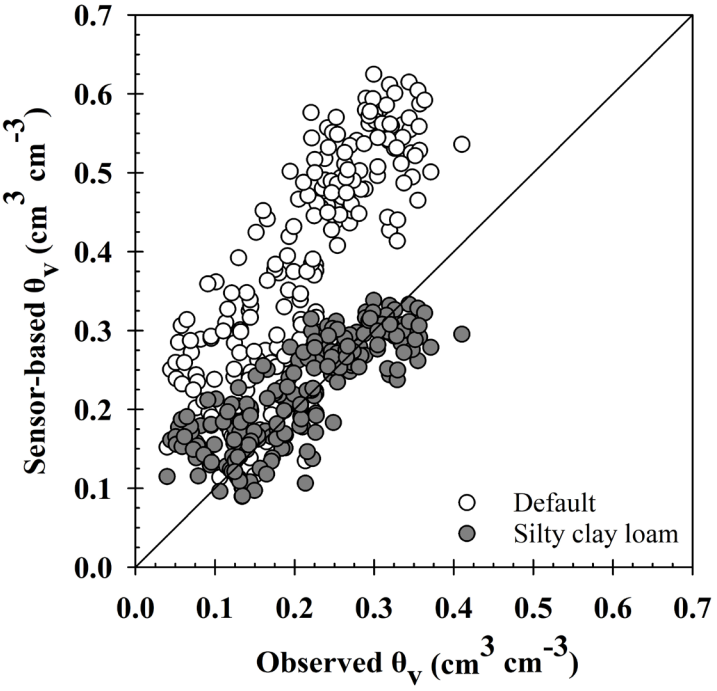

Figure 7. Comparison of default and silty clay loam calibrated readings against the observed values in terms of volumetric water content (θ_v; $cm^3\ cm^{-3}$).

4. Discussion and Conclusions

The results showed that the sensors were generally effective in near real-time monitoring of soil water content at multiple root zone depths. However, their accuracy degraded rapidly as the clay content and salinity increased. Almost all the sensors and calibrations overestimated soil moisture, which could lead to underirrigation and possibly yield-loss. Among the different calibrations provided by the sensor manufacturer, the texture-adapted silty clay loam calibration performed the best and the default calibration was the poorest in terms of accuracy. The main finding is that these sensors are effective when clay content and salinity are low, but site-specific calibration is required as these two parameters increase.

5. Summary

Reducing unnecessary water consumption is paramount to broad-scale sustainability, particularly regarding crop production. In operations that use irrigation, soil moisture sensors can be utilized to better apply irrigation management techniques. Sentek Drill & Drop soil moisture probes are a cost-effective option for producer to implement. However, proper calibrations must be applied to obtain acceptable levels of accuracy in problematic soil conditions.

6. Appendices

6a. Acknowledgements

Thank you to the staff at the Oklahoma Agricultural Experiment Stations where the experiment was conducted. Thank you to Dr. Tyson Oschner for the use of his soil physics laboratory in analyzing collected soil samples. I would like to especially thank Dr. Saleh Taghvaeian, Dr. Sumon Datta, and Mukesh Mehata for welcoming me to the project, answering my many questions, and never failing to aid in my development as a researcher. To Dr. and Mrs. Niblack, I cannot express how much this opportunity has meant to me. Through the Niblack Research Scholars Program, I have been able to take incredible steps toward reaching my goal as a career researcher early on. I cannot imagine my time in undergraduate studies without my experiences in this wonderful program. Thank you so much!

6b. Papers Published

June 2022 Farm Foundation Round Table Meeting Poster Presenter – Fire and Water: Managing Complex Tradeoffs to Support Agriculture and Sustainability.

2022 Oklahoma Research Day at the Capitol Poster Presenter

2022 Oklahoma State University Undergraduate Symposium Poster Presenter

6c. Literature Cited

(dataset) National Drought Mitigation Center, U.S. Department of Agriculture, National Oceanic and Atmospheric Administration. United States Drought Monitor. University of Nebraska-Lincoln.

OWRB, 2012. Oklahoma Comprehensive Water Plan (OCWP) Water Demand Projections Fact Sheet. Oklahoma Water Resources Board. Oklahoma City, Oklahoma.

United States Department of Agriculture, 2019. 2018 Irrigation and water management survey. USDA National Agricultural Statistics Service. Washington, D.C.

Effectiveness of Soil Moisture Sensors to Improve Irrigation Management

RIO BONHAM, MUKESH MEHATA, SUMON DATTA, ALI MIRCHI, SALEH TAGHVAEIAN

Background – Water Resource Depletion

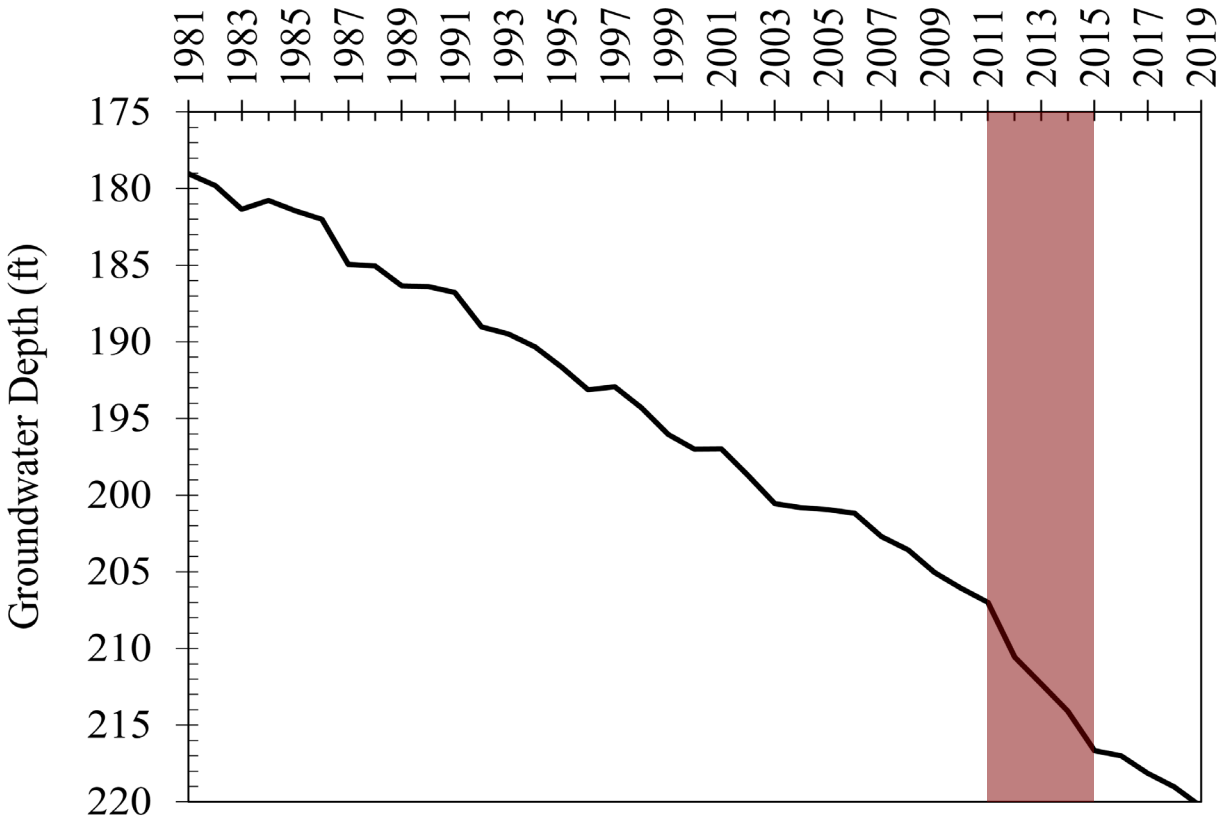

Figure 1. Average depth to water table in Oklahoma portion of Ogallala aquifer. Sourced from OWRB Monitoring Well Data.

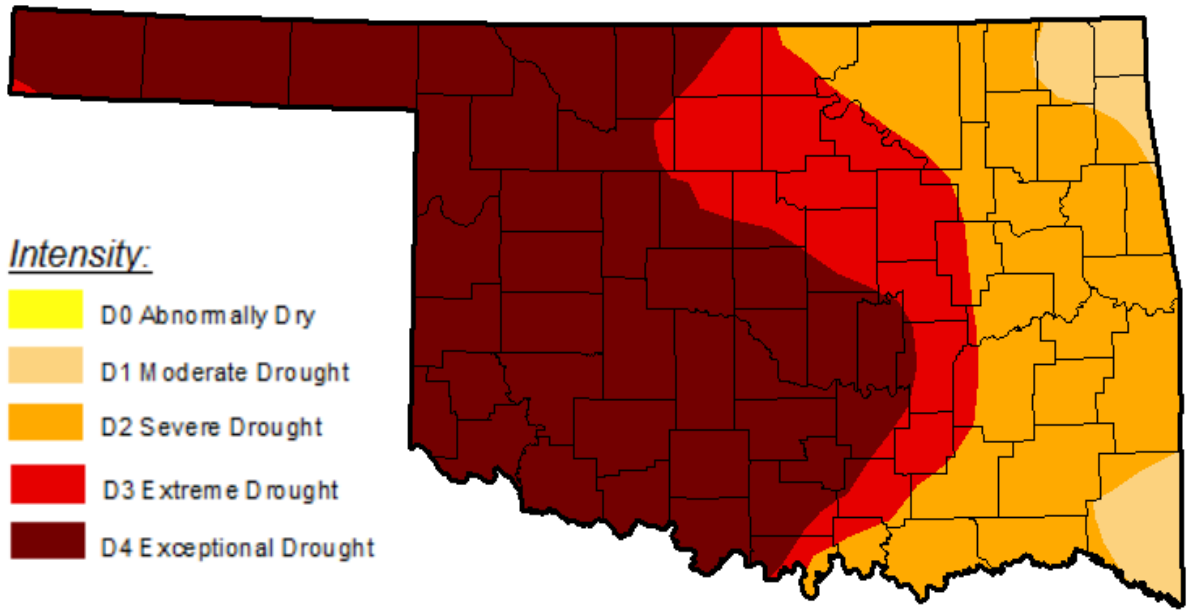

Figure 2. Oklahoma drought map, July 2011. Sourced from the U.S. Drought Monitor.

Background – Projected Demand

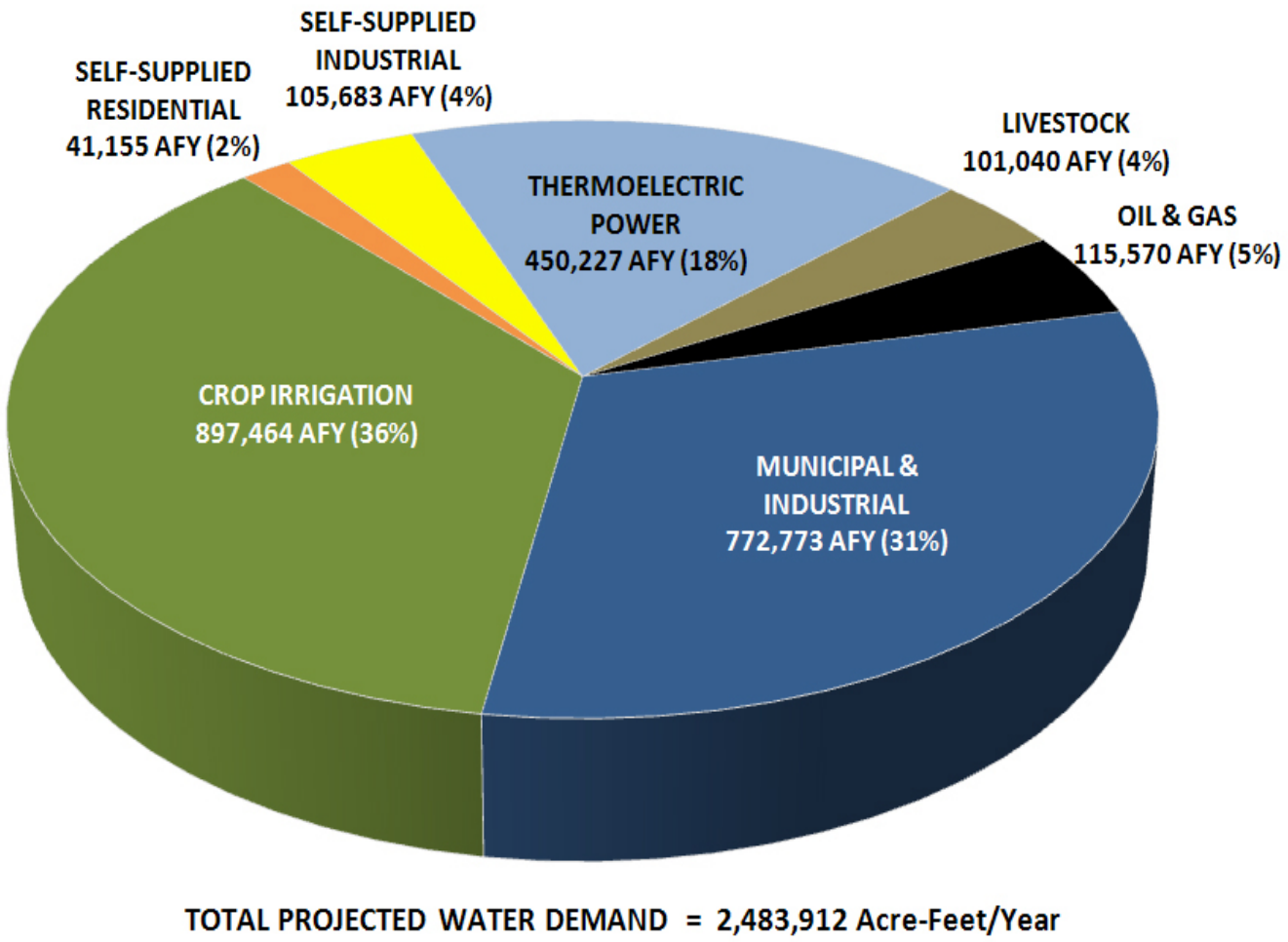

Figure 3. Oklahoma Water Resource Board 2060 Projected State-Wide Water Demands.

Background – Soil Moisture Responses

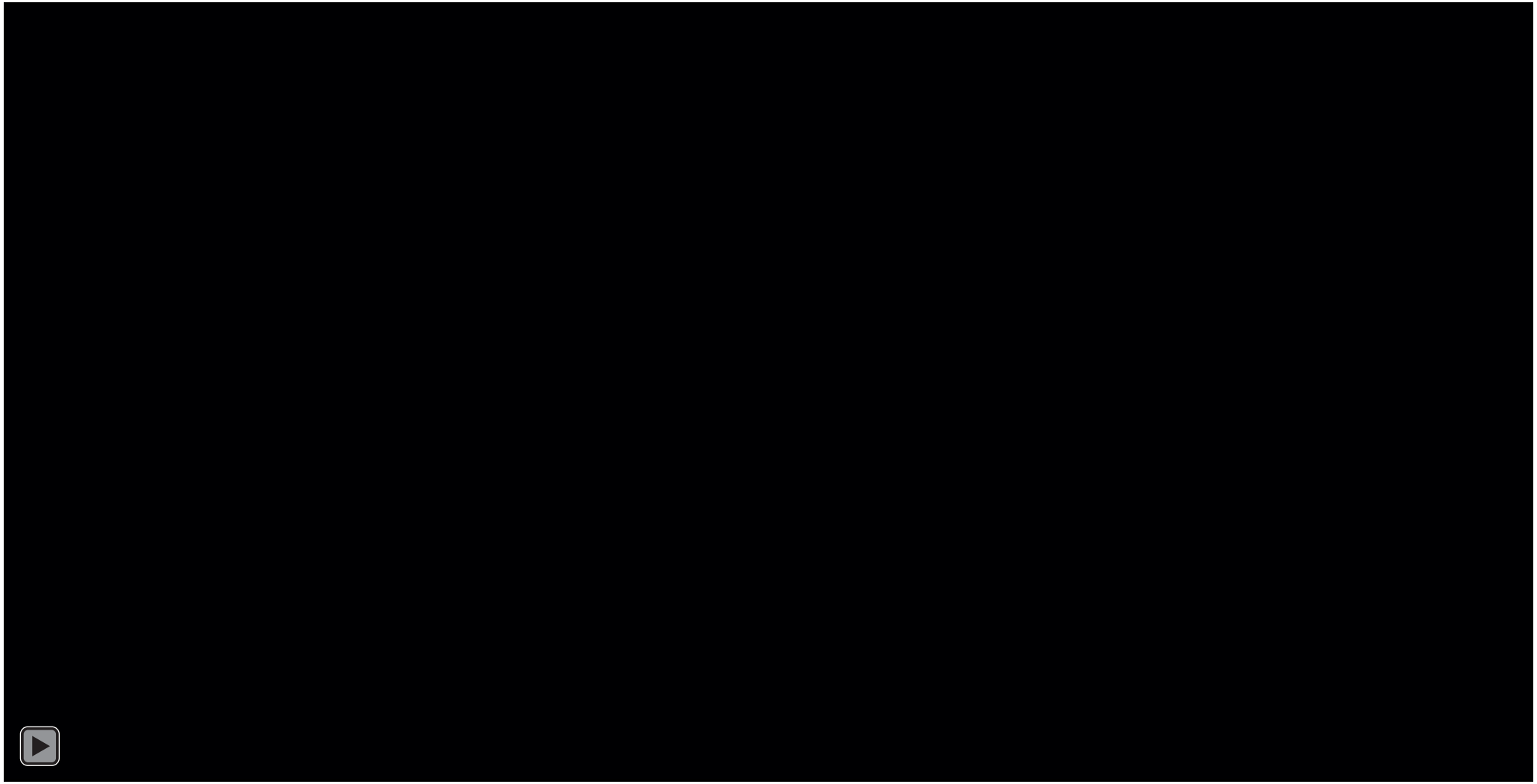

Table 1. State adoption rate of 'smart' irrigation technologies. Sourced from 2018 USDA Survey.

State	Adoption Rate
Oklahoma	5%
Texas	10%
Arkansas	11%
Kansas	19%
Nebraska	33%
Nationwide	**12%**

Need for Study

Methodology

Methodology

Install sensors and retrieve data throughout growing season.

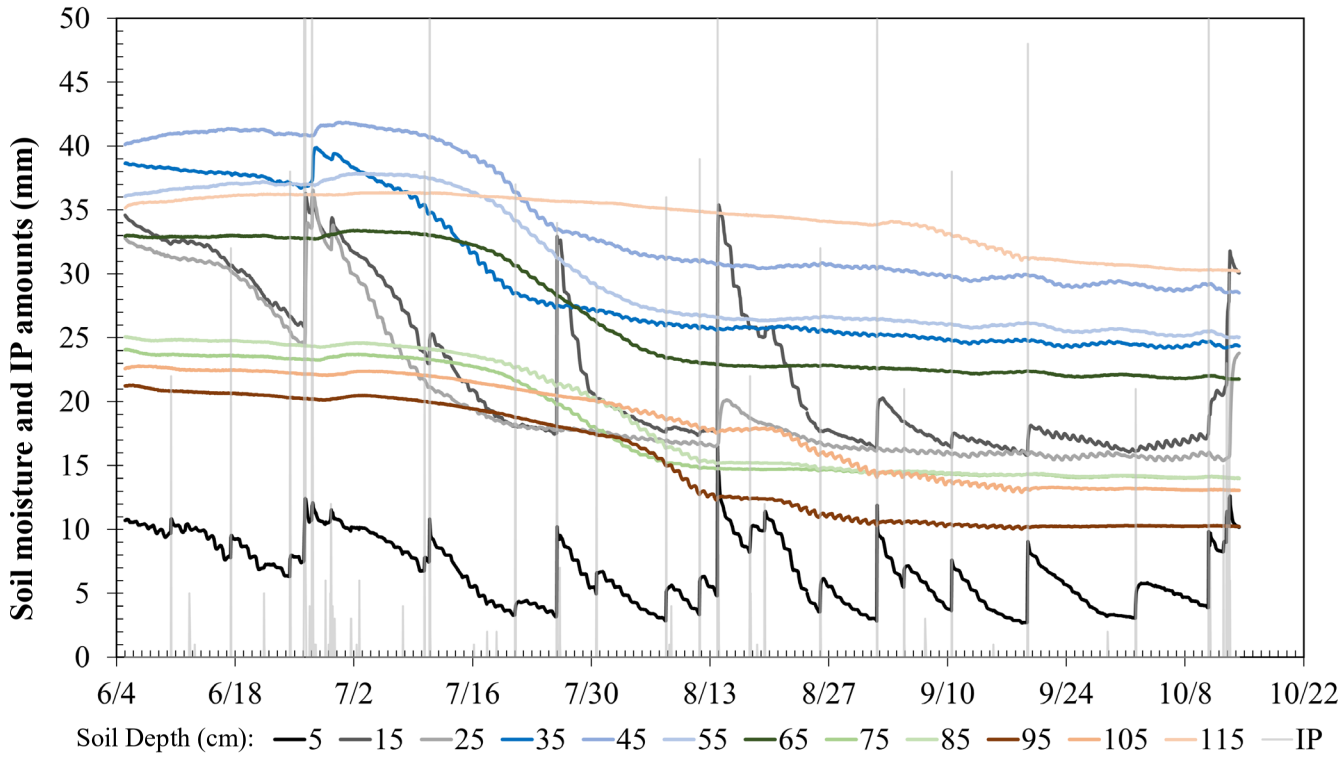

Figure 4. Example of collected sensor data.

Collect soil samples throughout growing season.

Analyze samples for moisture content and physical properties

Analyze accuracy of sensor readings for multiple soil types.

Results

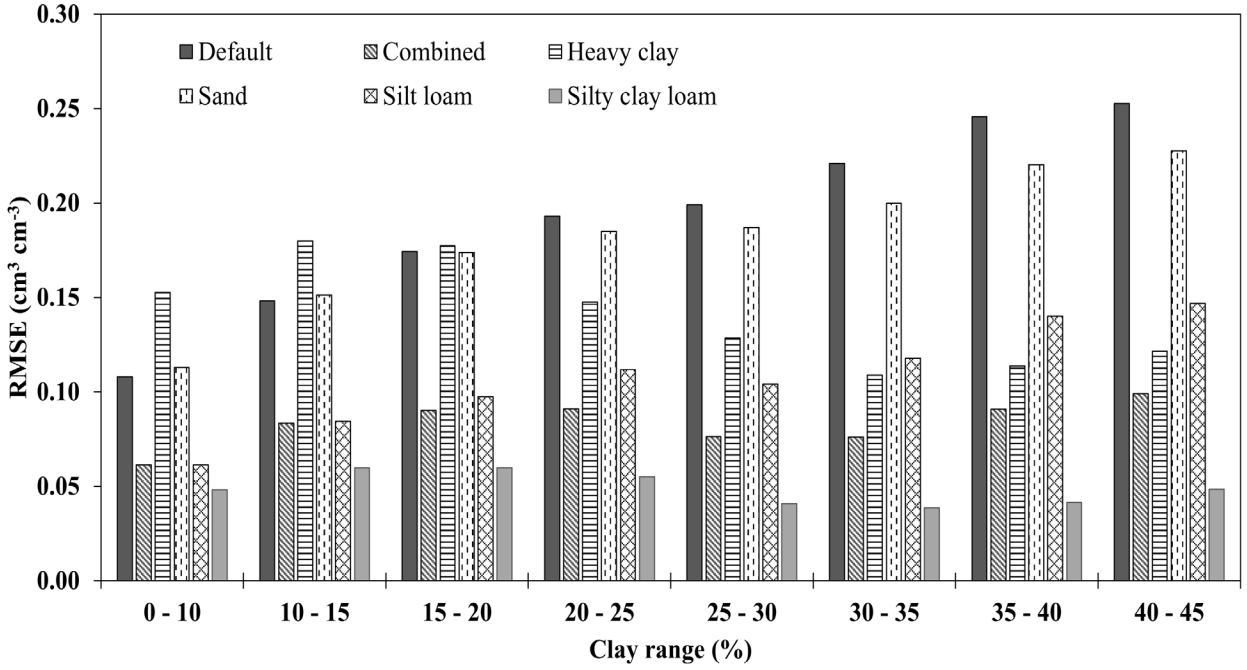

Figure 5. Sensor errors for different calibrations at various ranges of clay content.

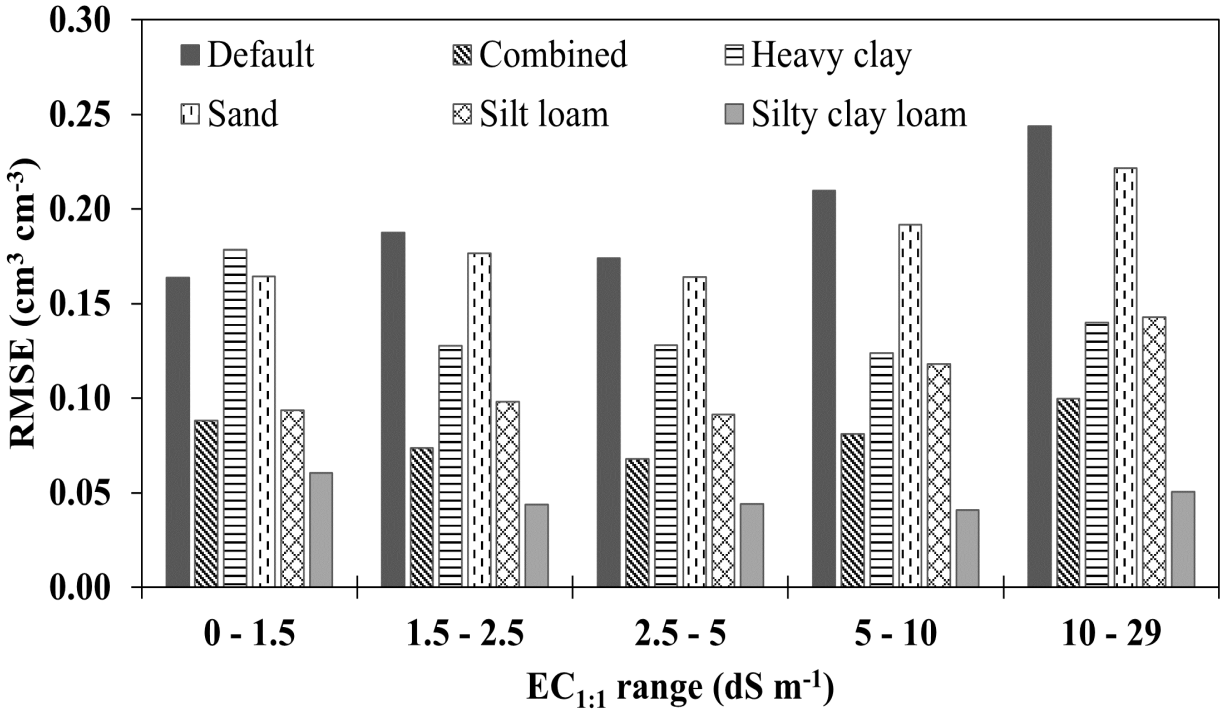

Figure 6. Sensor errors for different calibrations at various ranges of soil electrical conductivity (EC).

The main finding is that these sensors are effective when clay content and salinity are low, but site-specific calibration is required as these two parameters increase.

Acknowledgements

- Oklahoma Agricultural Experiment Station Staff
- Dr. Tyson Oschner
- Dr. Mukesh Mehata, Dr. Sumon Datta, Dr. Ali Mirchi, Dr. Saleh Taghvaeian
- Dr. and Mrs. Niblack

SESSION TWO:

Jillian Gore

“PGC1α Overexpression Protects against Cardio-Metabolic Disease and Skeletal Muscle Dysfunction in Type 2 Diabetic Mouse Model”

Research Area: Physiological Sciences
Faculty Sponsor: Dr. Joshua Butcher
Graduate Student Mentor: Emily Nunan

Manoj Jagadeesh

“Obesity-Induced Sympathoexcitation Causes Down-Regulation of Glutamate Transporters Expression in Human Brainstem Astrocytes”

Research Area: Physiological Sciences
Faculty Sponsor: Dr. Madhan Subramanian
Graduate Student Mentor: Mahesh Kumar Sivasubramanian

Carson Wright

“Exercise and Kidney Function: A Novel Link”

Research Area: Physiological Sciences
Faculty Sponsor: Dr. Joshua Butcher
Graduate Student Mentor: Emily Nunan

PGC1α Overexpression Protects against Cardio-Metabolic Disease and Skeletal Muscle Dysfunction in Type 2 Diabetic Mouse Model

Jillian Gore

Department of Physiological Sciences in the College of Veterinary Medicine
Faculty Sponsor: Dr. Joshua T. Butcher
Graduate Student Mentor: Emily L. Nunan

ABSTRACT

Diabetes currently afflicts 37 million Americans, and approximately 1 in 3 are prediabetic.[1] Type 2 diabetes (T2D) is a metabolic disorder characterized by hyperglycemia due to the combination of insulin resistance and insufficient insulin production. Reoccurring hyperglycemia and long-term insulin malfunction have been tied to damage or failure of differing organs such as kidney, nerves, and vasculature.[2] Predispositions for T2D negatively affect an individual's skeletal muscle mass as well. Skeletal muscle can be categorized into oxidative and glycolytic fibers; however, oxidative fibers are more insulin sensitive and resistant to fatigue. Overexpression of peroxisome proliferator-activated receptor gamma coactivator 1 alpha (PGC1α) is known to increase insulin-sensitive oxidative muscle fibers but what remains unknown is whether it is effective at preventing cardiometabolic disease and skeletal muscle dysfunction in a *db/db* mouse model of T2D. Our hypothesis is that overexpression of PGC1α will improve muscle performance by preventing fatigability, will preserve glucose homeostasis, and protect against kidney function in a mouse model of T2D. Overexpression of adult PGC1α mice was obtained by crossing the MCK-PGC1α transgenic mice onto the *db/db* background. Four mouse groups (lean control, lean PGC1α overexpression, an obese control, and an obese PGC1α overexpression) were used to assess multiple variables including glucose homeostasis (plasma glucose, HbA1c, IGTT), muscle function (*in vivo* plantarflexion of gastrocnemius muscle), and fluid dynamics (via metabolic cages). Overexpression of PGC1α improves glucose homeostasis, decreases muscle fatigability, conserves fluid dynamics, and improves blood glucose levels and renal function in the T2D models back to levels of the controls, restoring them to a normal physiological state. Altogether, this data suggests that targeting PGC1α is a possible intervention for T2D and potentially other metabolic diseases.

1. Introduction

Type 2 diabetes is a metabolic disease that results from chronic hyperglycemia. Diabetes is a prevalent disease in the United States with nearly 37 million currently afflicted and is the 7th leading cause of death.[1] Over a third of American adults (96 million) are pre-diabetic, and 8 out of 10 do not know they have it.[1] After a meal, glucose is broken down from carbohydrates and is released into the bloodstream. The hormone insulin transports glucose molecules into the cells for use as energy.[3] Diabetes is categorized into two groups: Type 1 and Type 2. Type 1 diabetes occurs in individuals whose pancreas either does not secrete insulin or has dysfunctional pancreatic beta cells. In type 2 diabetes, the body becomes insulin resistant, or the pancreas does not produce insulin in an adequate amount. Type 2 diabetes (T2D) accounts for 90-95% of all diabetes diagnoses.[1] Predispositions to T2D include obesity, poor nutrition, aging, and a sedentary lifestyle, which all affect an individual's skeletal muscle mass.

Skeletal muscle is regarded as the largest metabolic reservoir due to its role as a glucose sink. Escorted by insulin, glucose enters muscle cells through GLUT4 transporters and is phosphorylated into gluose-6-phosphate (G6P).[4] G6P then undergoes glycolysis and the Kreb's cycle to produce ATP (energy) or stored as glycogen for energy use later.[4] 70-90% of disposable blood glucose will be taken into skeletal muscle for energy production; therefore, skeletal muscle is the major tissue responsible for blood glucose regulation.[5] Skeletal muscle can be categorized into glycolytic and oxidative fibers. Glycolytic (type 2) muscle fibers are responsible for rapid and forceful contractions that are associated with explosive movements, but due to their anaerobic nature, these fibers fatigue quickly. Oxidative (type 1) muscle fibers do not provide as much power, but instead are resistant to fatigue. Oxidative fibers are much more concentrated in mitochondria and function aerobically to contract for longer periods of time. Because of their ability to contract for longer periods, oxidative fibers are more insulin sensitive and have more GLUT4 transporters for greater glucose uptake during prolonged contractions. This can serve as a target for regulating blood glucose concentrations.

In both diabetic types, glucose is unable to be utilized by cells and remains in the bloodstream after eating leading to hyperglycemia. Reoccurring hyperglycemia in combination with insulin dysfunction is linked to damage or failure of many different organs such as kidney, nerves, and vasculature.[2] Diabetic nephropathy is prominent clinical symptom of diabetes. Chronic hyperglycemia decreases the elasticity of blood vessels, which in turn, affects the filtering capabilities of blood vessels within the kidneys. The overwhelmed vessels are no longer able to remove glucose from the urine which increases the osmotic concentration.[2] The concentrated urine pulls water from the less-concentrated body and results in larger urine output (polyuria) and increased thirst (polydipsia).[6] Diabetic nephropathy can lead to kidney disease or kidney failure, both life-threatening conditions.

Peroxisome proliferator-activated receptor gamma coactivator 1 alpha (PGC1α) is an endogenous protein and potent activator of many metabolic pathways including mitochondrial biogenesis and liver gluconeogenesis. Foremost, PGC1α is responsible for fiber-type switching and blood glucose absorption and handling in skeletal muscle. PGC1α controls the ratio of oxidative versus glycolytic fibers within the skeletal muscle cells. By overexpressing PGC1α, the composition of skeletal muscle leans towards insulin-sensitive, oxidative fibers rather than glycolytic. The increased contractions and neuromuscular output in high oxidative stress scenarios from endurance-type exercise can increase PGC1α expression by releasing many transcription factors like CaMK and MEF2 to bind on PGC1α's promotor region.[7] Endurance exercise can be simulated genetically by increasing muscle creatine kinase (MCK) that results in an overexpression of PGC1α as well.[7] These observations suggest that certain muscle cell types may yield cardiometabolic benefits when faced with obesity but through different routes. Insight into how cardiometabolic dysfunction is improved with alterations to glycolytic or oxidative expression in skeletal muscle would help uncouple obesity from its associated metabolic consequences. Using this knowledge, we wanted to know if oxidative fibers protect against Type 2 Diabetes and improve glucose homeostasis. Additionally, could it improve related conditions like general cardiometabolic health, fluid dynamics in the kidneys, and muscle function in regard to function and fatiguability? We hypothesized that upregulation of oxidative fiber types, via PGC1α overexpression, improves glucose homeostasis and other metabolic indices along with improvement of overall muscle function.

2. Experimental Details

All mice utilized in this study were young adult (12-30 weeks of age) females on the C57 background, a genetically identical strain of inbred laboratory mice. To get the colonies, a transgenic PGC1α mouse bought from Jackson laboratories (008231) was crossed onto a *db/db* background mouse. The PGC1α transgenic mice show oxidative overexpression by muscle creatine kinase (MCK) direction. *Db/db* mice are homozygous for the Lep^r mutation giving them a chronically hyperphagic and obese phenotype. These mice are well characterized as a model for Type 2 Diabetes. The MCK-PGC1α and *db/db* mice cross resulted in 4 experimental mouse groups: Lean, Lean PGC1α, Obese control (*db/db*), and Obese PGC1α. To address muscle function, glucose handling, and fluid dynamics, 3 different protocols were used. *In vivo* muscle performance was measured using Aurora Scientific's Dynamic In-Vivo Muscle Analyzer with electrical stimulation of the gastrocnemius muscle in the calf. 4 tests in this order were run to characterize muscle function of each mouse: tetanic, twitch, force frequency test, and fatigue test. The tetanic test consisted of a single electrical stimulation at 100Hz for 500ms, and the twitch test was a pulse at 100Hz at a width of 0.2ms. The force frequency test consisted of 7 stimulations at 10, 20, 40, 60, 80, 140, and 180Hz for 200ms each at 3 minutes apart. The fatigue test produces 60 tetanic stimulations at

60Hz for 200ms with 5000ms of rest between each hit. Glucose homeostasis was evaluated using 3 common blood glucose tests: fasting plasma glucose, Glycosylated Hemoglobin (HbA1c's), and fasted Intraperitoneal Glucose Tolerance Test (IGTT) For fasting plasma glucose, the mice were fasted for 16 hours then check their blood glucose levels via tail vein prick. Similarly, HbA1c's were measured via tail vein prick. For the IGTT, mice were fasted for 16 hours then injected subcutaneously with 20% glucose water solution and blood glucose was checked every 15 minutes for 1 hour then at the 2-hour mark. Lasty, fluid dynamics were measured using individual metabolic cages. After a 24-hour acclimation period, water, and food consumption as well as urine production were collected for 2 days. Significance was reported by a One-Way Anova with a Turkey Multiple Comparison's Test or Two-Way Anova based on $p<0.05$.

3. Results

Muscle Function:

In Figure 1, tetanic force shows a significant difference between lean and obese control. The lean and obese PGC1α groups were not significantly different between any of the other groups. Tetanic force is normalized with PGC1α overexpression. Both twitch and ½% relaxation was nonsignificant between groups. The force frequency test showed a significant difference between lean and obese controls with obese controls showing significant blunting in muscle function. PGC1α overexpression again normalized force and showed nonsignificant differences between the groups. Significance for tests were determined by either a One-Way Anova with a Turkey Multiple Comparison's Test or Two-Way Anova with $p<0.05$. In Figure 2, the lean and obese control show the normal fatigue curve. PGC1α significantly blunted muscle fatiguability in both lean and obese groups by showing a significantly higher area under the curve. The obese control showed significantly more fatiguability when compared to the lean control and obese PGC1α. N=5-7 mice per group for all 4 muscle characterization tests.

Figure 1: PGC1α Overexpression Modestly Improves Muscle Function in Obesity

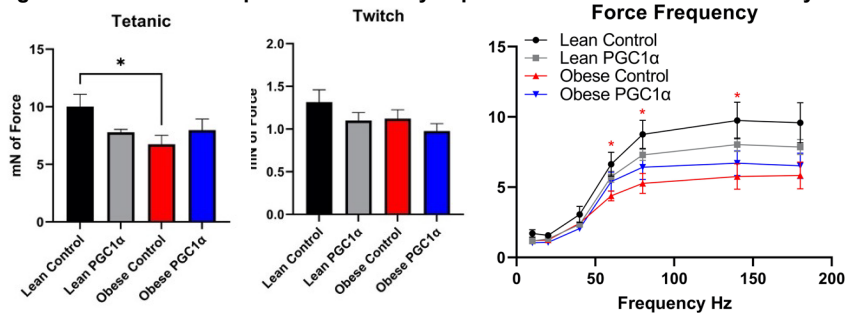

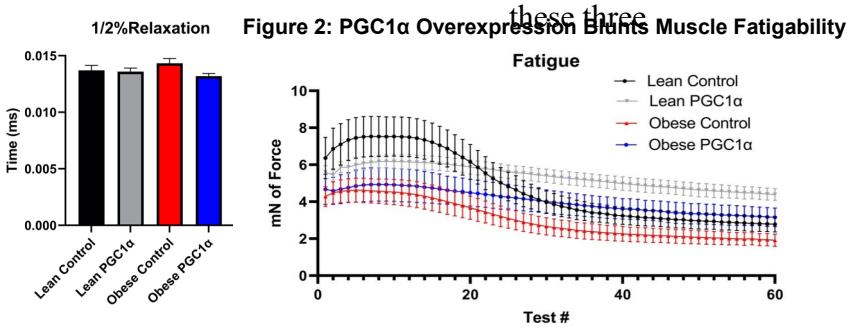

Figure 2: PGC1α Overexpression Blunts Muscle Fatigability

Glucose Homeostasis:

Figure 3: PGC1α Overexpression Improves Glucose Homeostasis in Obesity

Figure 4: PGC1α Overexpression Does not Alter Metabolic Indices in Obe

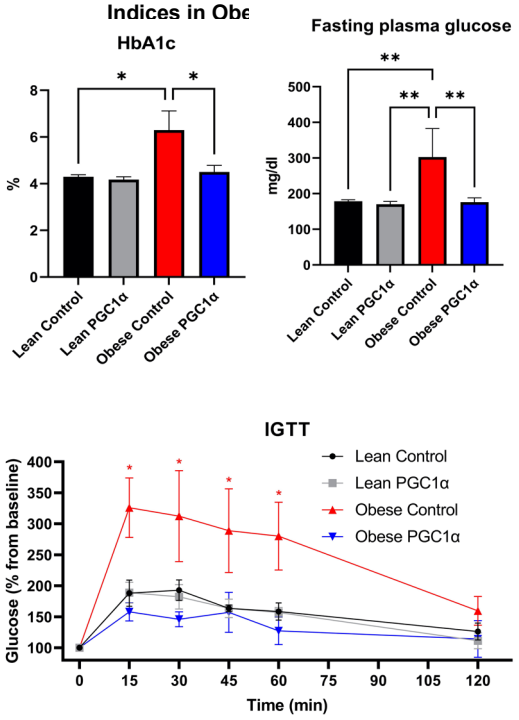

Figure 3 shows the three glucose handling tests: fasting plasma glucose, HbA1c, and IGTT. In fasting plasma glucose, the obese control shows a significantly higher glucose level than all other groups. The obese PGC1α group shows a significantly lower blood glucose level than the obese control. There is no significant different between lean control and lean PGC1α groups. Similarly, in HbA1c's, the obese control exhibits the statistically highest percentage of glycosylated hemoglobin when compared to the other three groups. The lean PGC1α does not show any significant difference from the lean control or obese PGC1α. The obese PGC1α exhibits significantly lower A1c percentage than its obese control counterpart. The obese control showed a significantly higher blood glucose during the IGTT throughout the first hour when compared to the remaining three groups. The lean control, lean PGC1α, and obese PGC1α were not significantly different amongst themselves. Significance for the three glucose homeostasis tests were determined using a One-Way Anova with a Turkey Multiple Comparison's Test or Two-Way Anova. N= 3-6 per group for each of the three tests.

Fluid Dynamics:

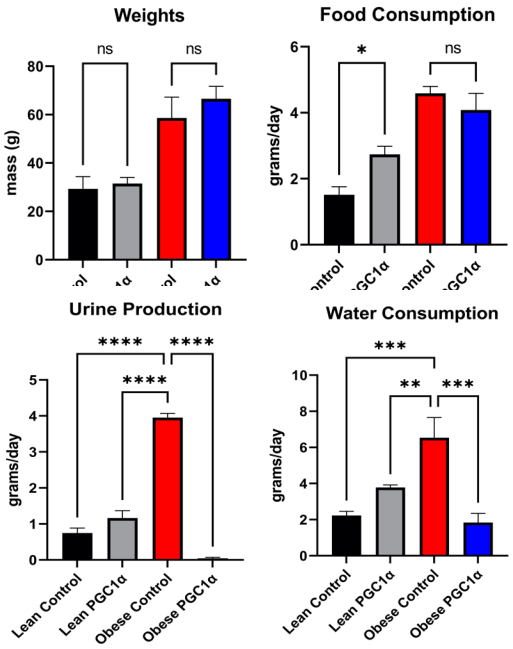

Figure 4 displays the data obtained during the two days in metabolic cages to evaluate fluid dynamics. Notably, full body weights between the two lean groups and two obese groups are nonsignificant. Food consumption is significantly increased between the lean control and lean PGC1α, but there is no significant difference between the two obese groups. Water consumption is noticeably elevated in the obese control and is significantly higher than all other mouse groups. The obese PGC1α's water consumption is glaringly lower than the obese control. There is no significant difference in water consumption between the lean control and lean PGC1α. Urine production is also obviously elevated in

the obese control. All other groups are significantly lower in urine production including the obese PGC1α. The obese PGC1α displays almost no urine production and is lower than all other group. There is no significant difference between the two lean control and lean PGC1α in urine production.

4. Discussion and Conclusions

First, this project determined that PGC1α overexpression improved muscle function by inhibiting fatiugability in both lean and obese phenotypes. These findings in Figure 1 and 2 align with our hypothesis. Although fatiugability is blunted, power and force are also reduced. Because skeletal muscle is more oxidative in PGC1α overexpression, there is a reduced amount of forceful glycolytic fibers therefore reducing the amount of power exerted by the muscle. The power loss is insignificant in all the twitch, tetanic, and force frequency, so the trade-off between power loss and significantly extended muscle fatigue is a very easy bargain. Alternatively, there is significant force reduction in the obese control for every muscle test. A complication of obesity is muscle atrophy shown in the obese control phenotype; however, muscle function is preserved in the obese PGC1α phenotype. This suggests that not only does PGC1α overexpression blunt muscle fatiguability, but it also prevents muscle wasting when faced with obesity. This conclusion aligns with another study investigating the link between PGC1α and FoxO3 transcription factors. Release of FoxO3 leads to the expression of atrogin-1 and MuRF-1 (atrophy-related ligases) to substantially degrade muscle mass, but when challenged with PGC1α overexpression, both ligases decreased in prevalence and muscle mass was preserved.[8] Taken together, our hypothesis was supported, and oxidative overexpression did decrease muscle fatiguability in both PGC1α lean and obese groups.

Our hypothesis was also supported that PGC1α overexpression protects against glucose dysfunction in female, young adult, Type 2 Diabetic mouse models. The obese control group displayed diabetic diagnostic criteria in both fasting plasma glucose and HbA1c levels. A fasted blood glucose level above 250mg/dL and HbA1c's above 6.5% in mice indicate diabetes. The obese cohort displayed a fasting plasma glucose level around 300mg/dL and HbA1c's above 6% both reaching the diabetic threshold. However, the obese PGC1α cohort did not show elevated blood sugar or HbA1c levels despite being obese. The obese PGC1α overexpression showed a fasting plasma glucose of around 150mg/dL and HbA1c's around 4% which are much within normal levels. This shows that oxidative overexpression via PGC1α does improve glucose handling within the skeletal muscle. The obese control group displayed a typical diabetic IGTT as well. With diabetes, glucose remains in the blood for a much longer period due to insulin insensitivity. The obese controls blood glucose skyrockets post-injection and remains much higher than the remaining 3 cohorts until near the 2-hour mark. In contrast, the obese PGC1α displays similar glucose handling over time as both the

lean groups indicating again improved glucose handling regardless of obesity. There is no significant improvement in the lean PGC1α group when compared to the lean control since increased adiposity causes insulin resistance from elevated levels of pro-inflammatory cytokines that block the insulin signaling pathway.[9] Lean individuals do not have excess adiposity and therefore do not develop insulin resistance, so glucose handling is not significantly affected in the lean groups. Nevertheless, PGC1α overexpression does protect against glucose dysfunction in obese, Type 2 Diabetic models.

Fluid dynamics within the kidneys were conserved as well in accordance with our hypothesis. As discussed earlier, two clinical signs of diabetes are polyuria (increased urine output) and polydipsia (increased water consumption). The obese controls exhibited just that with significantly increased water consumption and urine production; however, the obese PGC1α group did not show any significant increase in water or urine. The obese PGC1α overexpression cohort showed almost no urine production, and we believe this to be a collection error. The obese mice sit inside their food canisters, urinate into their food, and urine is not able to be collected. Since water consumption is so significantly different between the obese control and obese PGC1α, we can assume that urine production would also be substantially decreased when comparing the obese PGC1α and obese control. These findings correlate with other studies focusing on the relationship between PGC1α and renal dysfunction from diabetic kidney disease. A different study found decreased mRNA expression of PGC1α in cortical tubulointerstitial samples from mice with diabetic nephropathy.[10] Decreased PCG1α expression was also noted in mesangial expansion within glomerulus cells of kidneys with diabetic nephropathy.[10] Both other studies and these results show that PGC1α overexpression can improve renal fluid dynamics and prevent against diabetic nephropathy.

There are many future directions for this project we would like to explore. We would like to increase the male PGC1α overexpression cohort in both lean and obese mice. All graphs shown in this report are of female mice. Our laboratory breeds the mice used in this study, and we have been unable to breed enough males for reliable data. Estrogen-related receptor alpha (ERRα) is also serves as a pivotal point in the PGC1α cascade during transcription of genes that direct mitochondrial energy pathways in cardiac and skeletal muscle.[11] We would like to acquire more males either by breeding or purchase to increase the male cohort and determine if PGC1α overexpression can protect against cardiometabolic dysfunction in males with Type 2 Diabetes as they have decreased estrogen. We would also like to explore using PGC1α overexpression as a type of prescription exercise through dietary supplements. These ‘vitamins’ would enhance the oxidative capacity within the user’s skeletal muscle to prevent muscle atrophy in obese patients. There are natural foods that can increase the prevalence of PGC1α now. Kiwi’s or human breastmilk are high in pyrroloquinoline quinone (PQQ) that activates PGC1α and kickstart mitochondrial

biogenesis. Similarly, we would be producing a pill that activates PGC1α as well to boost oxidative fiber content in skeletal muscle. Lastly, we would like to apply our findings towards other cardiometabolic diseases. Diabetes is detrimental to many different tissues in nearly every area of the body. There are multiple endothelial, cardiovascular, cerebral, lymphatic, and other conditions that occur in conjunction with diabetes and obesity. PGC1α is multifaceted and also impacts many different pathways, so we would like to apply our approach to corresponding cardiometabolic diseases associated with obesity. We hope to continue our study and continue finding novel therapeutic targets to uncouple obesity and its related cardiometabolic dysfunction.

5. Summary

The conclusion of this study is that PGC1□ overexpression protects against glucose dysfunction in a Type 2 Diabetic mouse model in young adult female mice. This is independent of changes in overall weight. PGC1□ overexpression also improves muscle function, driving an overall oxidative phenotype and this is remarkably inhibited fatigability in both lean and obese mice. Taken together, oxidative fiber overexpression is a unique and novel therapeutic target for Type 2 Diabetes.

6. Appendices

6a. Acknowledgements

I would like to thank my colleagues in Dr. Butcher's Laboratory including all listed authors. Specifically, I would like to thank my thesis mentor Dr. Josh Butcher, second reader Dr. Jennifer Rudd, and graduate student mentor DVM/PhD Candidate Emily Nunan for their support and guidance. I would also like to thank the Oklahoma Center for Advancement of Science and Technology (OCAST HR21-045-1, PI: Butcher), National Institute on Aging (NIA 5K01AG064121, Butcher), and National Institute of General Medical Sciences (NIGMS P30GM122744, PI: Ma, Pilot Study: Butcher) for funding Dr. Butcher's lab and giving me the opportunity to partake on this project. In addition to those, I would like to especially thank the Niblack Research Scholars program at Oklahoma State University, particularly Dr. and Mrs. John Niblack, for providing significant support and funding to myself. Finally, I would like to thank the OSU Honors College for a wonderful experience in research during my undergraduate career and granting me my Honors College Degree based on this project.

6b. Papers Published

Poster Presentations

1. Experimental Biology; April 2-5, 2022; Philadelphia, PA

2. Undergraduate Research Symposium; April 19, 2022; Oklahoma State University, Stillwater, OK

We are currently working on submitting a paper for this project. Stay tuned!

6c. Literature Cited

2. American Diabetes Association, 2007, Diabetes Care. American Diabetes Association, 30: S4-S41.

1. Center for Disease Control and Prevention, 2021, Diabetes. U.S. Department of Health & Human Services.

11. Huss, J.M., Torra, I.P., Staels, B., Giguére, V., Kelly, D.P., 2004, Estrogen-related receptor alpha directs peroxisome proliferator-activated receptor alpha signaling in the transcriptional control of energy metabolism in cardiac and skeletal muscle. Molecular and Cellular Biology 24(20): 9079-9091.

5. Jensen, J., Rustad P.I., Kolnes, A.J., Lai, Y.C., 2011, The role of skeletal muscle glycogen breakdown for regulation of insulin sensitivity by exercise. Frontiers in Physiology 2:112.

7. Liang, H., and Ward, W.F., 2006, PGC-1α: a key regulator of energy metabolism. American Physiological Society 30(4):145-151.

10. Lynch, M.R., Tran, M.T., Parikh, S.M., 2018, PGC1α in the kidney. American Journal of Renal Physiology 314(1): F1-F8.

3. Mayo Clinic Staff, 2021, Using insulin to manage your blood sugar. Mayo Foundation for Medical Education and Research.

6. Mayo Clinic Staff, 2021, Diabetic nephropathy (kidney disease). Mayo Foundation for Medical Education and Research.

4. Murray, B. and Rosenbloom, C., 2018. Fundamentals of glycogen metabolism for coaches and athletes. Nutrition Reviews 76(4): 243-259.

8. Sandri, M., Lin, J., Handschin, C., Yang, W., Arany, Z.P., Lecker, S.H., Goldberg, A.L. Spiegelman, B.M., 2006, PGC-1alpha protects skeletal muscle from atrophy by suppressing FoxO3 action and atrophy-specific gene transcription. Proceedings of the National Academy of Sciences of the United States of America 103(44): 12620-12625.

9. Ye, J., 2013, Mechanisms of insulin resistance in obesity. Frontiers in Medicine 7: 14-24.

PGC1α Overexpression Preserves Cardio-Metabolic and Skeletal Muscle Function in a Type 2 Diabetic Mouse Model

COLLEGE OF VETERINARY MEDICINE

Jillian Gore 2021-2022 Niblack Research Scholar

Emily Nunan DVM/PhD Candidate

Mentor: Dr. Joshua Butcher

Thank you!

Acknowledgements

- I'd like to thank my colleagues in Dr. Butcher's Laboratory, including all listed authors
- I'd like to especially thank the Niblack Research Scholars Program and Summer Research Training Program, which have provided significant support and funding to myself

Funding

- NIA 5K01AG064121 (Butcher)
- NIGMS P30GM122744 (PI: Ma, Pilot Study: Butcher)
- OCAST HR21-045-1 (PI: Butcher)

Introduction

- Almost 42% of Americans are obese, and obesity signifcantly increases your risk for Type 2 Diabetes (CDC, 2017)
- 37.3% of Americans have diabetes and nearly 1 in 3 are considered pre-diabetic (CDC, 2022)
- Diabetes is currently the 7th leading cause of death (CDC, 2021)

Introduction

- Reoccurring hypergycemia and insulin malfunction are tied to damage or failure of differing organs such as kidneys, nerves, vasculature, and skeletal muscle (American Diabetes Association, 2007).
- Upregulation of oxidative skeletal muscle fibers are known to increase insulin sensitivity, lower blood pressure, and decrease fat
- PGC1α (peroxisome proliferator-activated receptor gamma coactivator 1 alpha) is known to increase oxidative fibers

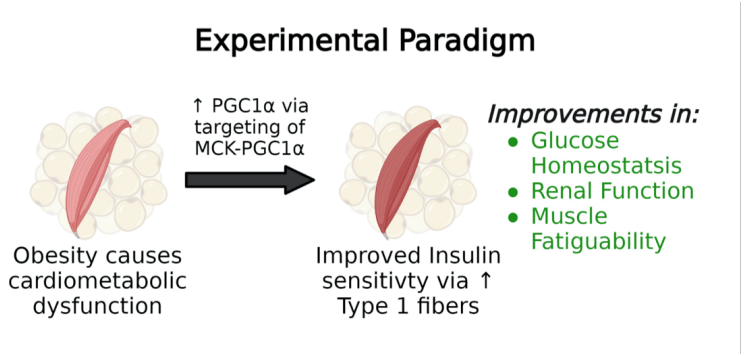

Hypothesis

Can increases in oxidative muscle fibers increase muscle performance and improve glucose handling and kidney function in a mouse model of Type 2 diabetic patients?

Mouse Models

https:/ / www.jax.org/ strain/ 000632

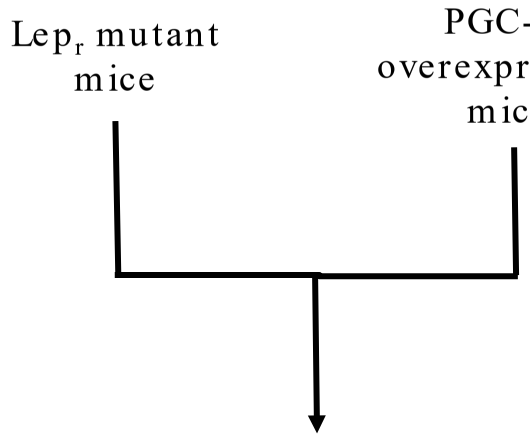

$H_{db}W_{PGC1\alpha}$ = Lean Control

$H_{db}H_{PGC1\alpha}$ = Lean PGC1α Overexpression

$K_{db}W_{PGC1\alpha}$ = Obese Control

$K_{db}H_{PGC1\alpha}$ = Obese PGC1α Overexpression

Methods

Muscle Fatiguability

- Twitch
- Tetanic
- Force Frequency
- Fatigue Curve

Glucose Handling

- Fasting Plasma Glucose
- HbA1c's
- Insulin ELISAs
- IGTT

Renal Function

- Metabolic Cages

Model Verification

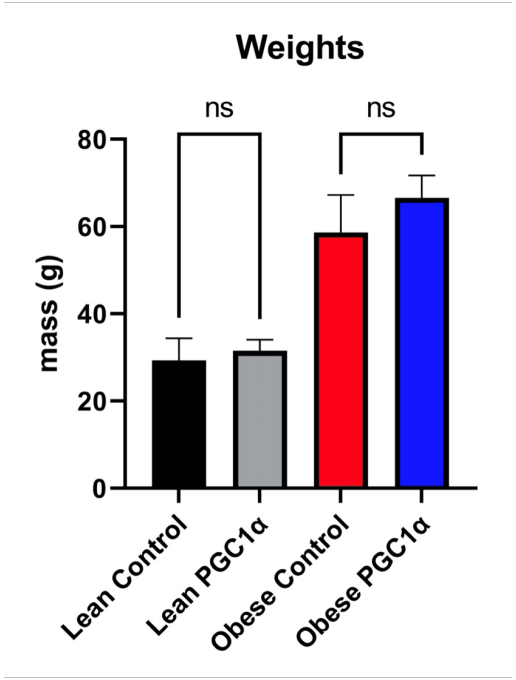

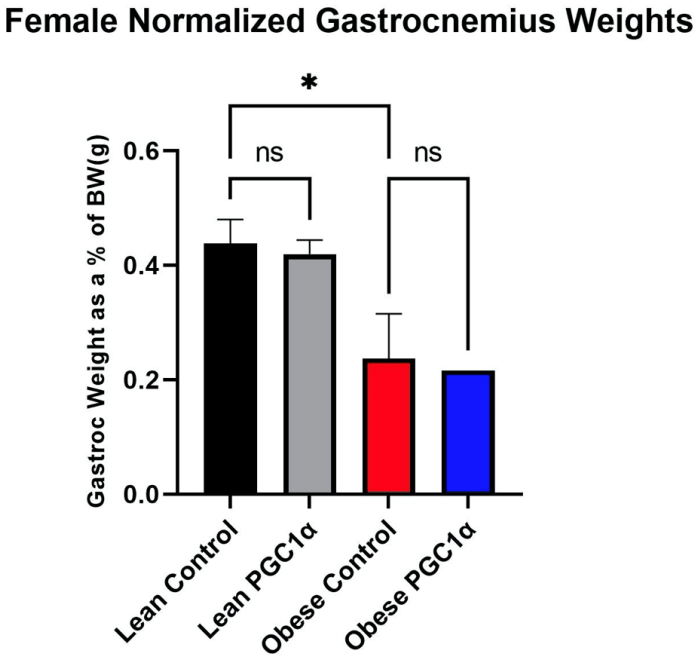

Results: Muscle Function

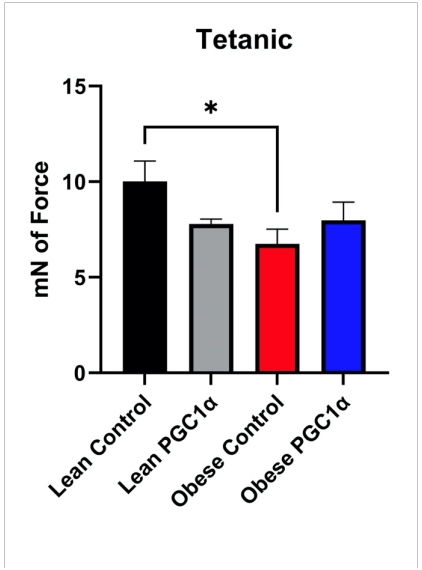

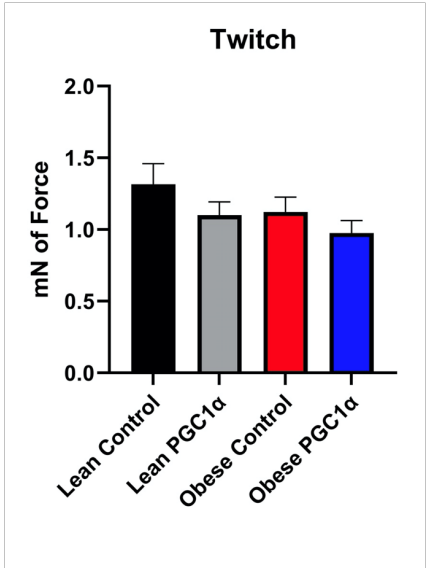

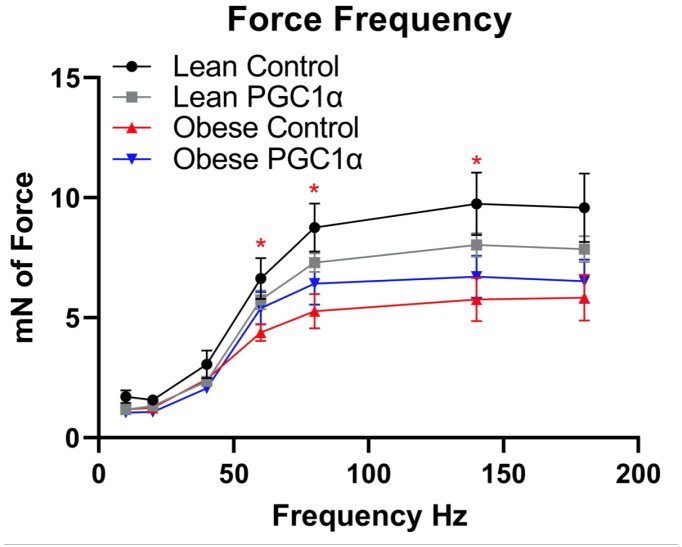

Results: Muscle Function

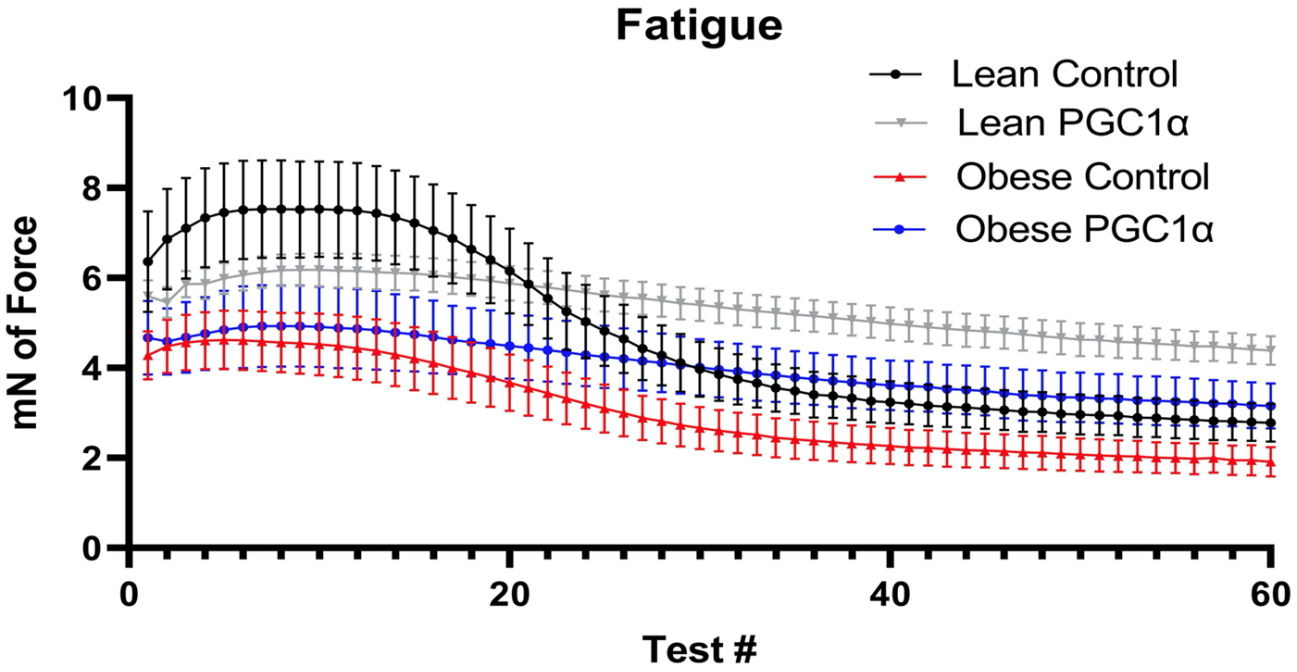

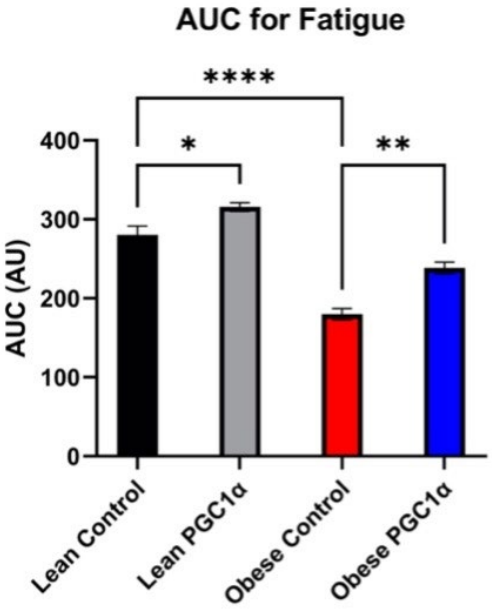

Results: Glucose Handling

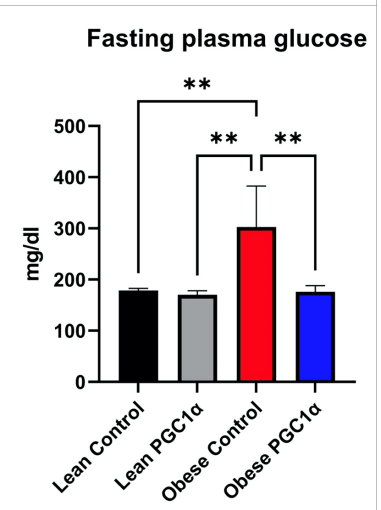

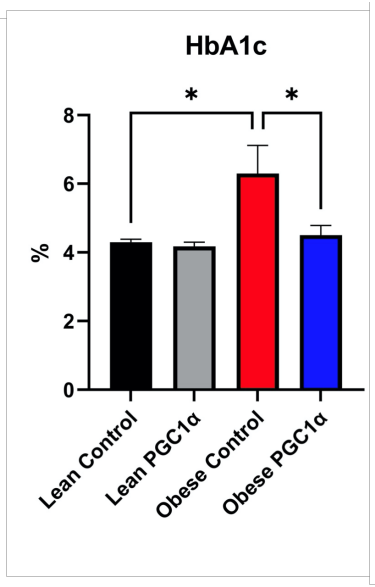

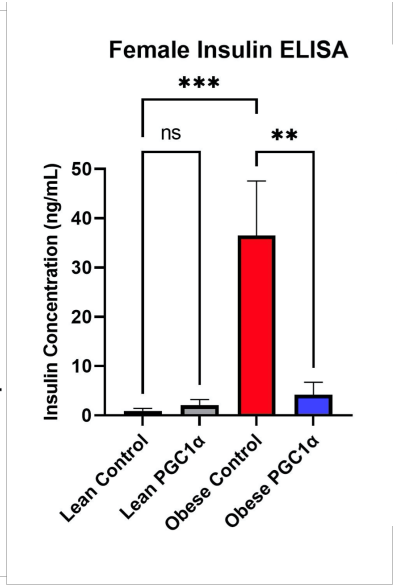

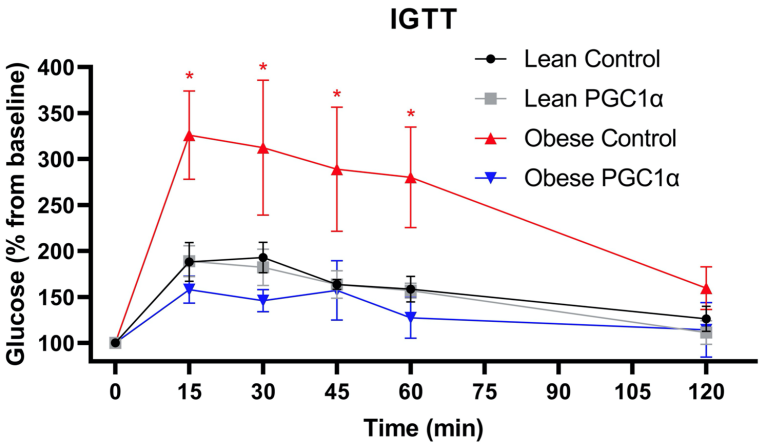

Results: Renal Function

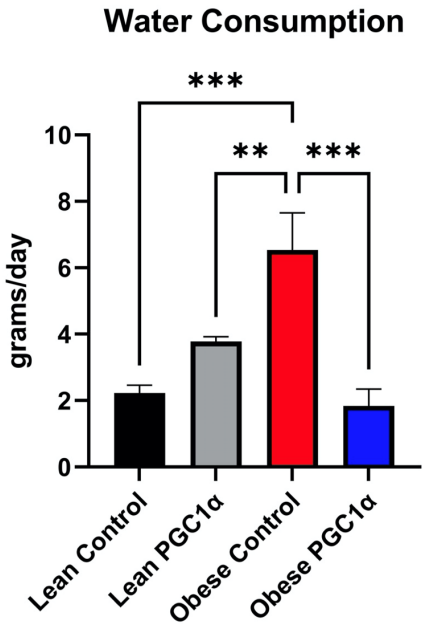

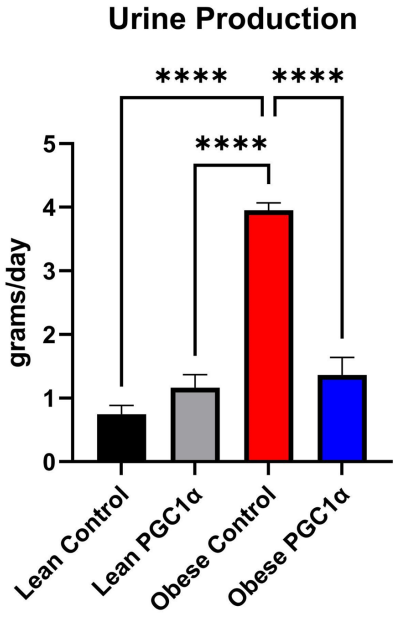

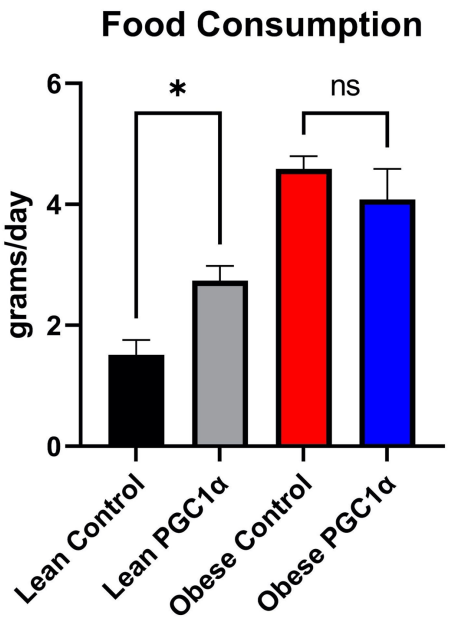

Conclusions

PGC1α overexpression

- improves muscle function inhibits fatigability in both lean and obese female mice without increasing overall muscle mass
- preserves glucose handling in a Type 2 Diabetic mouse model in young adult female mice
- protects against polyuria/polydipsia and restores fluid dynamics when faced with Type 2 Diabetes
- **is a unique and innovative pathway that can be a future therapeutic target to improve glucose homeostasis, fluid dynamics, and muscle function in type 2 diabetes and other cardiometabolic diseases**

References

- "National Diabetes Statistics Report," *Center for Disease Control and Prevention*, U.S. Department of Health & Human Services, 2022
- "Adult Obesity Facts," *Center for Disease Control and Prevention*, U.S. Department of Health & Human Services, 2017.
- "Diabetes," *Center for Disease Control and Prevention*, U.S. Department of Health & Human Services, 2021
- "Diabetes Care," *American Diabetes Association* 30, S4-S41, doi: 10.2337/dc07-S004 (2007)

Questions?


If you think a minute goes by really fast, you've never been on a treadmill.
someecards
user card

Obesity-Induced Sympathoexcitation Causes Down-Regulation of Glutamate Transporters Expression in Human Brainstem Astrocytes

Manoj Jagadeesh

Department of Physiological Sciences
Faculty Sponsor: Dr. Madhan Subramanian
Graduate Student Mentor: Mahesh Kumar Sivasubramanian

ABSTRACT

Overactive sympathetic nerve activity (SNA) arising from oxidative stress as a consequence of obesity has been linked to an increase in the risk for cardiovascular disease. Previous research in our lab has pointed to the role of the rostral ventrolateral medulla (RVLM) of the brainstem, which is responsible for regulating many important cardiovascular functions such as heart rate and blood pressure. More specifically, our research has indicated that astrocytes may play a key role in regulating the RVLM itself. Astrocytes are vital for the removal of excess glutamate in synapse preventing sympathoexcitation. The main mechanism behind this phenomenon is still not well understood. In this study, we employed the use of cell culture to subject human brainstem astrocytes to conditions that mimicked that of obesity. Specifically, we examined the effects of obesity-induced oxidative stress on astrocytes to assess how they might affect the RVLM and as a result hypertension and cardiovascular disease. We subjected human brainstem astrocytes to obesity-like conditions with varying levels of insulin and glucose to induce hyperglycemia, a complication very closely associated with obesity. Upon completion of the growth period, the cells were collected and subjected to qPCR for analysis. Our results indicated that under hyperglycemic (high glucose) conditions, oxidative stress markers were significantly upregulated, and the glutamate transporters found in astrocytes were significantly downregulated. Our results also showed that GABA receptors were significantly downregulated indicating that GABA may also play a role in obesity-induced sympathoexcitation.

1. Introduction

Cardiovascular disease is one of the leading causes of death in the United States, and according to the Centers for Disease Control and Prevention (CDC), accounts for

approximately 25% of all deaths every year. One of the major risk factors implicated with cardiovascular disease is obesity, with nearly 42% of Americans being classified as obese from statistics provided by the CDC. While there has been significant progress in the development of preventions and treatments for cardiovascular disease, it remains a major killer (Reamy et al., 2018). The main role of obesity in the implication of heart disease is oxidative stress, which causes overactivation of the sympathetic nervous system through a paracrine manner resulting in sympathoexcitation and hypertension (Balasubramanian et al., 2020). The mechanism through which this occurs is by activation of glutamatergic receptors in the RVLM of the brainstem, the region of the brain responsible for regulating the sympathetic nervous system (SNS) (Balasubramanian et al., 2020). The SNS is very important as it oversees all the important body functions that keep us alive. Improper regulation of glutamate reuptake and inhibition leads to continuous activation of the SNS, excitotoxicity, and consequently the renin-angiotensin-aldosterone system (RAAS) (Kishi and Hirooka, 2013). Thus, it is important to study the mechanism behind sympathoexcitation and glutamate regulation in the obese population (Sivasubramanian et al., 2020).

The pathophysiology of cardiovascular disease is a multifaceted field of study that is still not well understood (Manna and Jain, 2015). A common complication of obesity is type 2 diabetes mellitus, in which the body is able to produce insulin but insulin receptor sensitivity results in increased extracellular concentrations of glucose, or hyperglycemia (DeBoer, 2013) (Vanessa Fiorentino et al., 2013). Neuronal cells are different in their nutritional needs compared to normal cells in that they cannot regulate glucose levels through the use of insulin. Rather, they rely on extracellular levels of glucose to provide a source of fuel for cellular metabolism. Previous work in our lab looked at the effects of high sugar diets and their effects on mice in vivo. The results from those studies have led us to investigate the effects of a high fat diet on humans in vitro (Balasubramanian et al., 2019). Further studies have been conducted showing evidence that hyperglycemia causes oxidative stress through activation of the hexosamine pathways promoting the increased production of reactive oxygen species (ROS). The increased production of ROS can lead to neurotoxicity and eventually neuronal cell death. It is also believed that the neuronal cell death caused by hyperglycemia could be indirectly affected by accessory glia (Li et al., 2018).

One emerging topic is the role of glial cells as a key player in the regulation of sympathoexcitation in the brainstem, more specifically astrocytes (Jagadeesh et al., 2021). Astrocytes are thought to play a key role in the strict regulation of glutamate through their excitatory amino acid transporters EAAT1 and EAAT2 (Sivasubramanian et al., 2020). Studying the role of astrocytes in glutamate regulation and how they are affected by oxidative stress can hopefully give us a greater understanding of the relative pathophysiology involved in cardiovascular disease and hypertension. In this study, we employed the use of cell culture to subject human brainstem astrocytes to conditions that mimicked that of

obesity. My goal is to investigate the effects of hyperglycemia on astrocytes in the RVLM and their role in obesity-mediated sympathoexcitation.

2. Experimental Details

Cell Culture

For the insulin experiment, human brainstem astrocytes isolated from the brainstem were obtained from ScienCell™ Research Laboratories and grown in Astrocyte Media (ScienCell™) and supplemented with Dulbecco's Phosphate-Buffered saline (PBS), Fetal Bovine Serum (FBS), and Astrocyte Growth Supplement, along with penicillin and streptomycin. The cells were allowed to grow in a 37°C incubator with 5% CO_2 until they reached approximately 80% confluency and were then split using Trypsin into two 6-well plates. Each well was treated with varying concentrations of human recombinant insulin or vehicle (HCl). The three concentrations used were 25 μM, 50 μM, and 100 μM; the first plate was treated for 24 hours, and then collected after 48 hours, and the second plate was treated for 48 hours and collected after 72 hours. After the 24- and 48-hour treatments respectively, the media was replaced with fresh Astrocyte Media to stop the treatment. This was repeated twice more (n = 3).

For the glucose experiment, Human brainstem astrocyte from ScienCell™ Research Laboratories were grown with the exception that Gibco™ DMEM low glucose (5 mM) media was used to initially culture the cells to 80% plate confluency. The cells were then split into three 6 well plates (only 4 wells on the third plate) to get n = 8. Each plate had 3 wells grown under hyperglycemic conditions with Gibco™ DMEM high glucose (25 mM) media, and 3 wells grown under normal glucose levels with Gibco™ DMEM low glucose (5 mM) media. The cells were grown for 5 days and then collected as with the insulin experiment. All media used for the glucose experiment were supplemented with 10% heat inactivated FBS.

mRNA Extraction

Cells were washed with PBS and then collected by scraping the wells using TRIzol™ Reagent (Thermo Fisher Scientific) and stored in -20°C for extraction. Extraction was done using a Direct-zol RNA kit from Zymo Research following the protocol established by the company. Once all the mRNA had been extracted, the mRNA purity was measured using a nano-drop machine and then converted into cDNA using a Thermo Fisher Scientific High-Capacity cDNA Reverse Transcription Kit and stored in -20°C until further use. The same was done for the glucose experiment.

PCR Analysis

Quantitative PCR analysis was done with iTaq SYBR Green kit from BioRad for 12 genes and 2 housekeeping/control genes, Glyceraldehyde-3-phosphate dehydrogenase

(*GAPDH*) and *Beta Actin*. The same 14 genes were analyzed for both the insulin and glucose experiments.

Statistical Analysis

All data were analyzed using a two-tailed Student's t-test with one independent variable to look for statistical significance. For all the data analyzed, statistical significance was defined as $p < 0.05$ (*). All the data are represented as bar graphs with standard error of mean (S.E.M).

3. Results

Effect of Hyperglycemia on the expression of oxidative stress markers

Astrocytes grown in the presence of high glucose (25 mM) showed significantly increased transcript levels of oxidative stress markers nuclear factor erythroid 2-related factor 2 (*Nrf2*), NADPH quinone dehydrogenase 1 (*NQO1*), and superoxide dismutase 2 (*SOD2*). In contrast, expression of antioxidant enzyme *Catalase* was downregulated at the same concentration of glucose.

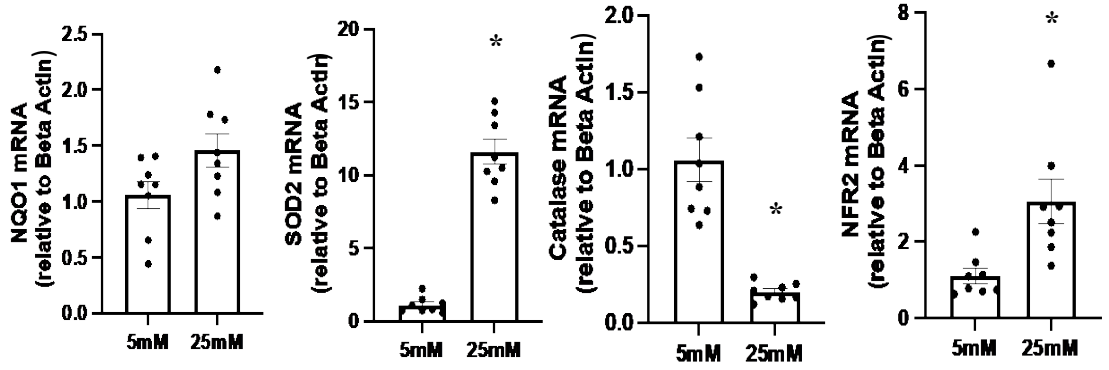

Fig. 1. Hyperglycemia induced changes in the expression of oxidative stress markers *NQO1*, *Nrf2*, *SOD2*, and *Catalase* in human brainstem astrocytes grown in 5mM (control) and 25mM (treatment) glucose media. Data are mean ± SEM (n = 8 per group). * denotes significance defined ($p < 0.05$) from control group.

Hyperglycemia reduced the expression of GABA receptors

In order to find the effect of hyperglycemia on the expression of GABA receptor, expression levels of three GABA receptors, Gamma-Aminobutyric Acid Type A Receptor Subunit D (*GABA A-D*), Gamma-Aminobutyric Acid Type A Receptor Subunit Alpha1 (*GABA A-a1*) and Gamma-Aminobutyric Acid Type A Receptor Subunit Alpha2 (*GABA A-a2*) were analyzed by growing astrocytes in the presence of 25 mM glucose in the media and compared to control (5 mM) conditions. Our results showed expression of all three GABA receptors *GABA A-D*, *GABA A-a1*, and *GABA A-a2* were significantly downregulated under hyperglycemic conditions.

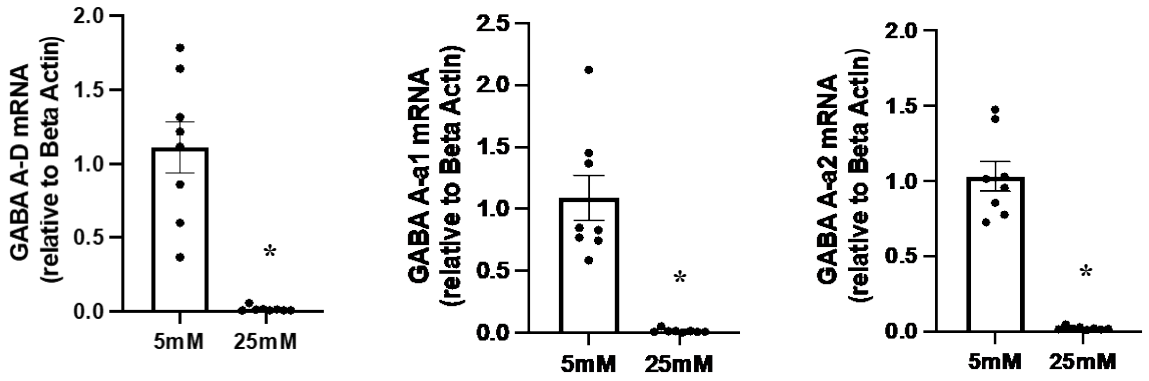

Fig. 2. Hyperglycemia induced changes in the expression of GABA receptors. Transcript levels (normalized to Beta actin) of GABA A-D, GABA A-a1, and *GABA A-a2* in human brainstem astrocytes grown in 5mM (control) and 25mM (treatment) glucose media. Data are mean ± SEM (n = 8 per group). * denotes significance defined ($p < 0.05$) from control group.

Hyperglycemia causes down-regulation of glutamate transporters

We also analyzed mRNA levels of genes involved in glutamate transport, *EAAT1* and *EAAT2*, in the human brainstem astrocytes treated with high glucose (25mM). Our data show expression of the two genes decreased and the downregulation of *EAAT2* was more drastic than that of *EAAT1*.

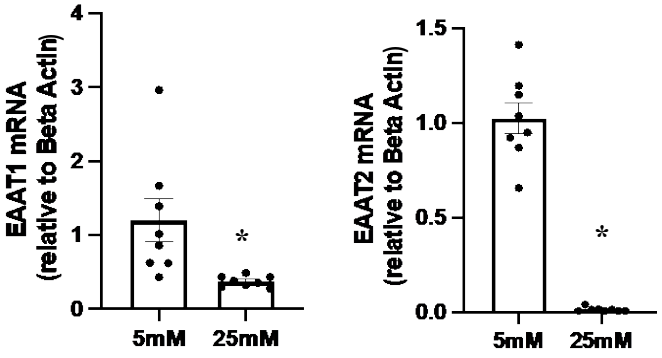

Fig. 3. Hyperglycemia induced changes in mRNA expression of *EAAT1* and *EAAT2* in human brainstem astrocytes grown in 5mM (control) and 25mM (treatment) glucose media. Data are mean ± SEM (n = 8 per group). * denotes significance defined ($p < 0.05$) from control group.

Effect of Hyperinsulinemia on the expression of oxidative stress markers

Astrocytes treated with 25 µM insulin for 48 hours showed decreased expression for oxidative stress markers *NQO1*, *Nrf2*, *SOD2*, and *Catalase*.

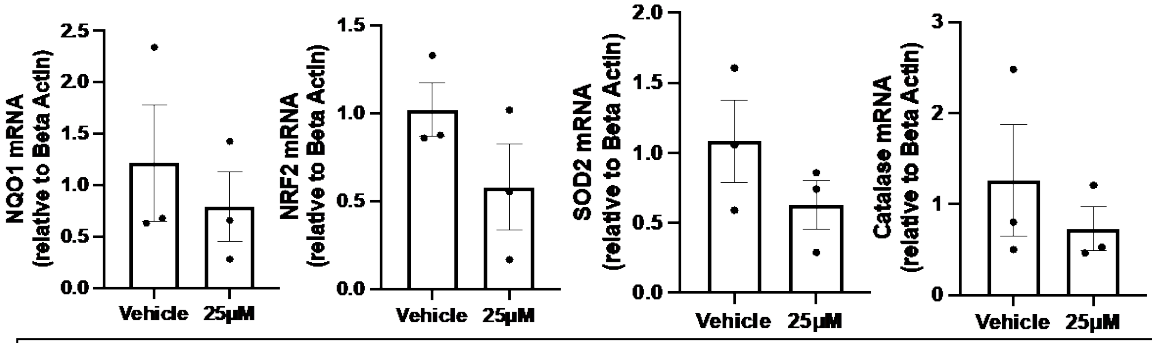

Fig. 4. Hyperglycemia induced changes in the expression of oxidative stress markers of *NQO1*, *Nrf2*, *SOD2*, and *catalase* in human brainstem astrocytes grown in vehicle (control) and 25µM (treatment) insulin. Data are mean ± SEM (n = 3 per group). * denotes significance defined ($p < 0.05$) from control group.

Effect of insulin treatment on the expression on glutamate transporter activity

Astrocytes treated with 25 µM insulin displayed a similar trend wherein the expression levels of glutamate transporters *EAAT1* and *EAAT 2* were downregulated.

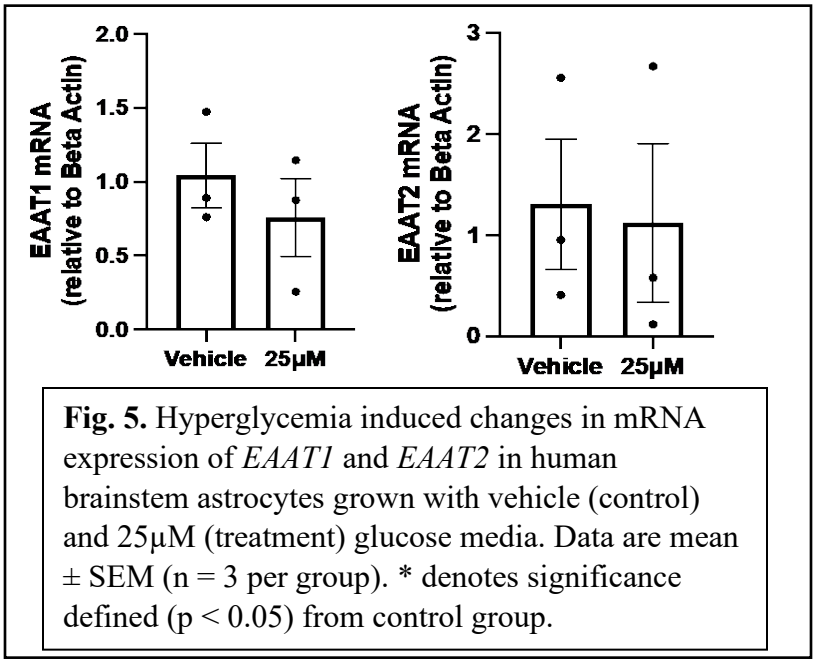

Fig. 5. Hyperglycemia induced changes in mRNA expression of *EAAT1* and *EAAT2* in human brainstem astrocytes grown with vehicle (control) and 25µM (treatment) glucose media. Data are mean ± SEM (n = 3 per group). * denotes significance defined ($p < 0.05$) from control group.

Effect of Hyperinsulinemia on the expression of GABA receptors

As in the cases of glutamate receptor, astrocytes treated with 25µM for 48 hours, showed a trend towards down-regulation in the expression levels of all GABA receptors tested in the analysis.

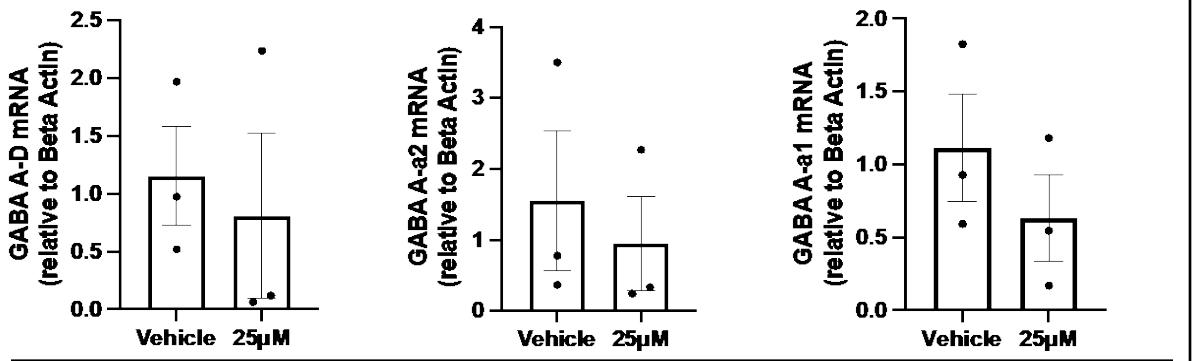

Fig. 6. Hyperglycemia induced changes in mRNA expression of *GABA A-D*, *GABA A-a1*, and *GABA A-a2* in human brainstem astrocytes grown with vehicle (control) and 25µM (treatment) glucose media. Data are mean ± SEM (n = 3 per group). * denotes significance defined ($p < 0.05$) from control group.

4. Discussion and Conclusions

The human brain is a complex organ that requires a high supply of glucose to keep it functioning optimally. While we must maintain a steady supply glucose to the brain, it is important to make sure that we don't overdo it. Too much glucose can lead to hyperglycemia and sympathoexcitation which can have detrimental effects to not only our brains but also our bodies. Several safeguards exist in place to ensure that excess glutamate can be dealt with properly. Glutamate transporters tightly regulate glutamate concentration in the synaptic cleft, specifically EAAT1 and EAAT2 are in charge of regulating synaptic levels of glutamate preventing sympathoexcitation. Although, these safeguards are present and do a pretty good job of keeping sympathoexcitation from occurring, they aren't foolproof. Obesity and high sugar/glucose diets cause oxidative stress which works against these safeguards and contributes to sympathoexcitation and excitotoxicity. Our results clearly show a high glucose diet leads to increased expression of ROS scavengers such as SOD2, NQO1, and Nrf2 leading us to believe that hyperglycemia is implicated in oxidative stress. Work in our lab has shown that while these ROS removers are upregulated to restore free radical levels, they don't last forever (Subramanian et al., 2020). In chronic obesity studies in mice done in our lab, we have found that these free radical removers can't be sustained for long periods of time and eventually stop working.

Furthermore, we have shown that hyperglycemia leads to down-regulation of the glutamate transporters EAAT1 and EAAT2. This data aligns with our hypothesis that a high sugar diet results in sympathoexcitation of the SNS leading to hypertension and cardiovascular disease. Additionally, our data points to the role of GABA in sympathoexcitation. In the astrocytes treated in the hyperglycemic environment, there was significant down-regulation of GABA receptors which function in an antagonistic role to glutamate and thus work to prevent sympathoexcitation. Other research has been done showing that astrocytes not only are impaired by obesity, but they naturally deteriorate as we age (Palmer and Ousman, 2018), contributing to other diseases like Alzheimer's (Rodríguez-Arellano et al., 2016). The data from the insulin trials indicates that insulin does not seem to be major player behind sympathoexcitation. While we were not able to see any changes in the astrocytes with insulin, studies have shown that insulin does a play a role in sympathoexcitation, but perhaps through a different mechanism than what we studied (Shi et al., 2020). These results further contribute to the role of obesity and diabetes mellitus type 2 as risk factors for cardiovascular disease.

Some of the limitations of this work are that we only looked at the effects of hyperglycemia and insulin at the level of astrocytes. It is also important to see the effects of high sugar diets on other glial cells. Also, the study was conducted in an isolated setting, and we could not see how hyperglycemia or hyperinsulinemia would work when other factors are in play. Our future studies will focus on replicating this study with microglia (another type of

glial cell) and to carry out this study in vivo with mice models to see if our results can carry over.

5. Summary

Thanks to the generosity of the Niblacks, I was able to not only enrich my knowledge of the pathophysiology of the brain but also experience what it is like to conduct my own research project from start to finish. Over the course of the last year, my research was focused on getter a better picture of the links between obesity and sympathoexcitation. Specifically, I wanted to understand the mechanism linking the two together and how we could remedy this issue. In order to achieve this, I set out to recreate cellular environments that simulated obesity through the use of insulin. Unfortunately, the data wasn't as promising as I hoped, so I had switch gears and use glucose. As I progressed with my research, I was able to obtain key research skills like managing delays and troubleshooting my experiments. Much of my work revolved around cell culture, mainly working with human brainstem astrocytes. Through the utilization of cell culture, I was able to look at gene expression and protein content to get a clear idea of what is happening to the brains of the obese population. The results from the data point to a key role between obesity and sympathoexcitation of the RVLM through a glucose meditated pathway rather than insulin. I was also able to discover new pathways I initially never thought to explore such as that of the neurotransmitter GABA. Through this research experience, I was able learn how to analyze and interpret data to get a deeper understanding of the human brain and how it is affected by chronic diseases like obesity.

6. Appendices

a. Acknowledgements

I would like to thank Dr. and Mrs. Niblack for giving me to opportunity to pursue a meaningful research experience as an undergraduate. I would also like to thank my research mentor Dr. Madhan Subramanian for taking a chance on me back when I was a freshman with no research experience and for helping me grow both as a researcher and as a student. Lastly, I would like to thank to my graduate mentor Mahesh Sivasubramanian, Raisa Monteiro, and all the other graduate students I worked with. They were all more than willing to meet with me according to my schedule and teach me many of the various research skills I have learned thus far. The funding for this research were provided by the NIH through the National Heart, Lung, and Blood Institute (1R15HL148844-01) and the American Heart Association Institutional Research Enhancement Award (959725).

b. Literature Cited

BALASUBRAMANIAN, P., ASIRVATHAM-JEYARAJ, N., MONTEIRO, R., SIVASUBRAMANIAN, M. K., HALL, D. & SUBRAMANIAN, M. 2020. Obesity-induced sympathoexcitation is associated with Nrf2 dysfunction in the rostral

ventrolateral medulla. *American Journal of Physiology-Regulatory, Integrative and Comparative Physiology,* 318**,** R435-R444.

BALASUBRAMANIAN, P., HALL, D. & SUBRAMANIAN, M. 2019. Sympathetic nervous system as a target for aging and obesity-related cardiovascular diseases. *Geroscience,* 41**,** 13-24.

DEBOER, M. D. 2013. Obesity, systemic inflammation, and increased risk for cardiovascular disease and diabetes among adolescents: a need for screening tools to target interventions. *Nutrition,* 29**,** 379-386.

JAGADEESH, M., SIVASUBRAMANIAN, M., MONTEIRO, R., BALASUBRAMANIAN, P. & SUBRAMANIAN, M. 2021. Senescence-Associated Secretory Phenotype (SASP) factors down-regulate glutamate transporter expression in human brainstem astrocytes through a paracrine fashion. *The FASEB Journal,* 35.

KISHI, T. & HIROOKA, Y. 2013. Sympathoexcitation associated with Renin-Angiotensin system in metabolic syndrome. *International Journal of Hypertension,* 2013.

LI, W., CHOUDHURY, G. R., WINTERS, A., PRAH, J., LIN, W., LIU, R. & YANG, S.-H. 2018. Hyperglycemia alters astrocyte metabolism and inhibits astrocyte proliferation. *Aging and disease,* 9**,** 674.

MANNA, P. & JAIN, S. K. 2015. Obesity, oxidative stress, adipose tissue dysfunction, and the associated health risks: causes and therapeutic strategies. *Metabolic syndrome and related disorders,* 13**,** 423-444.

PALMER, A. L. & OUSMAN, S. S. 2018. Astrocytes and aging. *Frontiers in Aging Neuroscience***,** 337.

REAMY, B. V., WILLIAMS, P. M. & KUCKEL, D. P. 2018. Prevention of cardiovascular disease. *Primary Care: Clinics in Office Practice,* 45**,** 25-44.

RODRÍGUEZ-ARELLANO, J., PARPURA, V., ZOREC, R. & VERKHRATSKY, A. 2016. Astrocytes in physiological aging and Alzheimer's disease. *Neuroscience,* 323**,** 170-182.

SHI, Z., ZHAO, D., CASSAGLIA, P. A. & BROOKS, V. L. 2020. Sites and sources of sympathoexcitation in obese male rats: role of brain insulin. *American Journal of Physiology-Regulatory, Integrative and Comparative Physiology,* 318**,** R634-R648.

SIVASUBRAMANIAN, M. K., MONTEIRO, R., BALASUBRAMANIAN, P. & SUBRAMANIAN, M. 2020. Oxidative Stress-Induced Senescence Alters Glutamate Transporter Expression in Human Brainstem Astrocytes. *The FASEB Journal,* 34**,** 1-1.

SUBRAMANIAN, M., EDWARDS, L., MELTON, A., BRANEN, L., HERRON, A., SIVASUBRAMANIAN, M. K., MONTEIRO, R., STANSBURY, S., BALASUBRAMANIAN, P. & MORRIS, L. 2020. Non-invasive vagus nerve stimulation attenuates proinflammatory cytokines and augments antioxidant levels in the brainstem and forebrain regions of Dahl salt sensitive rats. *Scientific Reports,* 10**,** 1-9.

VANESSA FIORENTINO, T., PRIOLETTA, A., ZUO, P. & FOLLI, F. 2013. Hyperglycemia-induced oxidative stress and its role in diabetes mellitus related cardiovascular diseases. *Current pharmaceutical design,* 19**,** 5695-5703.

Obesity-induced sympathoexcitation causes down-regulation of glutamate transporter expression in human brainstem astrocytes

Manoj Jagadeesh

Background

- Cardiovascular disease (CVD) is the leading cause of death in the US.
- Link between obesity and CVD
- Indirect and direct risk factors
  - Diabetes and oxidative stress
- Effects of oxidative stress on brainstem
- Use of insulin and glucose

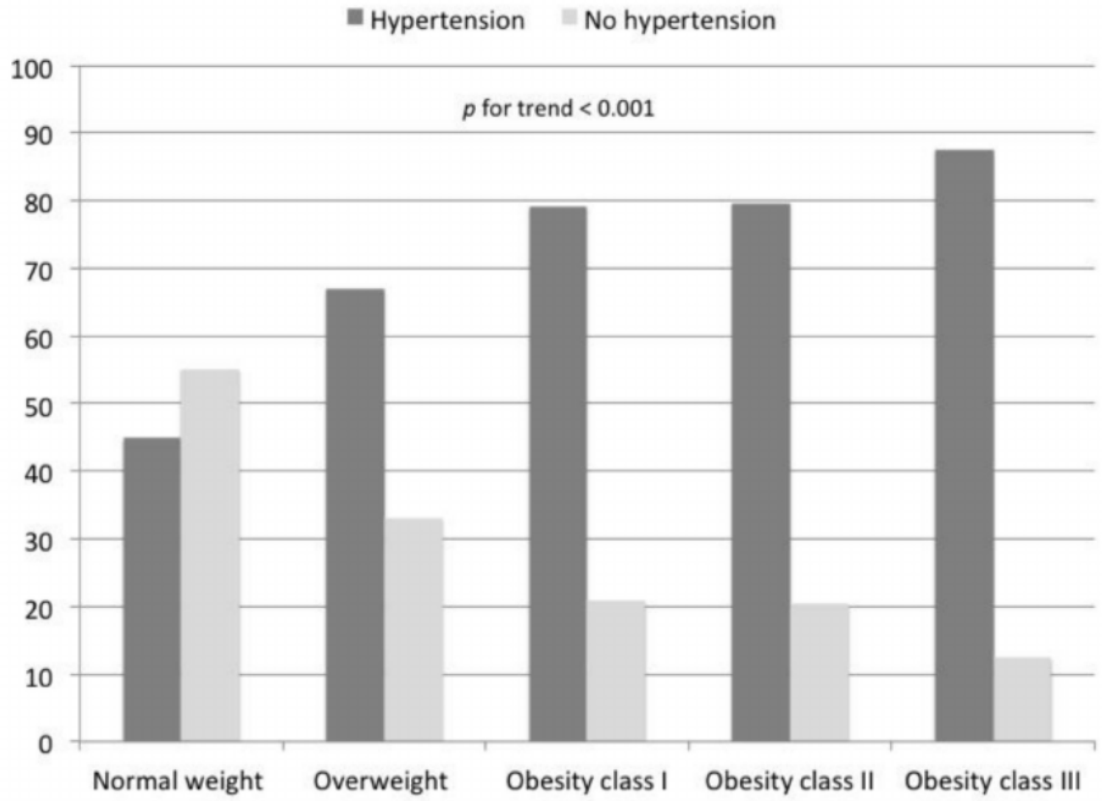

Landi, F., Calvani, R., Picca, A., Tosato, M., Martone, A. M., Ortolani, E., Sisto, A., D'Angelo, E., Serafini, E., Desideri, G., Fuga, M. T., & Marzetti, E. (2018). Body Mass Index is Strongly Associated with Hypertension: Results from the Longevity Check-up 7+ Study. *Nutrients*, *10*(12), 1976. https://doi.org/10.3390/nu10121976

Current Work in the Lab

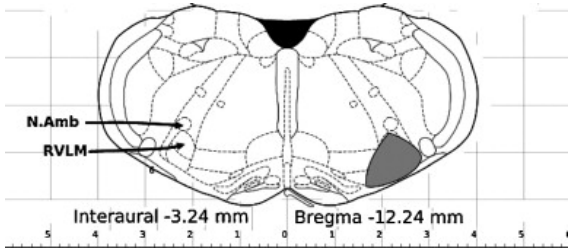

- Previous research on the effects of high fat diet in vivo in mice
  - Causes obesity and hypertension
  - Role of obesity in sympathoexcitation

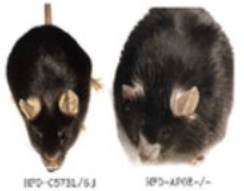

- Effects of senescence on glial cells in the rostral ventrolateral medulla of brainstem (RVLM)
  - Astrocytes (a type of glial cell) undergo senescence releasing senescence associated secretory phenotype (SASP) factors
  - Neuroinflammation and increase in sympathetic nerve activity (SNA)
- Effects of SASP factors on glutamate reuptake transporters in astrocytes
- Treatment of mice with senolytic drugs or Nrf2 vector to reverse senescence

Aims of Study

To understand the mechanisms by which insulin and/or glucose affect human brainstem (HBS) astrocytes and their effects on oxidative stress induced sympathoexcitation of the brainstem.

Hypothesis

Astrocytes treated with either insulin or glucose will lead to an increase in the presence of oxidative stress markers and downregulation of glutamate reuptake transporters as well as γ-Aminobutyric acid (GABA) receptors.

Methodology

Cell Culture

- Subject HBS astrocytes to treatment conditions

Treatment Conditions

- Insulin
- Glucose

Isolation of RNA

- Collection of cells
- mRNA extraction
- cDNA synthesis

Methodology Cont.

Quantitative rt-PCR

Statistical analysis

Results - Hyperinsulinemia

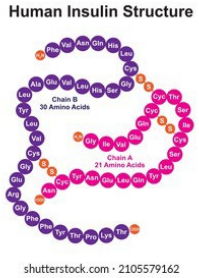

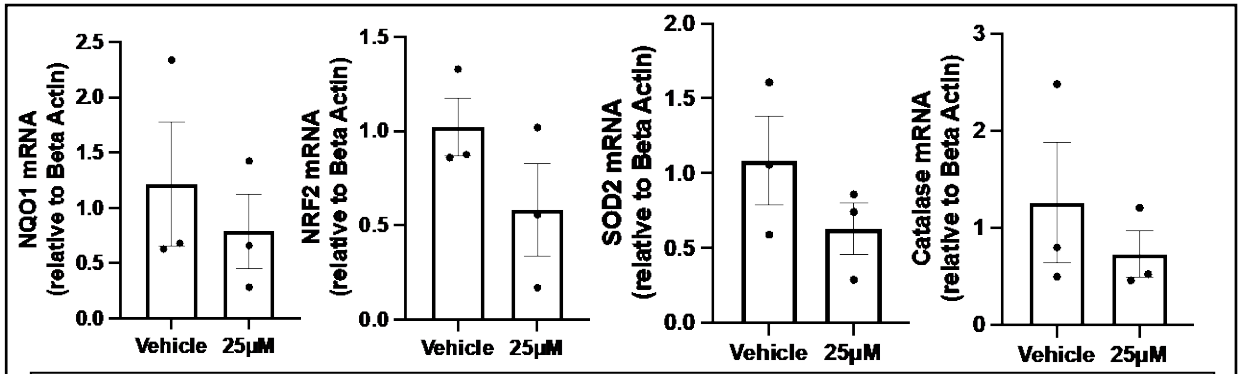

Fig. 1. Hyperinsulinemia induced changes in the expression of oxidative stress markers of *NQO1*, *Nrf2*, *SOD2*, and *Catalase* in human brainstem astrocytes grown in vehicle (control) and 25µM (treatment) insulin. Data are mean ± SEM (n = 3 per group). * denotes significance defined ($p < 0.05$) from control group.

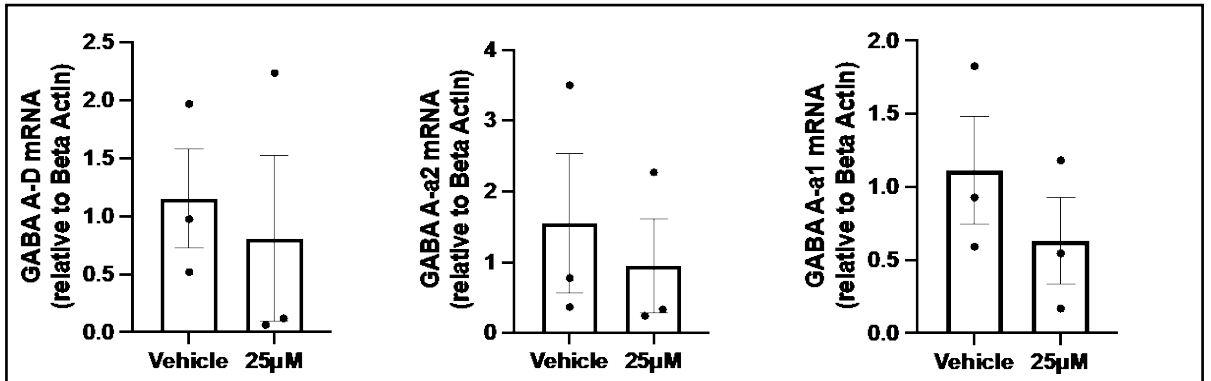

Fig. 2. Hyperinsulinemia induced changes in mRNA expression of *GABA A-D*, *GABA A-a1*, and *GABA A-a2* in human brainstem astrocytes grown with vehicle (control) and 25µM (treatment) glucose media. Data are mean ± SEM (n = 3 per group). * denotes significance defined ($p < 0.05$) from control group.

Results - Hyperinsulinemia

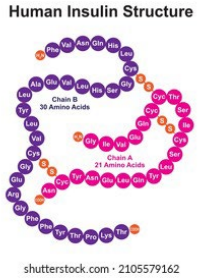

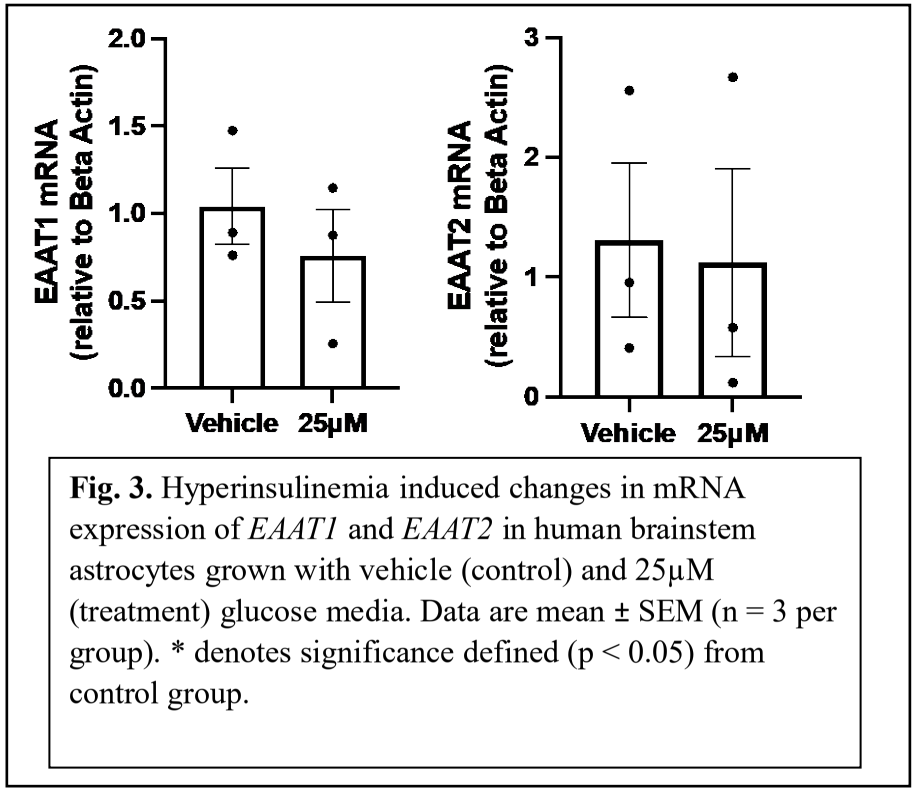

Fig. 3. Hyperinsulinemia induced changes in mRNA expression of *EAAT1* and *EAAT2* in human brainstem astrocytes grown with vehicle (control) and 25µM (treatment) glucose media. Data are mean ± SEM (n = 3 per group). * denotes significance defined ($p < 0.05$) from control group.

Results - Hyperglycemia

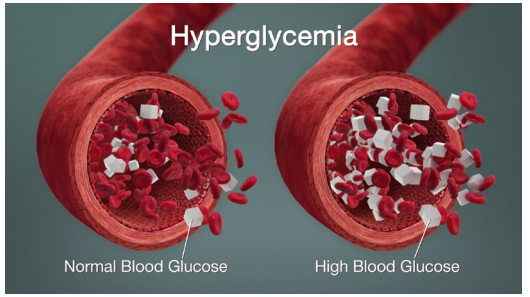

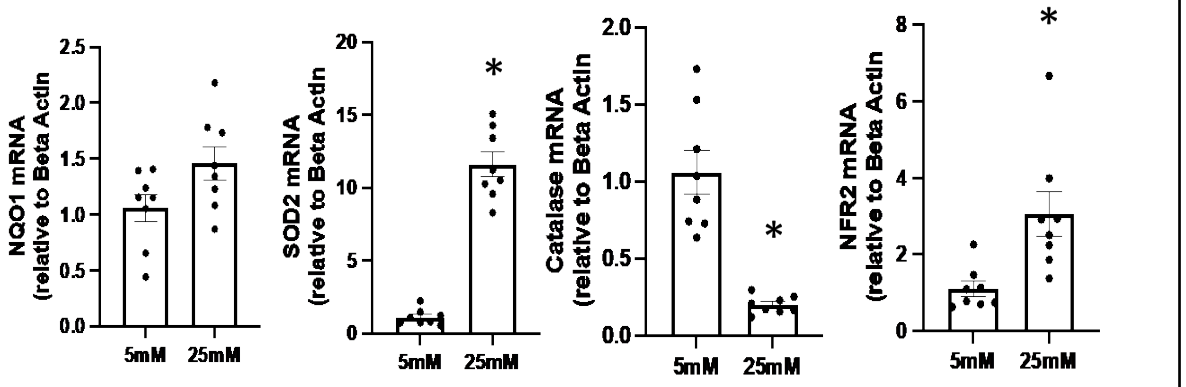

Fig. 4. Hyperglycemia induced changes in the expression of oxidative stress markers *NQO1*, *Nrf2*, *SOD2*, and *Catalase* in human brainstem astrocytes grown in 5mM (control) and 25mM (treatment) glucose media. Data are mean ± SEM (n = 8 per group). * denotes significance defined ($p < 0.05$) from control group.

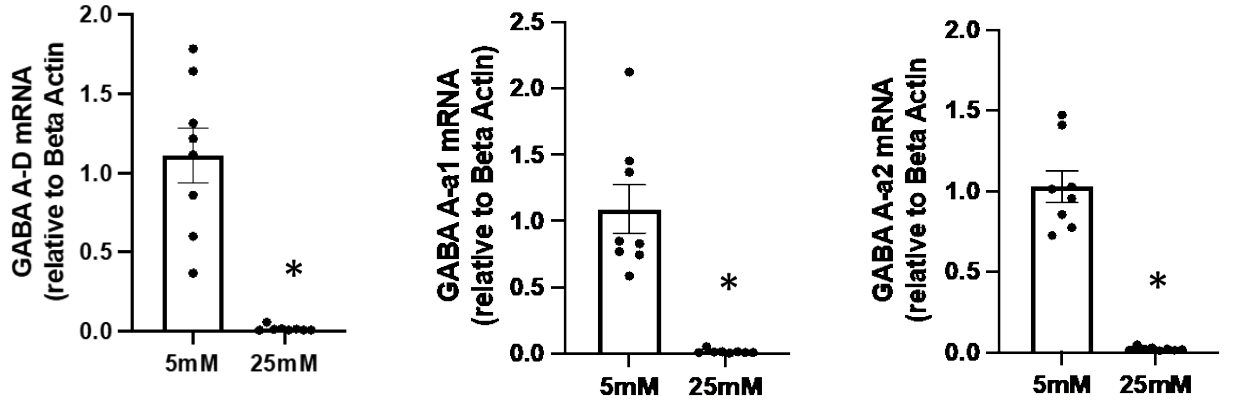

Fig. 5. Hyperglycemia induced changes in the expression of GABA receptors. Transcript levels (normalized to Beta actin) of GABA A-D, GABA A-a1, and *GABA A-a2* in human brainstem astrocytes grown in 5mM (control) and 25mM (treatment) glucose media. Data are mean ± SEM (n = 8 per group). * denotes significance defined ($p < 0.05$) from control group.

Results - Hyperglycemia

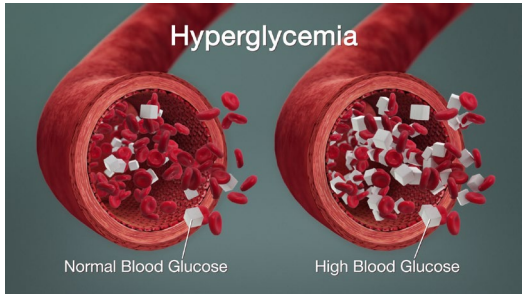

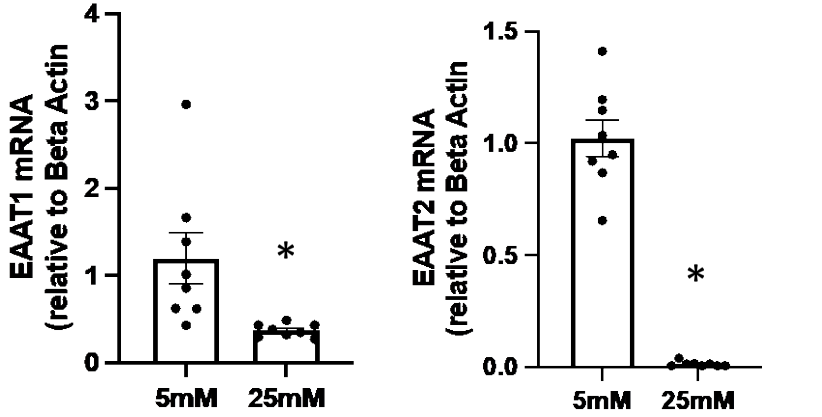

Fig. 6. Hyperglycemia induced changes in mRNA expression of *EAAT1* and *EAAT2* in human brainstem astrocytes grown in 5mM (control) and 25mM (treatment) glucose media. Data are mean ± SEM (n = 8 per group). * denotes significance defined ($p < 0.05$) from control group.

Summary

- Hyperglycemia:
  - Significant upregulation of oxidative stress marker gene expression
  - Significant downregulation of Glutamate reuptake transporter gene expression
  - Significant downregulation of GABA receptor gene expression

- Hyperinsulinemia:
  - No changes observed in oxidative stress marker expression
  - No changes of GABA receptor gene expression
  - No changes observed in Glutamate reuptake transporter expression

Implications

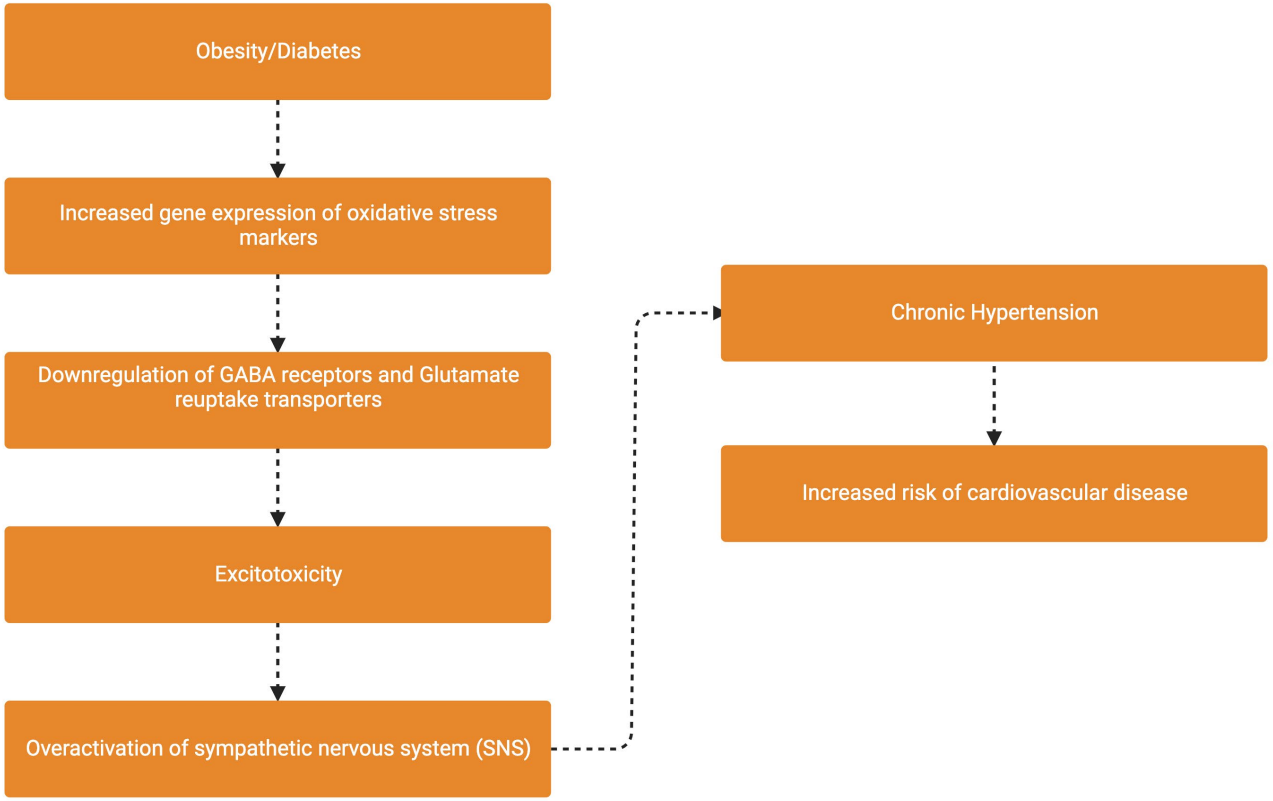

Conclusion

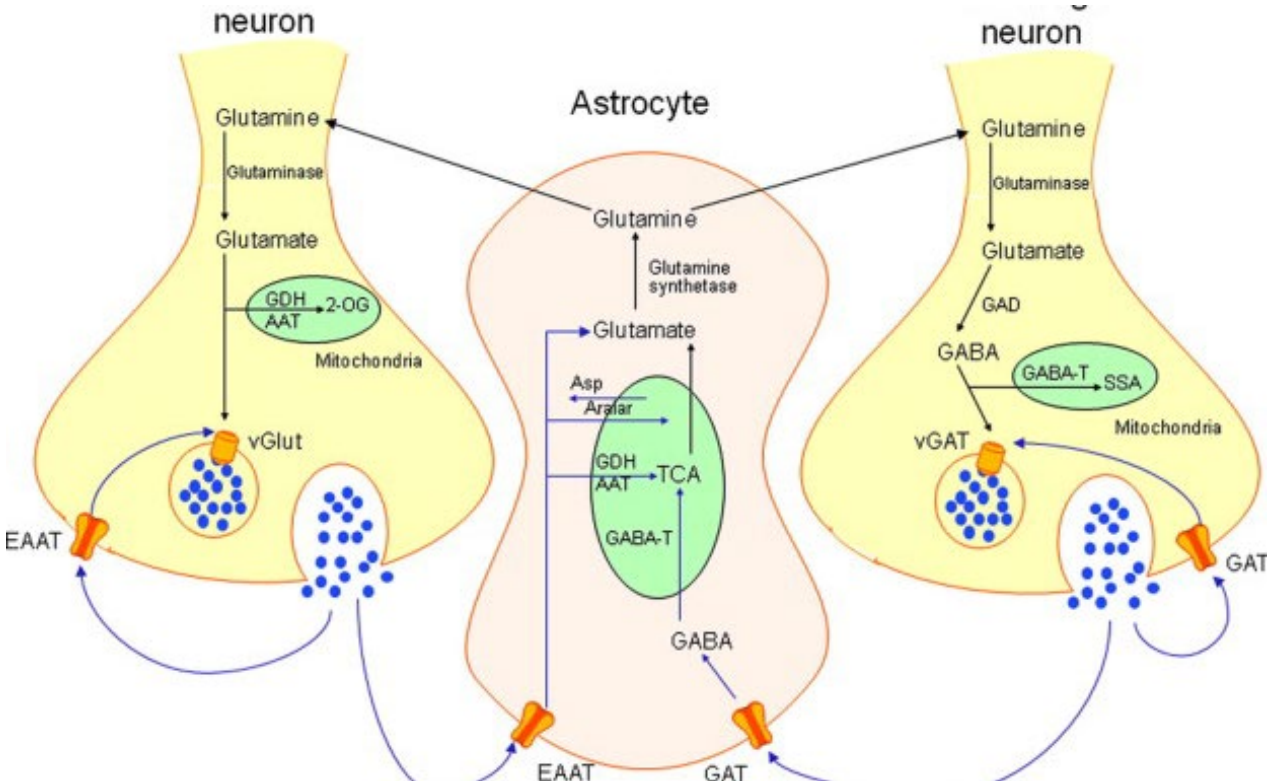

- Direct correlation between oxidative stress and sympathoexcitation
- Understand the mechanism by which obesity contributes to CVD
- Role of neurotransmitters (Glutamate and GABA)
- Link to other projects ongoing in the lab
- Limitations of study

Future Applications

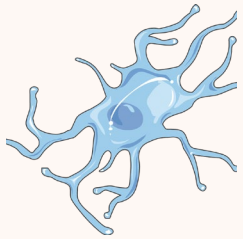

Test different glial cells

Test concept in vivo with mice models

Potential Therapeutic Treatment

Acknowledgements

Dr. and Mrs. Niblack
Dr. Madhan Subramanian
Mahesh Sivasubramanian
Raisa Monteiro

Thank you

Questions?

Exercise and Kidney Function: A Novel Link

Carson L. Wright

Physiological Sciences in the College of Veterinary Medicine:
Faculty Sponsor: Dr. Joshua T. Butcher
Graduate Student Mentor: Emily Nunan

ABSTRACT

Chronic Kidney Disease (CKD) afflicts ~15% of U.S. adults and occurs when the kidneys are ineffective in filtering the blood of waste products. CKD is irreversible and current interventions are focused on protecting and preserving renal function. Risk factors for CKD are multifactorial but growing evidence suggests that a key risk factor is dietary salt intake. A diet high in sodium will increase fluid retention, blood pressure, proteinuria, and ultimately drive the progression of kidney damage. Currently, it is estimated that 90% of the U.S. population consumes excess dietary sodium. As such, it is a medical necessity that interventions focus on ways to optimize renal sodium excretion and protect kidney function over time. Exercise is a key therapy to improve kidney function but a large amount of people are unable to exercise due to disability, lack of time or money, or a pandemic. Our lab has previously discovered that when myostatin, a negative regulator of skeletal muscle mass, is deleted from lean mice it also improves kidney function in diabetes, improves sodium handling, and protects against renal damage on a high salt (HS) diet. An exact mechanism has not been identified for this improved kidney function though. A possible mechanism could possibly be caused by an exercise induced release of a myokine (muscle protein) termed musclin (Subbotina et al. 2015) that mimics atrial natriuretic peptide (ANP), an important protein from the heart that helps the kidneys better excrete sodium (Kita et al. 2009). My hypothesis for this project is that myostatin deletion (or exercise) upregulates musclin, which acts on the ANP receptor in the kidneys, and allows the kidneys to better handle sodium and protect them against high salt and diabetes-induced damage.

1. Introduction

Chronic Kidney Disease (CKD) occurs when the kidneys become damaged to the point where they can no longer filter blood appropriately. It affects an estimated 15% of adults and is the 9th leading cause of death in America. Diabetes and high blood pressure are the leading problems associated with CKD (Saran et al. 2018). Too much salt consumption is another way that kidneys can be damaged and, according to Wright et al., 95% of American males and 75% of American females consume too much sodium. Exercise is a key therapy to improve kidney function but a large amount of people are unable to exercise due to disability, lack of time, lack of money, or a pandemic. Furthermore, the reason why exercise is so helpful to kidney function is not entirely known. Our lab has previously discovered that myostatin, a negative regulator of skeletal muscle mass, can be deleted from diabetic mice to restore muscle mass, but also improves kidney function. Key questions remain, will myostatin deletion protect against long-term dietary sodium perturbations, such as renal hypertrophy, blood pressure, renal dynamics, etc. Further, what are the mechanisms that might drive such a protection? Our hypothesis was that myostatin deletion protects against renal dysfunction during a high salt diet through increased levels of musclin.

2. Experimental Details

Adult male mice (aged 12-30 weeks of age) on the C57 background were used for the duration of the study. A mouse with myostatin constitutively deleted was crossed onto the C57 background. Blood pressure was monitored using DSI in vivo radiotelemetry. All diets were purchased from Envigo Teklab Custom 12 Diets. After baseline measurements with normal chow (0.4% NaCl) were obtained, each group was exposed to 14 days of high salt diet (4% NaCl). Metabolic cages were used to monitor water, food and urine production at baseline, day 3 (acute) of a high salt diet, and day 14 (long-term) of a high salt diet. Briefly, the mice were placed in metabolic cages for 24 hrs for acclimation and then data was collected over two subsequent days and averaged. After 2 weeks of diet, animals were sacrificed and relevant indices collected. 8-Isoprostane and aldosterone was measured using Cayman Chemical 8-Isoprostane ELISA kit (#516351) and ELISA kit (#501090). Specific group numbers are in the legends. Any significance reported was based on $p < 0.05$ and utilized a One-Way Anova with a Tukey Multiple Comparison's Test, Two-Way Anova, or a student's T-test, where appropriate. We have analyzed musclin concentrations in the gastrocnemius with ELISA. We have also used real time qRT-PCR to analyze musclin in the gastrocnemius and natriuretic peptide receptors in the kidney and are in the process of analyzing that data.

3. Results

Figure 1: Myostatin Deletion Protects Against Acute Increases in Blood Pressure

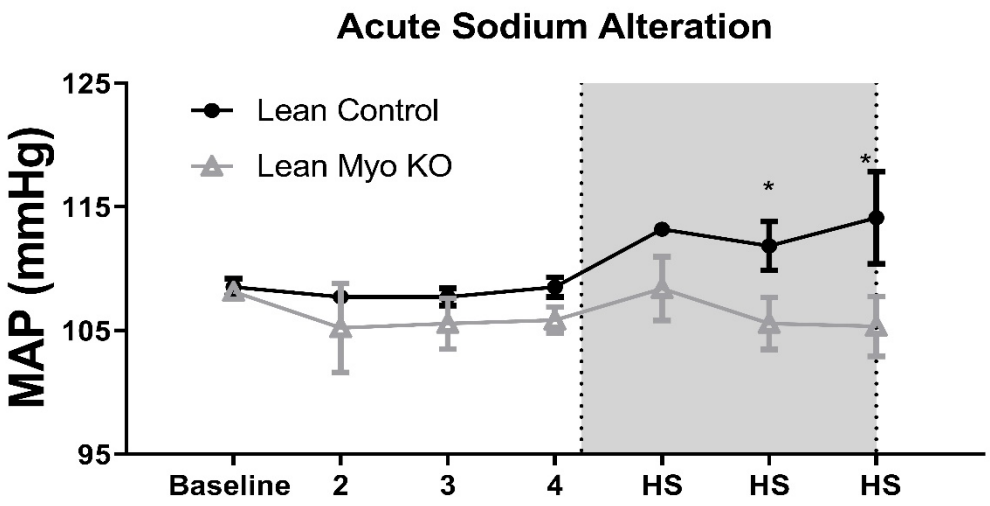

Figure 1: Blood pressure between the two groups of mice was obtained using radiotelemetry, and after implantation were allowed to recover for 7 days. Subsequently, a 4 day baseline was obtained before the animals were placed on a high salt diet (1.6% Na). Blood pressure increased in control mice with HS diet, but not with myostatin deletion.. N = 3-4 per group. Significance determined by $p < 0.05$ with a Two-Way ANOVA with Multiple Comparison's Test.

Figure 2: Myostatin Deletion Improves Renal Fluid Dynamics

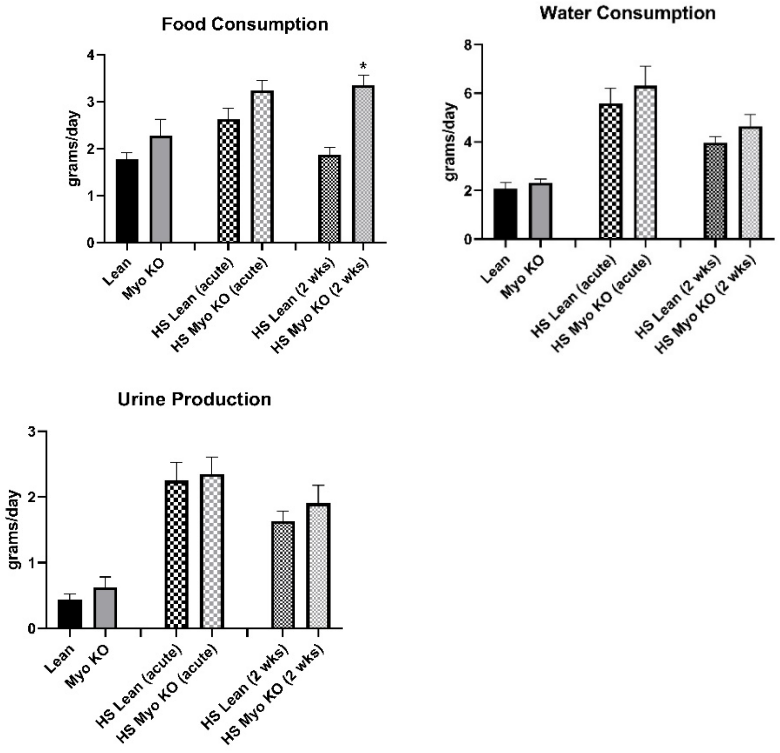

Figure 2: Food consumption between the two groups was unchanged until the end of the experiment, when myostatin deletion mice consumed significantly more salt than control mice. Water consumption and urine production remained similar between groups at all baseline, acute, and long-term (2 wk) high salt diet. N = 5-7 per group. Significance determined by $p < 0.05$ with a student T-test between relevant groups.

Figure 3: Myostatin Deletion Protects Against Renal Hypertrophy

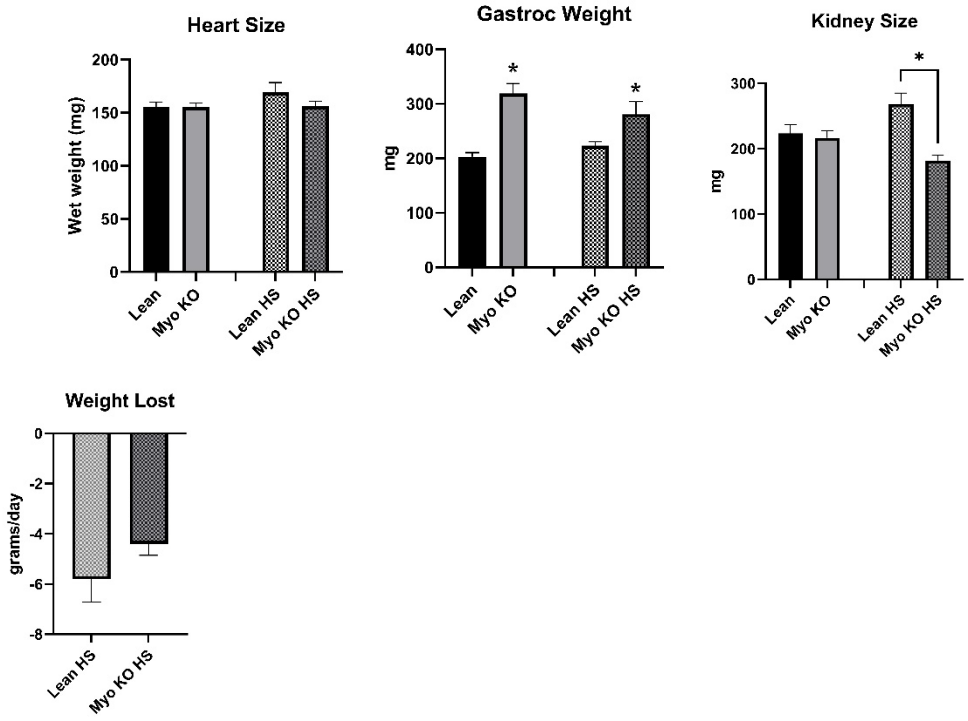

Figure 3: Relevant organ indices were obtained, with no changes in gastrocnemius or heart size. However, kidney size was significantly larger with high salt diet in the control mice compared to myostatin deletion. Weight loss at the end of the final metabolic cage experiment was unchanged, although trending lower. N = 4-6 per group. Significance determined by $p < 0.05$ with a student T-test between relevant groups.

Figure 4: Myostatin Deletion Protects Against Renal Injury During High Salt Diet

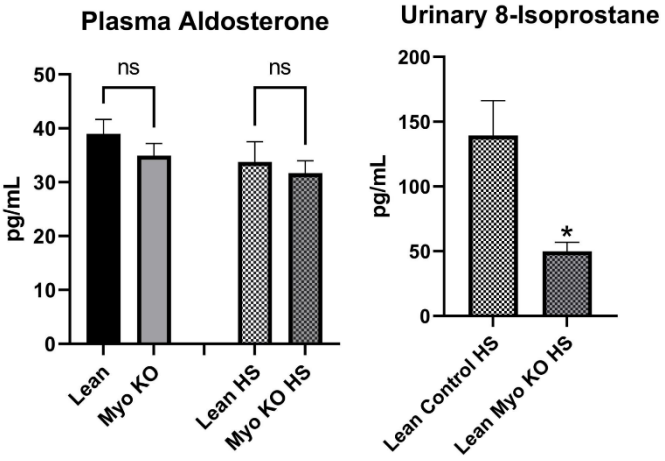

Figure 4: Aldosterone in plasma from all groups was assessed and found to be unchanged. Urinary 8-isoprostane, a marker of renal dysfunction was assessed and found to be downregulated with myostatin deletion after high salt diet. N = 2-6 per group. Significance determined by $p < 0.05$ with a student T-test between relevant groups.

Figure 5: Musclin in Gastrocnemius and Systemic Musclin Production

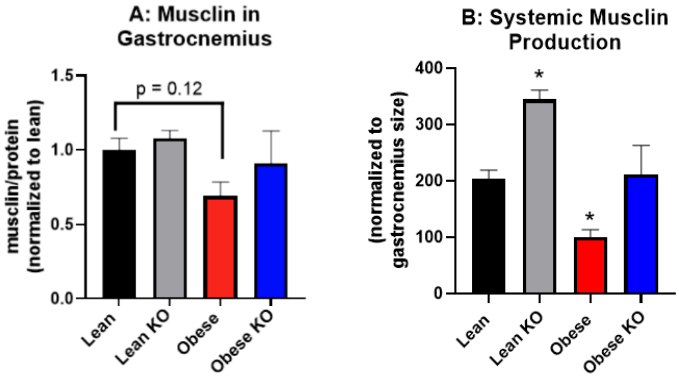

Figure 5: We used a sandwich ELISA to measure the amount of musclin in the gastrocnemius muscle in all four groups of mice (Figure A). While not significant, likely due to the small group size (N = 2-3), it looks like the obese diabetic mice have less musclin. We then normalized that concentration to overall gastrocnemius size (Figure B). Here it is clear and significant that the lean myostatin KO mouse has more musclin, which might explain why the lean myostatin KO mice were protected against the high salt diet. Thus, the musclin protein released from muscles may be why myostatin deletion (or exercise) allows for kidneys to be protected against high salt diet or diabetes.

4. Discussion and Conclusions

Figure 1 shows that when lean control mice and lean myo KO mice are placed on a HS diet for 3 days, the lean control mice had a significant increase in blood pressure while the lean myo KO mice maintained a healthy blood pressure. In figure 2 when both mice genotypes were placed on a HS diet for two weeks, the lean myo KO mice consumed almost twice as much food per day compared to the lean control. Both mice consumed similar amounts of water and excreted similar amounts of urine. When looking at this information combined, the lean myostatin mice consume twice as much salt and still excretes the same amount of urine. Preliminary data has shown that these mice are better able to excrete salt in their urine. After this two-week HS diet the mice where sacrificed and tissue samples were collected. The heart of the lean control was slightly larger, but not a significant amount statistically. If the HS diet were carried out longer it is reasonable to think that the heart may be significantly larger. We also saw significant kidney hypertrophy in the lean control after

the HS diet. The increase in kidney size is an indicator of kidney damage in the lean control mice. The lean myo KO mice also lost significantly less weight than the lean control, which makes sense since the lean myo KO mice maintained a healthy appetite. We used an ELISA to analyze serum Aldosterone and saw no significant difference. We used an ELISA to also analyze urine for 8-isoprostane which is a marker of oxidative stress in the kidneys and helps confirm that muscle mass protects the kidney. We are looking at trying to identify what is responsible for this increase in kidney function that is associated with muscle mass. Our preliminary data for musclin showed that lean myo KO mice had significantly more musclin than the lean control. Kita et al. states that musclin can competitively bind to ANP receptors (2009), which could possibly be why muscle mass improves kidney function. We are in the process of analyzing qRT-PCR data for natriuretic peptide receptors in the kidney and musclin in the gastrocnemius across different mice genotypes.

In the future we plan to look further into musclin with ELISAs and run more metabolic cages with mice on a HS diet. We also plan to assess serum Vasopressin with an ELISA. We also plan to determine if blood pressure is preserved in myostatin KO mice under a HS diet long-term using DSI in vivo radiotelemetry.

5. Summary

Myostatin deletion improves renal fluid balance with a high salt diet, despite significantly increased sodium load. Renal hypertrophy and markers of renal damage are also reduced with myostatin deletion. Taken together, this data suggests that myostatin deletion could be used to protect against the long-term renal damage that occurs with excessive dietary sodium consumption. Musclin and natriuretic peptides receptor expression could possibly be the mechanism for improved sodium handling during a HS diet.

6. Appendices

6a. Acknowledgements

I would like to thank my colleagues in Dr. Butcher's Laboratory, including all listed co-authors. I would like to especially thank Dr. and Mrs. Niblack, who have provided significant support and funding for this project. Additionally, this project received external grant support from the following agencies: NIA 5K01AG064121 (Butcher); NIGMS P30GM122744 (PI: Ma, Pilot Study: Butcher); and OCAST HR21-045-1 (PI: Butcher).

6b. Papers Published

Papers Published

Nunan, E., Wright, C., Semola, O., Subramanian, M., Balasubramanian, P., Lovern, P., Fancher, I. & Butcher, J. 2022b. Obesity as a premature aging phenotype — implications for sarcopenic obesity. *GeroScience,* 44.

Abstracts

Gore, J., Nunan, E., Wright, C. & Butcher, J. 2022. PGC1α Overexpression Protects against Cardio-Metabolic Disease and Skeletal Muscle Dysfunction in a Type 2 Diabetic Mouse Model. The FASEB Journal, 36.

Gore, J., Nunan, E., Wright, C. & Butcher, J. 2022. PGC1α Overexpression Preserves Cardio-Metabolic and Skeletal Muscle Function in a Type 2 Diabetic Mouse Model. National Veterinary Scholars Symposium.

Huff, D., Nunan, E., Gore, J., Wright, C., Valdez, C. & Butcher, J. 2022. Myostatin Deletion Preserves Cardio-Metabolic Function in Type 1 diabetes.

Wright, C., Nunan, E. & Butcher, J. 2022. Myostatin Deletion Protects Against Renal Dysfunction During a High Salt Diet. *The FASEB Journal,* 36.

Yeater, J., Janak, L., Nunan, E., Wright, C., Lovern, P., Brandão, J., Butcher, J. Characterization of glucose transport in skeletal muscle of the New Zealand White rabbit. National Veterinary Scholars Symposium.

Posters Presented

Wright, C., Nunan, E. & Butcher, J. 2022. Myostatin Deletion Protects Against Renal Dysfunction During a High Salt Diet. Presented at American Physiological Society Undergrad and General Symposiums.

Awards

American Physiological Society Barbara A. Horwitz John M. Horowitz Outstanding Abstract for Wright, C., Nunan, E. & Butcher, J. 2022. Myostatin Deletion Protects Against Renal Dysfunction During a High Salt Diet. *The FASEB Journal,* 36.

6c. Literature Cited

Kita, S., Nishizawa, H., Okuno, Y., Tanaka, M., Yasui, A., Matsuda, M., Yamada, Y. & Shimomura, I. 2009. Competitive binding of musclin to natriuretic peptide receptor 3 with atrial natriuretic peptide. *J Endocrinol,* 201**,** 287-95.

Saran, R., Robinson, B., Abbott, K. C., Agodoa, L. Y. C., Bragg-Gresham, J., Balkrishnan, R., Bhave, N., Dietrich, X., Ding, Z., Eggers, P. W., Gaipov, A., Gillen, D., Gipson, D., Gu, H., Guro, P., Haggerty, D., Han, Y., He, K., Herman, W., Heung, M., Hirth, R. A., Hsiung, J. T., Hutton, D., Inoue, A., Jacobsen, S. J., Jin, Y., Kalantar-Zadeh, K., Kapke, A., Kleine, C. E., Kovesdy, C. P., Krueter, W., Kurtz, V., Li, Y., Liu, S., Marroquin, M. V., Mccullough, K., Molnar, M. Z., Modi, Z., Montez-Rath, M., Moradi, H., Morgenstern, H., Mukhopadhyay, P., Nallamothu, B., Nguyen, D. V., Norris, K. C., O'Hare, A. M., Obi, Y., Park, C., Pearson, J., Pisoni, R., Potukuchi, P. K., Repeck, K., Rhee, C. M., Schaubel, D. E., Schrager, J., Selewski, D. T., Shamraj, R., Shaw, S. F., Shi, J. M., Shieu, M., Sim, J. J., Soohoo, M., Steffick, D., Streja, E., Sumida, K., Kurella Tamura, M., Tilea, A., Turf, M., Wang, D., Weng, W., Woodside, K. J., Wyncott, A., Xiang, J., Xin, X., Yin, M., You, A. S., Zhang, X., Zhou, H. & Shahinian, V. 2019. US Renal Data System 2018 Annual Data Report: Epidemiology of Kidney Disease in the United States. *Am J Kidney Dis,* 73**,** A7-a8.

Subbotina, E., Sierra, A., Zhu, Z., Gao, Z., Koganti, S. R., Reyes, S., Stepniak, E., Walsh, S. A., Acevedo, M. R., Perez-Terzic, C. M., Hodgson-Zingman, D. M. & Zingman, L. V. 2015. Musclin is an activity-stimulated myokine that enhances physical endurance. *Proc Natl Acad Sci U S A,* 112**,** 16042-7.

Wright, J. A. & Cavanaugh, K. L. 2010. Dietary Sodium in Chronic Kidney Disease: A Comprehensive Approach. *Seminars in Dialysis,* 23**,** 415-421.

Exercise and Kidney Function: A Novel Link

Carson L. Wright 2021-2022 Niblack Research Scholar
Emily Nunan DVM/PhD Candidate
Dr. Joshua T. Butcher PhD, MS

COLLEGE OF VETERINARY MEDICINE

Acknowledgements

- I’d like to thank my colleagues in Dr. Butcher’s Laboratory, including all listed authors.
- I’d like to especially thank the Dr. and Mrs. Niblack, who has provided significant support and funding to myself.
- NIA 5K01AG064121 (Butcher)
- NIGMS P30GM122744 (PI: Ma, Pilot Study: Butcher)
- OCAST HR21-045-1 (PI: Butcher)

Type 2 Diabetes

- Occurs when an individual is no longer able to regulate glucose in the blood due to receptors on glucose transporters losing the ability to respond to insulin.
- Commonly associated with obesity, cardiovascular disease, stroke, peripheral nerve damage, and chronic kidney disease.
- Diagnosed with A1C>6.5%.
- 11% of US population.
- Risk Increases with age.

Chronic Kidney Disease (CKD)

- Diabetes accounts for 39% of CKD cases.
- High Blood Pressure accounts for 26% of CKD cases.
- CKD is due to the kidneys losing the ability to filter blood efficiently.
- CKD affects 15% of adults and is the 9th leading cause of death in the US. (Saran et al. 2018).

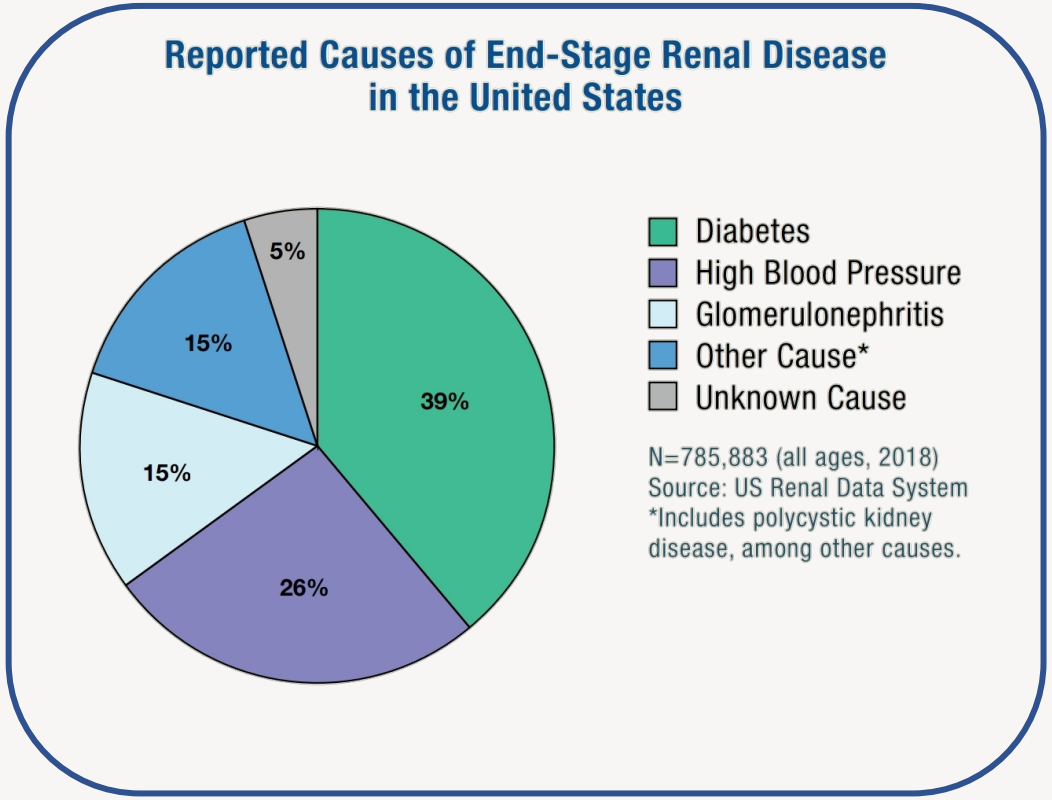

Figure adapted from Centers for Disease Control and Prevention. *Chronic Kidney Disease in the United States, 2021.*

The Western Diet

- 90% of US population exceeds recommended salt intake (Jackson et al., 2016).
- Diet is a major contributor to both Type 2 diabetes and CKD.

Mice Models Used

- **$H_{db}H_{Myo}$ = Lean Controls**
- $H_{db}K_{Myo}$ = Myostatin$^{-/-}$ mice
- $K_{db}H_{Myo}$ = Lep$_r^{-/-}$ mutant mice
- **$K_{db}K_{Myo}$ = Dual KO mice**

- Myostatin deletion increases glycolytic skeletal muscle mass.

Image from Se-Jin Lee (2007)

Blood Pressure and Salt Excretion

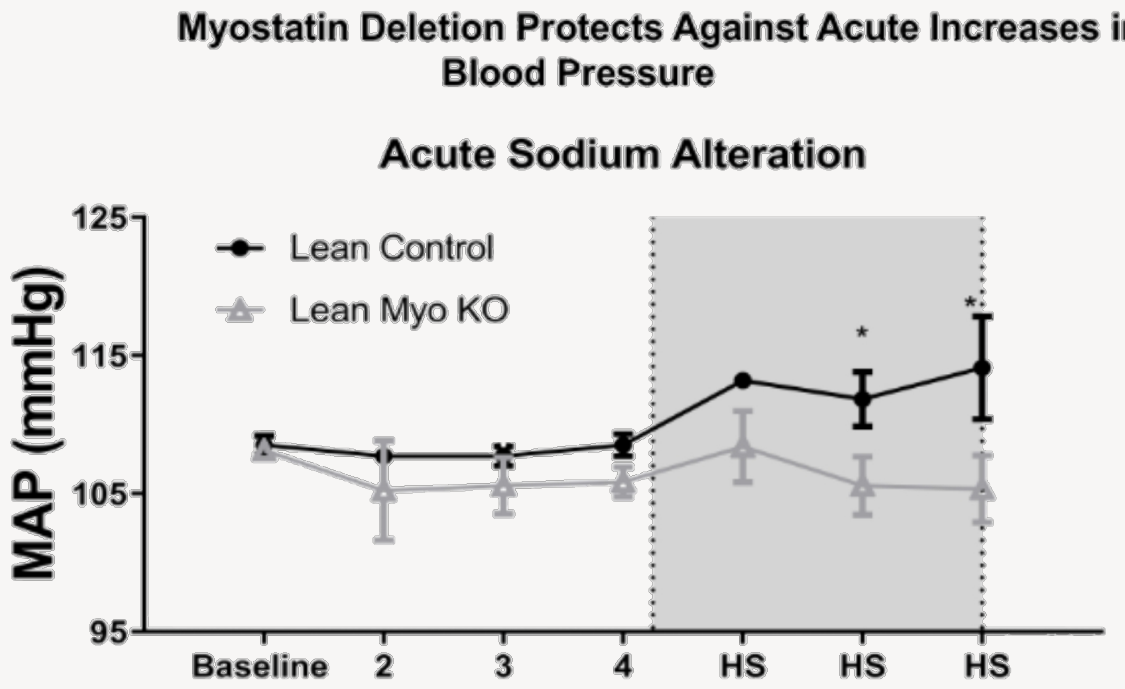

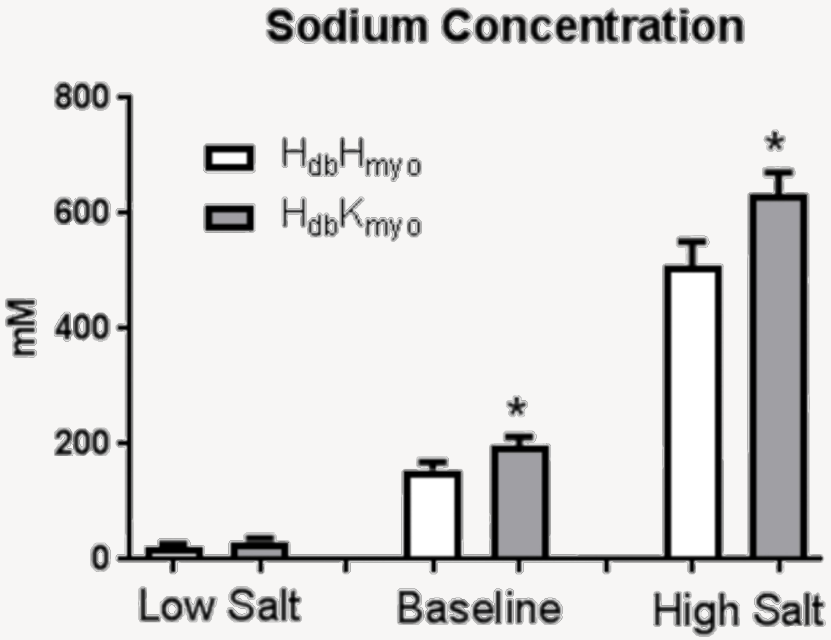

(Butcher et al., 2018)

Hypothesis

Myostatin deletion protects against renal dysfunction during a long-term high salt diet through increased levels of musclin.

Renal Fluid Dynamics 2 Weeks HS Diet

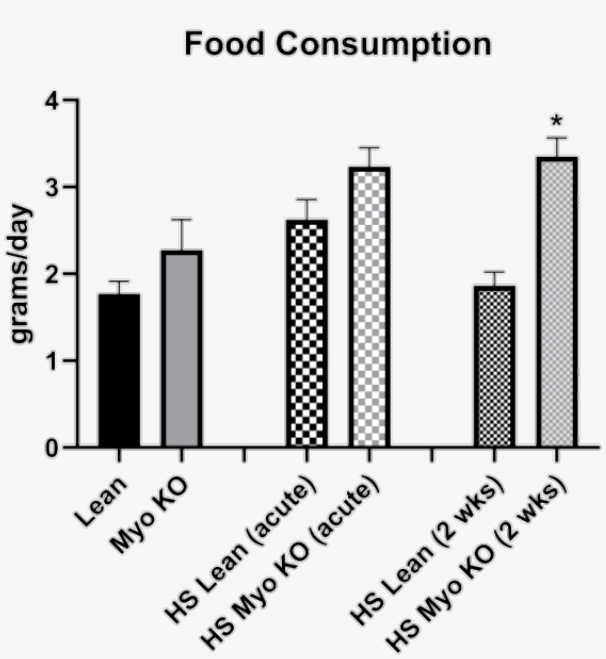

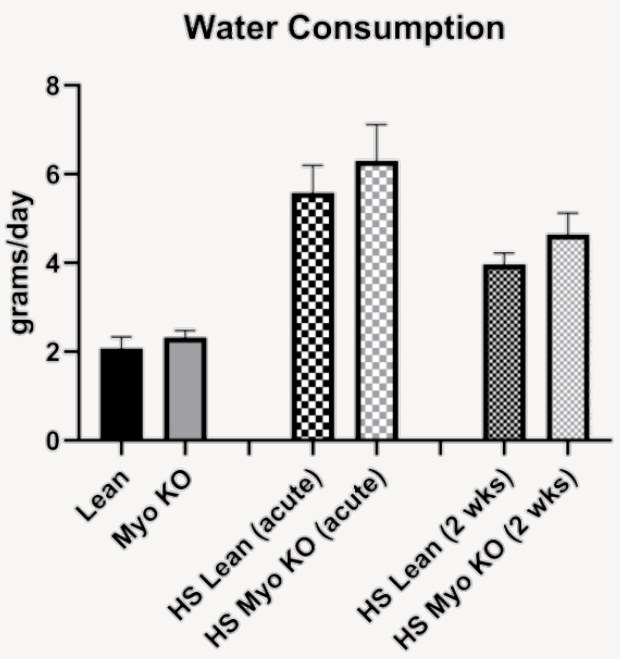

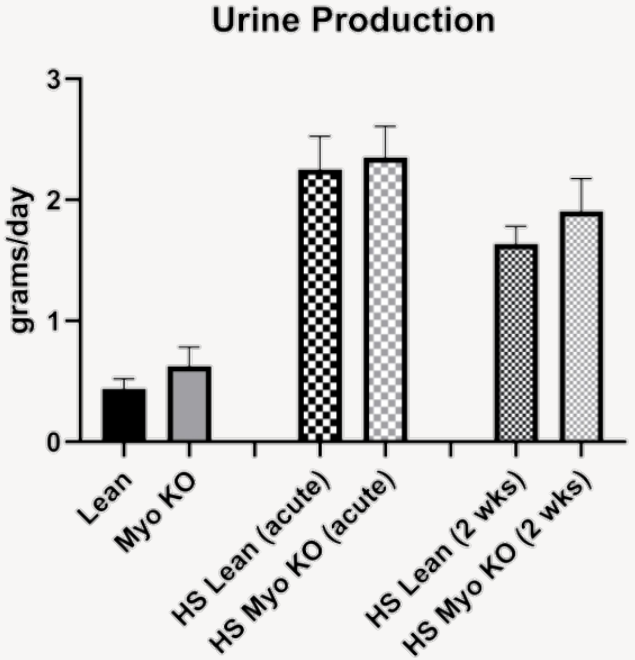

Myostatin Protects Against Renal Damage

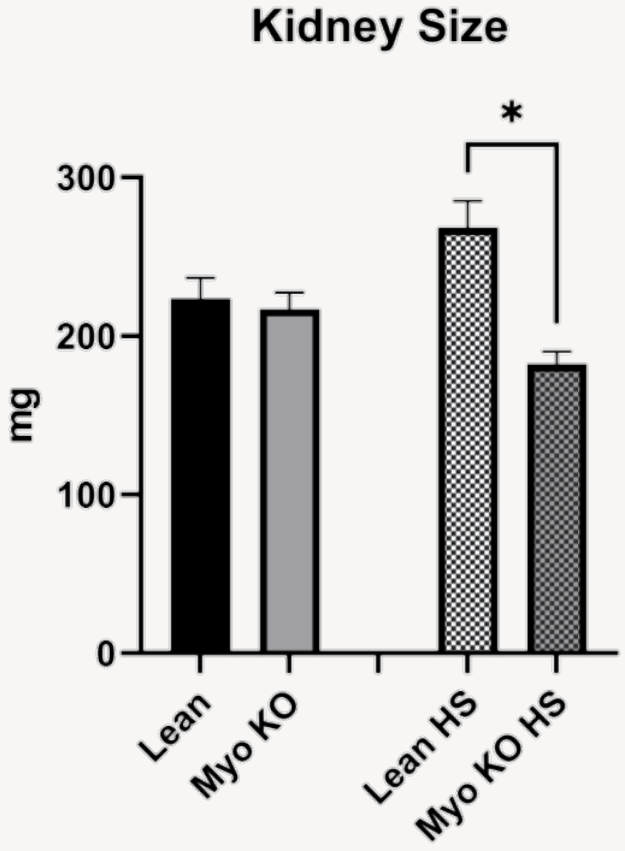

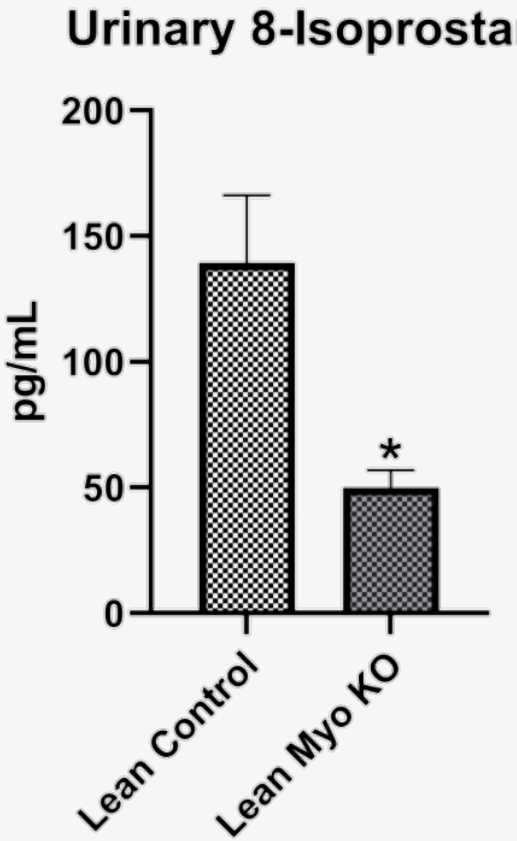

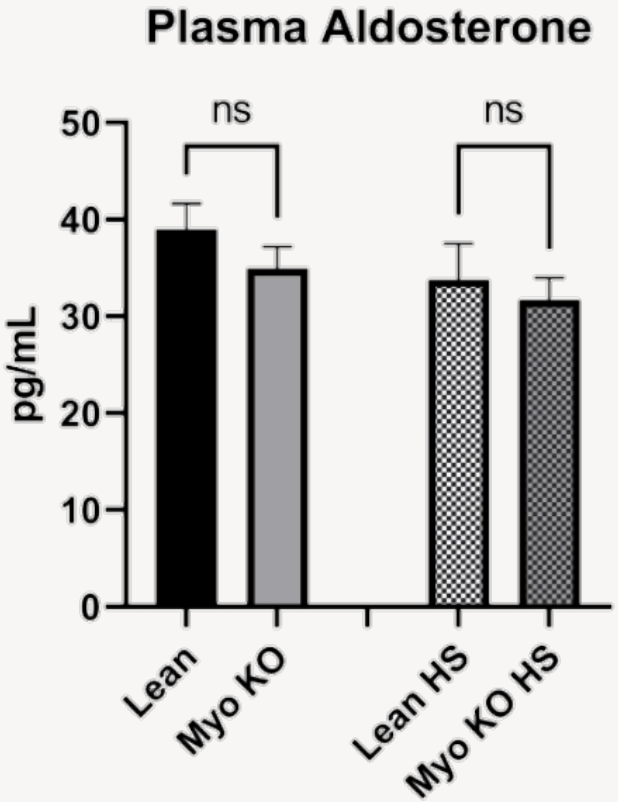

How Could Muscle Mass Do This?

- Through the activity of Musclin! Musclin is a protein secreted from muscle which can competitively binds to Natriuretic Peptide Receptor 3 (NPR3) (Kita et al., 2009) This receptors biggest responsibility is clearing ANP from the system.
- ANP plays an important role in Na+ regulation. ANP excretes Na+ into the lumen of nephrons in kidneys (Potter et al., 2016).

Musclin in the Gastrocnemius

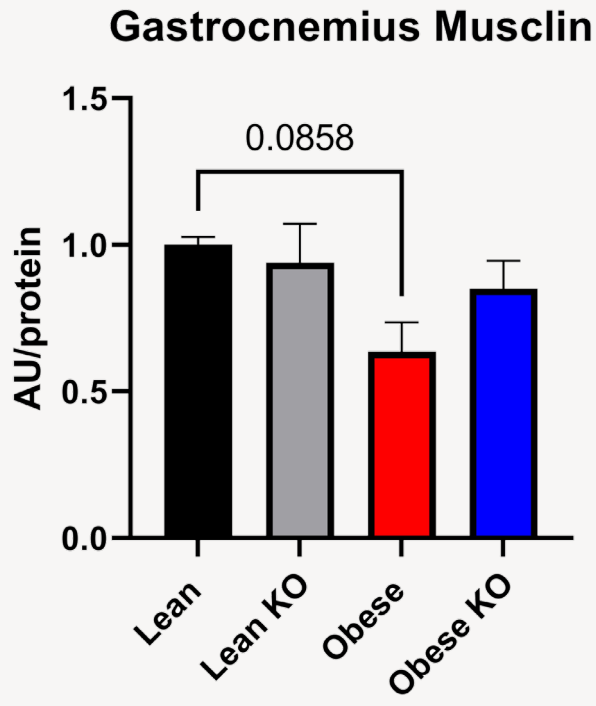

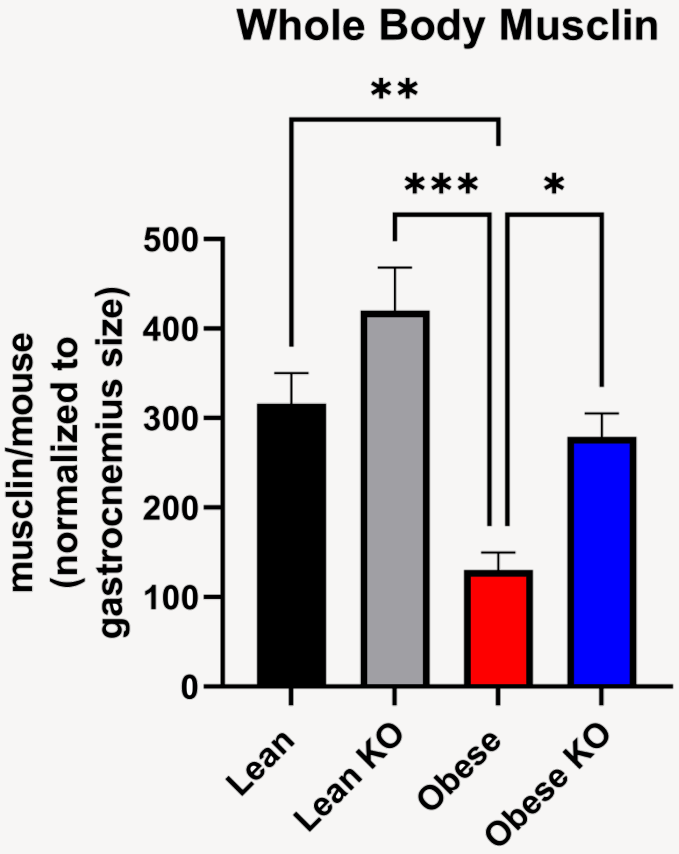

Musclin After High Salt Diet (2-weeks)

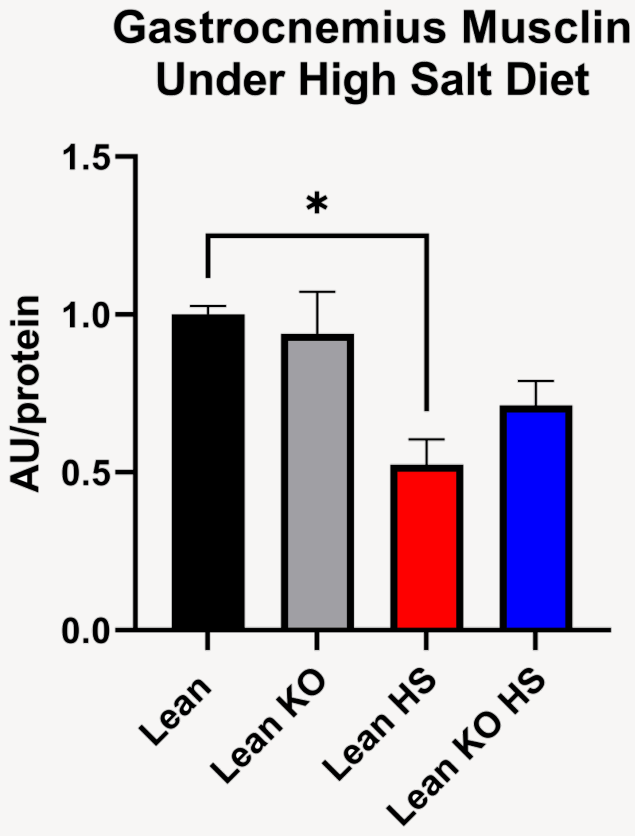

The Musclin Mechanism

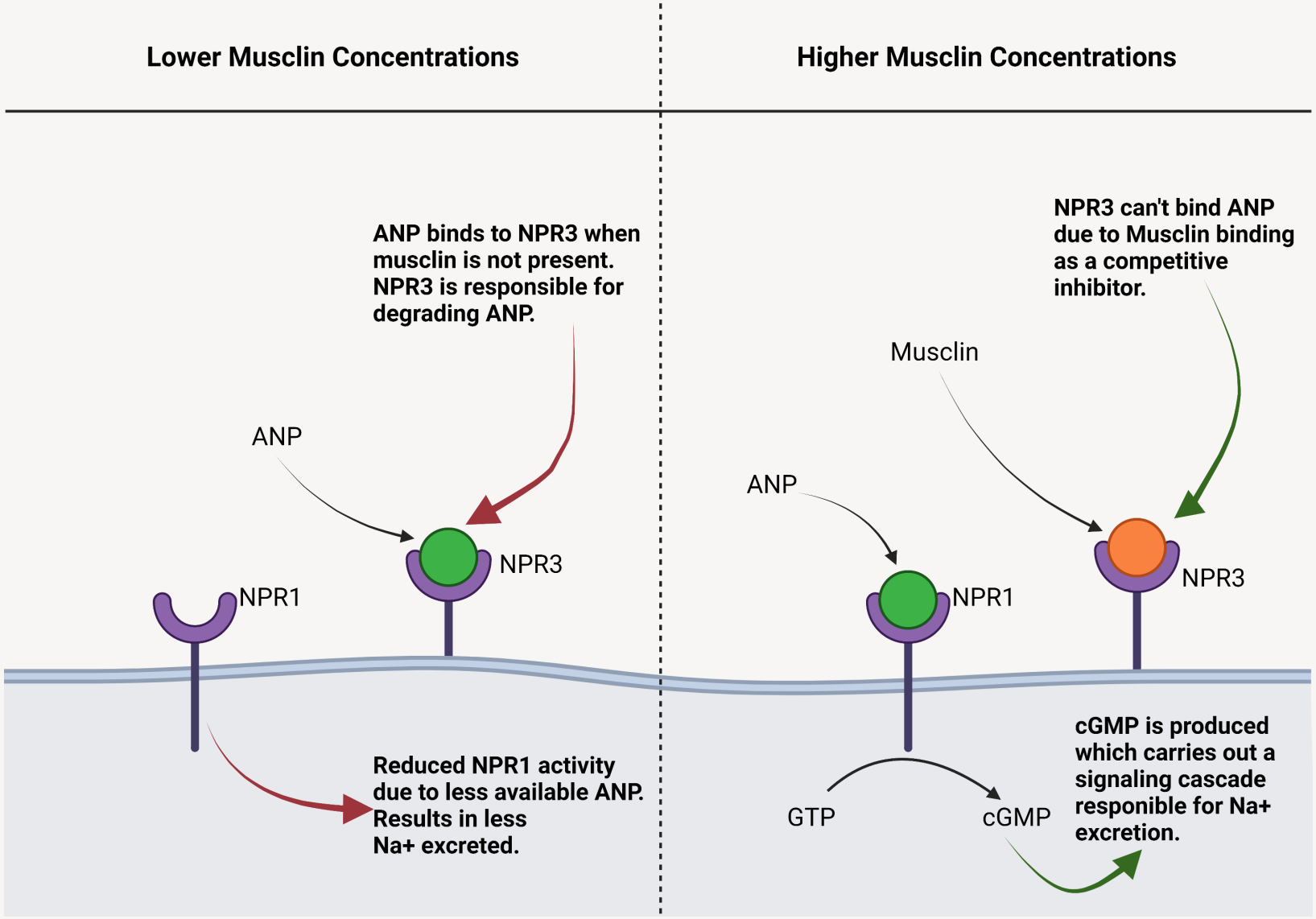

Created with BioRender.com

Natriuretic Peptide Receptor Expression

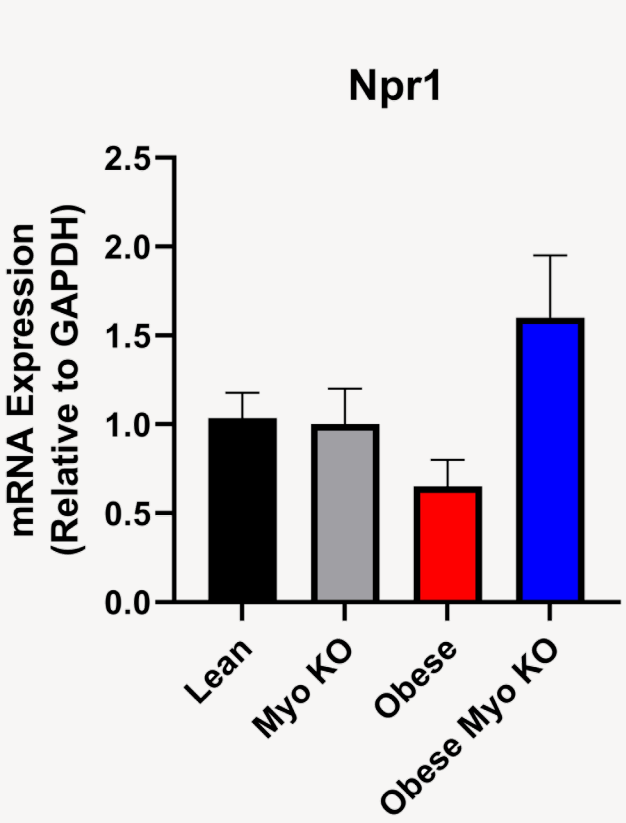

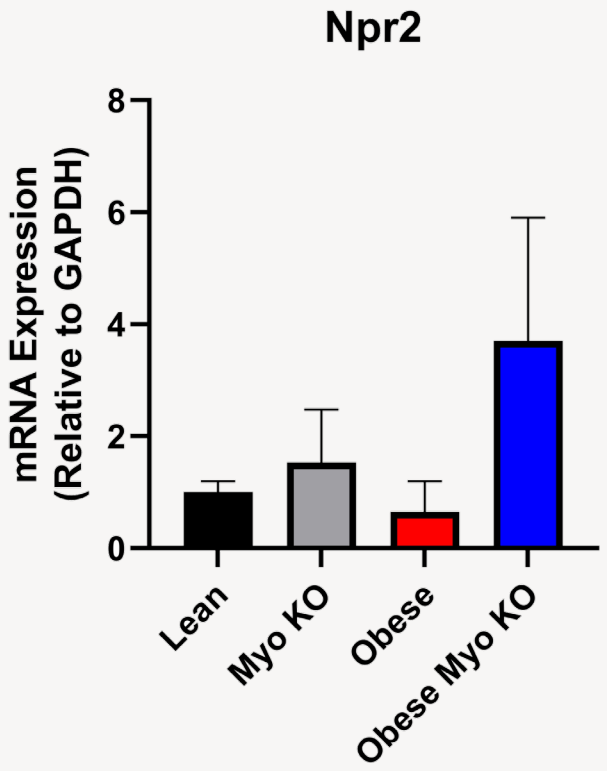

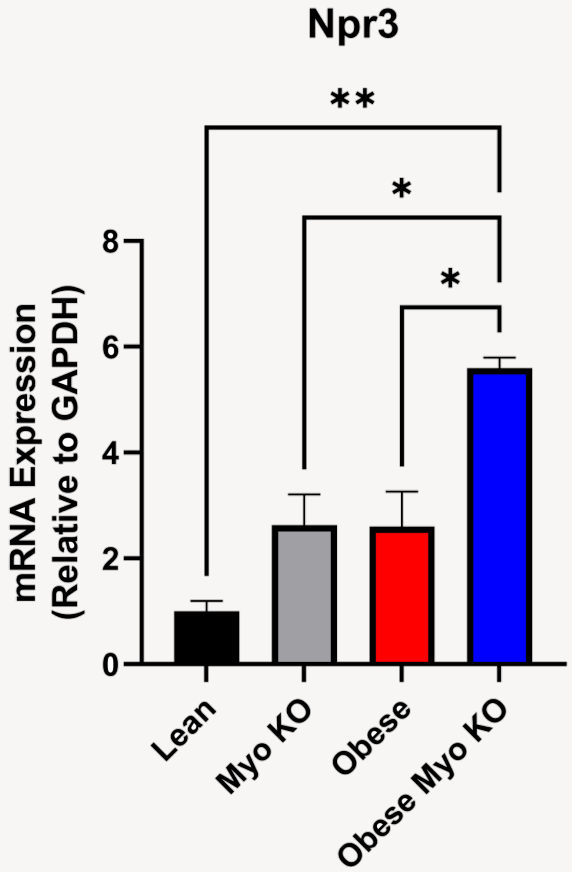

Conclusion

- Myostatin KO mice are better able to excrete salt.
- Myostatin KO mice have less markers of renal damage.
- Musclin is a competitive inhibitor that can bind to NPR3 and stop its function of clearing ANP.
- Inhibiting NPR3 allows more Na+ to be excreted due to increased available ANP which can act on NPR1.
- Musclin is increased in myostatin KO mice.

References

Butcher, J., Mintz, J., Larion, S., Qiu, S., Ruan, L., Fulton, D., & Stepp, D. (2018). Increased Muscle Mass Protects Against Hypertension and Renal Injury in Obesity. Journal of the American Heart Association, 7. doi:10.1161/JAHA.118.009358

Jackson, S. L., King, S. M., Zhao, L., & Cogswell, M. E. (2016). Prevalence of Excess Sodium Intake in the United States - NHANES, 2009-2012. MMWR Morb Mortal Wkly Rep, 64(52), 1393-1397. doi:10.15585/mmwr.mm6452a1

Kita, S., Nishizawa, H., Okuno, Y., Tanaka, M., Yasui, A., Matsuda, M., . . . Shimomura, I. (2009). Competitive binding of musclin to natriuretic peptide receptor 3 with atrial natriuretic peptide. J Endocrinol, 201(2), 287-295. doi:10.1677/joe-08-0551

Lee, S.-J. (2007). Quadrupling Muscle Mass in Mice by Targeting TGF-β Signaling Pathways. PLOS ONE, 2(8), e789. doi:10.1371/journal.pone.0000789

Center for Disease Control and Prevention (2021). Chronic Kidney Disease in the United States, 2021.

Questions

SESSION THREE:

Meji Jayaseelan

"Determining Respiratory Syncytial Virus Infectivity of Human Pulmonary Small Airway Epithelial Cells"

Research Area: Chemical Engineering

Faculty Sponsor: Dr. Heather Fahlenkamp

Graduate Student Mentor: Taylor Do

Karley White

"Determining the Effect of Respiratory Syncytial Virus on the Barrier Integrity of Cell Layers in a Three-Dimensional Human Tissue Lung Model"

Research Area: Chemical Engineering

Faculty Sponsor: Dr. Heather Fahlenkamp

Graduate Student Mentor: Taylor Do

Seth Robbins

"Effect of Nozzle Configuration on Thrust of a Novel Turbojet-Turboprop Engine for Small Unmanned Aircraft"

Research Area: Mechanical and Aerospace Engineering

Faculty Sponsor: Dr. Kurt Rouser

Graduate Student Mentor: Trey Schinzler

Determining Respiratory Syncytial Virus Infectivity of Human Pulmonary Small Airway Epithelial Cells

Mejalaa Mega Jayaseelan

Chemical Engineering
Faculty Sponsor: Dr. Heather Fahlenkamp
Graduate Student Mentor: Taylor Do

ABSTRACT

Respiratory Syncytial Virus (RSV) is one of the most prevalent lower respiratory infections among pediatric individuals that results in about 3.4 million hospitalizations a year[1]. Studying the effect this virus has on human lung cells will allow us to understand the extent of the interaction of the virus within the lungs as well as aid in the development of a vaccine. Small airway epithelial cells (SAECs) are the primary site of RSV adhesion and infection. The overall goal of our research is to validate the use of human primary SAECs for *in vitro* models used to study viral infections[3].Therefore, the focus of this project was to determine the infectivity of RSV on primary human SAECs. Primary human SAECs were first grown and cultured at an air-liquid interface (ALI). Infectivity of RSV was measured at 24, 48, and 72 hours post-infection. The infected cells were then stained using immunofluorescence and observed via confocal microscopy. We concluded that the SAECs demonstrated infection, and different infectivity was correlated to the varying incubation periods. SAECs grown at ALI proved suitable for *in vitro* models studying RSV. Future experiments will be conducted to determine viability of SAECs after infection with RSV.

1. Introduction

RSV is a common respiratory virus that attacks the small airways of the lungs. While people of all ages experience RSV infection, immunocompromised individuals suffer significant complications, such as pneumonia[4]. These issues that primarily affect elderly and neonates can lead to hospitalization and in rare cases death. Models have been used to aid in fully understanding the severity of RSV infection in immunocompromised individuals[2]. However, it is difficult to find an ideal model to study the interactions of RSV in the human small airway environment.

Previous studies have utilized animal cells or human cell lines, which do not always provide the same functionality as primary human cells. Therefore, this study will focus on validating the use of primary small airway epithelial cells (SAECs) for *in vitro* models to study RSV infectivity. To achieve this goal, the experimental conditions were altered to mimic *in-vivo* environments and RSV was introduced and allowed to infect the cells. Representative images were then used to draw conclusions about the resulting infectivity.

2. Experimental Details

Primary human SAECs were seeded onto a collagen hydrogel at air-liquid interface (ALI) to mimic *in-vivo* conditions. SAECs were then infected with red fluorescence protein (RFP)-labeled RSV at varying titers of MOI 10 and 15. After the respective samples had been incubated for 24, 48, and 72 hours, they were then fixed on the hydrogels using 4% paraformaldehyde. SAECs were then labeled using immunofluorescent techniques with cytokeratin 14 (CK-14) as a primary antibody and PE as a secondary antibody to identify SAECs. Stained samples were mounted on slides and imaged using a Zeiss LSM 980 Airyscan 2 confocal microscope.

2a. SAECs cell culture

The SAECs were cultured 10 days prior to seeding onto hydrogels. Two cell culture T-75 flasks were coated with 4 mL of a coating solution and the flasks were incubated at 37°C, 5% CO_2 for 2 hours. SAEC media Cell Culture Medium [Basal Small Airway Epithelial Medium (PromoCell Cat. No. C-21270) completed with Endothelial Cell MV2 SupplementMix (PromoCell Cat. No. C-39226)] was then added to the flasks and another incubation period of 1 hour at previously stated conditions were allowed. A cryo-vial of SAECs (PromoCell Cat. #C-12642 500,000 cells/mL) was introduced to each flask and media was changed every 72 hours.

2b. Collagen Hydrogel Preparation

The collagen hydrogel utilized in this experiment was first created from a mixture and was even distributed over the surface membrane of the nine hanging well inserts within a 24-well plate. The scaffolds were then incubated in the cell culture incubator (37°C, 5% CO_2) for 45 minutes. After the incubation period was completed, the SAEC media was warmed in the water bath and added to the scaffolds. The gels were incubated overnight in preparation of human small airway epithelial cells.

2c. Cell Seeding and growth on hydrogels

Once the hydrogels had spent the appropriate time in the incubator to gel, SAECs were introduced. First the SAEC media was carefully removed from the top of the hydrogels with

a pipette to avoid a puncture of the hydrogel. Then 100 µL/model of a 1:40 collagen: fibronectin solution was added to each model. The models were then incubated for 1.5 hours in the cell culture incubator.

During this incubation period the SAECs were lifted from the T-75 flasks and resuspended in SAEC media at a concentration of 495,000 cells/mL. The coating solution was then removed, and cells were added at 100 µL/model to result in a seeding density of 150,000 cells/cm^2. Samples were submerged in media for 7 days. On day 7, the cells were observed to be confluent and media from the top of the models were moved and thus the cells were introduced to ALI.

2d. Infection with RSV

The RSV was already prepared with red fluorescens protein markers (RPFs) (2.8 PFU/mL in 150 µL aliquots), and provided by Dr.Oomens laboratory in Veterinary Pathobiology. The RSV stock titer was diluted with SAECs media to create a solution with a multiplicity of 10 as well as a multiplicity of 15. The RSV in 30 µL of media was evenly distributed along the surface of the cells. The same number of media without RSV was used for control groups.

Plate Layouts:

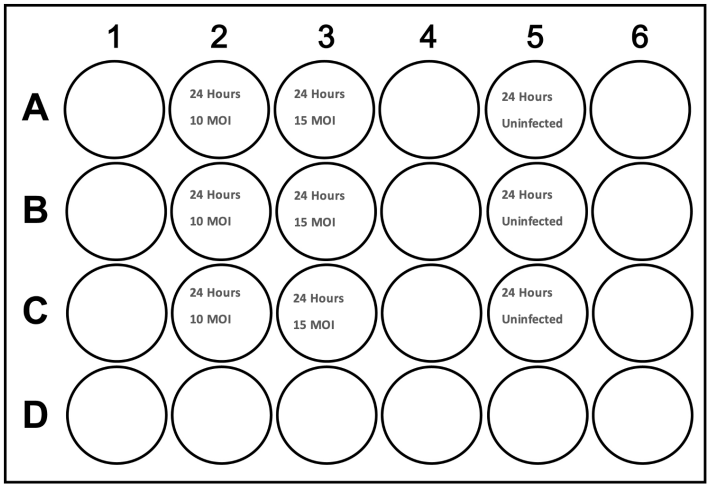

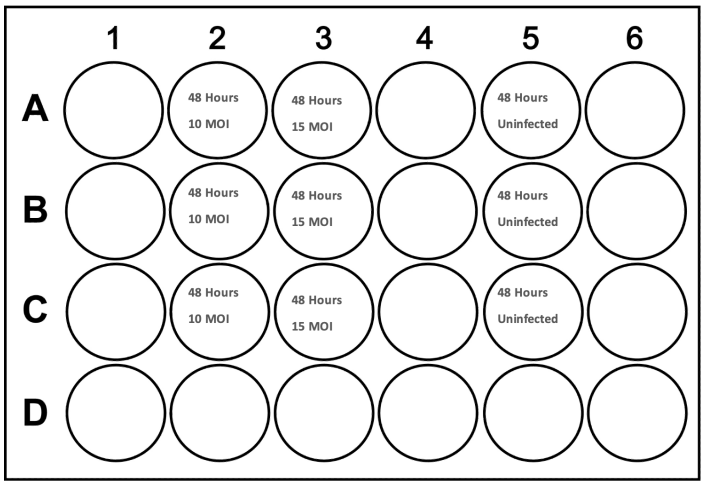

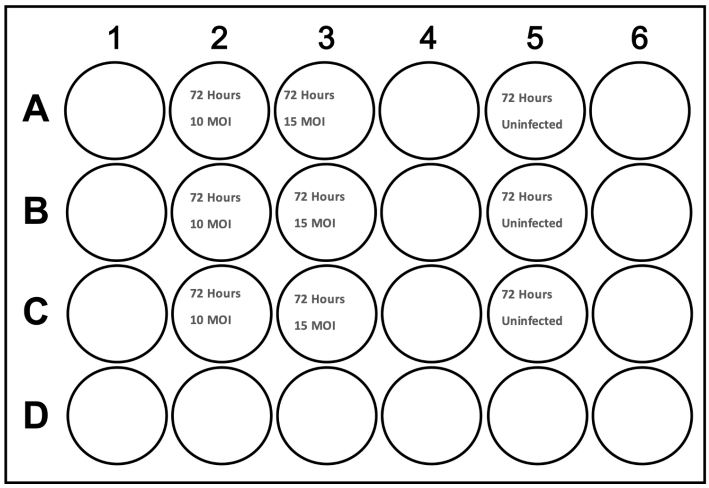

2e. Fixing Cells and Cell Staining

Antibody Panel:

- CK14 Primary: Mouse Anti-CK14 antibody $IgG2_a$0.2 mg/mL
- CK14 Isotype: Mouse $IgG2_ak$0.5 mg/mL
- CK14 Secondary: anti-mouse IgGk PE0.4 mg/mL
- Blocking Buffer: DPBS + 10% rabbit serum + 1% BSA
- Primary Staining Buffer: DPBS + 1% BSA + 0.1% Tween 20
- Secondary Staining Buffer: DPBS + 1% BSA

After the decided infection time period was allowed for each model, they were fixed using paraformaldehyde (Paraformaldehyde Solution, 4% in PBS). The cells were then cut from their respective models and the samples were transferred to a 48 well plate. Once the primary staining buffer process was completed the samples were left to incubate overnight at 4°C. The following day the second staining buffer process was preformed, and the samples were mounted on microscope slides. Mounting solution and coverslips were used to seal the sample in place for imaging.

3. Results

DAPI that stains cell nuclei was used to identify the cells in the samples. We concluded that the RSV was able to infect the cells at titers of MOI 10 and 15 and for varying incubation times of 24, 48, and 72 hours as demonstrated by the red coloring of the RPF. Infectivity of the SAECs increased with increased incubation times specifically for MOI 10 again which was determined by the observable increase in both the intensity and the number of the red florescence protein expression. For the incubation time of 24 hours, infectivity of the SAECs increased with the increase of MOI from 10 to 15. The trend for MOI 15 from 24-72 hours differed from MOI 10, as it was observed that as the incubation period increased with a MOI of 15 there was a decrease in the expression of the RPF. This was determined via visually inspecting the differences between images D, E, and F.

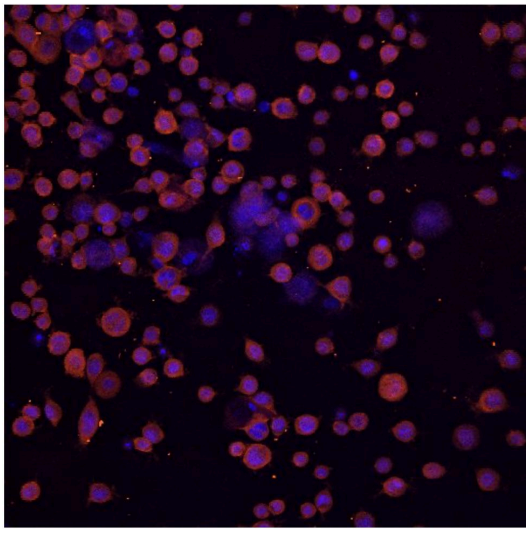

Figure 1. Confocal imaging (400x) of uninfected SAECs after a 48-hour incubation period. The nuclei of the cells are labeled with DAPI (blue) and SAECs are identified with primary antibody for cytokeratin 14 (CK-14), tagged with secondary antibody fluorophore R-PE (orange).

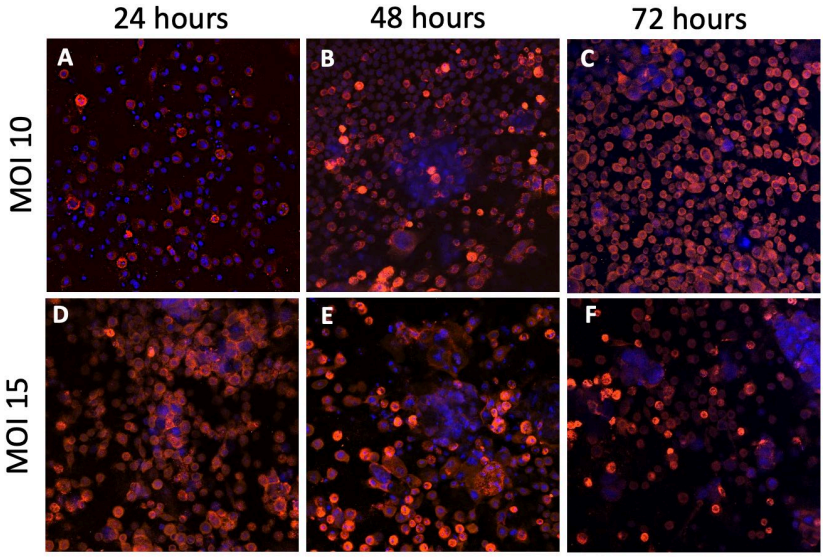

Figure 2. Confocal imaging (400x) of SAECs infected RSV MOI 10 for 24, 48, and 72 hours (A-C, respectively) and MOI 15 for 24, 48, and 72 hours (D-F, respectively). The nuclei of the cells are labeled with DAPI (blue) and SAECs are identified with CK-14 (R-PE) (orange). The RSV expresses a red fluorescence protein (RFP) once the epithelial cells are successfully infected. For an MOI of 10, a positive correlation can be seen between the incubation period and the infectivity. For the 24- and 48-hours time points, the infectivity also increased with the increase of MOI to 15. A decrease in infectivity was seen for the MOI of 15 for 72 hours compared to the MOI of 10 and other time points.

4. Discussion and Conclusions

SAECs grown at ALI in vitro were successfully infected with RSV at two different viral concentrations. Furthermore, infectivity varied for each concentration 24, 48, and 72 hours after infection. Infectivity was determined by analyzing fluorescent signals using confocal microscopy. We were able to verify that our cells were viable via cytokeratin 14 staining that highlighted the PE (orange) labeled cells. The peak infection time for MOI 10 in this experiment was observed to be at the 72-hour timepoint, while the peak infection for MOI 15 was determined at the 24-hour timepoint. We noticed that for our 15 MOI 48 hours and 72 hours timepoints that there was a decrease in cells overall. This could be due to possible cell death; however, future studies should be performed to confirm this possibility.

Our goal for this infectivity experiment was to establish that our SAECs within the 3D-HLTM mimic an *in-vivo* infection process with RSV. We were able to infect the SAECs in a productive manner and emulate the pulmonary response to viruses *in-vivo*. A study that looked at the different response of antibodies to RSV infections by obtained from a study by Cortjens et al., 2017 was able to obtain images of primary human airway epithelial cell culture that were infected with RSV type A2 labeled with Green Fluorescence Proteins (GFP). In this study they utilized primary human epithelial cells (HAEs) and subjected them to infection via RSV and observed the resulting effects of antibody expression. While they were not concerned with the infectivity of RSV, more the responses of antibodies, they also observed via immunohistochemical staining their green florescence labeled protein (GPF) RSV. We were able to refer to this study and observe similar results by the means of the RSV infectivity. While we used slightly varying staining techniques, we still observed our viable cells bound to densely concentrated RSV surrounding the nuclei of our SAECs[5]. This is further evidence we were able to infect our SAECs because RSV is a ribonucleic acid virus (RNA), meaning once the infection process occurs RSV replicates its RNA within the host cell, thus why both our study and Cortjens observed large concentrations of RSV crowding their HAEs. We were also able to observe similarities with another experiments imaging[6]. This study was also able to validate their live cells were infected via protein assays, and the cells were visualized with confocal laser scanning microscopy. Again we can observe that there is crowding of the human pulmonary cells by the RSV. This experiment utilized a smaller concentration of RSV (MOI 3) for 24 hours and was concerned with Oxygen-independent stabilization of hypoxia inducible factor (HIF)-1 during RSV infection, but we can still further validate our findings as we also observed similar distributions of our cells.

5. Summary

Complications from RSV infections are exceptionally prevalent among newborns and young children and is one of the main initiators of respiratory complications before the age of 2. In this experiment we utilized 3D primary SAEC cultures and infected the cells with RSV

at concentrations of MOI 10 and 15. Infectivity was measured at timepoints of 24, 48, and 72 hours. These cells were grown at air-liquid interface to mimic *in-vivo* conditions. After infection and incubation for the respective time points, the cells were fixed and stained using immunofluorescence techniques. Infectivity was determined by observing fluorescence of cells and RFP-tagged RSV using a confocal microscope.

At the conclusion of this experiment we were able determine that RSV did infect the small airway epithelial cells. We observed that infection increased as the incubation time increased for the MOI 10. However, when infected at a concentration of MOI 15, infectivity and cell numbers decreased between the 48- and 72-hour timepoints. This could indicate cell death caused by RSV infection, however further experiment must be performed to confirm this possibility.

6. Appendices

6a. Acknowledgements

The opportunity to participate in research this past year has been such an incredible experience, and I am so thankful for Dr. and Mrs. Niblack's support. I would also like to appreciate my research mentor Dr.Fahlenkamp and my graduate student mentor Taylor Do.

This project was funded through grant from NIH (1R 01 EB 025596 01)

6b. Literature Cited

[3]Borchers, A. T., Chang, C., Gershwin, M. E., & Gershwin, L. J. (2013). Respiratory Syncytial Virus—A Comprehensive Review. Clinical Reviews in Allergy & Immunology, 45(3), 331-79. doi:10.1007/s12016-013-8368-9

[5]Cortjens, B., Yasuda, E., Yu, X., Wagner, K., Claassen, Y. B., Bakker, A. Q., van Woensel, J. B., & Beaumont, T. (2017). Broadly reactive anti-respiratory syncytial virus G antibodies from exposed individuals effectively inhibit infection of primary airway epithelial cells. Journal of Virology, 91(10). https://doi.org/10.1128/jvi.02357-16

[4]Efstathiou, C., Abidi, S. H., Harker, J., & Stevenson, N. J. (2020). Revisiting respiratory syncytial virus's interaction with host immunity, towards novel therapeutics. Cellular and Molecular Life Sciences, 77(24), 5045-5058. doi:10.1007/s00018-020-03557-0

[2]Fronius, M. (2012). Mechanical forces impair alveolar ion transport processes – a putative mechanism contributing to the formation of pulmonary edema. *Lung Diseases - Selected State of the Art Reviews*. https://doi.org/10.5772/26036

[6]Haeberle, H. A., Dürrstein, C., Rosenberger, P., Hosakote, Y. M., Kuhlicke, J., Kempf, V. A., Garofalo, R. P., & Eltzschig, H. K. (2008). Oxygen-independent stabilization of hypoxia inducible factor (HIF)-1 during RSV infection. *PLoS ONE*, *3*(10). https://doi.org/10.1371/journal.pone.0003352

[5]Ptaschinski, C., & Lukacs, N. W. (2019). Early Life Respiratory Syncytial Virus Infection and Asthmatic Responses. Immunology and Allergy Clinics of North America, 39(3), 309-319. doi:10.1016/j.iac.2019.03.00

Determining the Infectivity of Respiratory Syncytial Virus on Small Airway Epithelial Cells

Mejalaa Mega Jayaseelan
School of Chemical Engineering, Oklahoma State University

Social Impact

Figure 1

Figure 2

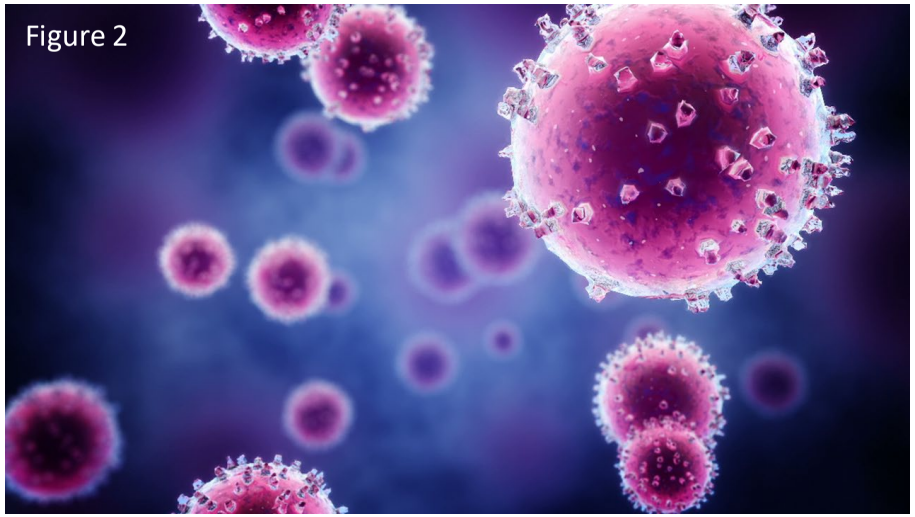

Figures 1 and 2. Centers for Disease Control and Prevention. (2020, December 18). *RSV (respiratory syncytial virus)*. Centers for Disease Control and Prevention. Retrieved September 19, 2022, from https://www.cdc.gov/rsv/

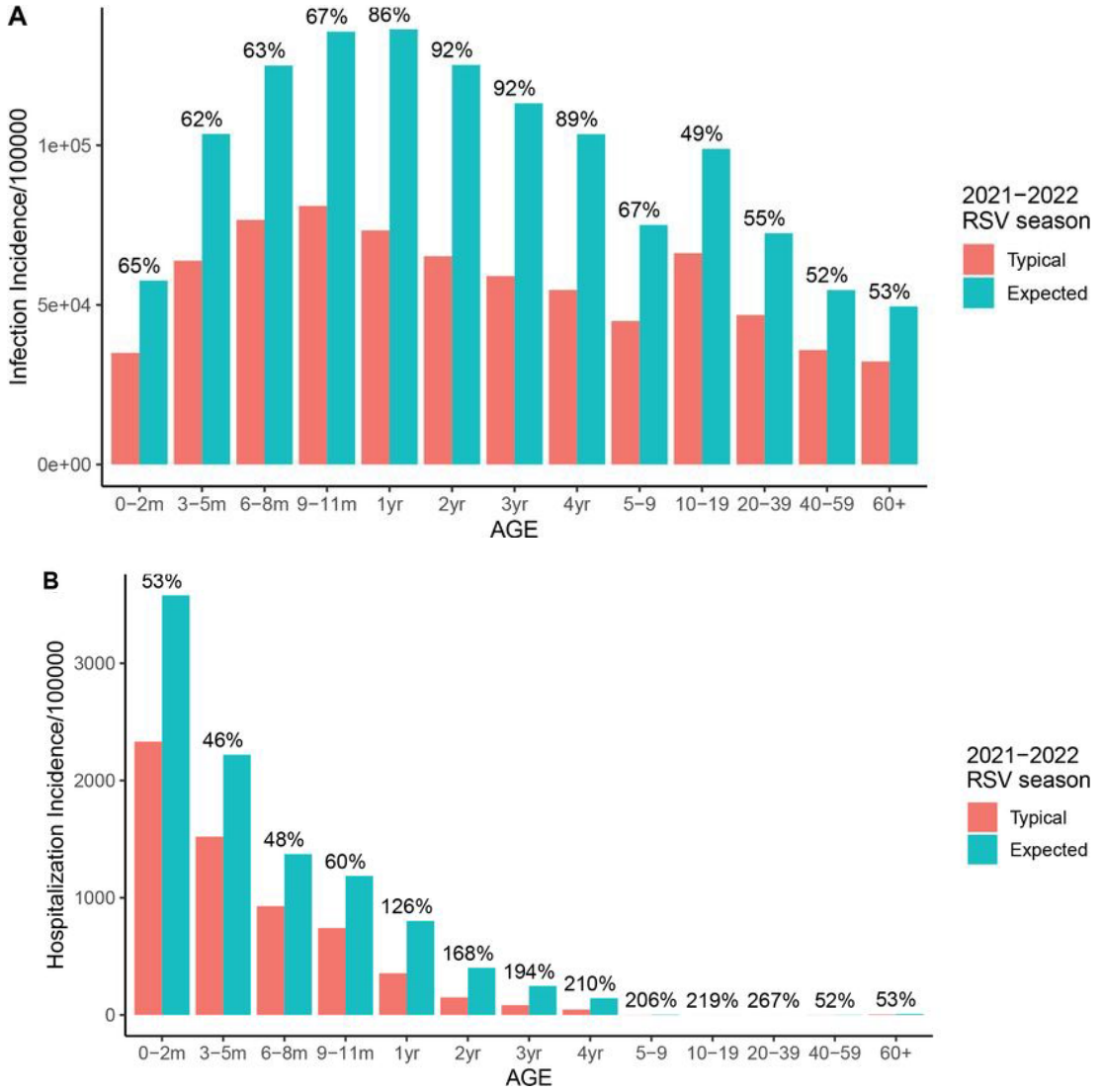

Graphs A and B demonstrate the expected resurgence of RSV infections and hospitalizations due to RSV. The red bars show the incidence of RSV cases during 2021-2022 if there was no COVID-19 pandemic. The blue bars show the expected incidence of RSV cases under 2021-2022. The percentages the top show difference between the expected and the typical values in each age group. These figures were adapted from Zheng, Z., Pitzer, V. E., Shapiro, E. D., Bont, L. J., & Weinberger, D. M. (2021). Re-emergence of respiratory syncytial virus following the COVID-19 pandemic in the United States: A modeling study.

3D Human Lung Tissue Model

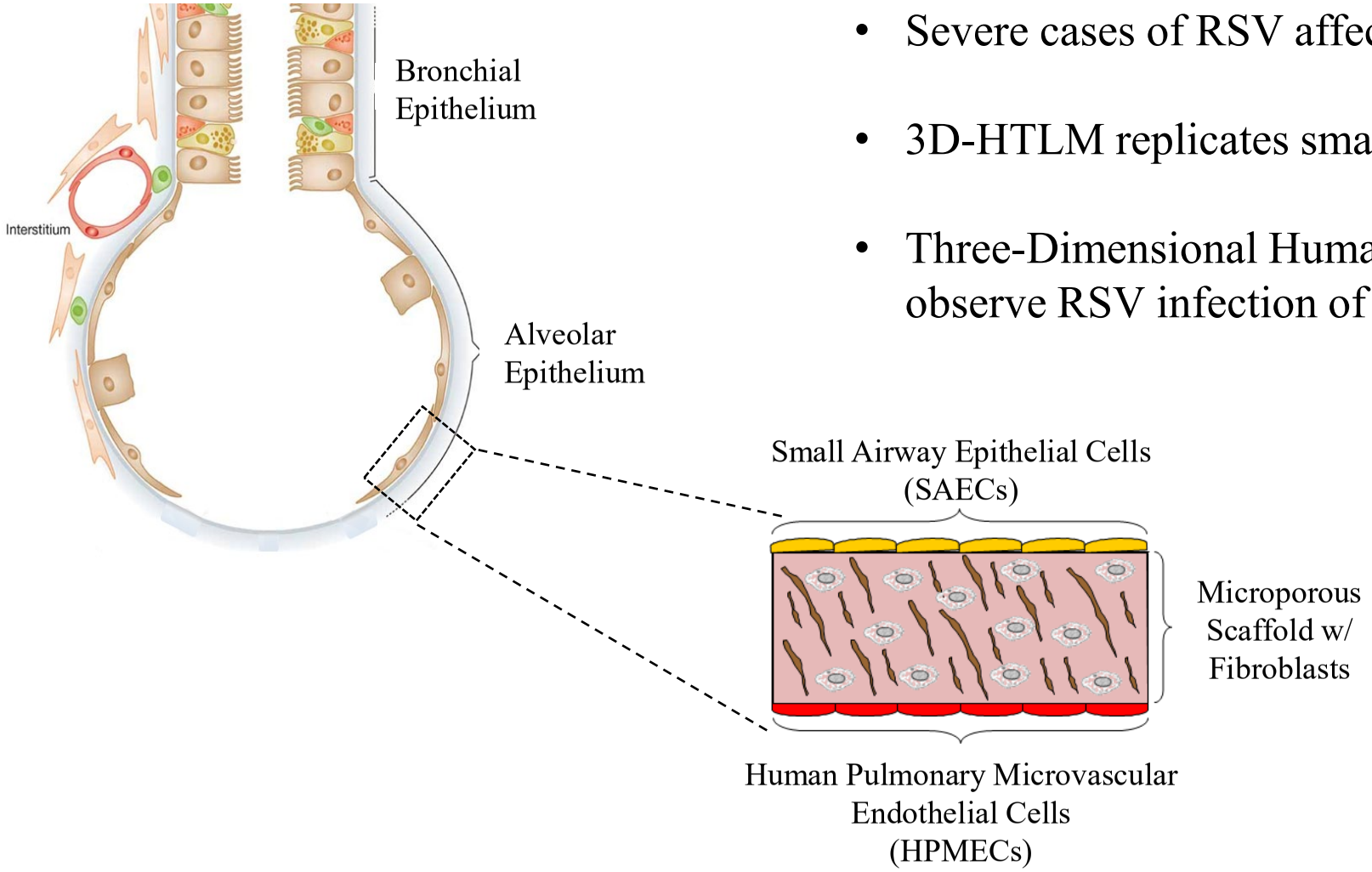

- Severe cases of RSV affect the small airway of the lung
- 3D-HTLM replicates small airway tissue of the human lung
- Three-Dimensional Human Tissue Lung Model is used to observe RSV infection of lung cells.

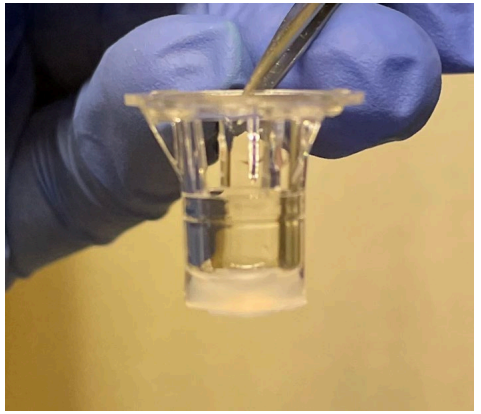

Königshoff, Melanie/Johannes Schwarz/Oliver Eickelberg (2011): Human lung stem cells: Oh, the places you'll go!, in: EMBO Molecular Medicine, EMBO, vol. 3, no. 10, pp. 575–577, [online] doi:10.1002/emmm.201100166.

Experimental Objectives

- Infect Small Airway Epithelial Cells (SACEs) in a 3D Human Tissue Lung Model with Respiratory Syncytial Virus (RSV)
- Determine the relationship between Multiplicity of Infection (MOI) on the infectivity of SAECs
- Determine the relationship between infection time periods on the infectivity of SAECs

Model Preparation

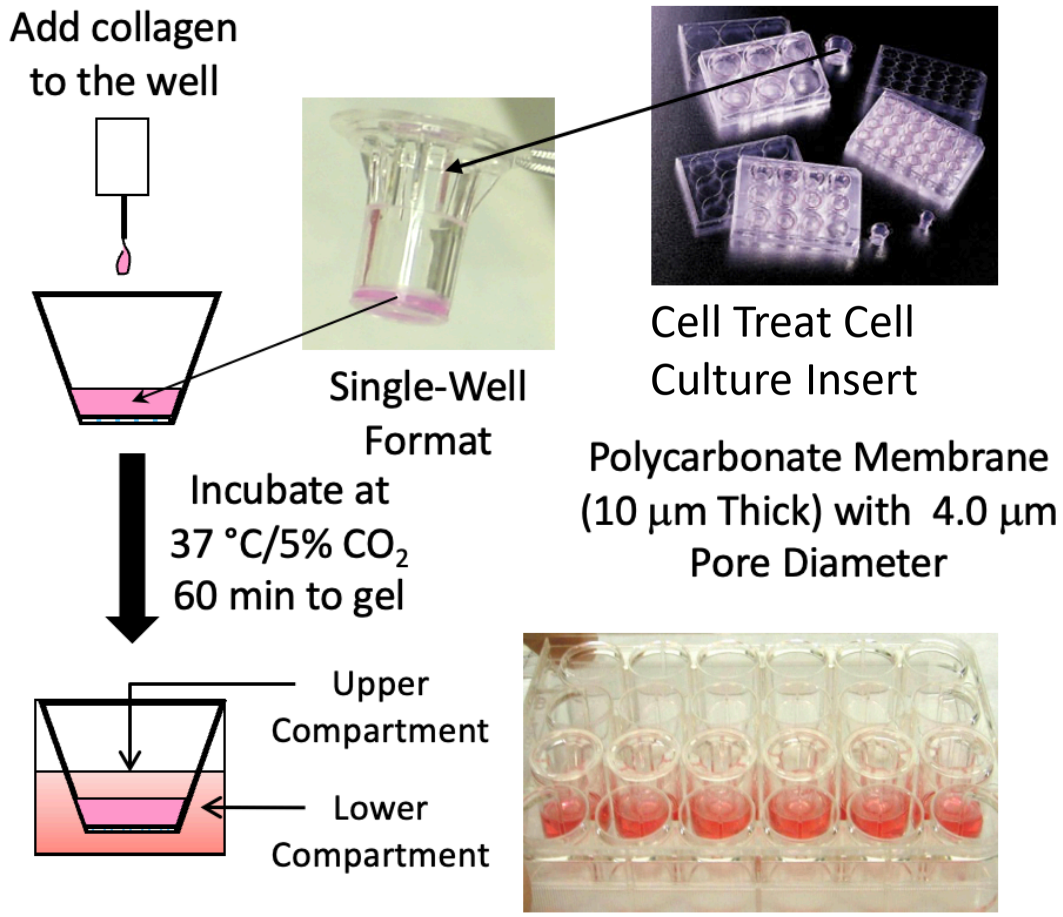

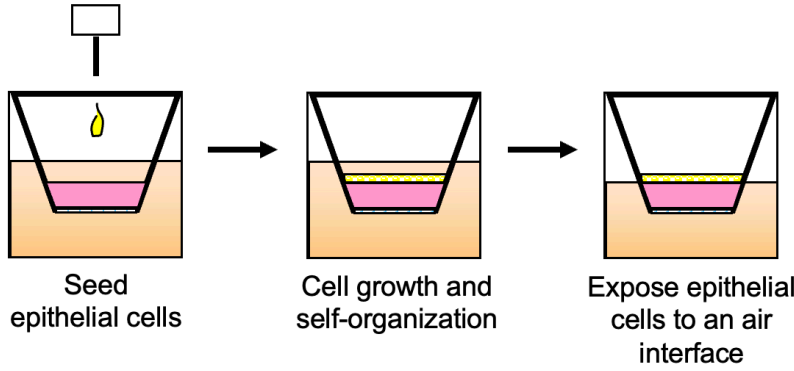

Models were submerged in media for 7 days, then subjected to ALI on day 7

Experimental Protocol To Measure Infection

Plate Layout for 24-hour Incubation Time:

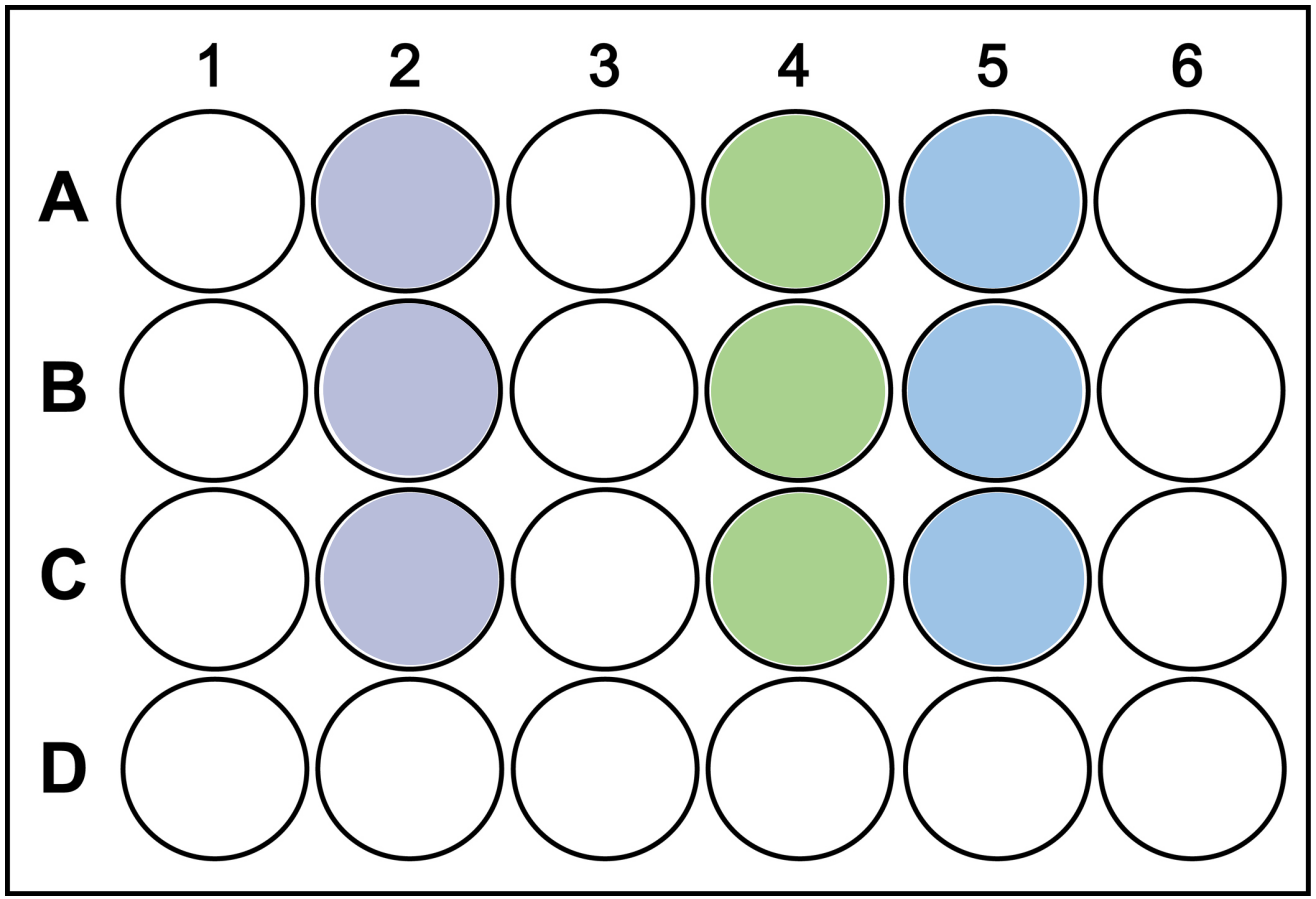

* Similar plate layout was used for 48- and 72-hour timepoints

RSV Concentrations:

10 Multiplicity Of Infection

15 Multiplicity Of Infection

RSV Infection Time Periods:

24 hrs, 48 hrs, 72 hrs

Antibody Panel

- PE- Labeled Cytokeratin-14
  - Used to identify epithelial cells
- TurboRFP-labeled RSV
  - Used to identify infected epithelial cells

Legend:

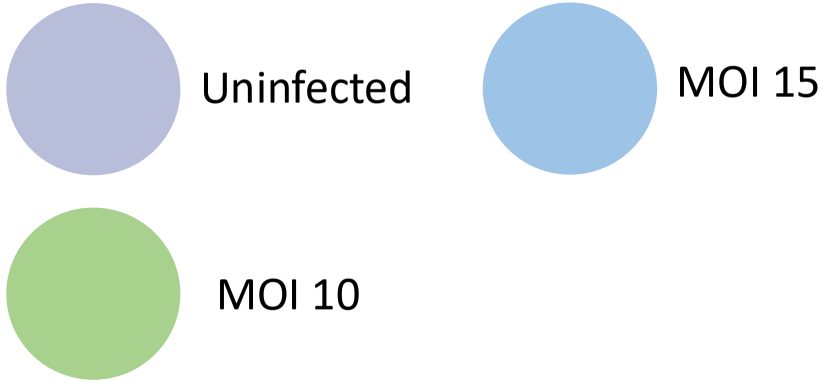

DAPI/Cytokeratin-14 Fluorescent Microscopy Images Control Sample

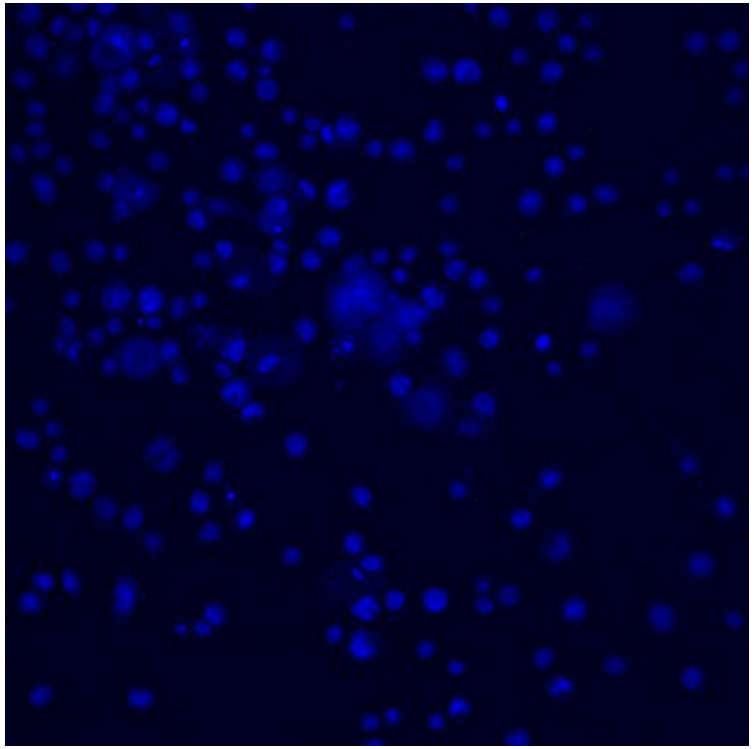

DAPI

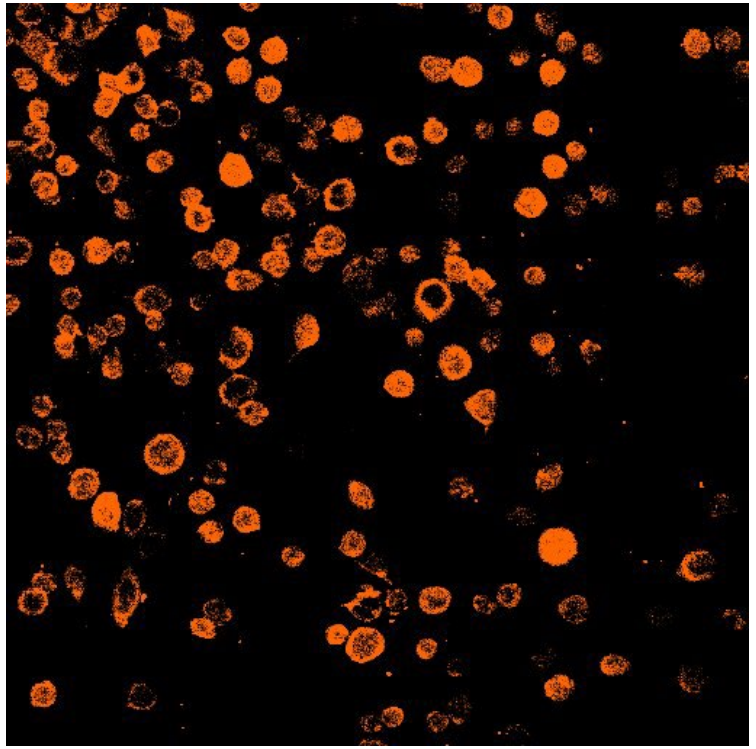

CK-14

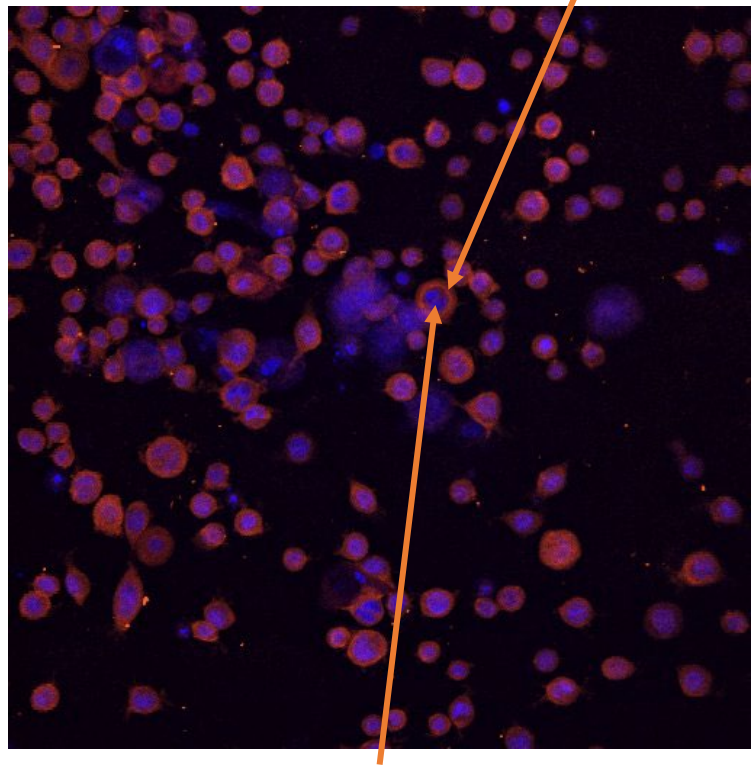

DAPI/Cytokeratin-14 Fluorescent Microscopy Images

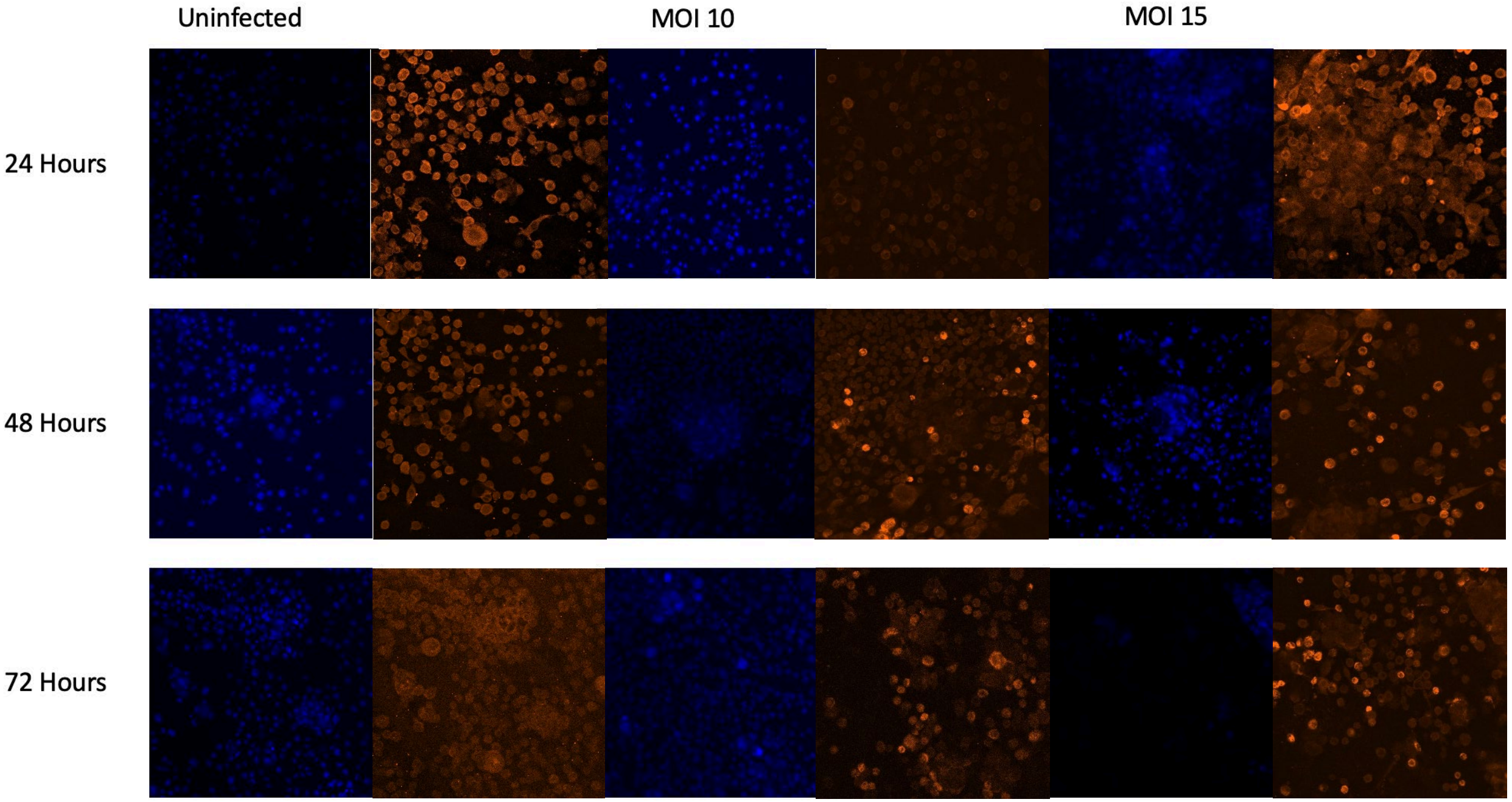

RFP-RSV Fluorescent Microscopy Images

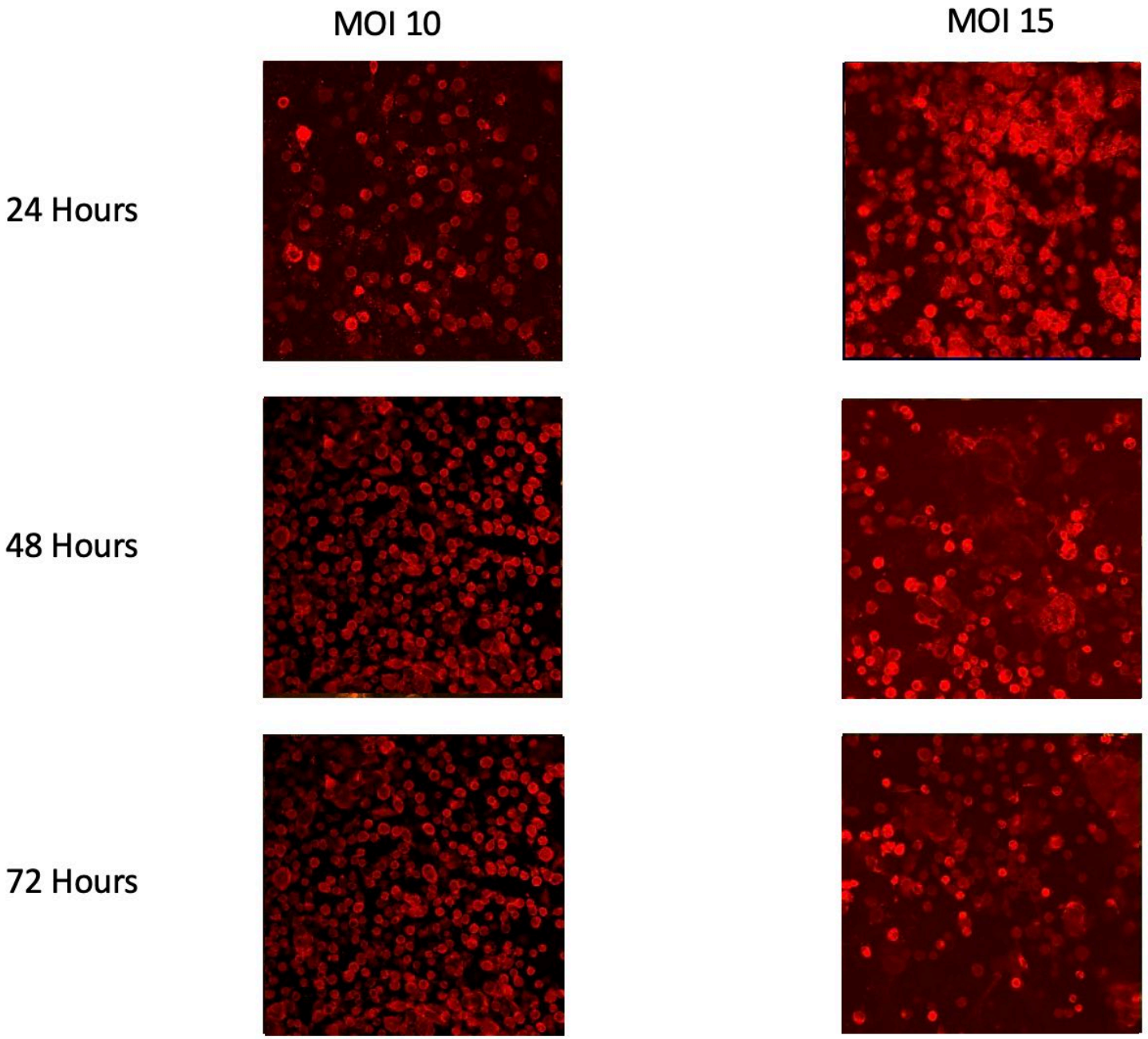

Conclusions

- SAECs were viable and infected with RSV at varying titers of MOI 10 and 15 and for varying incubation times of 24, 48, and 72 hours.
- For an MOI of 10, infectivity of the SAECs increased with increased incubation time.
- For the incubation time of 24 hours, infectivity of the SAECs increased with an increase of MOI from 10 to 15.
- For an MOI of 15, the number of infected cells decreased with increased incubation time, indicating possible cell death.

Acknowledgements

I would like to thank Dr. Niblack and Mrs. Nibalck for their generous donation so students like me can continue to be involved in such exciting research endeavors on campus!
I would also like to thank both Dr. Fahlenkamp and Taylor Do for their mentorship throughout this experience.

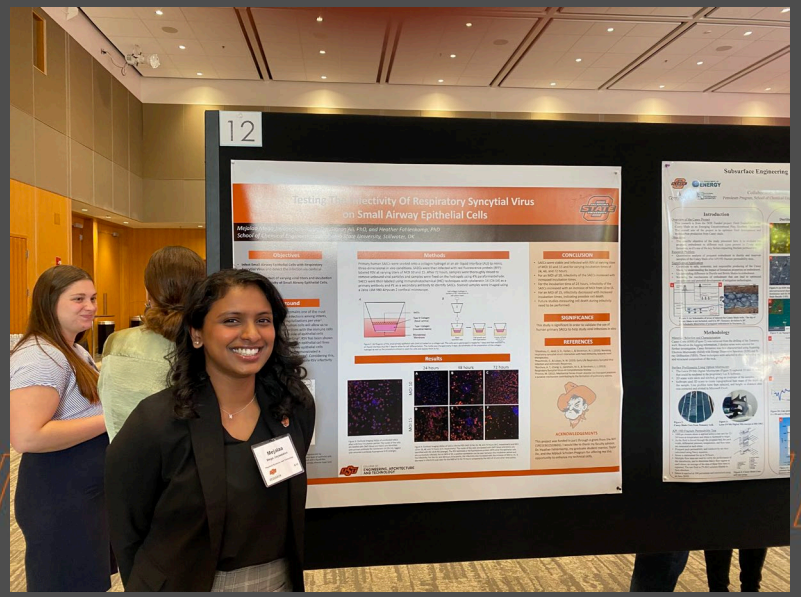

Determining the Effect of Respiratory Syncytial Virus on the Barrier Integrity of Cell Layers in a Three-Dimensional Human Tissue Lung Model

Karley White

Chemical Engineering
Faculty Sponsor: Dr. Heather Fahlenkamp
Graduate Student Mentor: Taylor Do

ABSTRACT

According to the World Health Organization, respiratory syncytial virus (RSV) causes approximately 34 million cases of acute respiratory infections annually. A three-dimensional human tissue lung model (3D-HTLM) has been engineered to observe the effects of RSV infection on cell layer function and behavior. This project analyzed the barrier integrity of cell layers within the 3D-HTLM in response to RSV infection using TEER and a permeability assay. Transepithelial electrical resistance (TEER) is a quantitative technique that uses electrical currents to measure the barrier integrity of cell layers and monitor cell layer behavior through stages of development. Permeability assay is a quantitative technique that determines membrane permeability by measuring the diffusion of a fluorescent probe through the model by recording fluorescent intensity values over time. Different variations of the 3D-HTLM consisting of a collagen base, fibroblasts, small airway epithelial cells, and human pulmonary microvascular endothelial cells were infected with RSV. The barrier integrity of the cell layers within each model was determined by taking TEER and permeability measurements 24, 48, and 72 hours after RSV infection. Results indicate a decrease in barrier integrity related to the degradation of cell layers within the 3D-HTLM after RSV infection.

1. Introduction

Respiratory Syncytial Virus, RSV, is the leading cause of respiratory infections in infants that require hospitalization in the United States. Due to the COVID-19 pandemic, there has been a reemergence of RSV in children 0 to 2 years old [Zheng et al., 2020]. A three-dimensional human tissue lung model (3D-HTLM), including collagen, fibroblasts, small airway epithelial cells, and human pulmonary microvascular endothelial cells, has been created to study the effects of RSV infection *in-vitro.* Small airway epithelial cells (SAECs) form a functional epithelial barrier to protect the lungs against infectious environmental agents. Human pulmonary microvascular endothelial cells (HPMECs) in the pulmonary endothelium of the lung can be used to study barrier integrity *in-vitro* due to their ability to form tight junctions within the extracellular matrix. Together, SAECs and HPMECs form a physical barrier that can be observed both in vivo and within 3D-HTLM. The effects of RSV on the barrier integrity formed by these cell layers within this model can be observed in-vitro. To determine the effect of RSV on barrier integrity, a TEER test and permeability assay were performed before RSV infection and 24, 48, and 72 hours after infection. Analyzing the barrier integrity of cell layers is important in understanding viral interactions with the lung epithelium, and it can provide information to aid in the advancement of treatments for RSV infection.

2. Experimental Details

Analyzing the barrier integrity of the 3D-HTLM before RSV infection and 24, 48, and 72 hours after infection required assembling the 3D-HTLM of each control and experimental group, performing TEER tests, and analyzing permeability assays at each time point.

The objective of this experiment was the measure the effect of RSV infection on the barrier integrity of the 3D-HTLM; however, due to the nature of the RSV virus, an experimental group of SAECs only and of SAECs and HPMECs were used in order to understand how endothelial cells (HPMECs) can influence the infection of epithelial cells (SAECs). Models designated ‘S’ contain SAECs only and models designated ‘M’ contain both SAECs and HPMECs. The control plate was not infected with RSV and was used to compare barrier integrity measurements 24, 48, and 72 hours after RSV was added to the infected plate. Since models cannot be used after performing the permeability assay, three separate sets of SAEC only and SAEC and HPMEC models were created to be tested 24, 48, and 72 hours after RSV infection.

Uninfected Plate

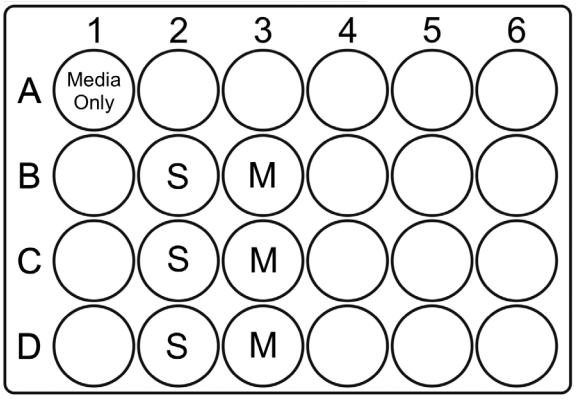

Media Only: Transwell with media used as control TEER measurement
S: SAECs Only
M: SAEC + HPMEC

Infected Plate - RSV of MOI 15

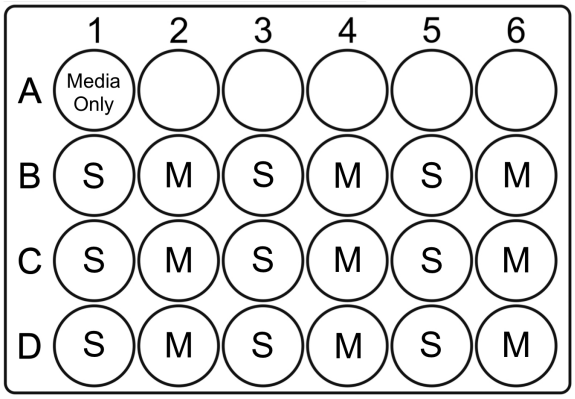

Media Only: Transwell with media used as control TEER measurement
S: SAECs Only
M: SAEC + HPMEC

2a. Assembly and Infection of the 3D-HTLM

Assembly and infection of the 3D-HTLM requires 24 well plates with transwell inserts, SAECs, HPMECs, fibroblasts, collagen hydrogel, and RSV of a multiplicity of infection value (MOI) of 15. This experiment required two different groups to be infected and observed: a model with only SAECs and a complete model with both SAECs and HPMECs. Both models were infected with RSV. The sequential process of assembling the 3D-HTLM is detailed in Figure 1.

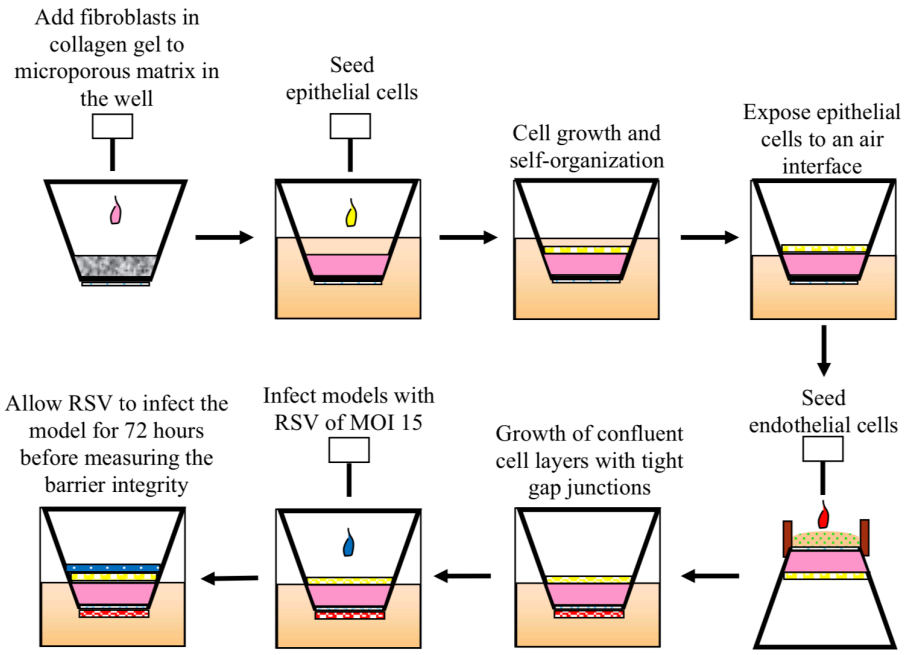

Fig. 1. The 3D-HTLM includes a collagen gel, fibroblasts, SAECs, and HPMECs. The collagen hydrogel, including fibroblasts, is added to a microporous transwell insert. The SAECs are added to the collagen and allowed to grow to confluency. The SAEC cells are then put at ALI to simulate an *in-vivo* environment. The HPMECs are added to the bottom of the transwell and are allowed to grow to confluency. After one week, the 3D-HTLM with confluent cell layers is infected with RSV.

2b. TEER Test

Transepithelial Electrical Resistance (TEER) is a quantitative method in measuring the barrier integrity of a cell layer or model. TEER measurements can be used to justify an increase or decrease in barrier integrity based on the model's ability to resist an electrical current. An electrical AC current is emitted between STIX 2 electrodes placed above and below the 3D-HTLM and a resulting resistance value, in Ohms, is reported on the EVOM 3 voltohmmeter.

Since the 3D-HTLM is put at air-liquid interface (ALI) to simulate an in vivo environment, media is added to the top and bottom of the model so an electrical current can be conducted from one electrode to the other. Once media is added, one electrode is placed in the apical side, or upper compartment, of the transwell just above the epithelial layer and the other electrode is placed in the basolateral side of the bottom of the well as shown Figure 2.

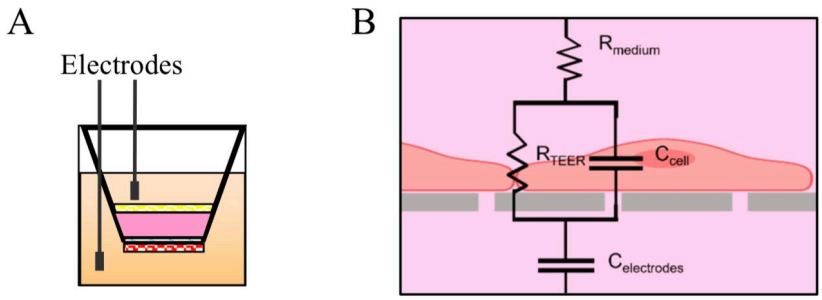

Fig. 2. (A) Electrode placement during a TEER test to allow for an AC current to pass through the 3D-HTLM. (B) An electrical circuit depicted on a cell layer to demonstrate the resistance value, R_{TEER}, recorded by the voltohmmeter [Tu et al., 2020].

The recorded resistance, R_{TEER}, is measured in ohms (Ω); however, final reported TEER values incorporate the surface area of the 24 well plate transwell, 0.33cm^2, and the measured resistance of a transwell with media only, R_{Medium} as seen in Eq. (1). The TEER measurement for each model was calculated, and an average TEER value of the three models in each experimental group was used to interpret results.

$$TEER\ (\Omega \cdot cm^2) = 0.33\ cm^2[R_{TEER} - R_{Medium}]\Omega \quad (1)$$

2c. Permeability Assay

Permeability assays can be used to calculate the apparent permeability of a model through the calculation of measured fluorescent intensity over time with respect to model area and initial fluorescent concentration. Apparent permeability values, P_{app}, represent the ability a cell model to allow the flow of fluid through the 3D-HTLM cell membrane.

After a TEER test of each model is conducted, the yellow-green fluorescent probe solution with a dilution of 0.08 µM is added to the top of each model in the apical compartment. At incubation times 0, 15, 30, 60, and 180 minutes after the fluorescent probe is added, 5µL of media is collected from the basal compartment of the well. The collected sample is placed in a 96-well plate with 45µL of PBS. Once all samples are collected, the fluorescent intensity is measured using the plate reader equipped with a 485nm excitation wavelength and a 535nm emission wavelength. [Sigma-Aldrich, 2022]. The concentration relative to each fluorescent intensity measurement is estimated based on a standard curve formed using varying concentrations of sodium fluorescein dilutions in culture media. The apparent permeability, Papp, of each model is calculated using a standardized engineering formula for the permeability of a membrane with respect to a specific compound.

$$P_{app} = \frac{\Delta Q}{\Delta t \cdot A \cdot C_0} \quad (2)$$

In this equation, ΔQ is the change in the amount of fluorescent sodium in the basal compartment of the well (mg), Δt is the duration of the experiment (seconds), A is the surface area of the transwell (cm^2), and C_0 is the initial concentration in the apical compartment of the transwell (mg/cm^3). The P_{app} (cm/s) of each model was calculated and the average of the three models in each group was used to interpret results [Chandra, 2007].

3. Results

The TEER results, shown in Figure 3, were analyzed using a paired t-test and ANOVA test via the graphing Prism software. Results show a significant difference between SAEC and SAEC + HMPEC models and between uninfected and infected models. Both uninfected experimental groups show an increase in barrier integrity from 0 to 72 hours with the SAEC + HPMEC group having an overall higher resistance and higher barrier integrity. There is a significant change in barrier integrity of both infected models between time points 0 and 24 hours after RSV infection. The infected SAEC + HPMEC models continue to have a degradation in barrier integrity 48 hours after infection while the SAEC models have an increase in barrier integrity at 48 hours.

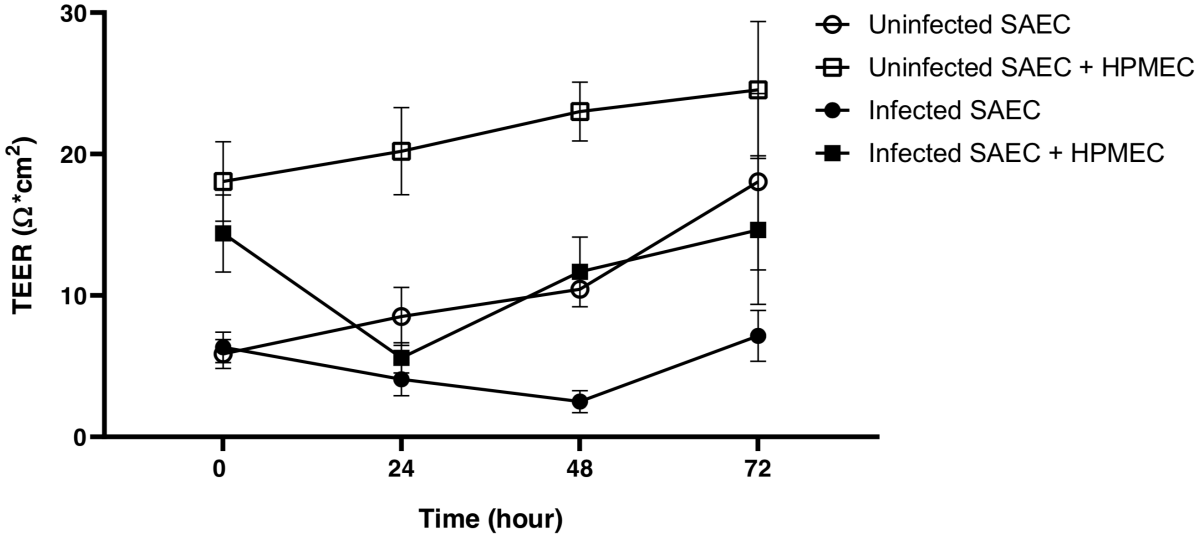

Fig. 3. TEER test of experimental groups, SAEC and SAEC + HPMEC, after infected with RSV of MOI 15. Values were compared to uninfected control models to determine

barrier degradation of the epithelial and endothelial layers over time due to RSV infection. Statistical significance: $p < 0.005$ comparing uninfected models from 0 to 72 hours, $p < 0.0001$ comparing SAEC and SAEC + HPMEC models at each time point, $p = 0.0188$ comparing time points 0 and 24 of infected models, $p = 0.0746$ comparing time points 0 and 48 of infected models, $p = 0.0977$ comparing infected models from 0 to 72 hours.

Permeability assay results, shown in Figure 4, did not have any significant differences between experimental groups or time points after statistical analysis. The results are inconsistent with the TEER results and expected P_{app} values related to barrier conditions before and after RSV infection. The P_{app} variable represents the fluorescent probe's ability to diffuse through the model. A higher P_{app} value means there is a lower barrier integrity.

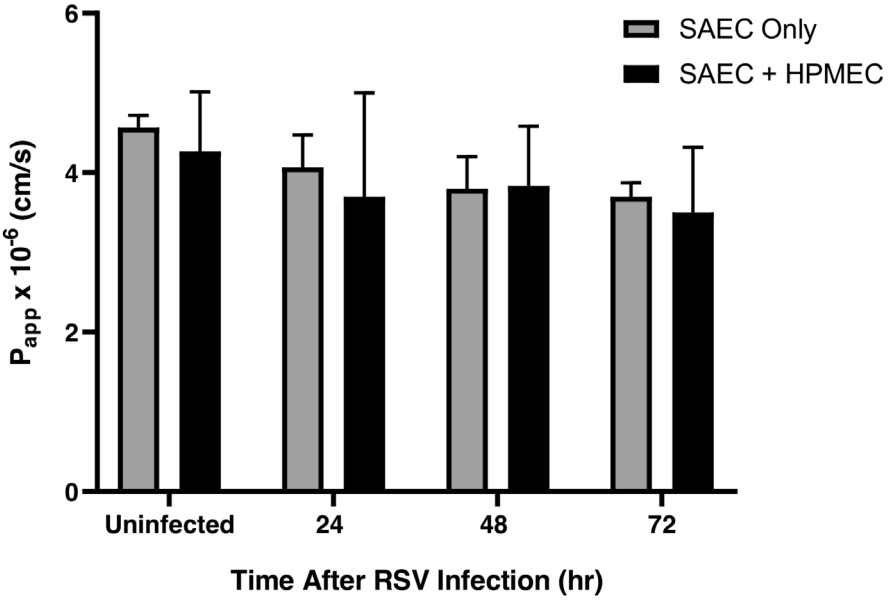

Fig. 4. Apparent permeability, Papp, of SAEC and SAEC + HPMEC models 24, 48, and 72 hours after infection with RSV of MOI 15 compared to uninfected models. Papp values of infected models show slightly decreased permeability which is inconsistent with expected results. There is no statistical significance between Papp values at any time points or between SAEC and SAEC + HPMEC groups.

4. Discussion and Conclusions

The TEER results show a decrease in barrier integrity of the cell layers within the 3D-HTLM after infection which is consistent with potential RSV interaction with the epithelial layer. The recorded resistance and barrier integrity of a model are directly correlated, so an increase in resistance signals an increase in barrier integrity [Derk et al., 2014]. In Figure 4, both infected SAEC and SAEC + HPMEC groups did not have a significant difference

between timepoints 0 and 72 hours showing a possibility of cell recovery or growth. The change in barrier integrity of both infected groups is greatest between time points 0 and 24 hours. This data could possibly show the infectivity timing of the RSV virus in relation to SAEC cells. The SAEC + HPMEC group was tested in order to observe the effect endothelial cells may have on the infection of epithelial cells. The SAEC only model has the lowest barrier integrity 48 hours after infection while the SAEC + HPMEC model has the lowest barrier integrity at 24 hours. The recovery time points, or increases in barrier integrity, of each model could correlate to the doubling times of SAECs and HPMECs. The doubling time of SAECs is slower than that of HPMECs, taking about 4 days [Wang et al., 2019]. The doubling time for HPMEC is much faster around 24 to 48 hours. These doubling times could explain the rate of barrier integrity increase being higher for the combined model and lower for the SAEC only model [Krump et al., 2001] The overall TEER results are consistent with a similar 3D model of the upper airway showing initial resistance readings of 130 to 220 Ω before using Eq. 1 [Harrington, 2017].

TEER results display a decrease in barrier integrity after RSV infection, and the permeability assay results were inconsistent with this barrier integrity observation. There was no significant difference between any results of the permeability assay. This inconsistency between barrier integrity tests could have been influenced by many factors. One noticeable difference is the logistics of each test itself indicating which part of the model is measured. TEER test probes can be placed in the middle of the model so the resistance is representative of a single point of the model which is multiplied by the surface area. The permeability test measures the permeability of the entire model at once. When the fluorescent probe is added to the top of the model, it could diffuse through the areas of lower barrier integrity. This feature of the permeability assay is notable when regarding this experiment due to the visible shrinking of the 3D-HTLM throughout this experiment. If a model were to pull away from the edges of the transwell, the fluorescent probe could pass through the transwell membrane where there is no cell growth resulting in permeability results that are not direct representations of the barrier integrity of the 3D-HTLM. Apparent permeability values between $1x10^{-6}$ and $10x10^{-6}$ cm/s are comparable to P_{app} values of a similar 3D hydrogel model of the stomach including fibroblasts [Lourenço, 2018].

5. Summary

The objective of this experiment was to determine the effects of RSV on the barrier integrity of a 3D human tissue lung model 24, 48, and 72 hours after infection. The permeability assay provided no significant finding related to barrier integrity; however, TEER tests indicated a significant decrease in barrier integrity of the epithelial and endothelial layers 24 hours after RSV infection. Models with HPMECs showed a faster recovery of barrier integrity after RSV infection when compared to the SAEC only models.

6. Appendices

6a. Acknowledgements

This project was funded through a grant from the NIH (1 R 01 EB 025596 01). I would like to thank Dr. and Mrs. Niblack and the Niblack Scholars program for the opportunity to present this project as an undergraduate student and my mentors Dr. Fahlenkamp and Taylor Do for the opportunity and assistance needed to complete this project.

6b. Papers Published

This work has been included in a paper submitted to the Journal of Tissue Engineering.

6c. Literature Cited

Chandra, A., Barillas, S., Suliman, A., & Angle, N. (2007). A novel fluorescence-based cellular permeability assay. *Journal of Biochemical and Biophysical Methods*, *70*(3), 329–333.

Derk, R., Davidson, D. C., Manke, A., Stueckle, T. A., Rojanasakul, Y., & Wang, L. (2015). Potential in vitro model for testing the effect of exposure to nanoparticles on the lung alveolar epithelial barrier. *Sensing and Bio-Sensing Research*, *3*, 38–45.

Harrington, H., Cato, P., Salazar, F., Wilkinson, M., Knox, A., Haycock, J. W., Rose, F., Aylott, J. W., & Ghaemmaghami, A. M. (2014). Immunocompetent 3D Model of Human Upper Airway for Disease Modeling and In Vitro Drug Evaluation. *Molecular Pharmaceutics*, *11*(7), 2082–2091.

Krump-Konvalinkova, V., Bittinger, F., Unger, R. E., Peters, K., Lehr, H. A., & Kirkpatrick, C. J. (2001). Generation of Human Pulmonary Microvascular Endothelial Cell Lines. *Laboratory Investigation*, *81*(12), 1717–1727.

Lourenço, B. N., dos Santos, T., Oliveira, C., Barrias, C. C., & Granja, P. L. (2018). Bioengineering a novel 3D in vitro model of gastric mucosa for stomach permeability studies. *Acta Biomaterialia*, *82*, 68–78.

Refsgaard, H. H. F., Jensen, B. F., Brockhoff, P. B., Padkjær, S. B., Guldbrandt, M., & Christensen, M. S. (2005). In Silico Prediction of Membrane Permeability from Calculated Molecular Parameters. *Journal of Medicinal Chemistry*, *48*(3), 805–811.

Sigma-Aldrich. (2022). Fluorescein Sodium Salt Safety Data Sheet, 518-47-8.

Tu, K.-H., Yu, L.-S., Sie, Z.-H., Hsu, H.-Y., Al-Jamal, K. T., Wang, J. T.-W., & Chiang, Y.-Y. (2020). Development of Real-Time Transendothelial Electrical Resistance Monitoring for an In Vitro Blood-Brain Barrier System. *Micromachines*, *12*(1), 37.

Wang, G., Lou, H. H., Salit, J., Leopold, P. L., Driscoll, S., Schymeinsky, J., Quast, K., Visvanathan, S., Fine, J. S., Thomas, M. J., & Crystal, R. G. (2019). Characterization of an immortalized human small airway basal stem/progenitor cell line with airway region-specific differentiation capacity. *Respiratory Research*, *20*(1).

Zheng, Z., Pitzer, V. E., Shapiro, E. D., Bont, L. J., & Weinberger, D. M., 2021. Estimation of the Timing and Intensity of Reemergence of Respiratory Syncytial Virus Following the COVID-19 Pandemic in the US. *JAMA network open*, *4*(12.

Determining the Effect of Respiratory Syncytial Virus on the Barrier Integrity of Cell Layers in a Three-Dimensional Human Tissue Lung Model

Karley White

Department of Chemical Engineering

College of Engineering, Architecture, and Technology

Oklahoma State University

COLLEGE OF ENGINEERING, ARCHITECTURE AND TECHNOLOGY

Respiratory Syncytial Virus

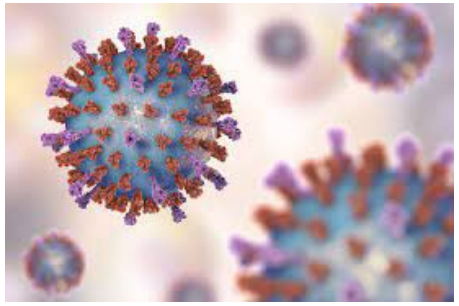

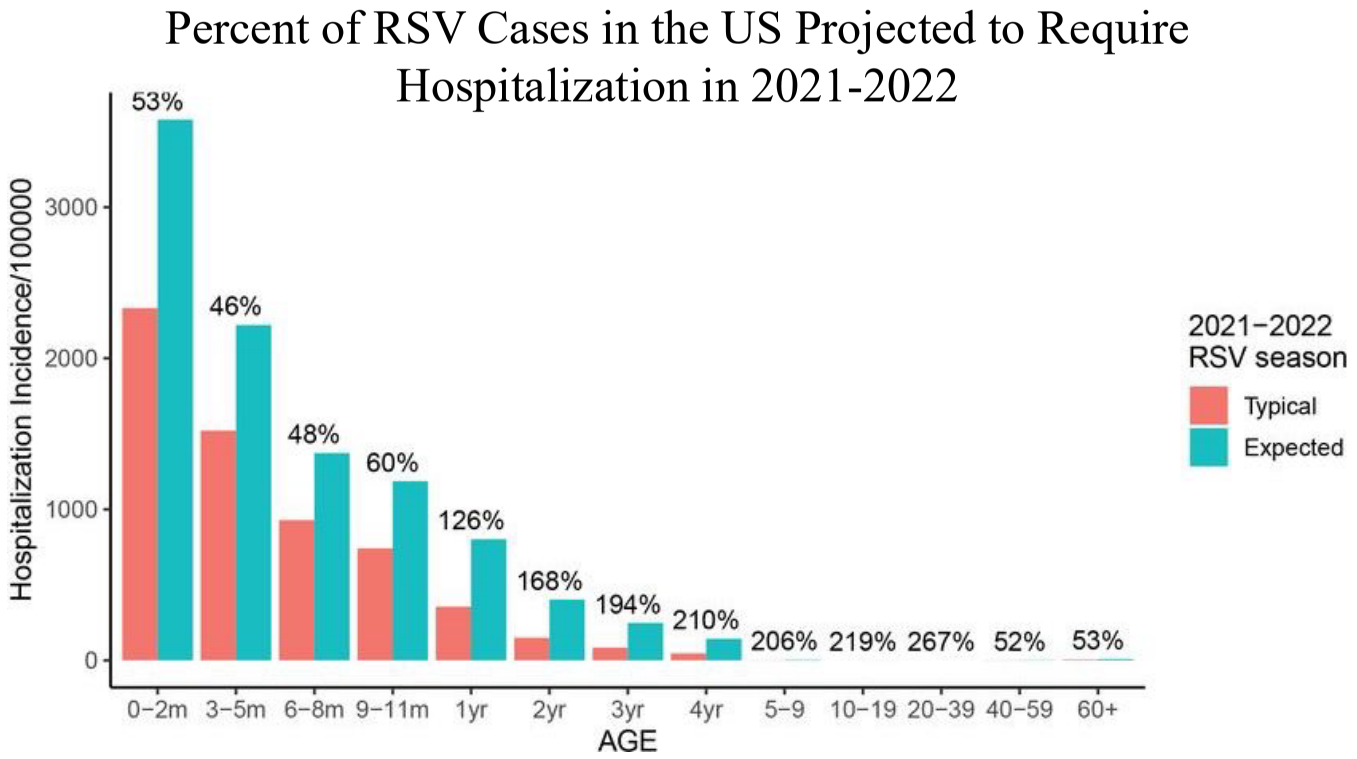

- RSV is the leading cause of respiratory infection requiring hospitalizations in infants.
- Re-emergence of RSV due to COVID-19 pandemic
- Investigating the physiological effects of RSV is beneficial in developing new treatment strategies.

Smith, Jake (2021): What Is RSV? CDC Warns of Respiratory Syncytial Virus Rising in the Southern U.S., Prevention.
Zheng, Zhe (2021): Re-emergence of respiratory syncytial virus following the COVID-19 pandemic in the United States: a modeling study, medRxiv.

3D Human Tissue Lung Model

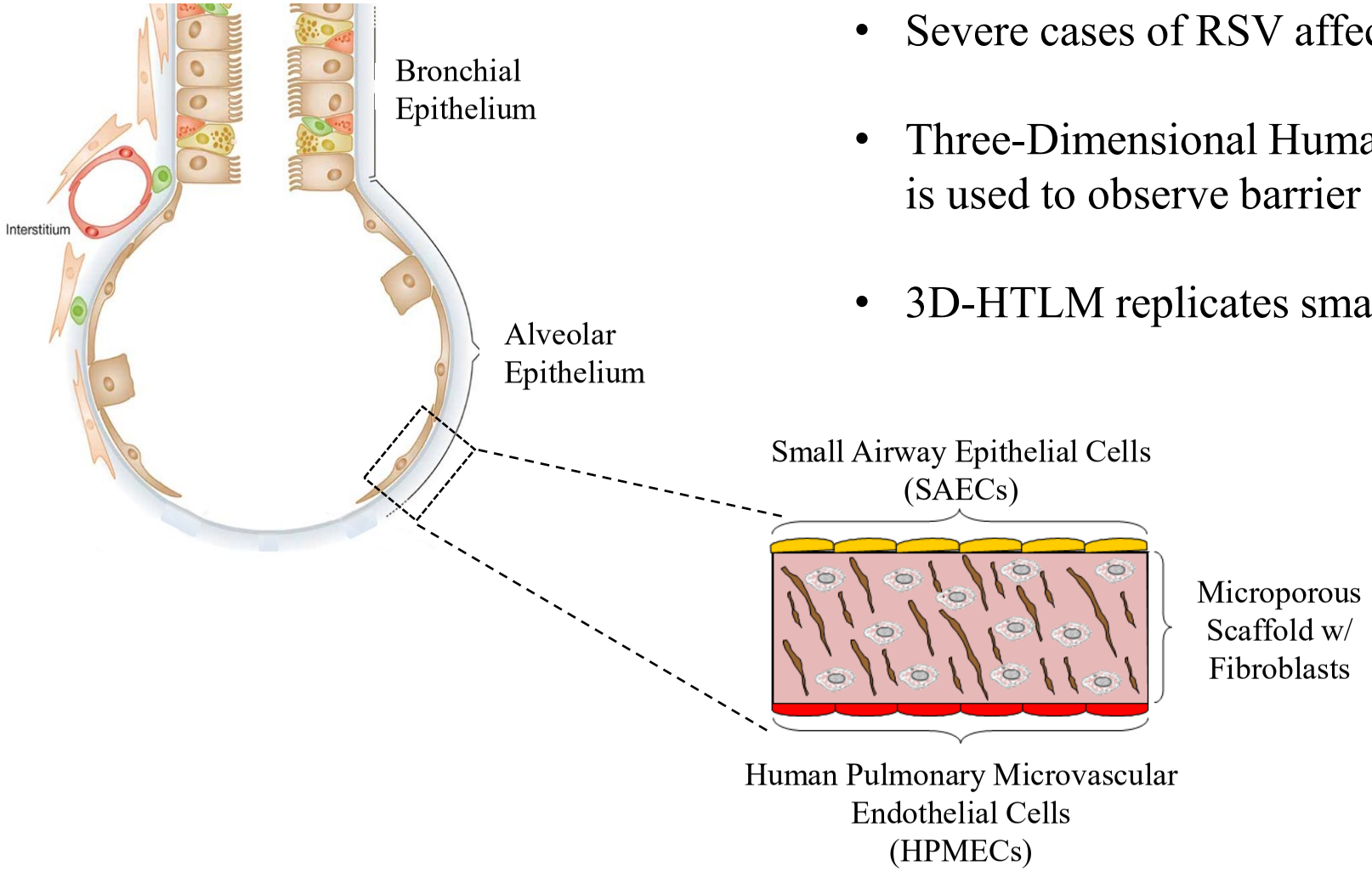

- Severe cases of RSV affect the small airway of the lung
- Three-Dimensional Human Tissue Lung Model (3D-HTLM) is used to observe barrier function and cell behavior.
- 3D-HTLM replicates small airway tissue of the human lung

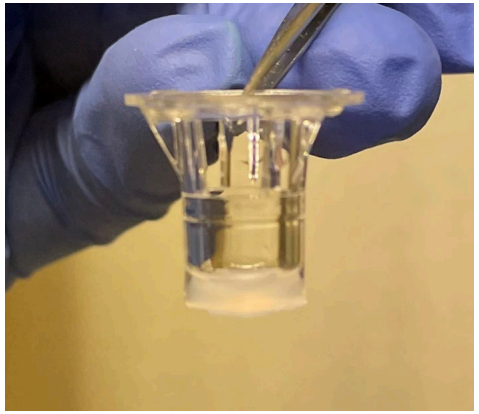

Königshoff, Melanie/Johannes Schwarz/Oliver Eickelberg (2011): Human lung stem cells: Oh, the places you'll go!, in: EMBO Molecular Medicine, EMBO, vol. 3, no. 10, pp. 575–577, [online] doi:10.1002/emmm.201100166.

Experimental Objectives

1. Create variations of the 3D-HTLM including SAECs and HPMECs

2. Test the effect of RSV on barrier integrity 24, 48, and 72 hours after infection using transepithelial resistance (TEER) and fluorescent permeability assay

3D-HTLM with SAECs Only

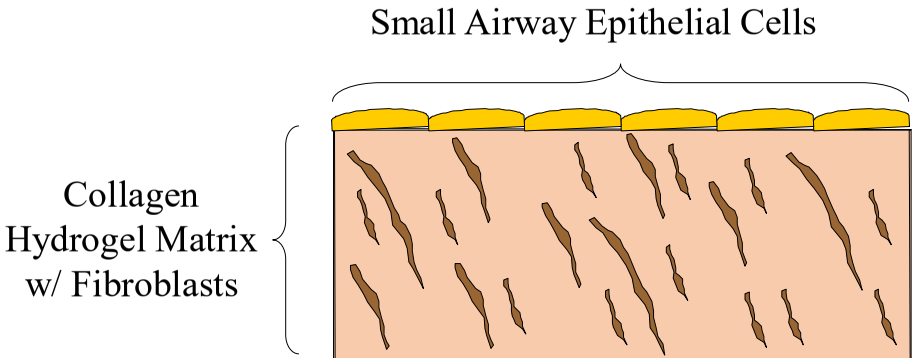

3D-HTLM with SAECs and HPMECs

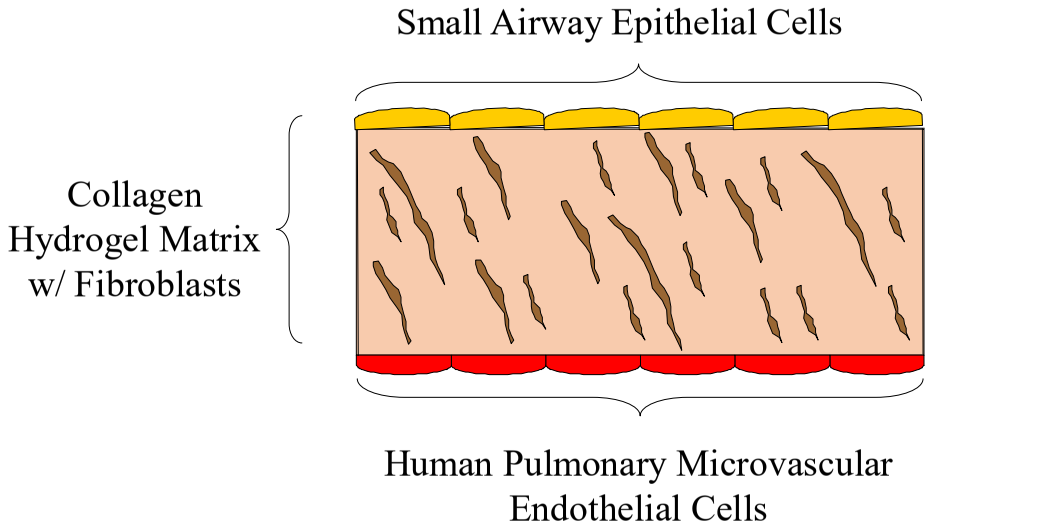

Experimental Design

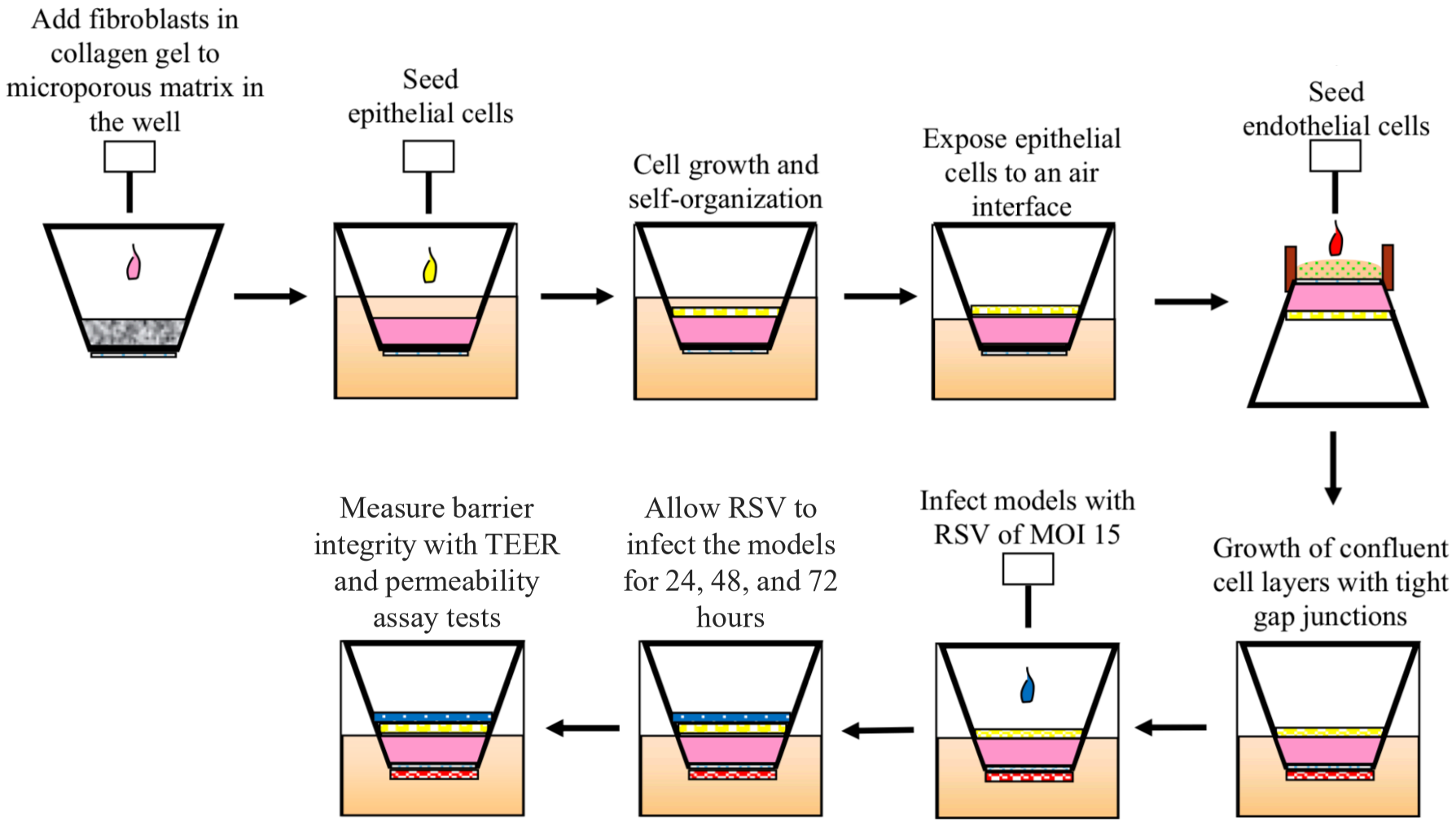

Experimental Design

Uninfected Plate:

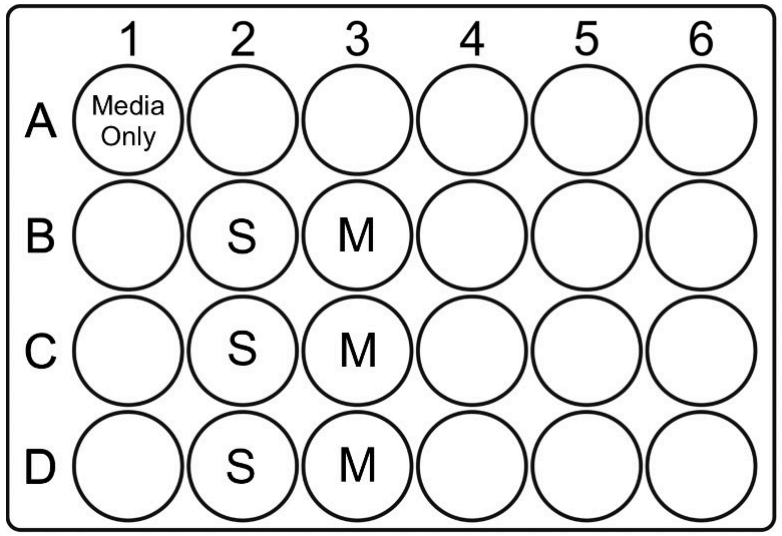

Infected Plate:

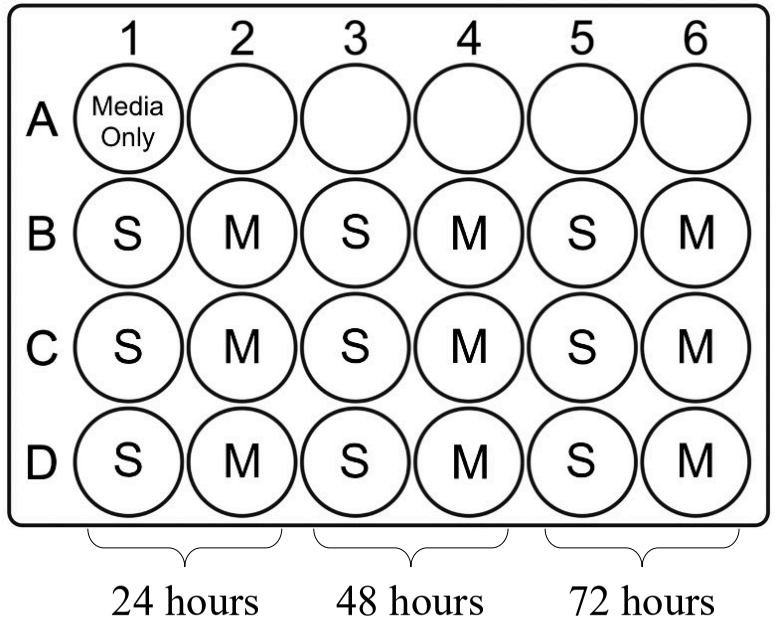

Media Only: Transwell with media

S: SAECs Only

M: SAEC + HPMEC

Transepithelial Electrical Resistance (TEER)

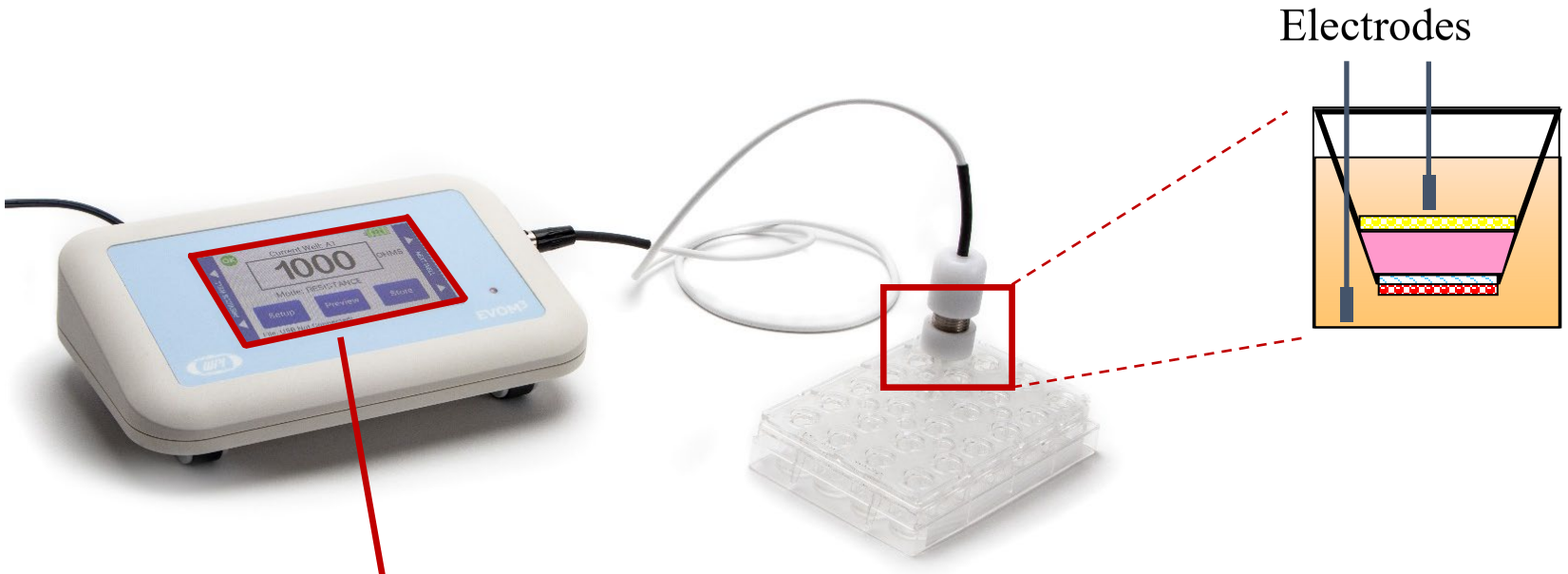

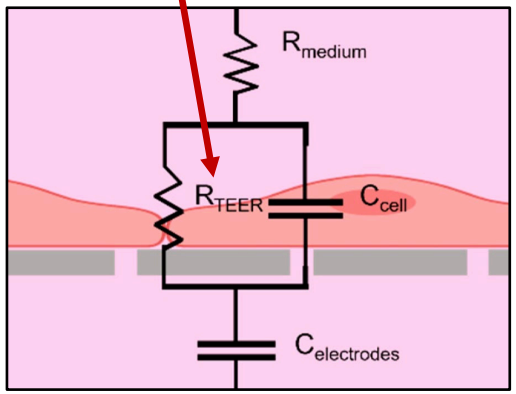

$$R_{cell\ layers}(\Omega \cdot cm^2) = SA * (R_{model} - R_{media})$$

- $R_{cell\ layers}$ represents resistance of the cell layers only
- R_{model} represents initial TEER readings of the model
- R_{media} represents the TEER value of a transwell with media only

Tu, Kai-Hong et al. (2020): Development of Real-Time Transendothelial Electrical Resistance Monitoring for an In Vitro Blood-Brain Barrier System, in: Micromachines, MDPI AG, vol. 12, no. 1, p. 37.

TEER Results

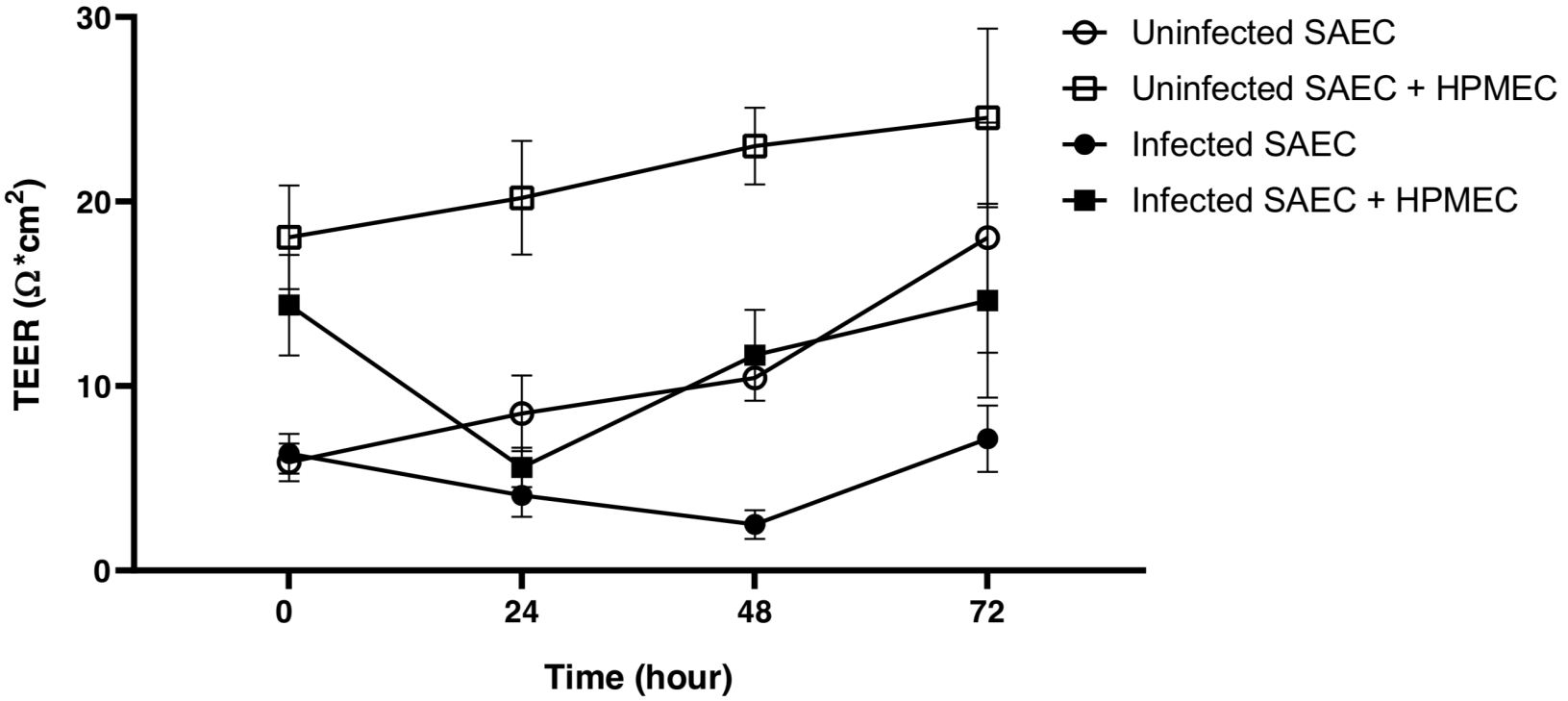

- Uninfected models show potential cell growth and development with values comparable to TEER results in a similar study of the 3D-HTLM[6].
- Infected SAEC + HPMEC models show a faster recovery, or increased slope, in barrier integrity after 24 hours compared to SAEC Only models.

Fluorescent Permeability Assay

Add fluorescent probe to the top of the cell layer

Allow fluorescent probe to diffuse through the model

Measure fluorescent probe from the basal compartment over time.

Analyze fluorescent intensity values using plate reader

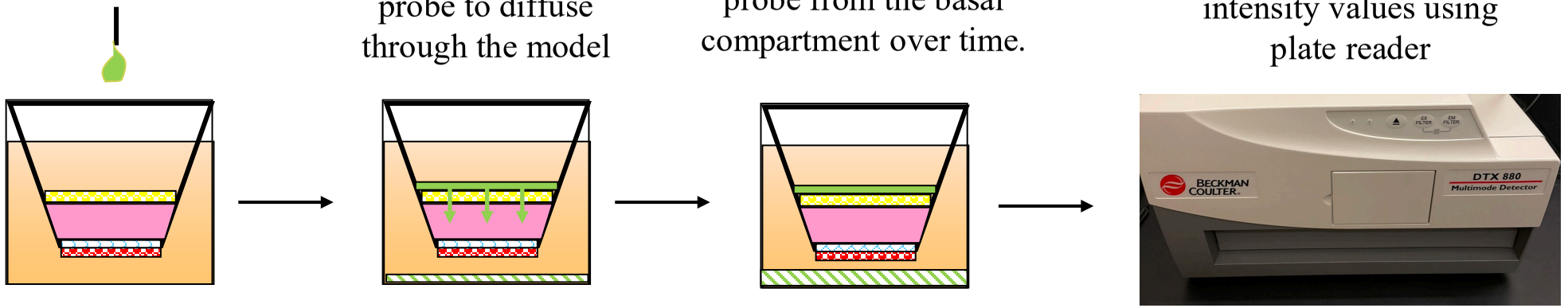

Apparent Permeability Calculation

$$P_{app} = \frac{\Delta Q}{\Delta t \cdot A \cdot C_0}$$

Q = amount of fluorescein isothiocyanate
t = time
A = surface area of transwell
C = initial concentration

- Apparent permeability, P_{app}, represents the ability of the fluorescent probe to travel through the cell layer
- Increases in P_{app} represent a decrease in 3D-HTLM barrier integrity

Chandra, A. et. al. (2007). A novel fluorescence-based cellular permeability assay. Journal of Biochemical and Biophysical Methods, 70(3), 329–333.

Permeability Results

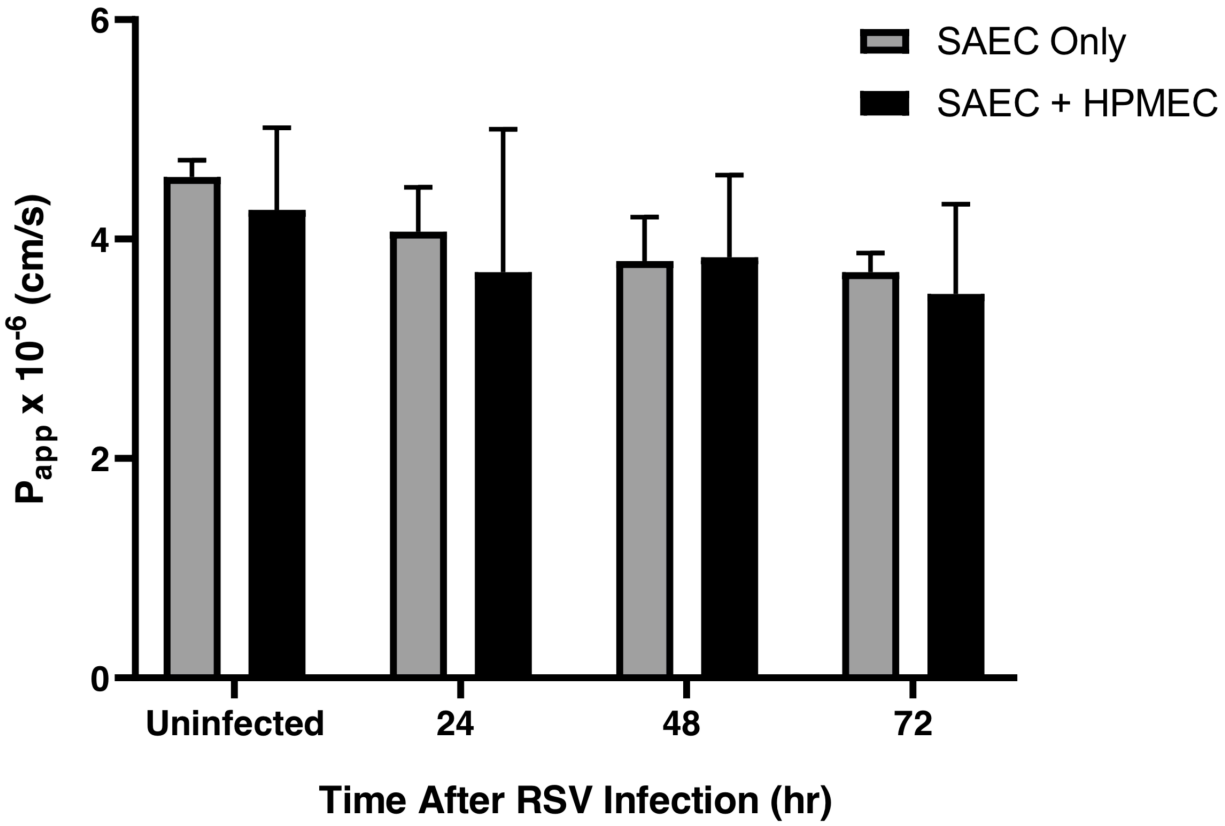

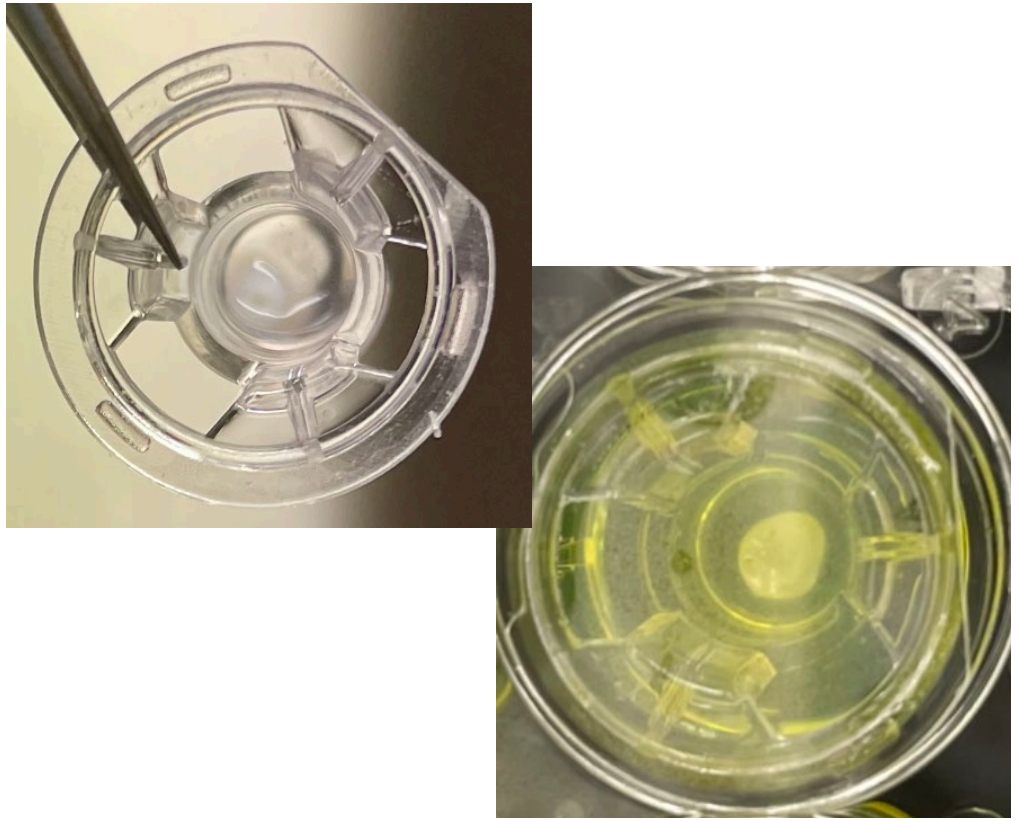

- P_{app} indicate increased barrier integrity over time which is inconsistent compared to TEER results and other experimental studies.
- Contraction of the collagen hydrogel matrix may contribute to the unreliable permeability trend.

Conclusions

- Infection of RSV can decrease the barrier integrity of cell layers present in the small airway of the lung
- Evidence of possible cell recovery or growth in SAEC and HPMEC layers after infection with RSV
- HPMECs play a role in barrier integrity increases after RSV infection
- Permeability assay experiment should be modified to be used on models with a contracted collagen matrix
- All results show cause for further investigation into the physiological effects of RSV infection in the human lung

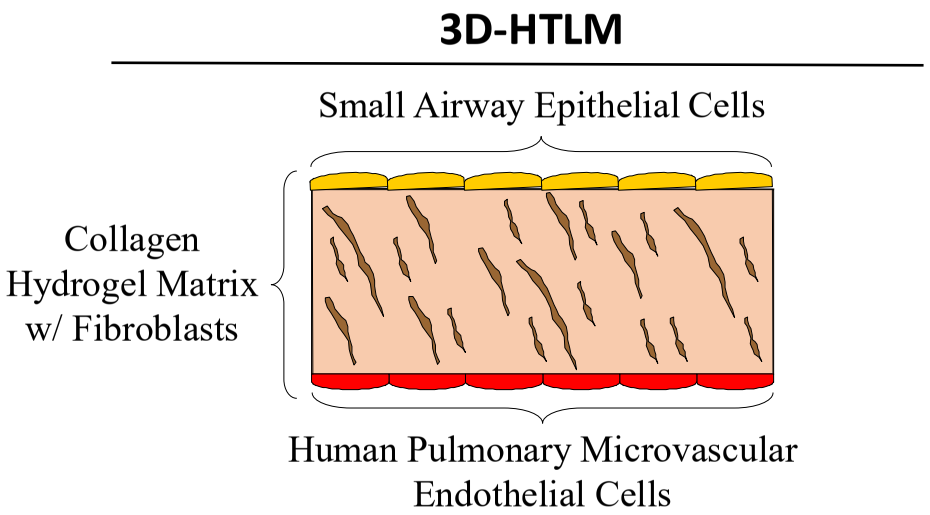

Acknowledgments

- Dr. and Mrs. Niblack and the Niblack Scholars program for the opportunity to present this project as an undergraduate student
- Mentors Dr. Fahlenkamp and Taylor Do for the opportunity and assistance needed to complete this project
- This project was funded through NIH grant 1 R 01 EB 025596 01

SCHOOL OF
CHEMICAL ENGINEERING
College of Engineering, Architecture and Technology

References

Chandra, A., Barillas, S., Suliman, A., & Angle, N. (2007). A novel fluorescence-based cellular permeability assay. *Journal of Biochemical and Biophysical Methods*, *70*(3), 329–333.

Derk, R., Davidson, D. C., Manke, A., Stueckle, T. A., Rojanasakul, Y., & Wang, L. (2015). Potential in vitro model for testing the effect of exposure to nanoparticles on the lung alveolar epithelial barrier. *Sensing and Bio-Sensing Research*, *3*, 38–45.

Harrington, H., Cato, P., Salazar, F., Wilkinson, M., Knox, A., Haycock, J. W., Rose, F., Aylott, J. W., & Ghaemmaghami, A. M. (2014). Immunocompetent 3D Model of Human Upper Airway for Disease Modeling and In Vitro Drug Evaluation. *Molecular Pharmaceutics*, *11*(7), 2082–2091.

Krump-Konvalinkova, V., Bittinger, F., Unger, R. E., Peters, K., Lehr, H. A., & Kirkpatrick, C. J. (2001). Generation of Human Pulmonary Microvascular Endothelial Cell Lines. *Laboratory Investigation*, *81*(12), 1717–1727.

Refsgaard, H. H. F., Jensen, B. F., Brockhoff, P. B., Padkjær, S. B., Guldbrandt, M., & Christensen, M. S. (2005). In Silico Prediction of Membrane Permeability from Calculated Molecular Parameters. *Journal of Medicinal Chemistry*, *48*(3), 805–811.

Sigma-Aldrich. (2022). Fluorescein Sodium Salt Safety Data Sheet, 518-47-8.

Tu, K.-H., Yu, L.-S., Sie, Z.-H., Hsu, H.-Y., Al-Jamal, K. T., Wang, J. T.-W., & Chiang, Y.-Y. (2020). Development of Real-Time Transendothelial Electrical Resistance Monitoring for an In Vitro Blood-Brain Barrier System. *Micromachines*, *12*(1), 37.

Wang, G., Lou, H. H., Salit, J., Leopold, P. L., Driscoll, S., Schymeinsky, J., Quast, K., Visvanathan, S., Fine, J. S., Thomas, M. J., & Crystal, R. G. (2019). Characterization of an immortalized human small airway basal stem/progenitor cell line with airway region-specific differentiation capacity. *Respiratory Research*, *20*(1).

Zheng, Z., Pitzer, V. E., Shapiro, E. D., Bont, L. J., & Weinberger, D. M., 2021. Estimation of the Timing and Intensity of Reemergence of Respiratory Syncytial Virus Following the COVID-19 Pandemic in the US. *JAMA network open*, *4*(12).

Effect of Nozzle Configuration on Thrust of a Novel Turbojet-Turboprop Engine for Small Unmanned Aircraft

Seth Robbins

Department of Mechanical and Aerospace Engineering
Faculty Sponsor: Dr. Kurt Rouser
Graduate Student Mentor: Trey Schinzler

ABSTRACT

This paper presents the results of testing the effects of nozzle exit diameter and downstream location on variable-cycle engine thrust for small, unmanned aircraft, such that the engine is capable of operating in turbojet and turboprop modes. The motivation of this project is to inform design decisions for a single aircraft with both high-speed dash and high-endurance loiter capabilities, creating a package that can perform both long-duration and rapid response mission legs. In this study, thrust was evaluated through static testing of a modified 6.7-hp KingTech K45TP engine with an array of turbojet nozzle exit diameters from 1.57in (40mm) to 0.94in (28mm), with offset from the turboprop exhaust exit between 0.75 inches and 1.75 inches. Additional testing was accomplished to measure static thrust with the different nozzle exit diameters and locations in turboprop mode with 2- and 3-bladed, 20-inch diameter propellers. Turbojet mode was achieved by locking the propeller to prevent rotation. Whereas the turboprop configuration experiences negligible thrust loss across many nozzle diameters and offsets, the turbojet had difficulty generating usable thrust with the propeller locked. Future research should consider rocket-assisted take-off for high-speed flight with a folding propeller, rather than attempting to achieve high-speed flight in a turbojet mode. Follow-on developments should include design and implementation of a mechanism for releasing the folding propeller after high-speed flight.

1. Introduction

When designing an unmanned aircraft in Department of Defense (DoD) unmanned aircraft system (UAS) Group 2 and Group 3, characterized by a Maximum Take-Off Weight (MTOW) between 21 and 1320lb (UAS Task Force Airspace Integration Integrated Product Team, 2011), two major powerplant contenders are a turbojet and a turboprop. These two

systems each have characteristics that are desirable for UAS designers, but are better suited to different mission sets, with turboprops being more optimized for endurance while turbojets are much better for high-speed flight. Naturally, there is a desire for a propulsion system capable of both roles for mission versatility, or for multistage missions. The solution proposed here is a turbine-based variable cycle engine, which can operate both as a turboprop and a turbojet. Study objectives are the exhaust nozzle location and geometry, which theoretically have a large effect on the performance of the system in both modes. The goal is to find a single location and size that causes minimal losses in thrust from both factory turbojet and turboprop configurations.

Background

Both systems have a core of a compressor, combustor, and turbine, but generate thrust in very different ways. A turbojet feeds the energy-rich flow through a nozzle to accelerate it, while a turboprop utilizes a secondary turbine connected to a reduction gearbox to spin a propeller. Below are diagrams of a turbojet and turboprop, respectively. These diagrams use a common convention of station numbers representing components of the cycle. The two stations of most interest to this paper are station 0, the free stream ahead of the engine, and station 9, the exhaust as it leaves the engine.

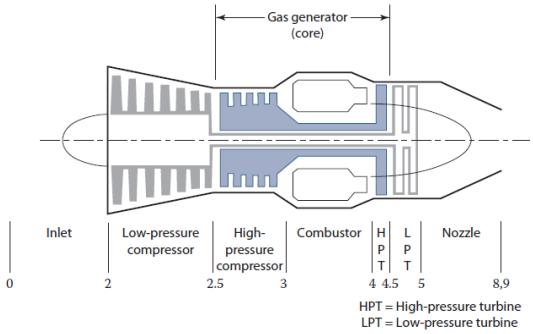

Figure 1: Turbojet Engine Diagram
(Mattingly, 2016)

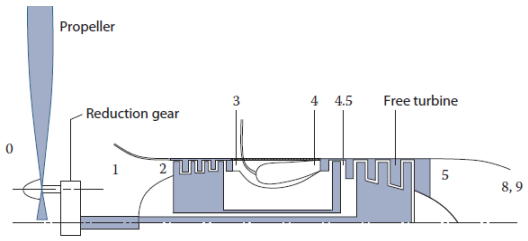

Figure 2: Turboprop Engine Diagram
(Mattingly, 2016)

The two primary figures of merit for engine performance are thrust and thrust specific fuel consumption (TSFC). Thrust is a derivation of Newton's Second Law. It should be noted that conventionally F refers to the uninstalled thrust an engine can produce, whereas T represents the installed thrust an engine makes in an aircraft. In order to remain consistent with the testing of engines on a static stand, our discussion will use uninstalled thrust.

$$F = \frac{(\dot{m}_0 + \dot{m}_f)V_9 - \dot{m}_0 V_0}{g_c} + (P_9 - P_0)A_9$$

(1)

In performing a basic analysis, the force due to the difference in pressures at the freestream and the outlet can be assumed to be zero, as both will be close to atmospheric. This allows us to eliminate the second term in the thrust equation, leaving us with the mass flow and velocity terms, which are effectively momentum terms. For a turbojet engine, the air-fuel mixture coming out of the nozzle is the propulsive fluid that produces thrust. For a turboprop, however, the exhaust velocity difference can be considered negligible for a simple analysis, so the propulsive fluid is the air accelerated by the propeller. For a given size of engine, a propeller can impart more momentum to the propulsive fluid by providing a small acceleration to a large mass flow, whereas a turbojet provides a large acceleration to a small mass flow. In general, a turboprop with an efficient propeller is capable of higher peak thrust than a turbojet with the same core. Another figure of merit is the specific thrust or thrust per unit mass flow rate. This is simply a rearrangement of the previous equation. This quantity is important because it can be used to compare engines regardless of size.

$$F_s = \frac{F}{\dot{m}_0}$$

(2)

Since specific thrust is dependent only on velocity, a turbojet configuration will produce a much higher value than a turboprop. Another important consideration is that thrust specific fuel consumption (TSFC) is inversely proportional to the overall system efficiency. This quantity is read as the rate of fuel mass burned for each unit of thrust produced and is also independent of engine size.

$$TSFC = \frac{\dot{m}_f}{F}$$

(3)

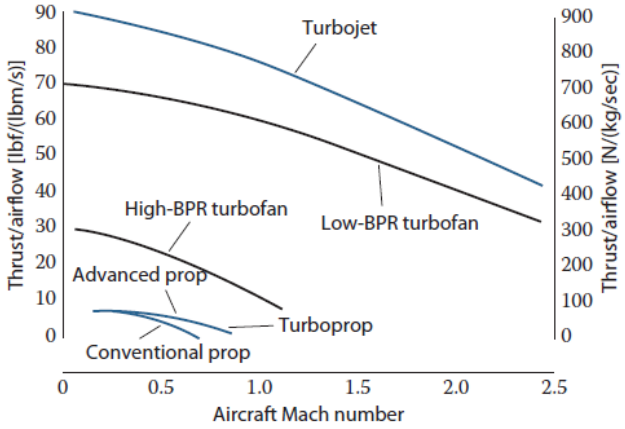

Figure 3: Specific Thrust vs. Velocity for Various Engine Types
(Mattingly, 2016)

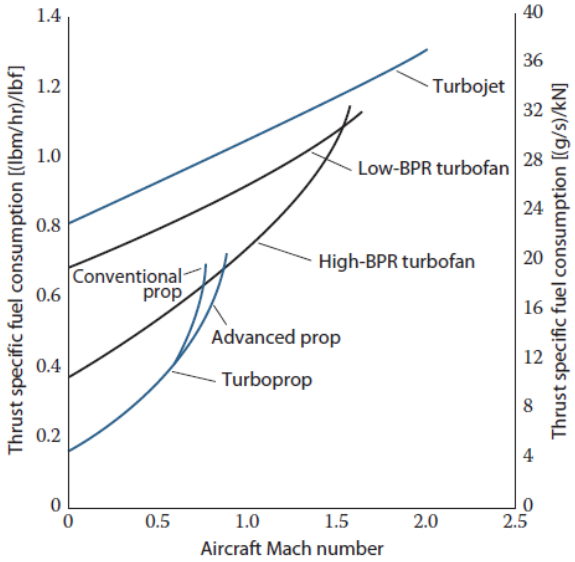

Figure 4: TSFC vs. Velocity for Various Engine Types
(Mattingly, 2016)

From the graphs, it can be seen that a turbojet accelerating a small mass flow to a very high velocity leads to excellent specific thrust and high TSFC, while a turboprop accelerating a large mass flow to a relatively low velocity provides lower specific thrust and TSFC. Turbojets can thus operate at much higher speeds, while turboprops are generally more fuel efficient. However, fixed-pitch propellers are only usable over a range of velocities, limiting the top speed of a turboprop system substantially.

Thusly, for an aircraft that requires the ability to fly at high speeds, a turbojet engine is desirable, while a system that requires high fuel efficiency will be much better served by a turboprop. This naturally poses the question of how to select an engine type for a system that requires both high speed dash and high endurance capabilities. The system proposed here aims to accomplish this by utilizing an off-the-shelf turboprop engine, with the propeller, gearbox, and power turbine locked in a turbojet mode. In order to accelerate the turbojet flow enough to make thrust, area reduction nozzles are added to the exhaust. These nozzles may have an adverse effect on turboprop performance, just as the locked turbine will have on the turbojet mode. However, if both of these losses are small enough to be tolerable in exchange for the added aircraft capability, then optimization of the design should certainly be pursued.

Previous Work

There are many previous studies on variable-cycle turbine engines [Refs. 1, 2, 4, 5, 7, 8, 10-13], that date back to the 1960's. Previous examples of variable-cycle turbine engines typically do not attempt completely switching modes of propulsion generation, but instead vary parameters of a single engine type. Prominent examples include Nascimento and Pilidus' work on selective bleed turbofans (Nascimento, 1992), which allow the bypass ratio to be adjusted in flight to provide higher performance over a greater range of airspeeds. Another notable example is the J58 engine used on the SR-71 Blackbird, which varies the fraction of air that bypasses the combustor and turbine to increase afterburner effectiveness (Olah, 2014).

Project Objectives

The primary variables examined in this project were the nozzle exit diameter and nozzle downstream location, which will be measured using a KingTech K45TP turboprop engine, an affordable and well understood engine also available as a turbojet. The exit diameters would range from 28mm to 40mm, and the offsets would range from 0.5 in to 2 in.

Figure 5: KingTech K45TP Engine in Standard Configuration
(KingTech Turbines, 2022)

2. Experimental Details

Experiments were conducted at the Richmond Hill Research Complex at the north loading dock. A mobile cart was used to support the engine, nozzles, fuel, control, and data collection hardware to allow for transportation without disassembly. The static stand was constructed from T-slot aluminum and was built on a previous test stand design to minimize fabrication time. A linear bearing was used to allow the nozzle subassembly to be moved towards and away from the exhaust outlet, and slotted L-brackets allowed nozzles to be centered in the other two axes. An SPT 70HV-180 servo was used to control the position of the nozzles on the rails. In order to measure and record the thrust, a 100 lb capacity Futek Model LSM300 load cell with a Model USB220 connector was used in conjunction with a laptop computer. To support the engine, structural brackets were designed and fabricated from aluminum flat stock, and fuel, heat shielding, and electronics subsystems were laid out. The engine was controlled and monitored using the factory KingTech ECU and GSU. Both the engine throttle and nozzle servo position were controlled by GT Power Professional Digital Servo Testers. As previously stated, the engine was a KingTech K-45TP series, an 1800g, 316mm turboprop engine with mounting points on each side of the core and surrounding the propeller reduction gearbox. The nozzles themselves were first cast pipe reduction fittings as a proof of concept, but were then laser cut from flats, rolled into the correct shape, and secured with a jewelry welder.

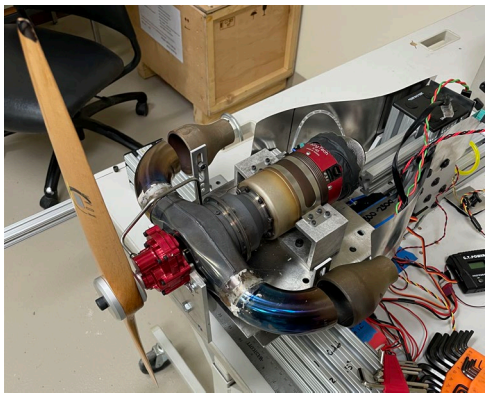

Figure 6: Test Stand with Preliminary Nozzles

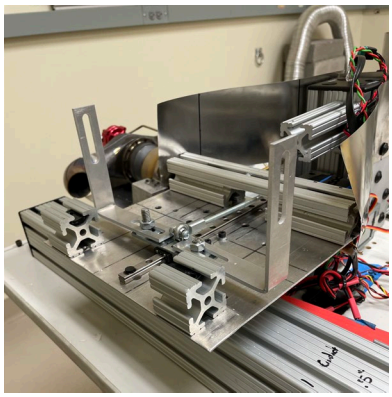

Figure 7: Nozzle Adjustment System

The procedure for collecting thrust data was as follows: The nozzles to be tested were installed, and a debris/fastener check of the engine cart was performed. The cart was then moved to the fuel cabinet above the loading dock, and the tank would be filled based on expected usage. The cart would then be moved into position below the loading dock. Electronics were connected and checked for functionality. Data collection equipment would be connected and initialized. The engine would then be started and allowed to go through its ignition staging procedure until it was operating steadily. Data collection would begin with

the nozzles set to the largest offset to minimize data loss due to back pressure engine failures. The nozzles would then be moved to the first offset being tested and allowed to settle for 10 seconds to approach steady state behavior. The nozzle was then moved to the next position and the process was repeated until all offsets were tested. The engine was then shut down and allowed to cool before the nozzles were replaced with the next diameter to be tested. This process was repeated as needed based on weather and time constraints.

3. Results

Data for both modes was collected at 28mm, 36mm, and 40mm, with turboprop data also being collected for 32mm. Then, a 24mm nozzle was attached directly to the exhaust system and data for both modes were collected.

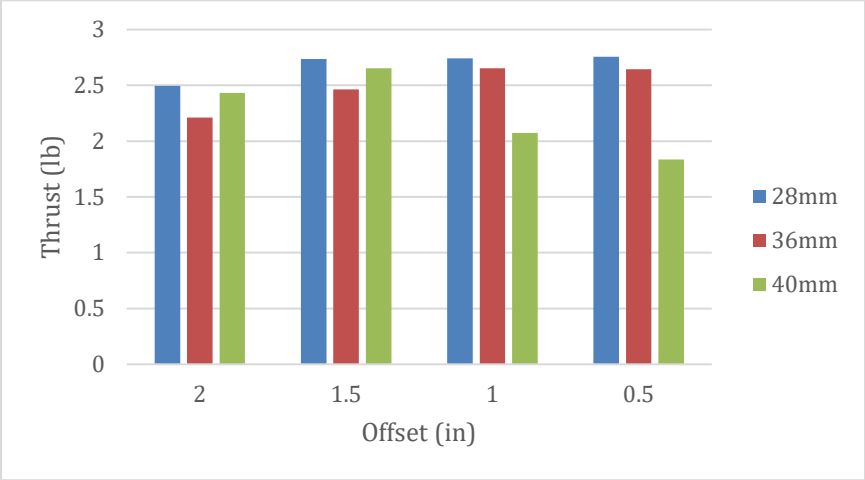

Figure 8: Turbojet Thrust vs. Offset

Figure 8 shows the trust value read after allowing the flow to settle at each offset position for 28mm, 36mm, and 40mm nozzles in turbojet mode. This allows us to establish a general trend of increasing thrust as offset decreases for the 28mm and 36mm, while thrust decreases as offset decreases for the 40mm nozzle. Perhaps more important, it is also clear that there is no thrust data above 3 lb for any of the diameters or offsets tested. Therefore, while there do appear to be different correlations between offset and thrust for different diameters, none of these configurations produce acceptable thrust.

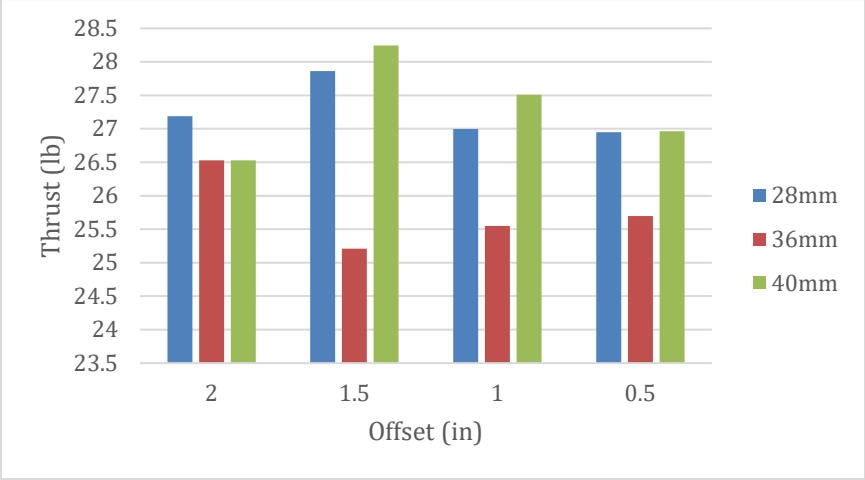

Figure 9: Turboprop Thrust vs. Offset

Figure 9 is analogous to Figure 8 but holds data for the turboprop configuration. Trends for this mode appear to be higher order, with the 28mm and 40mm peaking at an offset of 1.5 in, while the 36mm has a minimum there. This is contrary to the turbojet data, where the 36mm trended with the 28mm instead of opposing both smaller and larger diameters as it does here. We can also see that the range of the data is between 25 and 28.5 lb, well within acceptable thrust for a turboprop of this size.

4. Discussion and Conclusions

Based on the results, the 28mm nozzle appears to have the best turbojet performance, while the 40mm has the best turboprop performance. However, the most thrust that could be generated in a turbojet configuration is only 33.2% of the 10 lb of thrust that a pure turbojet should produce. This calls the utility of the design without substantial modification into question. For future research, use of a controllable locking system as an engine idle setting in conjunction with a folded propellor, allowing for a compact, rocket-launchable turboprop system seems promising. In order to make this concept function as intended, use of variable inlet ducting to bypass the secondary turbine in turbojet mode may also have merit.

5. Summary

In short, this study was an examination of the feasibility of a variable cycle turbojet/turboprop fabricated from an existing design on a small scale. Variables examined were nozzle offset downstream of the exhaust outlet and nozzle diameter. After testing, it has been determined that while the turboprop is capable of workable thrust with many offsets and diameters, the turbojet mode does not make acceptable thrust in any configuration tested. This indicates that bypassing the secondary turbine in turbojet mode is not optional, but that use of this mode as a locked idle position may have use for rocket launched craft.

6. Appendices

6a. Acknowledgements

I would like to thank Dr. and Mrs. Niblack for making this research possible with their generosity, Dr. Rouser for being a constant source of advice and expertise, Trey Schinzler for being an excellent mentor, and the Office of the Vice President for Research, for coordinating and supporting this program.

6b. Papers Published

A poster titled "Effect of Nozzle Configuration on Thrust of a Novel Turbojet Turboprop Engine for Small Unmanned Aircraft" was presented at the 2022 Undergraduate Research Symposium as a result of this work.

6c. Literature Cited

Alan Wood, P. P. (1997). A variable cycle jet engine for ASTOVL aircraft. *Aircraft Engineering and Aerospace Technology*.

Allen, R. D. (1979). General Electric Company variable cycle engine technology demonstrator programs. *15th Joint Propulsion Conference.* Las Vegas: AIAA.

Anderson, J. D. (1999). *Aircraft Performance and Design.* Boston: WCB/McGraw-Hill.

Brown, R. H. (1978). Integration of a variable cycle engine concept in a supersonic cruise aircraft. *14th Joint Propulsion Conference.* Las Vegas: AIAA.

Johnson, J. E. (1996). Variable Cycle Engine Development at General Electric - 1955-1995. In E. T. S. N. B. Murthy, *Developments In High-Speed Vehicle Propulsion Systems* (pp. 105-108). Reston: AIAA.

KingTech Turbines. (2022, 6 3). *KingTech K-46TPG4+.* Retrieved from KingTech Turbines: http://www.kingtechturbines.com/products/index.php?main_page=product_info&cPath=1&products_id=128

Linyuan Jia, Y. C. (2021). Designing method of acceleration and deceleration control schedule for variable cycle engine. *Chinese Journal of Aeronautics*.

Marco A. R. Do Nascimento, P. P. (1991). *the Selective Bleed Variable Cycle Engine.* New York City: The American Society of Mechanical Engineers.

Mattingly, J. D. (2016). *Elements of Propulsion Gas Turbines and Rockets.* Reston, VA: American Institute of Aeronautics and Astronautics.

Nascimento, M. A. (1992). *The selective bleed variable cycle engine.* Cranfield: Cranfield Institute of Technology.

Olah, A. B. (2014). The possibilities of integrated propulsion system. *50th AIAA/ASME/SAE/ASEE Joint Propulsion Conference.* Cleveland: AIAA.

Peter Vyvey, W. B. (2011). Study of an Airbreathing Variable Cycle Engine. *47th AIAA/ASME/SAE/ASEE Joint Propulsion Conference & Exhibit.* San Diego: AIAA.

U. T. J Gronstead, P. P. (2000). Control Optimization of the Transient Performance of the Selective Bleed Variable Cycle Engine During Mode Transition. *Journal of Engineering For Gas Turbines and Power*.

UAS Task Force Airspace Integration Integrated Product Team. (2011). *Unmanned Aircraft System.* Department of Defense.

Ya Lyu, H. T. (2016). A Study on Combined Variable Geometries Regulation of Adaptive Cycle Engine during Throttling. *Applied Science*.

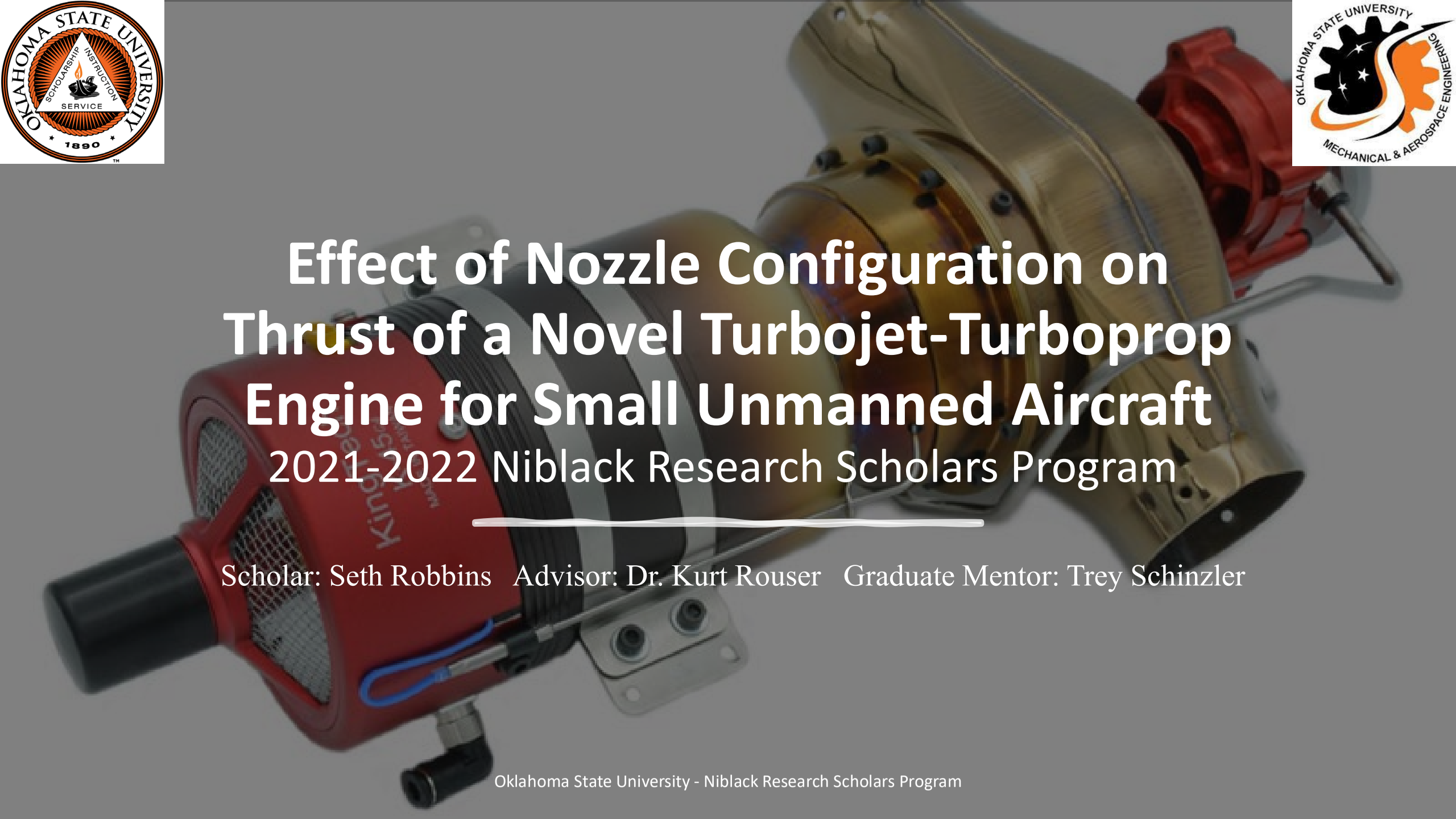

Effect of Nozzle Configuration on Thrust of a Novel Turbojet-Turboprop Engine for Small Unmanned Aircraft

2021-2022 Niblack Research Scholars Program

Scholar: Seth Robbins Advisor: Dr. Kurt Rouser Graduate Mentor: Trey Schinzler

Overview

- This presentation displays the results of testing the effects of nozzle area ratio, nozzle downstream location, propeller shape, and propeller size to determine the feasibility of a variable-cycle turboprop/turbojet powerplant for small unmanned applications
- Based on initial results, it appears that while the turboprop configuration generates excellent thrust across many nozzle diameters and offsets, the turboprop has difficulty generating usable thrust with the propeller's turbine locked in the flow

Motivation

- When designing an unmanned aircraft in Department of Defense (DoD) unmanned aircraft system (UAS) Group 2 and Group 3, characterized by a Maximum Take-Off Weight (MTOW) between 21 and 1320lb, two major powerplant contenders are a **turbojet** and a **turboprop**.
- Both systems have a core of a compressor, combustor, and turbine, but generate thrust in very different ways.
- Turboprop:
  - Utilizes a secondary turbine connected to a reduction gearbox to spin a propeller.
  - More optimized for endurance
- Turbojet:
  - Feeds the energy-rich flow through a nozzle to accelerate it
  - much better for high-speed flight

UAS Groups	Maximum Weight (lbs) (MGTOW)	Normal Operating Altitude (ft)	Speed (kts)	Representative UAS	
Group 1	0 – 20	<1200 AGL	100	Raven (RQ-11), WASP	
Group 2	21 – 55	<3500 AGL	< 250	ScanEagle	
Group 3	< 1320	< FL 180		Shadow (RQ-7B), Tier II / STUAS	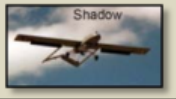
Group 4	>1320		Any Airspeed	Fire Scout (MQ-8B, RQ-8B), Predator (MQ-1A/B), Sky Warrior ERMP (MQ-1C)	
Group 5		> FL 180		Reaper (MQ-9A), Global Hawk (RQ-4), BAMS (RQ-4N)	

Background

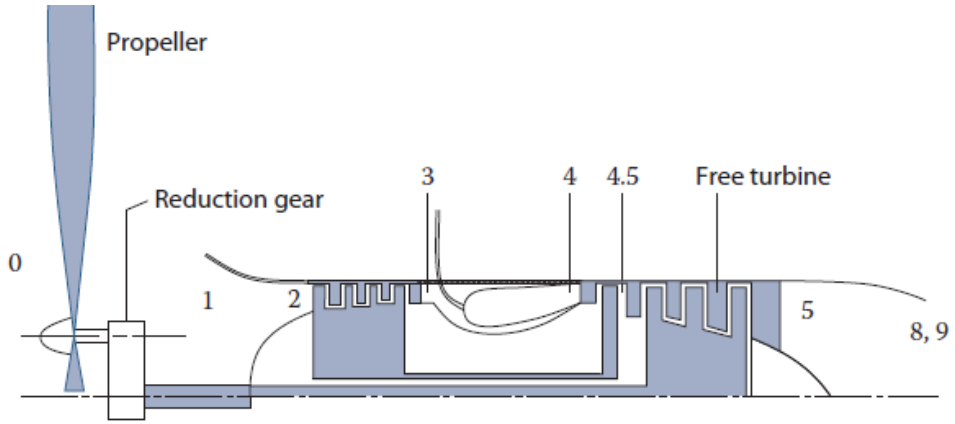

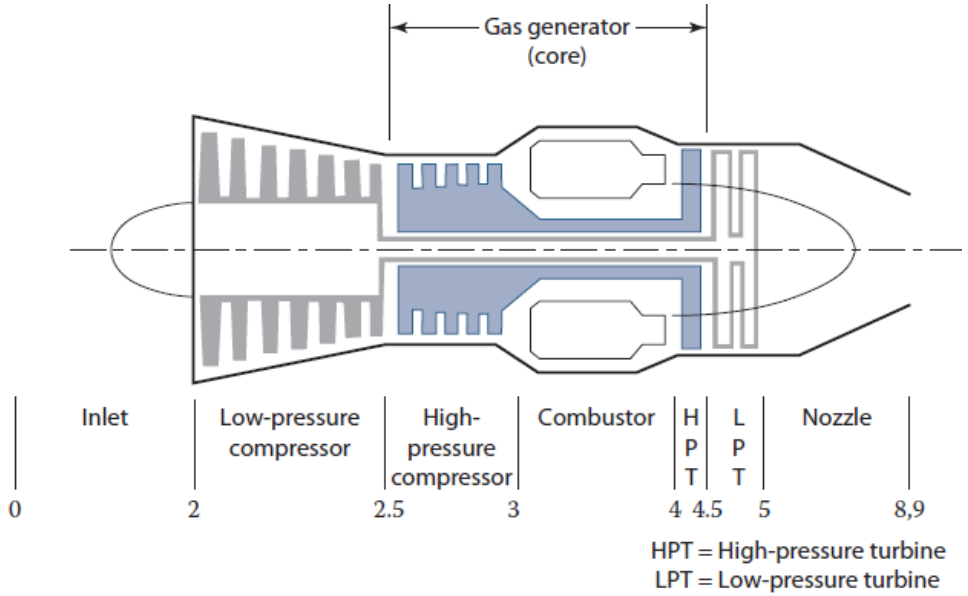

- These diagrams use a common convention of station numbers representing components of the cycle.
- Two stations of most interest:
  - 0, the free stream ahead of the engine
  - 9, the exhaust as it leaves the engine
- The two primary figures of merit for engine performance:
  - T**hrust**
  - **Thrust specific fuel consumption (TSFC)**

Theory

- Thrust equation, general form: $F = \frac{(\dot{m}_0 + \dot{m}_f)V_9 - \dot{m}_0 V_0}{g_c} + (P_9 - P_0)A_9$
- In performing a basic analysis, the force due to the difference in pressures at the freestream and the outlet can be assumed to be zero, as both will be close to atmospheric
- Propulsive Fluid:
  - Turbojet: the air-fuel mixture coming out of the exhaust nozzle
  - Turboprop: the air accelerated by the propeller (the difference between exhaust velocity and free stream is minimal)
- In general, a turboprop with an efficient propeller is capable of higher peak thrust than a turbojet with the same core

Theory

- A second figure of merit is the specific thrust, or thrust per unit mass flow rate: $F_s = \frac{F}{\dot{m}_0}$
  - Can be used to compare engines regardless of size
  - Since specific thrust is dependent only on velocity, a turbojet configuration will produce a much higher value than a turboprop

- Another important consideration is thrust specific fuel consumption ($TSFC = \frac{\dot{m}_f}{F}$)
  - Inversely proportional to the overall system efficiency
  - Rate of fuel mass burned for each unit of thrust produced and is also independent of engine size

Theory

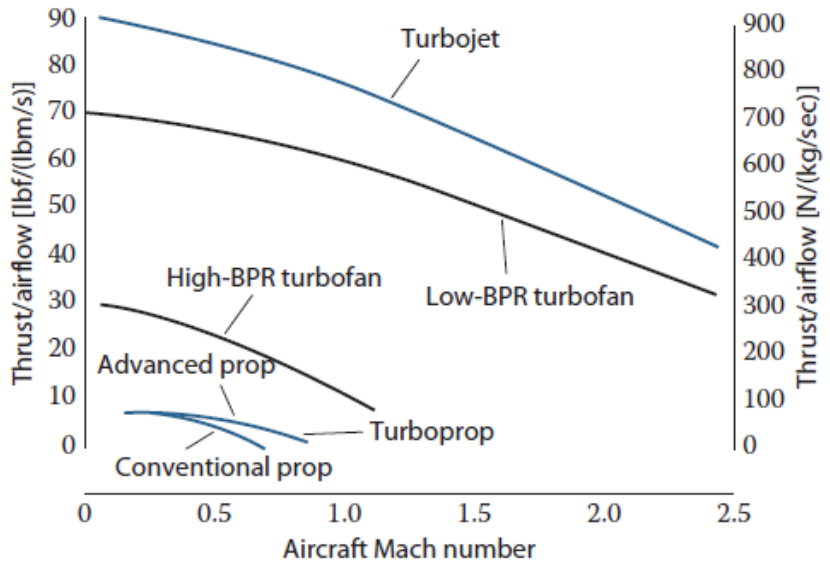

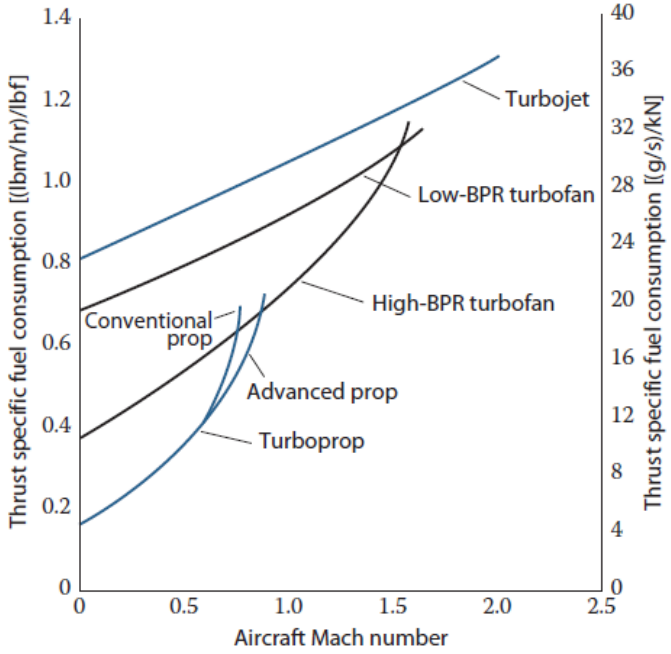

Turbojet:

- Accelerates a small mass flow to a very high velocity—excellent specific thrust, high TSFC

Turboprop:

- Accelerates a large mass flow to a relatively low velocity—lower specific thrust, lower TSFC

The ability to choose high specific thrust or high fuel efficiency at will is very desirable

Arrangement

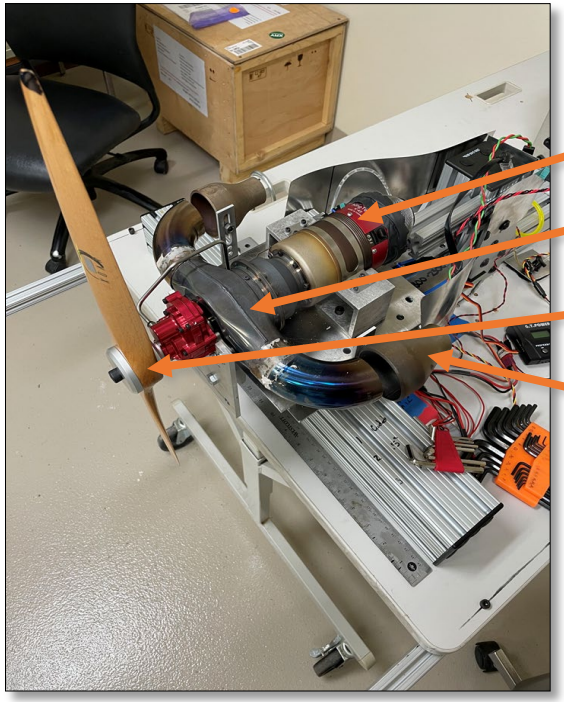

- K45TP engine core
- Exhaust manifold
- 2-blade propeller
- Area reduction nozzles

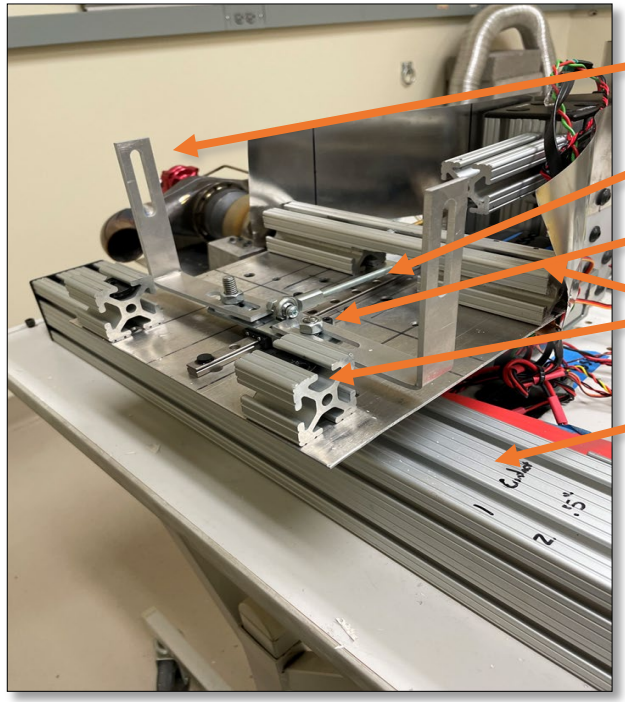

- Nozzle L-brackets
- Servo pushrod
- Bracket subassembly track
- Engine core plate mounts
- Test stand base

Procedure

- Tests performed outdoors using a static test stand and a calibrated load cell with a 6.7 horsepower KingTech K45TP
- A linear actuator was used to adjust the downstream distance of the nozzles
- Nozzle exit diameters of 24mm, 36mm, and 40mm as well as nozzle downstream positions from 0.5in to 2in were used
- Tests were also run with 24mm nozzles directly attached to the exhaust in both modes

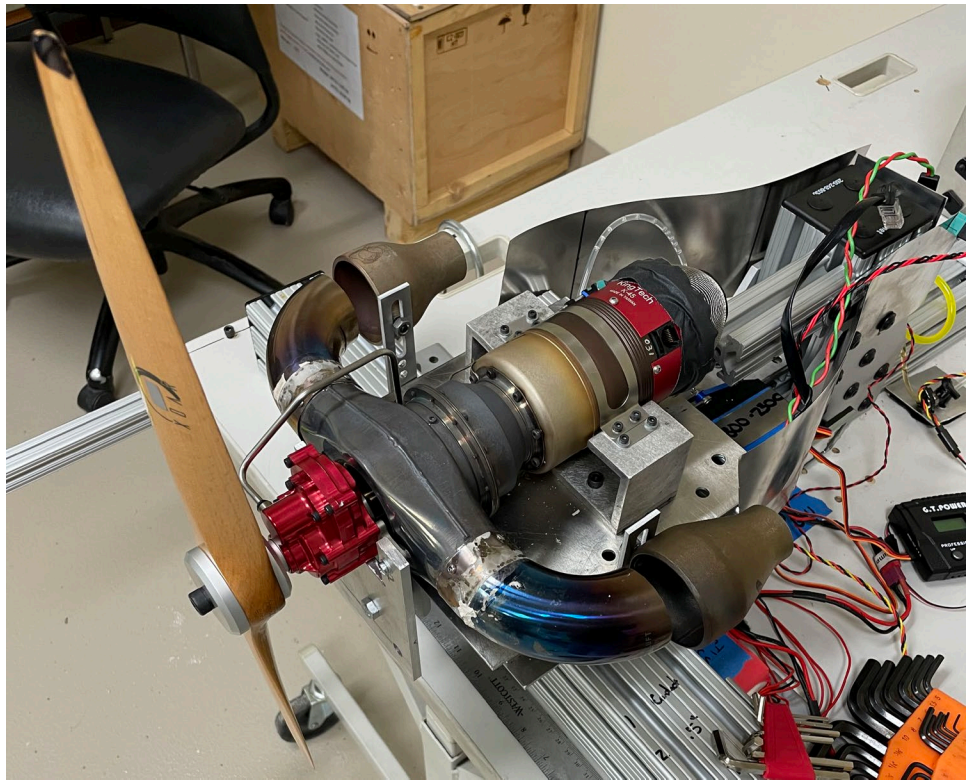

Results

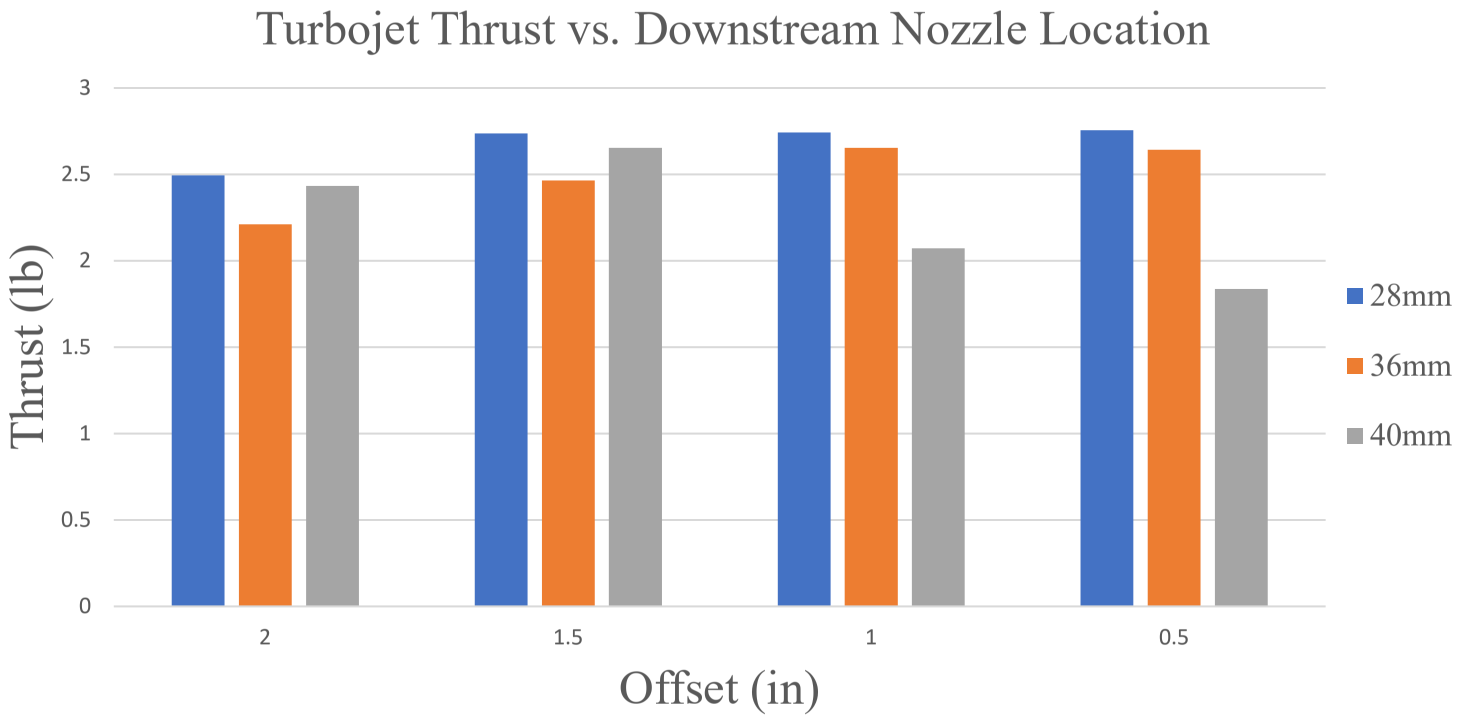

- General trend of increasing thrust as offset decreases for the 28mm and 36mm, while thrust decreases as offset decreases for the 40mm nozzle

Results

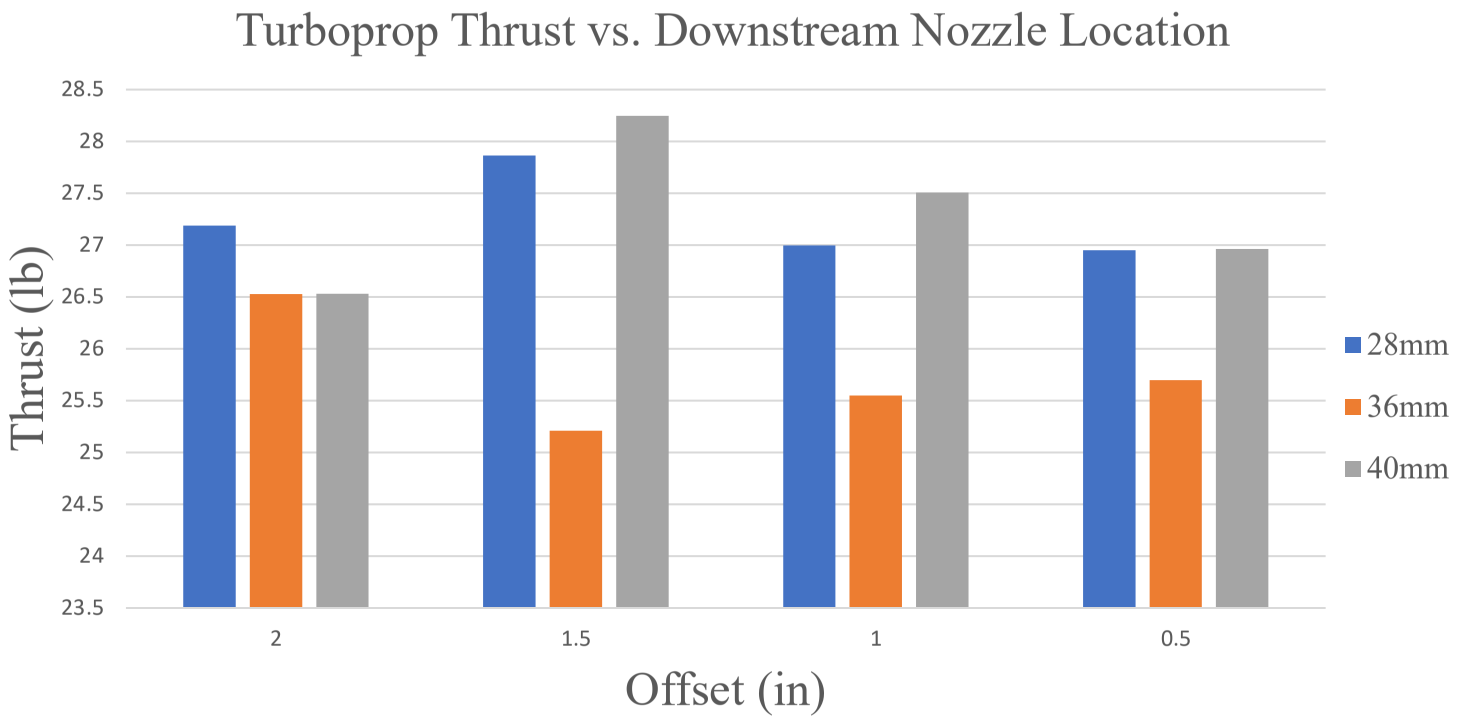

- Most extreme highs for 28mm and 40mm occur at 1.5in of offset, as does the low of 36mm
- The middle diameter displaying a similar but opposite trend to the extremes is interesting

Conclusion

- Based on the results, the 28mm nozzle appears to have the best turbojet performance, while the 40mm has the best turboprop performance
- However, the most thrust that could be generated in a turbojet configuration is only 33.2% of the 10 lb of thrust that a pure turbojet should produce
- Future research:
  - Use of the locking system as an engine idle setting in conjunction with a folded propellor, allowing for a compact, rocket-launchable turboprop system
  - In order to make this concept function as intended, use of variable inlet ducting to bypass the secondary turbine in turbojet mode

Special Thanks

I would like to take this time to thank my sponsor, Dr. Rouser, my mentor, Trey Schinzler, Dr. Johnson as well as the entire Division of the Vice President for Research, and the Niblacks for this incredible opportunity. I greatly appreciate your investment in myself and my professional growth.

References

Alan Wood, P. P. (1997). A variable cycle jet engine for ASTOVL aircraft. *Aircraft Engineering and Aerospace Technology*.

Allen, R. D. (1979). General Electric Company variable cycle engine technology demonstrator programs. *15th Joint Propulsion Conference.* Las Vegas: AIAA.

Anderson, J. D. (1999). *Aircraft Performance and Design.* Boston: WCB/McGraw-Hill.

Brown, R. H. (1978). Integration of a variable cycle engine concept in a supersonic cruise aircraft. *14th Joint Propulsion Conference.* Las Vegas: AIAA.

Johnson, J. E. (1996). Variable Cycle Engine Development at General Electric - 1955-1995. In E. T. S. N. B. Murthy, *Developments In High-Speed Vehicle Propulsion Systems* (pp. 105-108). Reston: AIAA.

KingTech Turbines. (2022, 6 3). *KingTech K-46TPG4+.* Retrieved from KingTech Turbines: http://www.kingtechturbines.com/products/index.php?main_page=product_info&cPath=1&products_id=128

Linyuan Jia, Y. C. (2021). Designing method of acceleration and deceleration control schedule for variable cycle engine. *Chinese Journal of Aeronautics*.

Marco A. R. Do Nascimento, P. P. (1991). *the Selective Bleed Variable Cycle Engine.* New York City: The American Society of Mechanical Engineers.

Mattingly, J. D. (2016). *Elements of Propulsion Gas Turbines and Rockets.* Reston, VA: American Institute of Aeronautics and Astronautics.

Nascimento, M. A. (1992). *The selective bleed variable cycle engine.* Cranfield: Cranfield Institute of Technology.

Olah, A. B. (2014). The possibilities of integrated propulsion system. *50th AIAA/ASME/SAE/ASEE Joint Propulsion Conference.* Cleveland: AIAA.

Peter Vyvey, W. B. (2011). Study of an Airbreathing Variable Cycle Engine. *47th AIAA/ASME/SAE/ASEE Joint Propulsion Conference & Exhibit.* San Diego: AIAA.

U. T. J Gronstead, P. P. (2000). Control Optimization of the Transient Performance of the Selective Bleed Variable Cycle Engine During Mode Transition. *Journal of Engineering For Gas Turbines and Power*.

UAS Task Force Airspace Integration Integrated Product Team. (2011). *Unmanned Aircraft System.* Department of Defense.

Ya Lyu, H. T. (2016). A Study on Combined Variable Geometries Regulation of Adaptive Cycle Engine during Throttling. *Applied Science*.

Questions?

SESSION FOUR:

Garrett Thornton

"Cost-Effective Semiconductor Detection System for Flight Altitude Dosimetry"
Research Area: Physics
Faculty Sponsor: Dr. Eric Benton
Graduate Student Mentor: Tristen Lee

Alex Bias

"Single-Point Modeling of Water Using Spherical Harmonics"
Research Area: Chemistry
Faculty Sponsor: Dr. Christopher Fennell

Andrew Thomas

"Economic Production of Hydrolytic Enzymes Pertinent to Biofuel Production from Overexpressed *Aspergillus nidulans* Transcription Factor and Recombinant Hydrolase Promoter"
Research Areas: Microbiology and Molecular Genetics
Faculty Sponsor: Dr. Rolf Prade
Graduate Student Mentor: Rebekkah Friske-Pope

Cost-Effective Semiconductor Detection System for Flight Altitude Dosimetry

Garrett Thornton

Department of Physics
Faculty Sponsor: Dr. Eric Benton
Graduate Student Mentor: Tristen Lee

ABSTRACT

Crew and passenger exposure to atmospheric ionizing radiation at flight altitudes remains a concern for safe air travel. High-energy cosmic rays entering the atmosphere create showers of secondary particles through which commercial aircraft commonly fly. The fundamental goal of our research is the development of compact and cost-effective detectors for deployment aboard aircraft and the study of secondary cosmic ray particles at flight altitudes. Emphasis has been placed on developing economical replacements for existing detector amplification electronics by creating systems of comparable performance using conventionally-available electronic components. Of concern for this research is the charge-sensitive preamplifier, which collects low-magnitude current pulses induced by incident radiation in a semiconductor sensor and converts them into measurable voltage pulses. Subsequent amplification, shaping, and digitization of signals enables determination of absorbed dose. The charge-sensitive preamplifier is the primary stage of signal amplification and is thus vital for the functionality of ionizing radiation detectors. Our methodology centers on the design and construction of printed circuit boards, along with spectral calibration using known radionuclides. Concurrent testing seeks to determine optimal photodiode-amplifier combinations. Prototypical models effective in the detection of α and β particles are under development and calibration, and successive field testing and deployment is anticipated. The development of compact and economical charge-sensitive preamplifiers should enhance our capacity to study the impacts of atmospheric ionizing radiation at flight altitudes.

1. Introduction

We aim to produce a compact and cost-effective ionizing radiation detector for analysis of the galactic cosmic ray (GCR) environment at aviation altitudes. The prototype uses a silicon PIN photodiode detector head and purpose-built charge-sensitive preamplifier named CSP4. Extant standards of nuclear instrumentation used in charged particle detection are fundamentally limited by cost and size, especially when field applications arise. We thus seek production of a system of comparable detection capabilities at a fraction of the cost and size. A compact ionizing radiation detector could fill the niche of high-altitude dosimetry and address a deficit in the volume of existing data concerning the radiation environment at aviation altitudes [Benton, 2004].

GCRs are high energy charged particles that originate from outside of the solar system. Of these particles, 98% are protons – hydrogen nuclei – and completely ionized nuclei of heavier elements, while 2% are electrons and positrons [Benton, 2004]. GCRs in our galaxy propagate primarily from stellar material and interstellar gases under excitation by nearby supernovae [Friedberg & Copeland, 2011]. Upon entry into the local heliosphere, they are modulated by a fluctuating solar wind composed of charged particles emitted by the sun [Reames, 2017]. And upon entry into Earth's magnetosphere, their trajectories are deflected parallel to the magnetic fields lines, resulting in minimized atmospheric entry in the equatorial regions and maximized entry in the polar regions [Leprince-Ringuet, 1950]. Thus, the cosmic ray flux reaches a maximum in the Arctic region, an area frequented by long-haul intercontinental flights between Europe, Asia, and North America.

When the cosmic rays interact with nuclei of gases in the upper atmosphere, they produce showers of secondary particles composed of muons, neutrons, protons, and various other particles [Friedberg & Copeland, 2011]. These extensive air showers are present at aviation altitudes, and thus pose a concern for humans [Benton, 2004]. Although computer models have been developed to analyze atmospheric cosmic ray flux, there exists a deficit of experimentally collected data from commercial aviation altitudes. Silicon PIN photodiode-based detectors provide a low-cost, high-resolution approach to detecting many of the ionizing particles present in these air showers.

Silicon PIN photodiodes, shown in Figure 1, operate by electron hole-pair generation in response to incident ionizing radiation like α particles, β particles, and high-energy photons such as X-rays and γ-rays [Knoll, 2000]. Electrons liberated by incident radiation are collected out of the detector head by a high-voltage reverse bias [Knoll, 2000]. The number of charge carriers released in a given detection event is proportional to the energy of the incident particle, and thus the output pulse height is linearly related to particle energy [Tsoulfanidis & Landsberger, 2015]. Subsequent analog signal conditioning and digitization enables spectra and absorbed dose data to be collected using photodiodes.

Figure 1. An assortment of silicon PIN photodiodes used in the development of the CSP4 circuit. At left is the Hamamatsu S3590, middle Hamamatsu S5107, and right OSI PIN RD-100.

2. Experimental Details

Our detector requires a photodiode and charge-sensitive preamplifier combination capable of charged particle detection. Verification of prototype circuit operationality necessitates first testing using waveform generators, and second collection of spectra from calibration radionuclides. The schematic of the preamplifier circuit developed for testing is displayed in Figure 2, and the printed circuit board is shown in Figure 4.

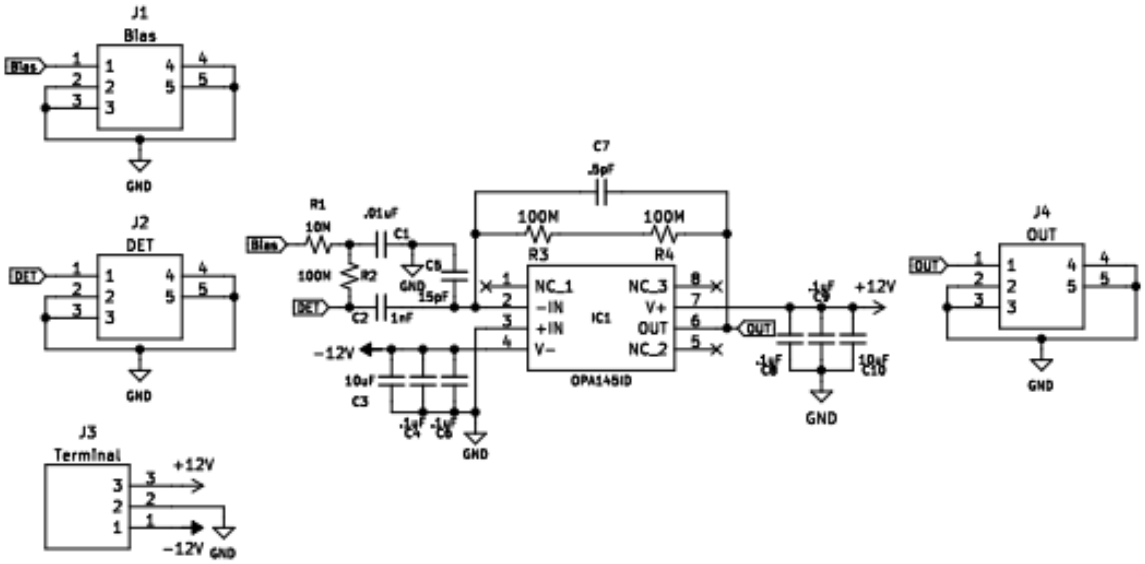

Figure 2. CSP4 circuit developed and tested in this study.

The charge-sensitive component of the CSP4 circuit is the 0.5-picofarad feedback capacitor about the OPA-145 operational amplifier at the center of the schematic. This component converts an input current pulse into a voltage step [Hamamatsu Photonics, 2001]. This voltage step decays exponentially via the 200-megaohm feedback resistor, enabling the circuit to reset for subsequent detection events and resulting in the tail pulse transmitted to the shaping amplifier for further analog signal conditioning. Given the sensitivity of the CSP4 circuit and the small current pulses from the photodiode, the preamplifier must be shielded in a grounded aluminum faraday cage for optimal operation.

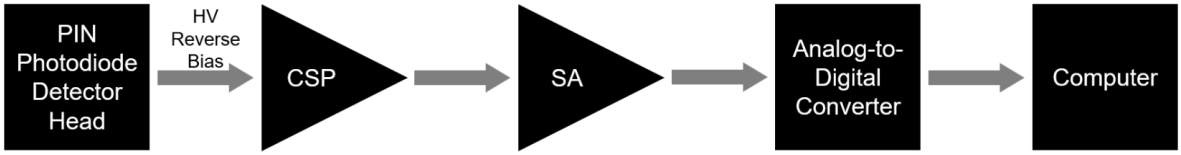

Figure 3. Flowchart of detector functionality.

Spectral testing of the charge-sensitive preamplfier requires an extensive array of external equipment, as shown in Figure 3. An ORTEC 459 high-voltage supply was employed to establish a 70-volt reverse bias across the photodiode, and a Murata +/- 12-volt supply powered the operational amplifier. A pulse shaping amplifier developed by a fellow undergraduate conditioned the signals outputted by CSP4, while an ORTEC 920E MCB operated in a data acquisition and analog-to-digital conversion capacity. The MAESTRO software package was used to log output signals into spectra [ORTEC, 2005].

For the initial wave tests, a 1.225-kilohertz square wave was injected into the CSP4 circuit. The test signal was inserted via a 1-picofarad coupling capacitor connected to the operational amplifier input. Experimental data was collected from an oscilloscope via a BNC cable connected to the circuit output.

For the collection of spectra from radionuclides, a source isotope was placed in direct contact with the photodiode active region. This configuration is ideal for both α particle and β particle detection. The photodiode was directly mounted on the printed circuit board to

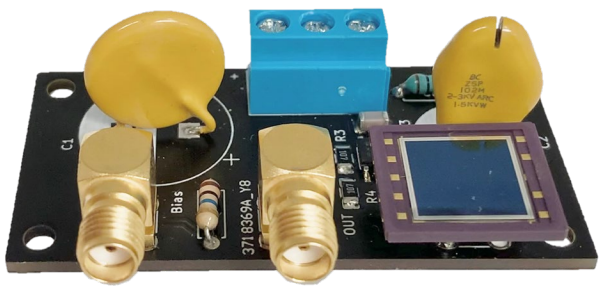

Figure 4. CSP4 printed circuit board with Hamamatsu S5107 photodiode on bottom right.

minimize signal attenuation and electronic noise through extended connections. These tests serve as fundamental assessments of the operationality of CSP4.

3. Results

Provided in Figure 5 are results of the square wave response simulation generated via the LTspice software application [Analog Devices, Inc., 2021]. Each shift in the input voltage signal generates a small current pulse via the 1-picofarad coupling capacitor. Thus, one can test the sensitivity and response of a charge-sensitive preamplifier to small current pulses using a waveform generator.

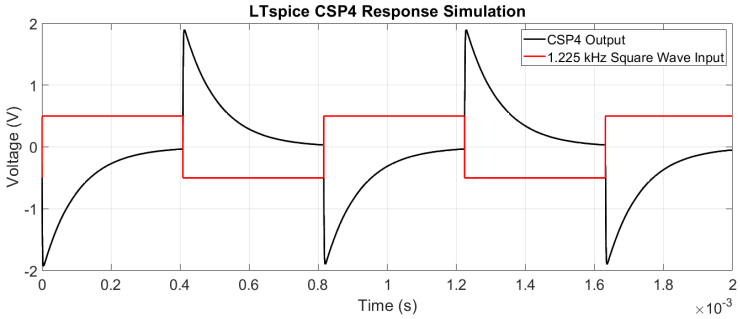

Figure 3. Square wave input (red) and simulated CSP4 response (black).

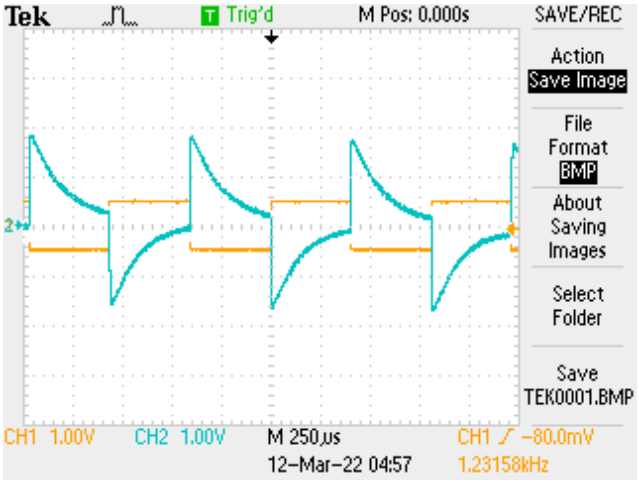

Figure 4. Square wave (yellow) and measured circuit output (blue) as recorded by an oscilloscope.

Figure 6 corroborates simulation and verifies the responsiveness of the circuit to small current pulses. Both the voltage step and exponential decay introduced on page 3 are clearly seen to constitute the circuit response for each current pulse produced by the waveform generator via the coupling capacitor. Given this result, test observations of source radionuclide decay may be undertaken.

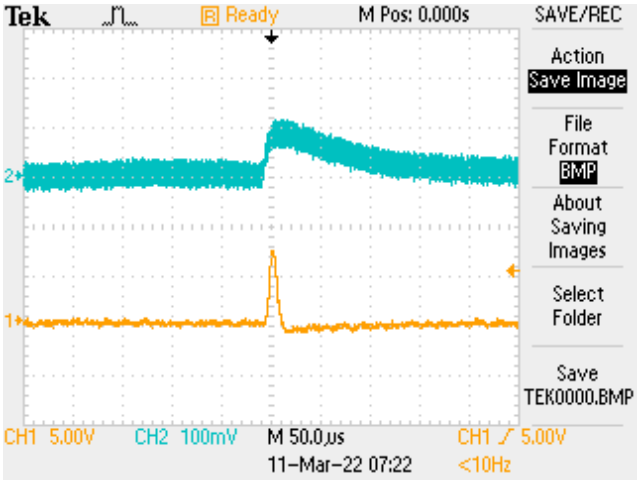

Figure 5. Successful observation of a β particle from the decay of Sr-90.

Displayed in Figure 7 is the tail pulse output of CSP4 (blue) and the processed gaussian pulse from the shaping amplifier (yellow). The CSP4 output once again produces a rapid-rise, exponential-decay pulse as confirmed in the waveform generator test. The gaussian shaping amplifier output is then digitized and subsequently binned by sorting software, enabling the assembly of spectra from a range of incident particles. The voltage amplitude of each gaussian output pulse is linearly related to the energy of its respective incident particle. Thus, a lower energy particle will create a smaller pulse, which is binned in a channel corresponding to a lower energy. A higher energy particle will create a larger pulse, which is binned in a channel corresponding to a higher energy. The relationship between these two channels and the energy of each particle is described via a linear calibration function. The detection event in this figure along with 85,303,199 other such pulses were used in the creation of the spectra in the succeeding figure.

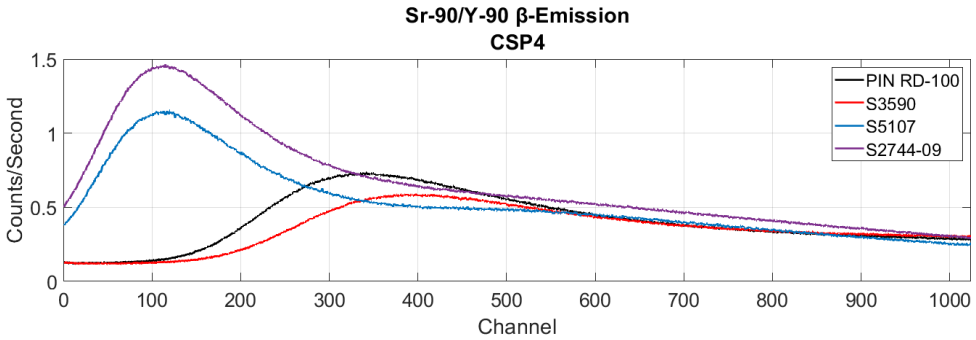

Figure 8. Various energy spectra of Sr-90 β particles assembled using different photodiodes in combination with CSP4.

Figure 8 shows a β spectrum from CSP4. The effects of varying photodiode surface area and capacitance can be seen on count rate and gain. These spectra are of the correct form, thereby verifying the correct operation of CSP4 with regards to β particle detection.

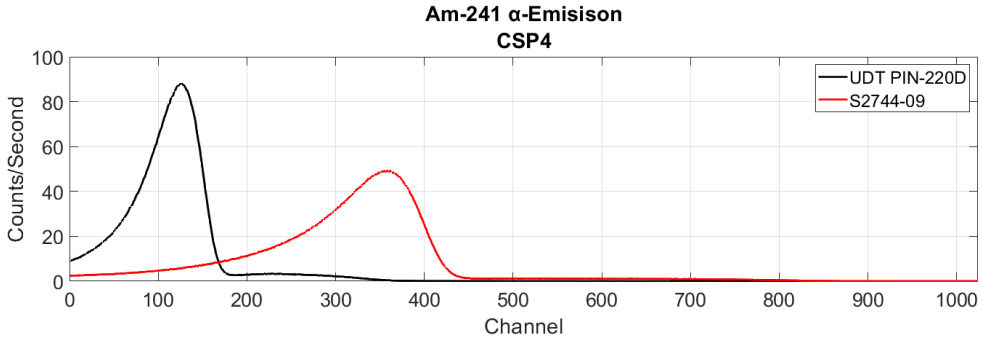

Figure 9. Two energy spectra of Am-241 α particles via two different photodiodes in combination with CSP4.

Figure 9 shows an α spectrum from CSP4. Once again, the effects of characteristics intrinsic to each photodiode are evident on the collected data. These spectra are also of the correct form, showing the ability of CSP4 to detect heavy charged particles like α particles. These results demonstrate that a functional charge-sensitive preamplifier has been developed. Square wave tests have confirmed the desired charge-sensitive response of the developed circuit. Additionally, the circuit has been shown to be capable of charged particle detection via correct observations of α and β particles. The desired voltage pulse response to a detection event has been achieved, and the assembly of these pulses into correct spectra has been performed.

4. Discussion and Conclusions

A compact and cost-effective charge-sensitive preamplifier has been produced for use in a Si PIN photodiode-based aviation dosimeter. Proper operation has been confirmed via waveform generator testing, and its capacity for ionizing particle detection has been demonstrated through effective α and β particle spectroscopy. Additionally, it has been demonstrated to be compatible with extant laboratory hardware and software.

Such a system is ideal for analysis of the ionizing radiation environment at aviation altitudes and in low-Earth orbit. Its small size makes it more deployable across a range of platforms, and its minimized cost makes it more accessible to budget-constrained researchers in academia and industry. By deploying CSP4 on a wide array of airborne platforms, we can more effectively study the exposure of humans to GCRs at aviation altitudes and in space.

Given that Earth is continuously showered by high-energy GCR particles, advances in ionizing radiation detection technology will provide a more informed assessment of human radiation exposure at commercial flight altitudes. A detector capable of analyzing secondary

particle showers could assess the dosages crew members and passengers receive in flight. Such a system would also benefit Astronauts, who are exposed to heavier, more damaging GCR particles in low-Earth orbit than are present in the atmosphere [Friedberg & Copeland, 2011]. CSP4 has been developed to fill the niche of high-altitude ionizing particle detection.

The most pressing application of CSP4 is implementation via the Atmospheric Ionizing Radiation Silicon Detector (AirSiD) platform displayed in Figure 10. This platform consolidates all of the subsystems necessary for atmospheric ionizing radiation detection into a 10 x 10 x 30 cm steel enclosure. An initial test flight aboard a rocket developed by the OSU High-Power Rocketry Team has been conducted in Oklahoma to verify payload integration and deployment capabilities, as shown in Figure 11. Another test flight with the OSU High-Power Rocketry team will soon occur in New Mexico. Subsequent flight platforms for the AirSiD system include Blue Origin's suborbital New Shepard launch vehicle and NASA's WB-57 high altitude research aircraft.

Figure 10. Launch configuration of the AirSiD system with side panel removed for visibility of the interior electronics.

Figure 11. Launch preparations for the inaugural AirSiD test flight.

In addition to test flights aboard rockets and aircraft, a major initiative of future research is development of a more sensitive charge-sensitive preamplifier capable of X-ray fluorescence spectroscopy. X-ray fluorescence occurs when energetic incident photons cause the ejection of an inner-shell electron from an atom [Knoll, 2000]. An upper-shell electron must quickly transition to the lower shell to fill the vacancy, emitting characteristic X-ray photons in the process [Krane, 1988]. Thus, X-ray fluorescence spectroscopy can be employed to identify unknown substances. The system under development is based on the CSP4 platform. It features an upgraded operational amplifier to decrease output pulse rise time and an improved PCB layout to minimize circuit size. A cost-effective charge-sensitive preamplifier capable of X-ray detection could have major implications for both academia and industry.

5. Summary

A small and economical charge-sensitive preamplifier for atmospheric ionizing radiation detection has been developed. Laboratory testing of the system was conducted using waveform generators and calibration radionuclides, and an initial test flight has been completed. An array of suborbital test flights is planned for the near future.

6. Appendices

6a. Acknowledgements

Many thanks to Dr. and Mrs. Niblack for their contribution to this research. Their interest in cultivating undergraduate research through the Niblack Research Scholars program has played an important role in my scientific experience. Learning by doing is fundamental to an impactful and effective education, and the Niblack Research Scholars program facilitates just that.

Thanks to Dr. Kenneth Sewell, Vice President for Research, for his contributions via the Niblack Research Scholars program.

Many thanks to Dr. Christine Johnson, Associate Vice President for Research, for her effective management of the Niblack Research Scholars program and engagement with participants.

Sincere appreciation is expressed to faculty sponsor Dr. Eric Benton for his advice, insight, and unparalleled teaching. He is a major reason I am pursuing my studies in radioactivity and nuclear physics.

Thanks to graduate student mentor Tristen Lee for his advice and assistance. His critiques of presentations and knowledge of electronics have proven very useful to this research.

Thanks to graduate student research collaborator Martin Yang for his advice and input, and especially for his assistance in converting the CSP4 protoboard circuit to a printed circuit board platform.

Thanks to undergraduate research collaborators Ryan Boyce and Conner Heffernan for their cooperation and work ethic. Ryan developed the shaping amplifier used with CSP4, and Conner coordinated with the engineers to launch the detector. They have been a pleasure to work with on this project.

Thanks to the Oklahoma State University High-Power Rocketry Team for flying our detector as an experimental payload on low-altitude test flights.

Many thanks to NASA and Blue Origin for flying our detector as an experimental payload on future high-altitude test flights.

6b. Papers Published

Thornton, G., Boyce, R., and Heffernan, C., 2022. Compact Silicon PIN Photodiode Sensor for Secondary Cosmic Ray Detection at Aviation Altitudes. Virtual presentation: National Conference on Undergraduate Research, 5 April.

Thornton, G., Lee, T., Yang, M., Boyce, R., Heffernan, C., Benton, E. R., 2022. Cost-Effective Semiconductor Detection System for Flight Altitude Dosimetry. Institutional presentation: OSU Undergraduate Research Symposium, Oklahoma State University, Stillwater, Oklahoma, 15 April.

6c. Literature Cited

Analog Devices, Inc., 2021. *LTspice XVII* (17.0.27). [Software]. [Accessed 11 March 2022].

Benton, E. R., 2004. *Radiation Dosimetry at Aviation Altitudes and in Low-Earth Orbit*. PhD thesis. Dublin, Ireland: National University of Ireland, 1-48.

Friedberg, W. and Copeland, K., 2011. *Ionizing Radiation in Earth's Atmosphere and in Space Near Earth*. Washington, D.C.: Federal Aviation Administration, Office of Aerospace Medicine, 5-17.

Hamamatsu, 2001. *Characteristics and Use of Charge Amplifier – Technical Information*. Hamamatsu City, Japan: Hamamatsu Photonics K.K., 3-4.

Knoll, G. F., 2000. *Radiation Detection and Measurement*. 3rd edn. John Wiley & Sons, 15-391.

Krane, K. S. and Halliday, D., 1988. *Introductory Nuclear Physics*. John Wiley & Sons, 276.

Leprince-Ringuet, L., 1950. *Cosmic Rays*. Translated by F. Ajzenberg. New York City, New York: Prentice-Hall.

ORTEC, 2005. *MAESTRO* (6.05). [Software]. [Accessed 11 March 2022].

Reames, D. V., 2017. *Solar Energetic Particles: A Modern Primer on Understanding Sources, Acceleration, and Propagation*. Cham, Switzerland: Springer Nature, 1-110.

Tsoulfanidis, N. and Landsberger, S., 2015. *Measurement & Detection of Radiation*. 4th edn. Washington, D.C.: CRC Press, 219-245.

SESSION FOUR:

Garrett Thornton

"Cost-Effective Semiconductor Detection System for Flight Altitude Dosimetry"
Research Area: Physics
Faculty Sponsor: Dr. Eric Benton
Graduate Student Mentor: Tristen Lee

Alex Bias

"Single-Point Modeling of Water Using Spherical Harmonics"
Research Area: Chemistry
Faculty Sponsor: Dr. Christopher Fennell

Andrew Thomas

"Economic Production of Hydrolytic Enzymes Pertinent to Biofuel Production from Overexpressed *Aspergillus nidulans* Transcription Factor and Recombinant Hydrolase Promoter"
Research Areas: Microbiology and Molecular Genetics
Faculty Sponsor: Dr. Rolf Prade
Graduate Student Mentor: Rebekkah Friske-Pope

Cost-Effective Semiconductor Detection System for Flight Altitude Dosimetry

Garrett Thornton

Faculty Sponsor: Dr. Eric Benton

Graduate Student Mentor: Tristen Lee

E. V. Benton Radiation Physics Laboratory

Department of Physics

Oklahoma State University

Introduction

- Goal: Develop a cost-effective ionizing radiation detector for dosimetry at commercial aviation altitudes and above.
- Of interest is the study of human exposure to air showers created by galactic cosmic rays (GCR).
- High-energy particles that originate from outside the solar system.
- Mainly protons, along with heavier nuclei, electrons, and positrons.
- The cosmic rays interact with gases in Earth's upper atmosphere, producing extensive air showers of secondary particles.
- These air showers penetrate downward through commercial aviation altitudes.

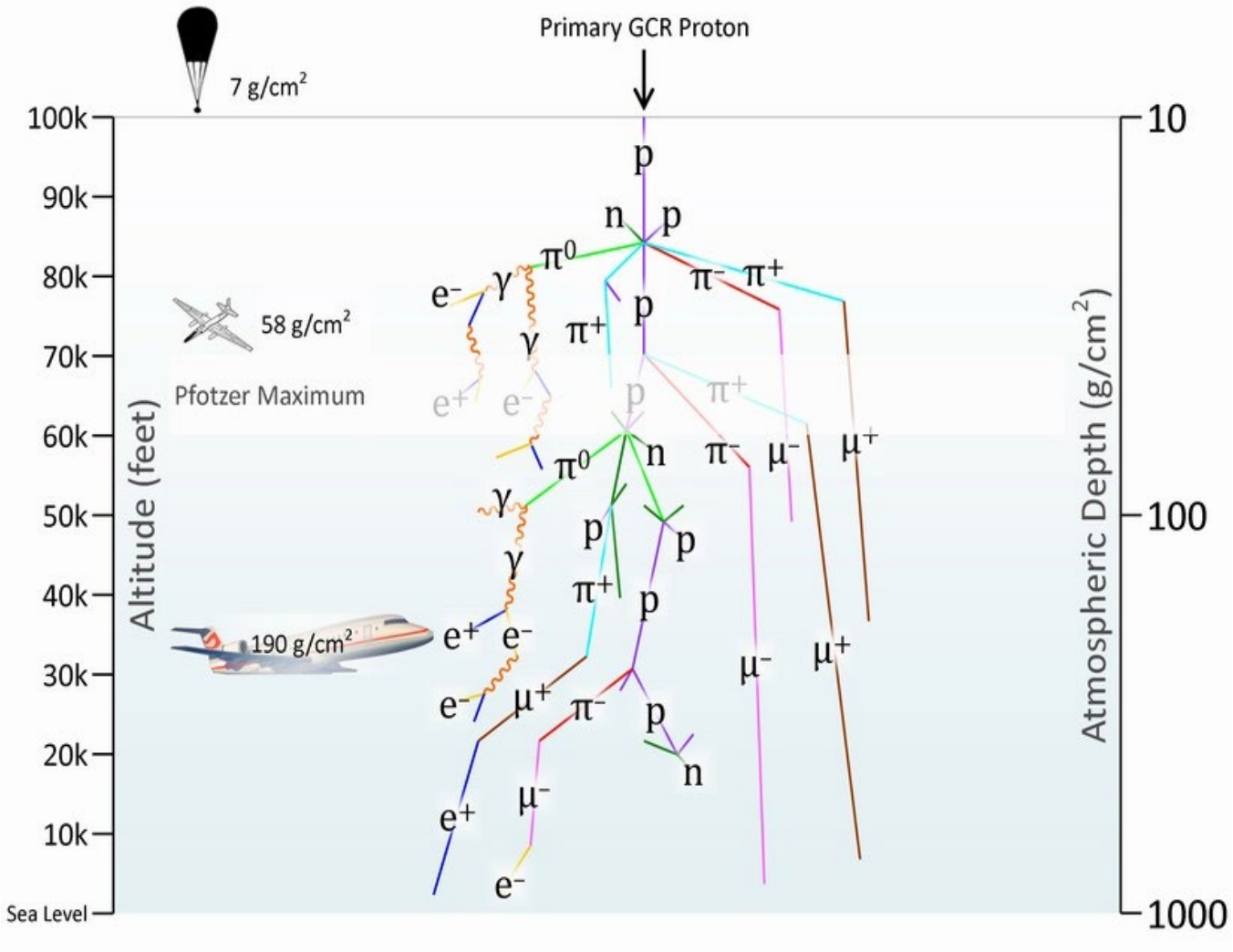

Diagram depicting an extensive air shower.

PIN Photodiodes and CSPs

Silicon PIN Photodiode

- Semiconductor detector head sensitive to charged particles and x-ray/γ-ray photons. (Also visible light and IR wavelengths.)
- Incident radiation generates electron-hole pairs in quantities linearly related to deposited energy.

Charge-Sensitive Preamplifier

- Converts picocoulomb charge pulses from a photodiode into millivolt tail pulses via a small valued feedback capacitor.
- Sensitivity requires enclosure in a grounded, light-tight compartment.
- Output pulses delivered to shaping amplifier for further analog signal conditioning.

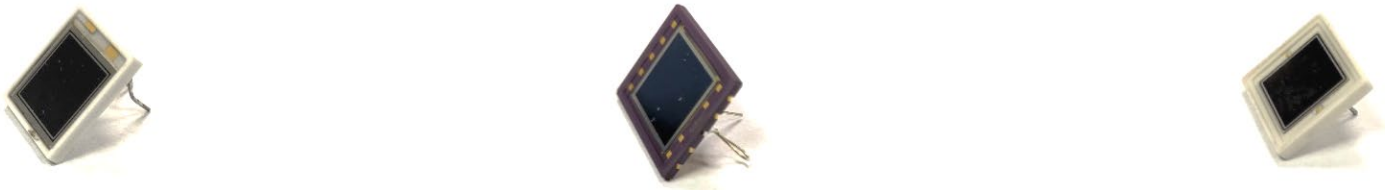

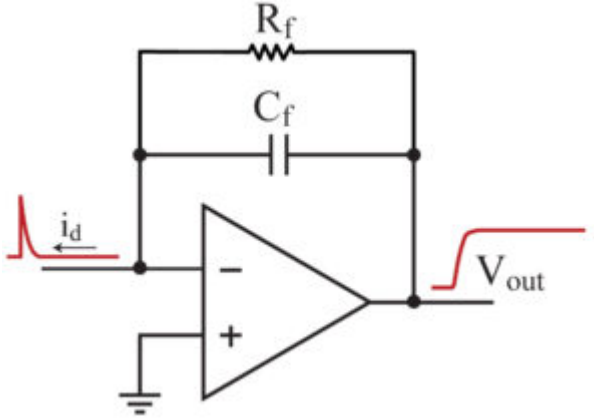

Generalized charge amplifier concept. (Credit: Cremat)

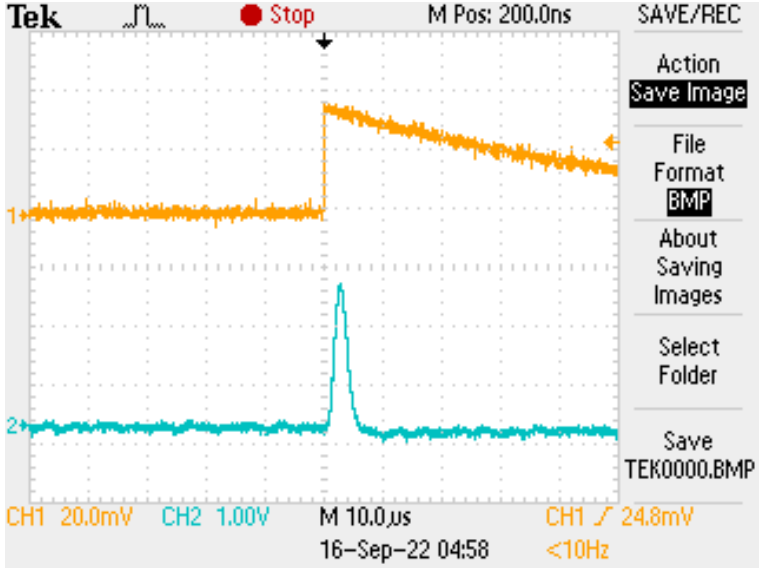

Measured CSP5 response to Sr-90/Y-90 β-particle (top) along with gaussian shaping amplifier output (bottom).

CSP4

Design Attributes

- Compact PCB Format
- OPA145 Operational Amplifier
- 200 MΩ Feedback Resistor
- 0.5 pF Feedback Capacitor
- SMA-Compatible Output
- ~10 µs Rise Time

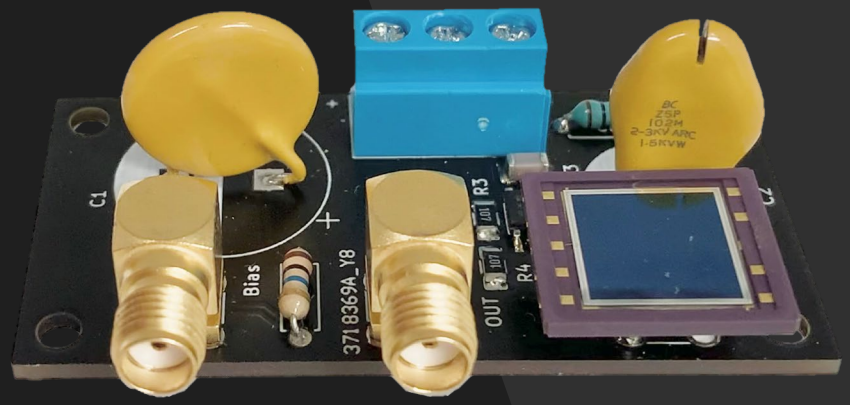

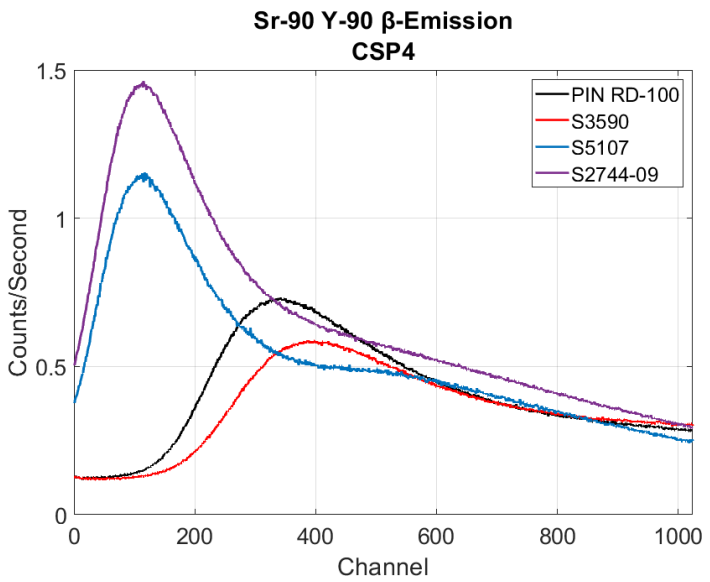

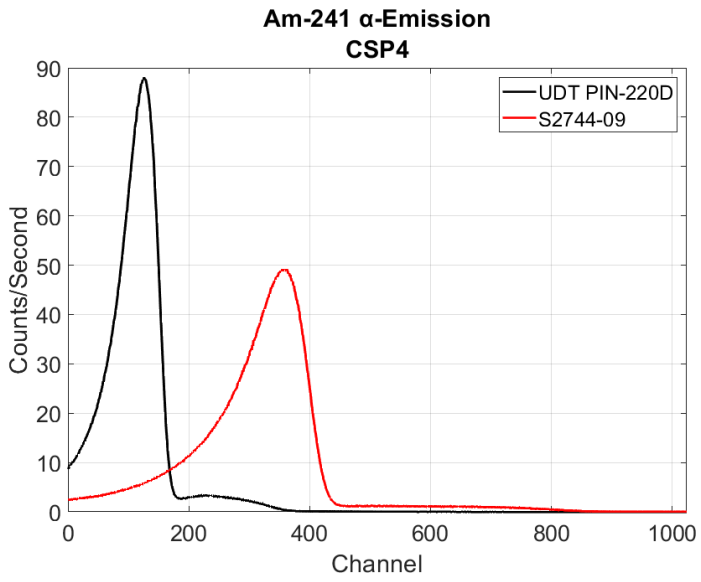

Demonstration of charged particle detection by CSP4 using a variety of photodiodes. At left are spectra of β-electrons emitted by a Sr-90/Y-90 source. At right are spectra of α-particles emitted by an Am-241 source.

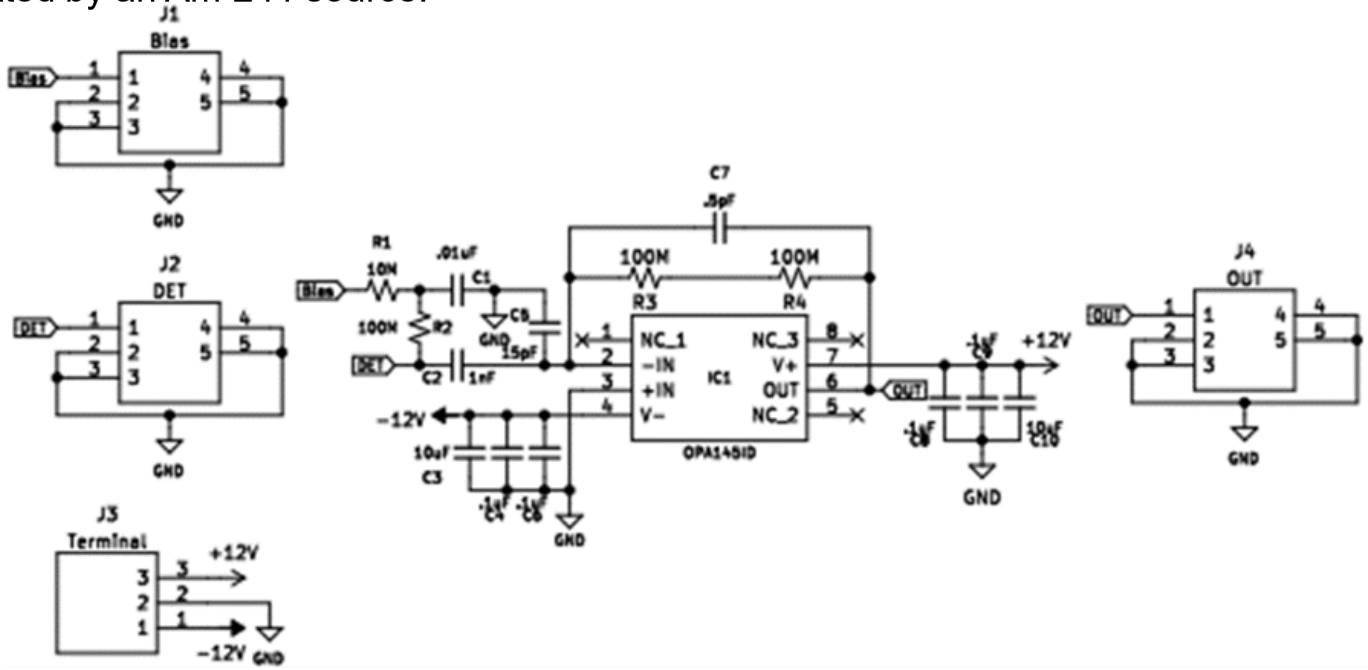

Schematic diagram of the CSP4 PCB. (Credit: Martin Yang)

CSP5

Design Attributes

- Compact PCB Format
- OPA657 Operational Amplifier
- 50 MΩ Feedback Resistor
- 1 pF Feedback Capacitor
- BNC-Compatible Output
- ~30 ns Rise Time

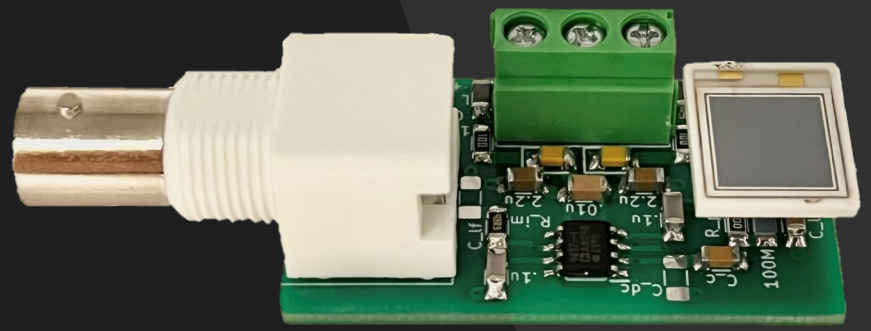

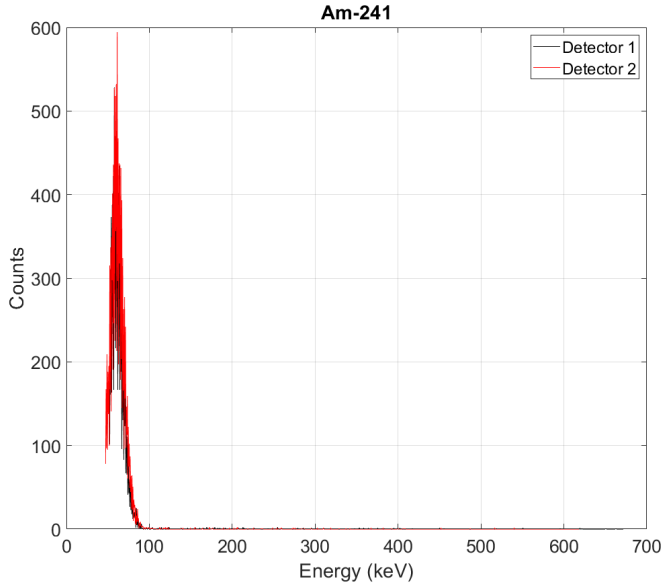

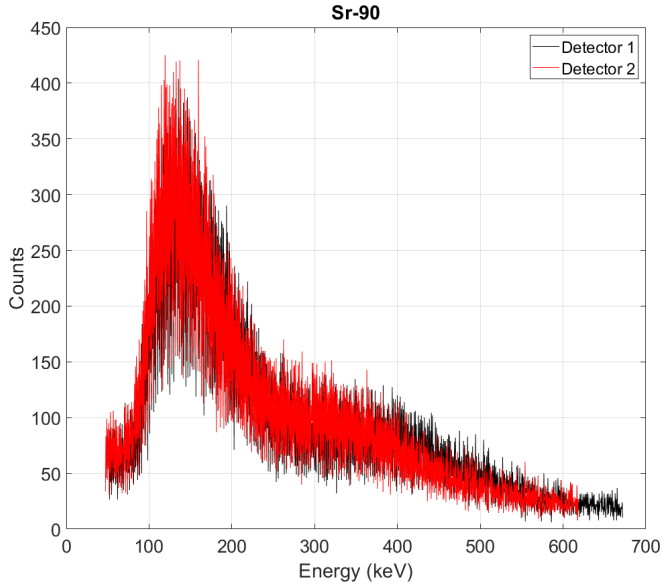

Calibration data from the dual-channel AirSiD 3.0 detector employing CSP5 charge amplifiers. Detection of γ-rays and β-electrons is demonstrated. Data collected via a Red Pitaya ADC.

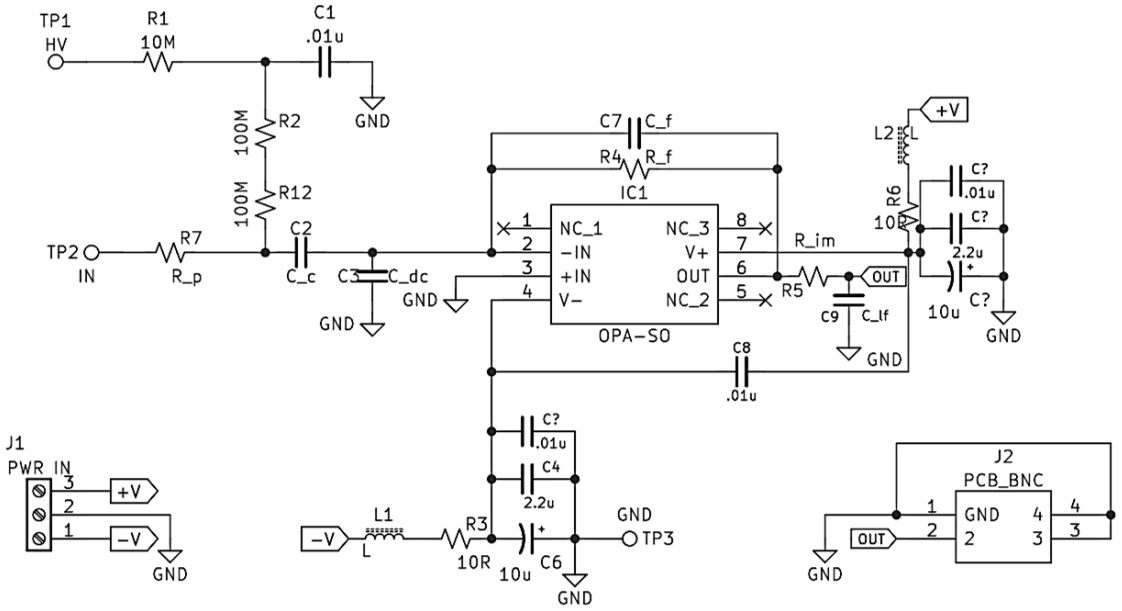

Schematic diagram of the CSP5 PCB. (Credit: Martin Yang)

AirSiD 1.0

Contents

- Cremat CSPs
- OSURPL Shaping Amplifiers
- Commercial DC-DC Power Converters
- Battery Power Supply

Requirements

- Compact 3-U CubeSat form factor for sounding rocket payload integration.
- High g-force/temperature survivability.

Test Flight

- Launch from OSU Unmanned Aircraft Flight Station to test payload survivability for subsequent Spaceport America flight.
- Parachute deployment anomaly caused 100 ft/s impact.
- Data recovered. Electronics survived and were successfully re-flown.

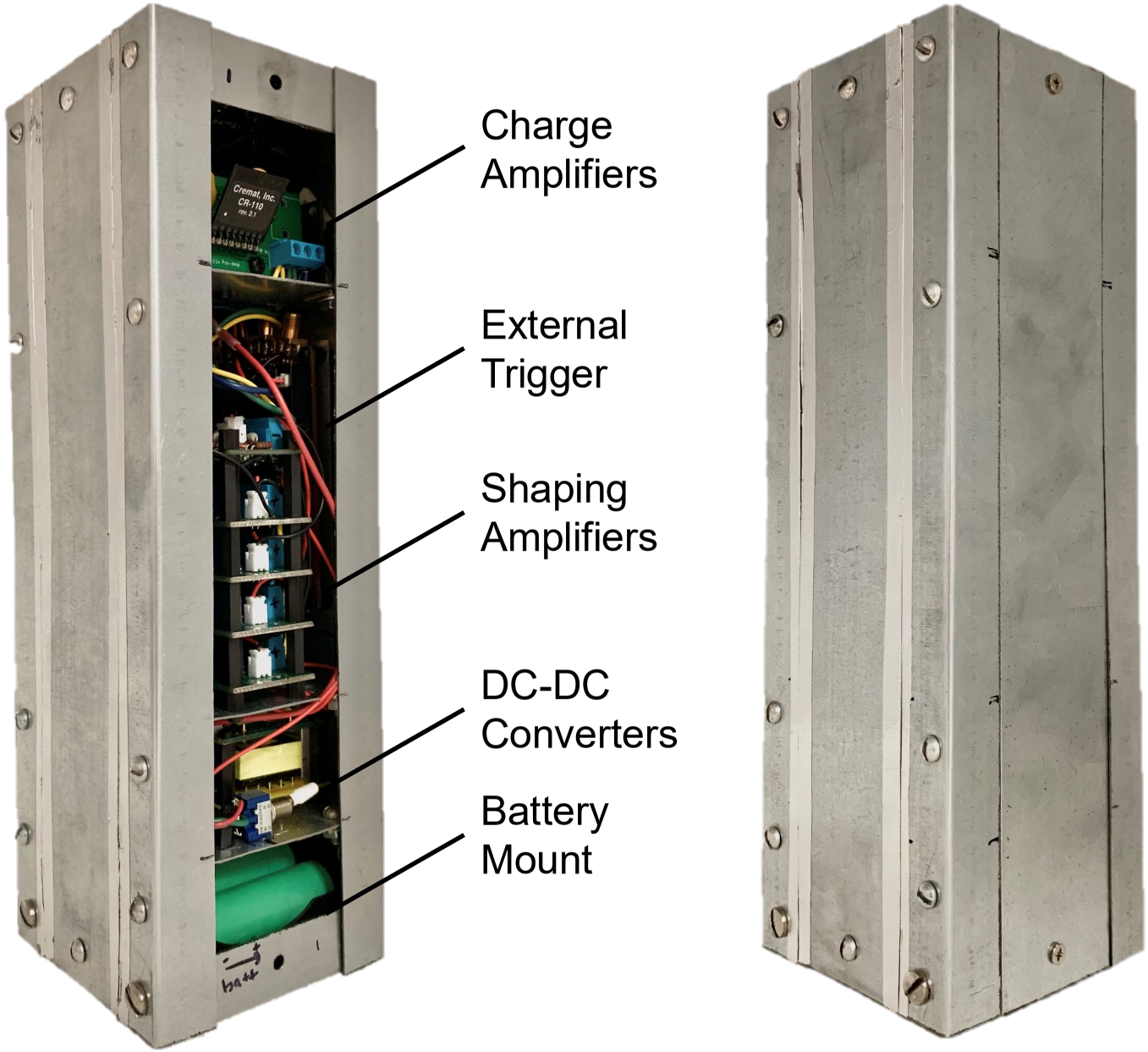

AirSiD 2.0

Contents

- CSP4 Charge Amplifiers
- OSURPL Shaping Amplifiers
- Commercial DC-DC Power Converters
- Battery Power Supply

Requirements

- Same form factor constraints and environmental survivability requirements as AirSiD 1.0.
- Added necessity for long-duration standby power capacity.

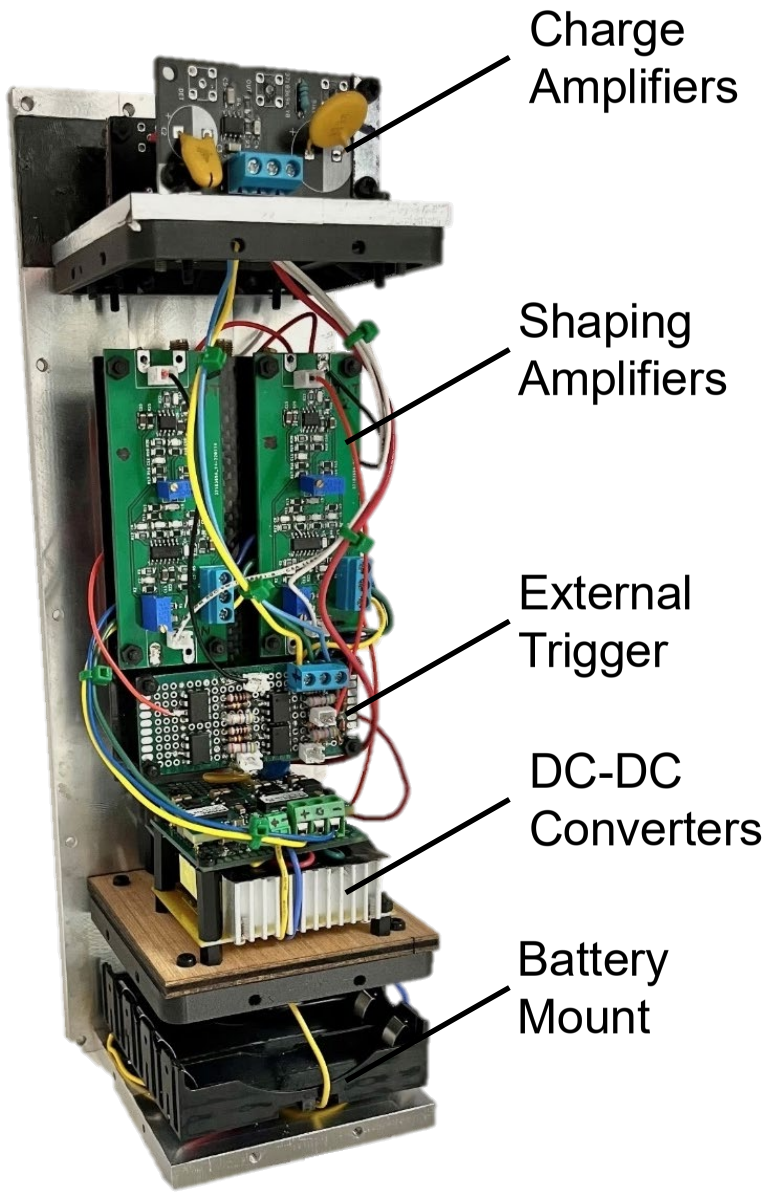

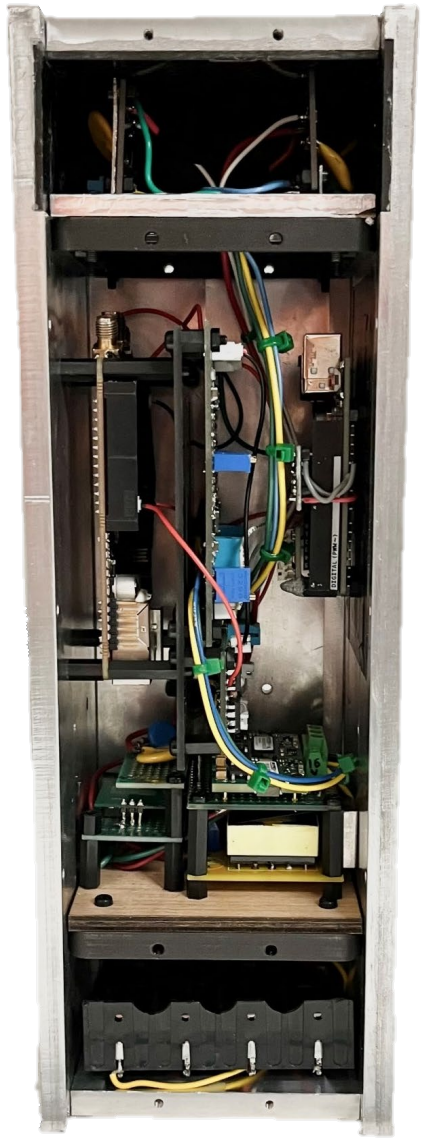

AirSiD 2.0 Spaceport America Flight

- Collaboration with OSU High-Power Rocketry Team.
- 23 June 2022, Truth or Consequences, NM
- Apogee: 3702 m (12,145 ft) ASL
- Maximum Acceleration: 13.99 g (137.29 m/s²)
- Maximum internal payload temperature: 60 °C (140 °F)
- Flight Duration: 138 s

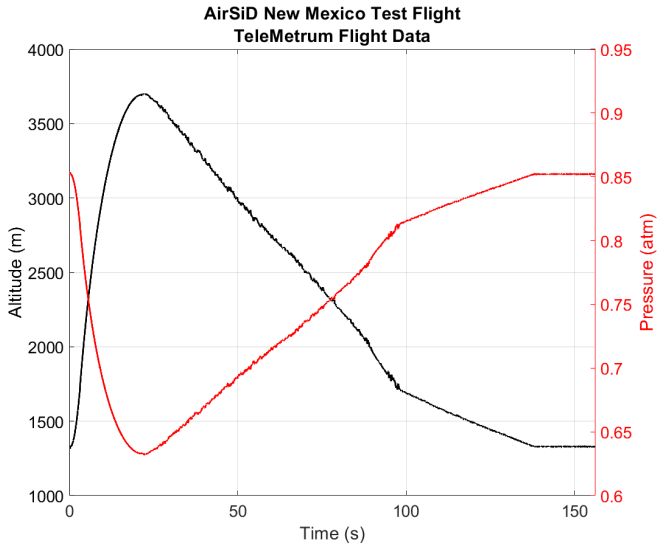

Flight telemetry data comparing rocket altitude and atmospheric pressure.

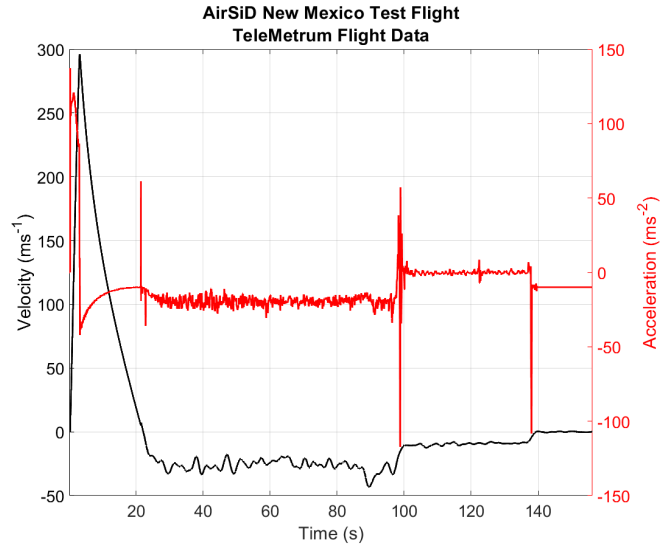

Flight telemetry data comparing rocket velocity and acceleration.

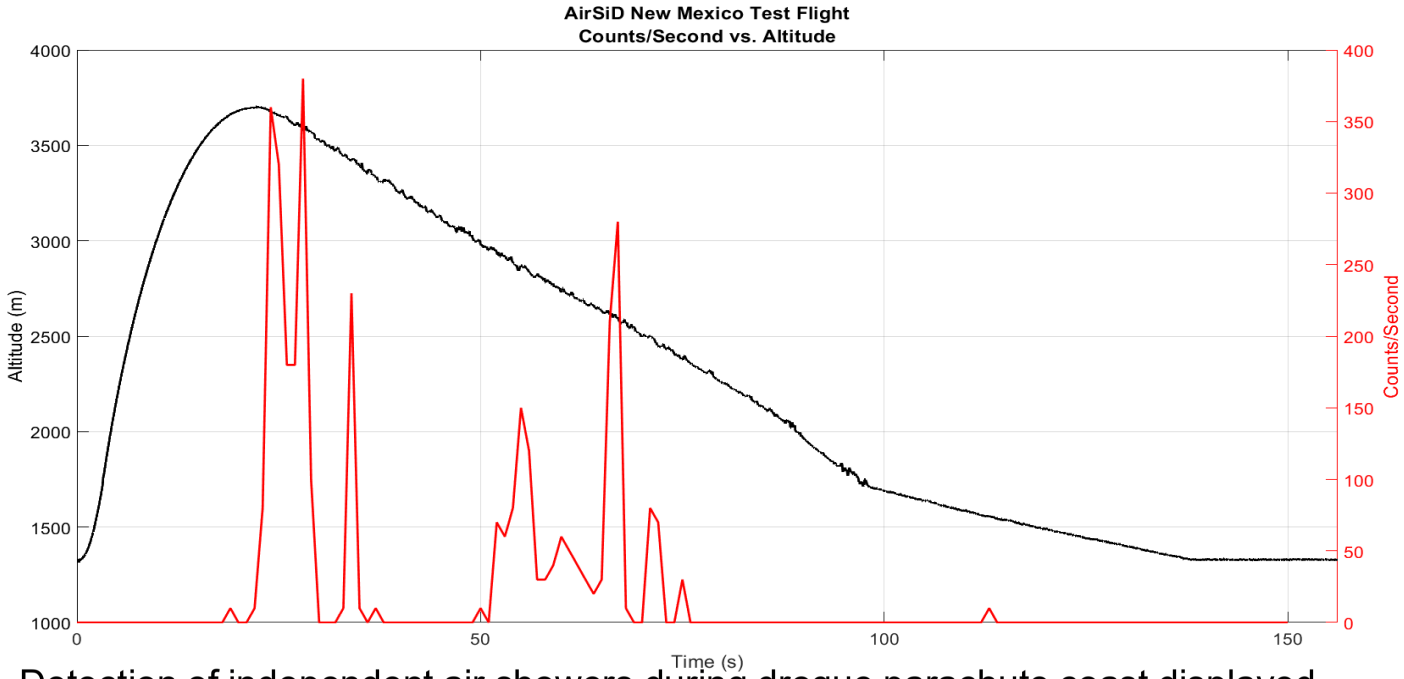

Detection of independent air showers during drogue parachute coast displayed with simultaneous reference altitude.

Tahoma Photography 202

Tahoma Photography 202

AirSiD 3.0

- Designed for solar balloon flights.
- Tested at Los Alamos National Laboratory’s Neutron Science Center.
- Custom-built steel enclosure with dual-channel CSP5 setup.
- High-voltage supplies integrated within enclosure and shielded inside grounded copper shells.
- Externally mounted OSURPL-developed shaping amplifiers and power distribution board.
- Entire stack designed with Red Pitaya screw-hole spacing in mind, enabling direct attachment.

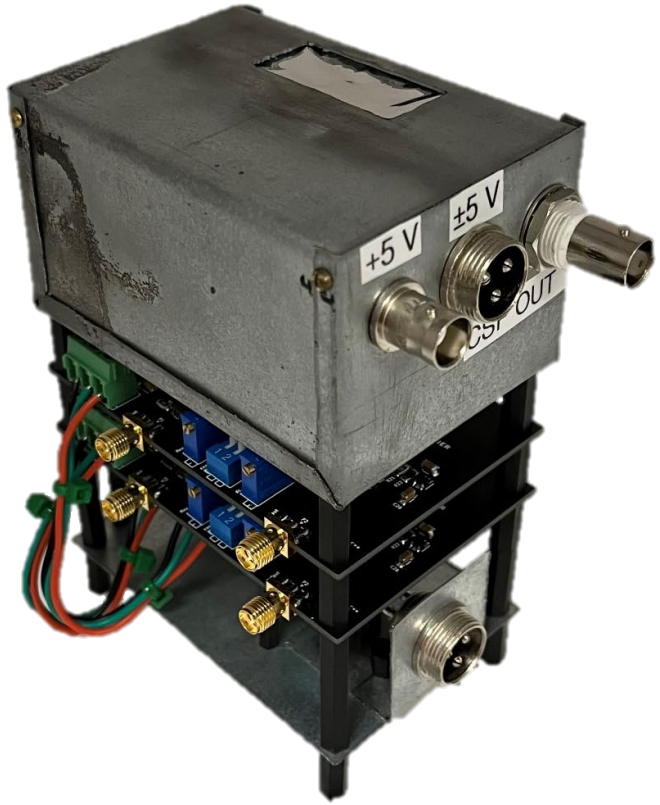

Conclusions

- A compact and cost-effective solid state aviation dosimeter has been developed.
- Functionality of the CSPs demonstrated with calibration spectra and test flights.
- High-altitude tests planned for the near future.

Further Tests

- Solar balloon flights via OSU MAE.
- HIMAC heavy ion accelerator in Chiba, Japan.
- New Shepard flight from Van Horn, TX.
- International Space Station via Falcon 9 and Crew Dragon.
- WB-57 high-altitude flights via NASA JSC.

OSU MAE solar balloon of the type that will fly AirSiD 3.0.

Acknowledgements

- Dr. John and Heidi Niblack
- Dr. Christine Johnson
- Dr. Kenneth Sewell
- Faculty Sponsor Dr. Eric Benton
- Graduate Student Mentor Tristen Lee
- Martin Yang
- Ryan Boyce and Conner Heffernan
- OSU High-Power Rocketry Team
- NASA
- Blue Origin

Still image from GoPro footage of the New Mexico detector flight (Credit: GoPro). Many thanks to the OSU High-Power Rocketry Team for facilitating this flight.

Single-Point Modeling of Water Using Spherical Harmonics

Alexandria Bias

Department of Chemistry
Faculty Sponsor: Dr. Christopher Fennell

ABSTRACT

Three-point models are currently the most used water models to best balance efficiency and accuracy. A single-point model for molecules is a benefit to computational research because it will allow higher efficiency in simulations and calculations. The use of spherical harmonics allows a single-point model to have directionality, which is important in appropriately modeling certain molecules. By targeting variables only for strength of intermolecular interaction and size, spherical harmonic water accurately approximates the behavior of water found through experimental data. Using a narrower interaction function allows for spherical harmonic water to create hydrogen bonds in a more realistic way, creating a more organized structure which is expected based on experimental data. An accurate single-point model for water will aid in computationally linking the microscopic and macroscopic worlds by reducing the amount of resources required for simulations addressing this connection.

1. Introduction

The most used water models in computational chemistry research are rigid three-point models because they are considered the most efficient currently used models. One widely used model is TIP3P, which is a three-point model placing one point on the oxygen with a negative charge and one point on each hydrogen with a partial positive charge. TIP4P is a similar model that adds an additional point between the two hydrogen atoms for a total of four points and TIP5P has two points more than TIP3P for the lone pair of electrons and a total of five points. These and other common rigid models tend to optimize the geometry of a water model to target specific relevant experimental bulk properties of water, particularly liquid water. This comes with much difficulty, as even small changes in geometry may drastically change certain parameters and current optimization strategies typically only capture a few bulk parameters or these parameters in specific temperature or pressure ranges (Izadi 2016).

Much research continues to be focused on improving three-point models, but a single-point model may provide an alternative solution. Using spherical harmonic equations allows a model to be built from the foundational interactions of water while retaining the geometric directionality that three-point models currently aim to accurately portray. By reducing a water model from three points to just a single point, the computational efficiency is improved by an order of magnitude, and as more molecules are added, the reduction in computational cost is exponential. A successful single-point model could not only address the struggle with widespread accuracy three-point models continue to experience, but also change the standard of efficiency for molecular modeling.

Spherical harmonic equations have been established for intermolecular interactions, including hydrogen bonding and Leonard-Jones potential. These functions allow the intermolecular interactions of a molecule to be parameterized around the surface area of a sphere based on size and interaction strength. **Equation 1** and **Equation 2** show the established spherical harmonic equation for Leonard-Jones potential and hydrogen bonding respectively (Price, 1984 and Bratko, 1985).

$$V_{LJ} = 4\epsilon_{LJ}\left[\left(\frac{\sigma_{LJ}}{r_{ij}}\right)^{12} - \left(\frac{\sigma_{LJ}}{r_{ij}}\right)^{6}\right] \qquad \textbf{Equation 1}$$

$$V_{HB} = v_0 \cdot \left(cos(\theta)cos(2\phi)sin^2(\theta)\right) \qquad \textbf{Equation 2}$$

The most similar water model to the one being developed through this work is the soft sticky dipole (SSD) model. This is a single-point model that uses the forces and torques created by intermolecular interactions to simulate the behavior of water using the spherical harmonic equations used by Price and Bratko. This model was found to not only increase efficiency, but also improve upon the TIP3P model in accuracy to experimental values of most dynamical properties (Chandra 1999).

There is still room for improvement in the established spherical harmonic equations because they do not exactly capture the intermolecular interactions of water. Particularly, these equations create an interaction that behaves like a negative hydrogen bond as shown in **Figure 1**, which is not representative of true hydrogen bonding and the intermolecular interaction of water. By transforming the spherical harmonic equation for hydrogen bonding in the form shown in **Equation 3**, the curve may be smoothed, reducing the negative hydrogen bonding phenomenon.

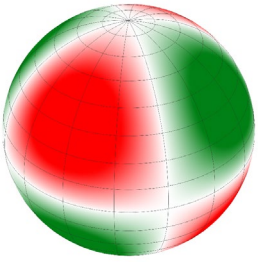

Figure 1

$$V_{HB} = aV_{HB} - bV_{HB}{}^2, \qquad a + b = 1 \qquad \textbf{Equation 3}$$

Water is an important molecule of focus because it continues to be widely studied due to the complexities that are still not understood. Particularly, there is a struggle with understanding the connection between the microscopic interactions of water and the macroscopic formation of complex ice structures such as snowflakes. Studies of this nature are widely outside of the current computational reach, so increasing the efficiency of molecular modeling techniques for water may provide a solution to increase understanding of water.

2. Experimental Details

The efficacy of a single-point model for water was determined by running thousands of trials with different parameter values and comparing simulated data to experimental data. The parameter values that were changed were σ_{LJ}, the size of the water molecule, ϵ_{LJ}, the coefficient for magnitude of the Leonard-Jones potential, and v_0, the coefficient for strength of hydrogen bonding. The models created using these three parameters were fitted to experimental values for density and an estimated value for the apparent coefficient of diffusion.

The new spherical harmonic function, transformed as specified in **Equation 3**, was first implemented in OpenMD. For the first set of trials, the coefficients a and b were set to 0.5 and 0.5 as a baseline to show whether this type of transformation was appropriate in better approximating the behavior of experimental water. The coefficients were later set in the second set of trials to 2/3 and 1/3, respectively, based on a differential optimization of **Equations 1-3**. The reduction of the negative hydrogen bonding phenomena can be seen in **Figure 2** and **Figure 3** for the first set of trials and the second set of trials respectively. In **Figure 2**, there is an area in the center of the red negative hydrogen bonding phenomenon which is much lighter than the rest of that quadrant, which is removed by the differential optimization implemented for the second set of trials.

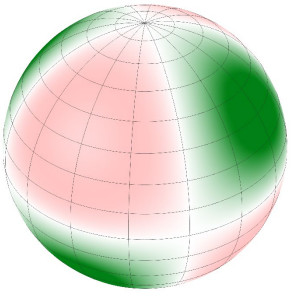

Figure 2

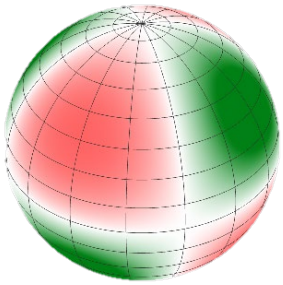

Figure 3

The parameter values for σ_{LJ}, ϵ_{LJ}, and v_0 were chosen to approximate experimental values of about 2.74 Å, 0.5 kcal/mol, and 5 kcal/mol respectively. Tens of thousands of trials were performed in a series of three narrowing parameter spaces using 100 ps of equilibration and a 5 ns simulation of a 256-particle system using isotropic NPT ensemble calculations. Selection criteria for the models were based on the density and apparent coefficient of diffusion. All models which fell within an acceptable range of the expected values of these variables were then tested at a temperature range from 240K to 360K, and based on the calculated densities across this temperature range, the best models were chosen. This process was repeated for the first and second set of trials.

3. Results

The first set of trials used values of 0.5 and 0.5 for a and b respectively in **Equation 3**. The two best models based on a summation of error at all temperature values tested were chosen with parameters as shown in **Table 1**.

Model	σ_{LJ}	ϵ_{LJ}	v_0
1	2.92	0.40	4.90
2	2.83	0.20	4.20

Table 1

The density across the temperature range tested and radial distribution function for Model 1, Model 2, and experimental water are shown in **Figure 4** and **Figure 5** respectively.

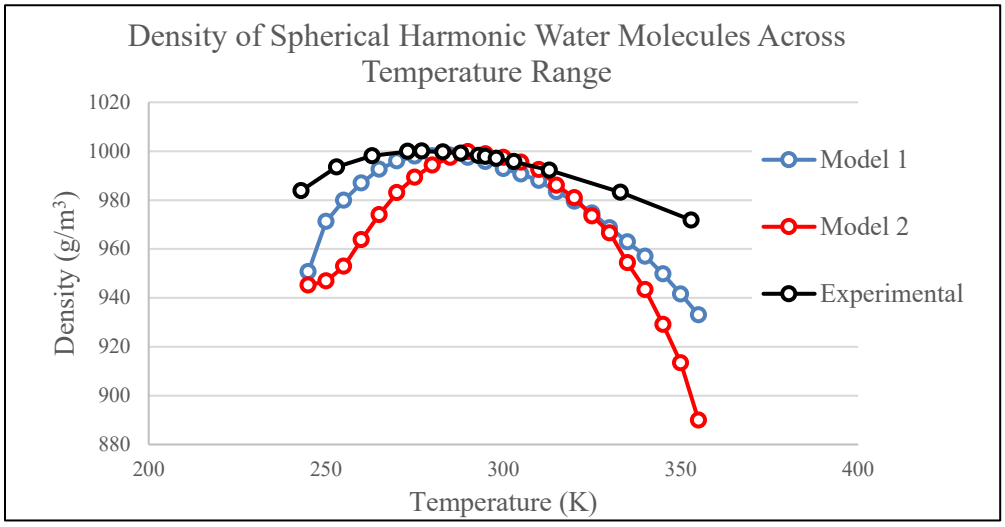

Figure 4

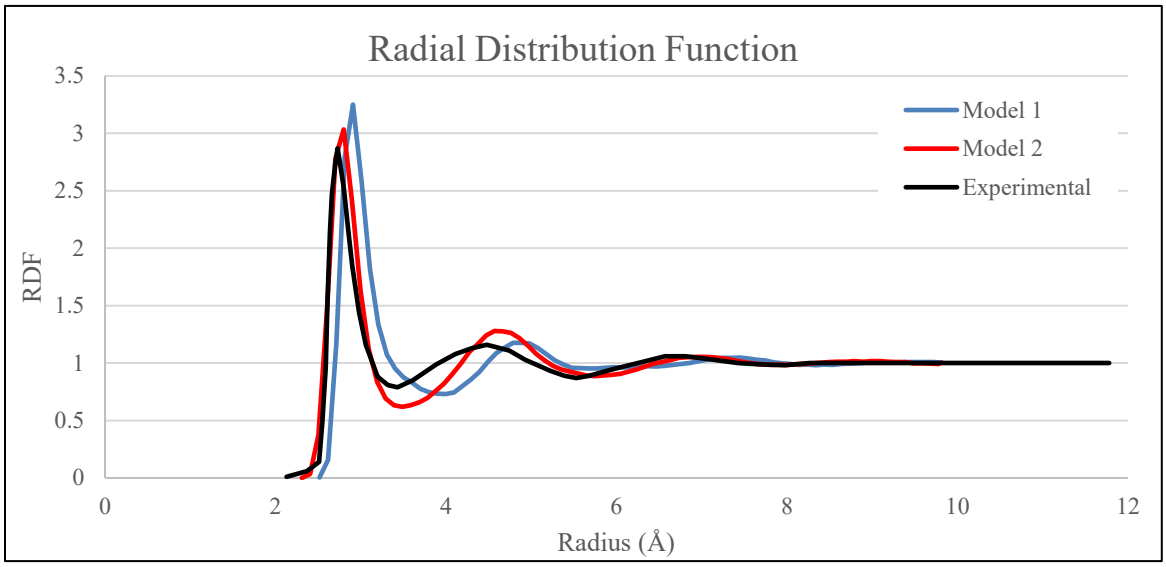

Figure 5

The second set of trials used values of 2/3 and 1/3 for a and b respectively in **Equation 3**. The three best models based on a summation of error at all temperature values tested were chosen with parameters as shown in **Table 2**.

Model	σ_{LJ}	ϵ_{LJ}	v_0
1	2.74	0.32	4.40
2	2.74	0.30	4.30
3	2.79	0.44	4.60

Table 2

The density across the temperature range tested and radial distribution function for Model 1, Model 2, and experimental water are shown in **Figure 6** and **Figure 7** respectively.

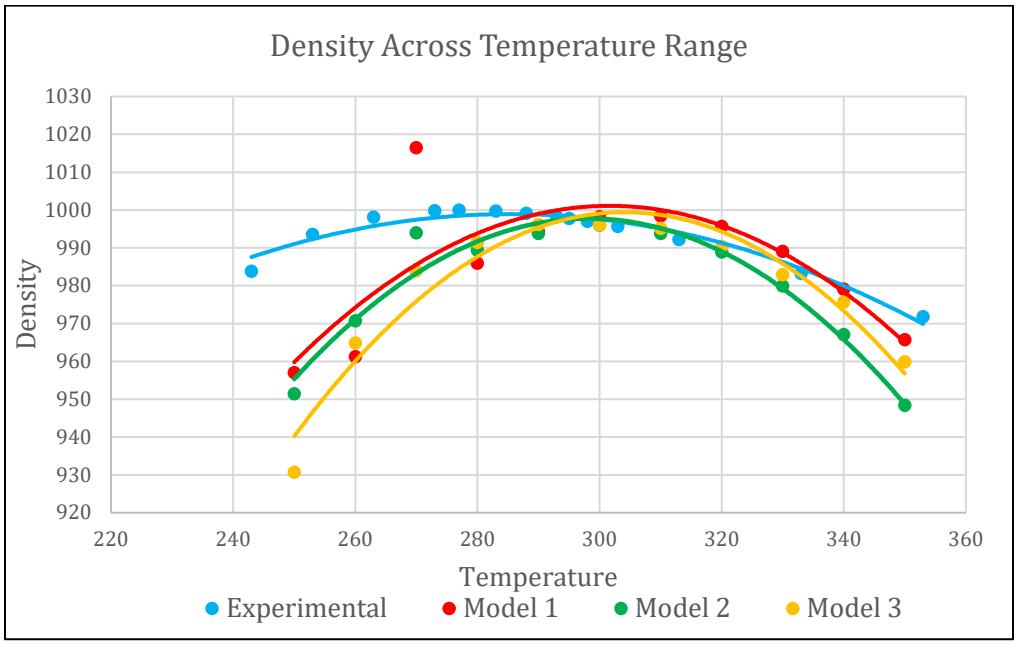

Figure 6

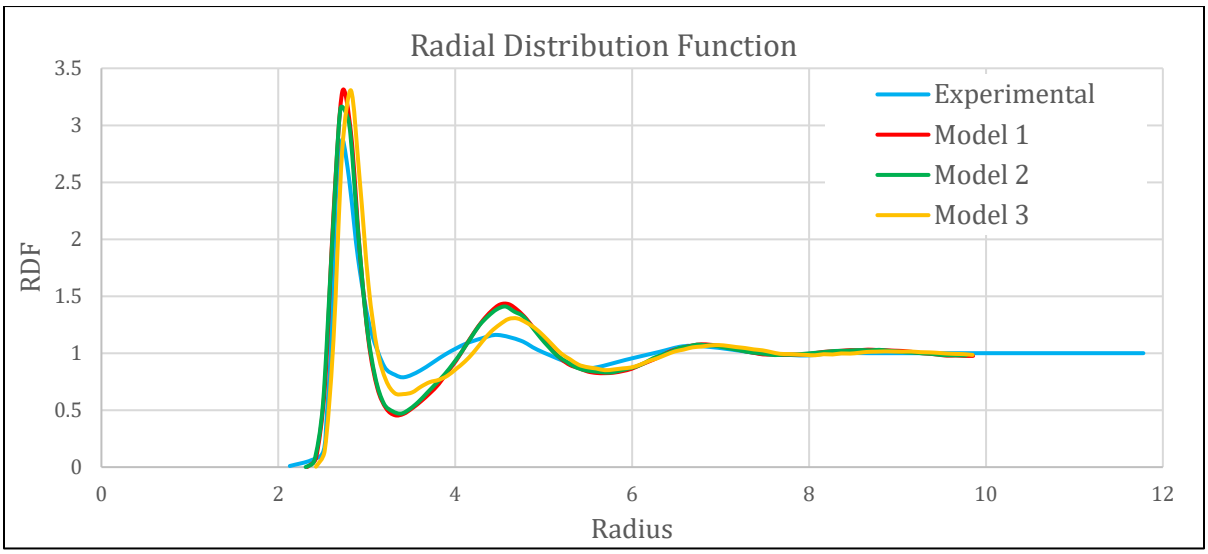

Figure 7

4. Discussion and Conclusions

Examining the results from the first set of trials, from **Figure 4,** the two models, particularly Model 1, well-approximate the radial distribution function given by experimental data. Both models have a more defined second peak than the experimental value, signifying that they are still more structured than experimental water. The initial peak of both models is skewed slightly right from the experimental value, which is closely related to the σ_{LJ} value. From **Figure 5,** the two models, particularly Model 1, are have similar curvature and maximum to the experimental curve. Model 1 is most accurate from about 260K to 310K while Model 2 is most accurate from about 290K to 330K. From this analysis, Model 1 appears to be the closest approximation to experimental water.

In the second set of trials, from **Figure 6,** the three models, particularly Model 2, well-approximate the radial distribution function given by experimental data. All the models have a more defined first and second peak than the experimental value, and therefore are still more structured than experimental water, although all these models are closer in structure to experimental water than the models from the first set of trials. The abnormality in the curve at the first valley, particularly in Model 3, is likely due to the cutoff function implemented in the OpenMD program, which stops interaction between molecules at about 3.5 Å. From **Figure 7**, the three models, particularly Model 2, well capture the curvature and maximum of the experimental curve. Model 1 is most accurate from about 290K to 350K, Model 2 is most accurate from about 280K to 330K, and Model 3 is most accurate from about 280K to 340K. From this analysis, Model 2 appears to be the closest approximation to experimental water.

Comparing the first and second set of trials, the value of σ_{LJ} stands out as being vastly different. The values of σ_{LJ} in the second set of trials is much closer to the expected value of 2.72 Å based on the size of experimental water. This along with the overall more similar structure from the radial distribution function shows that the optimized values for a and b in **Equation 3** made this model closer to what is expected of experimental water, and therefore these values for a and b are more promising moving forward. A further, more fine-grain search through the scans across temperature ranges may yield results more like the experimental curvature, particularly in the second set of scans.

The three models chosen from the second set of scans are three of over three thousand trials. Future work includes looking more closely at the results of other trials with reasonable amounts of error. Approximately ten promising models will be chosen based on a closer analysis of these three thousand trials and more bulk properties, such as actual coefficient of diffusion, will be tested and compared to experimental values. If this model can approximate properties that were not targeted in the scans, that will signify success in building a model that accurately captures the behavior of experimental water. Additionally, future projects may include expanding this modelling technique to tetrahedrally interacting atomic level materials, like silicon and germanium, and construct spherical harmonic potential functions that capture non-tetrahedral geometries, like halogen containing molecules.

5. Summary

The work done through this project shows that the structure and density of water can be well-approximated by spherical harmonic modeling. Modifying the spherical harmonic function to remove the influence of the negative hydrogen bonding phenomenon gives the model a structure more like that of real water, particularly when this modification is optimized. The density of spherical harmonic water is particularly accurate to experimental density within a specific range of temperatures around 300K. The water model is still slightly too structured and the curve for the density of modeled water has a greater concavity than that of real water with a shifted maximum. This may be solved by looking more closely at additional models.

By building up from the fundamental basics of intermolecular interactions, the spherical harmonic water model was able to well-approximate some properties of experimental water. This computationally efficient and adaptable model may create a new avenue in a limited field of options for studying phase change, nucleation, crystal growth, and other phenomena that connect the microscopic and macroscopic worlds.

6. Appendices

6a. Acknowledgements

This work was supported by the National Institutes of Health: RM1 GM135136-01. Computing is from the OSU HPCC thanks to National Science Foundation MRI: OCI-1126330. We thank Dr. and Mrs. Niblack for their support.

6b. Papers Published

Bias, A and Fennell, C. Single-point modelling of water using spherical harmonics. Poster presented at: American Chemical Society Southwest Regional Meeting; 11/01/2021; Austin, TX.

6c. Literature Cited

Bratko, D., Blum, L., and Luzar, A., 1985. A simple model for the intermolecular potential of water. The Journal of chemical physics, 83:12, 6367-6370.

Chandra, A., and Ichiye, T., 1999. Dynamical properties of the soft sticky dipole model of water: molecular dynamics simulations. The Journal of chemical physics, 111:6, 2701-2709.

Izadi, D., and Onufriev, A., 2016. Accuracy limit of rigid 3-point water models. The Journal of chemical physics. 145(7): 074501.

Price, S. L., Stone, A. J. and Alderton, M., 1984. Explicit formulae for the electrostatic energy, forces and torques between a pair of molecules of arbitrary symmetry. Molecular Physics, 52:4, 987 — 1001.

SINGLE-POINT MODELING OF WATER USING SPHERICAL HARMONICS

Alexandria Bias

Department of Chemistry

Faculty Sponsor: Dr. Christopher Fennell

Niblack Scholars Program

OVERVIEW

- Background
- Benefits of a Single-Point Model
- Modifying Spherical Harmonic Equations
- Methods/Results
- Conclusions

WATER MODELS

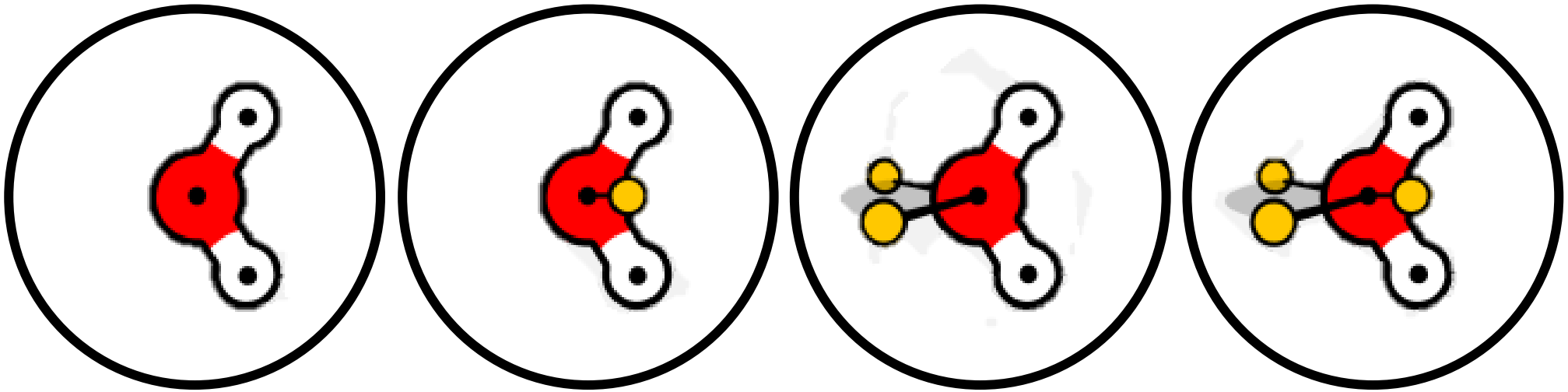

Three-point model

Four-point model

Five-point model

Six-point model

BENEFITS OF A SINGLE-POINT MODEL

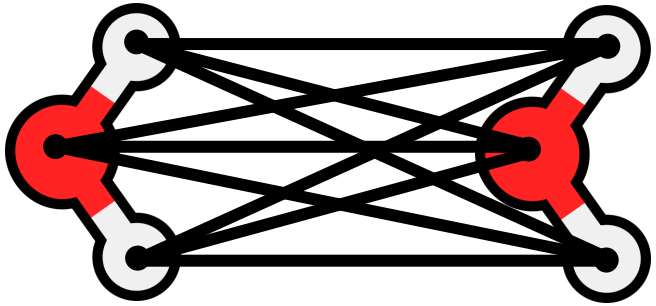

Each Atom as a Point → 9 interactions

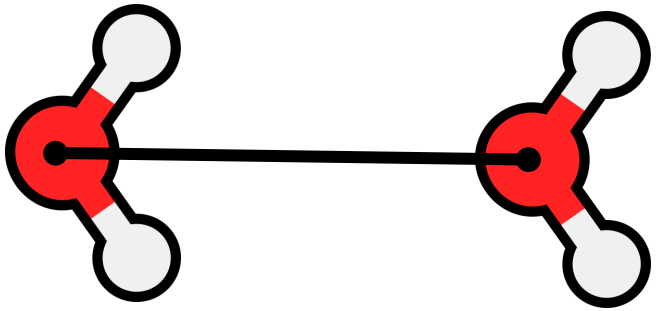

Single Point → 1 interaction

Computational cost increases by a factor of N^2 with N = Number of Molecules

SPHERICAL HARMONIC EQUATIONS

$$V_{LJ} = 4\epsilon_{LJ}\left[\left(\frac{\sigma_{LJ}}{r_{ij}}\right)^{12} - \left(\frac{\sigma_{LJ}}{r_{ij}}\right)^{6}\right]$$

$$V_{HB} = v_0 \cdot \left(cos(\theta)cos(2\phi)sin^2(\theta)\right)$$

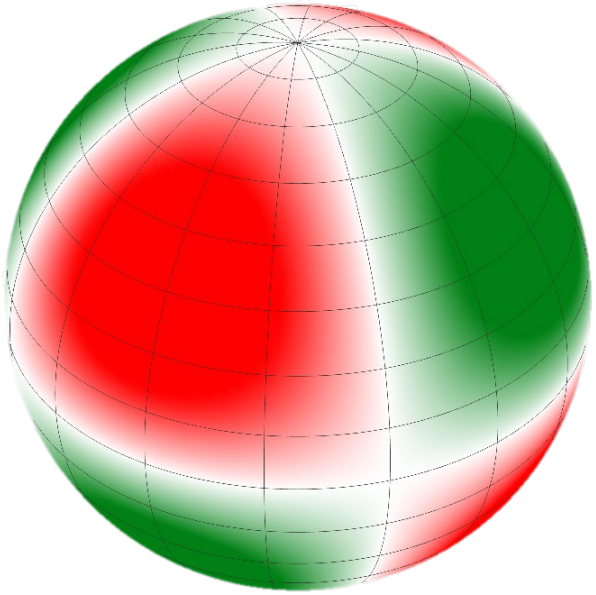

PREVIOUS MODEL

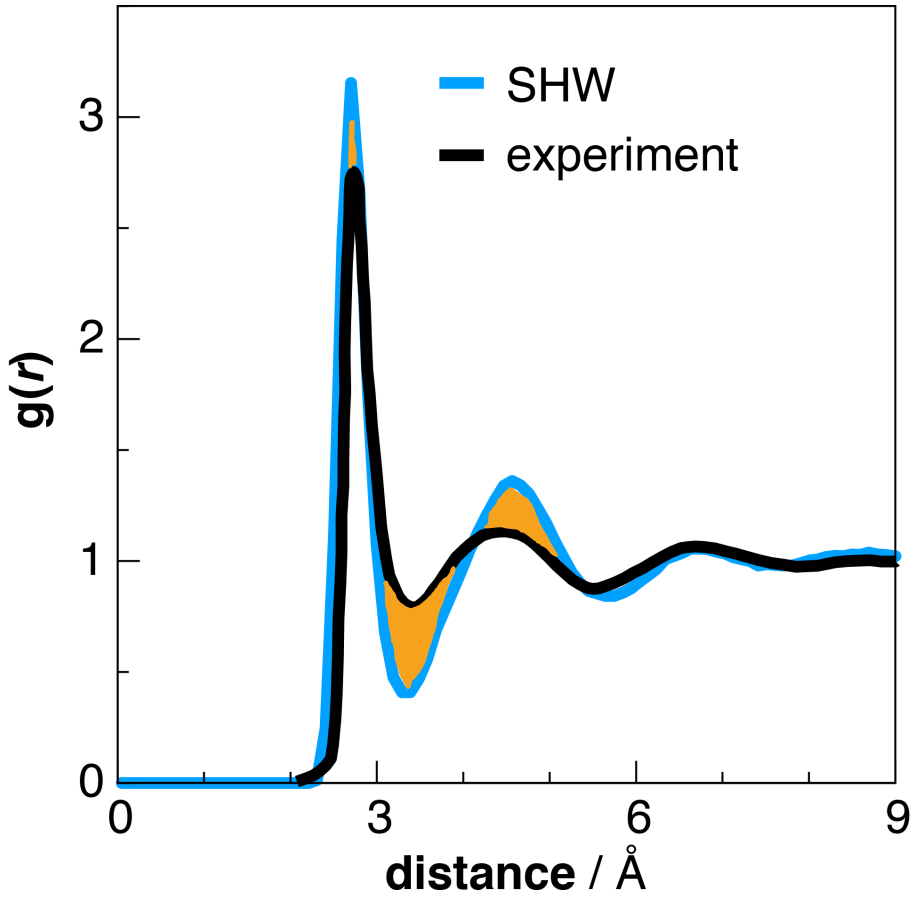

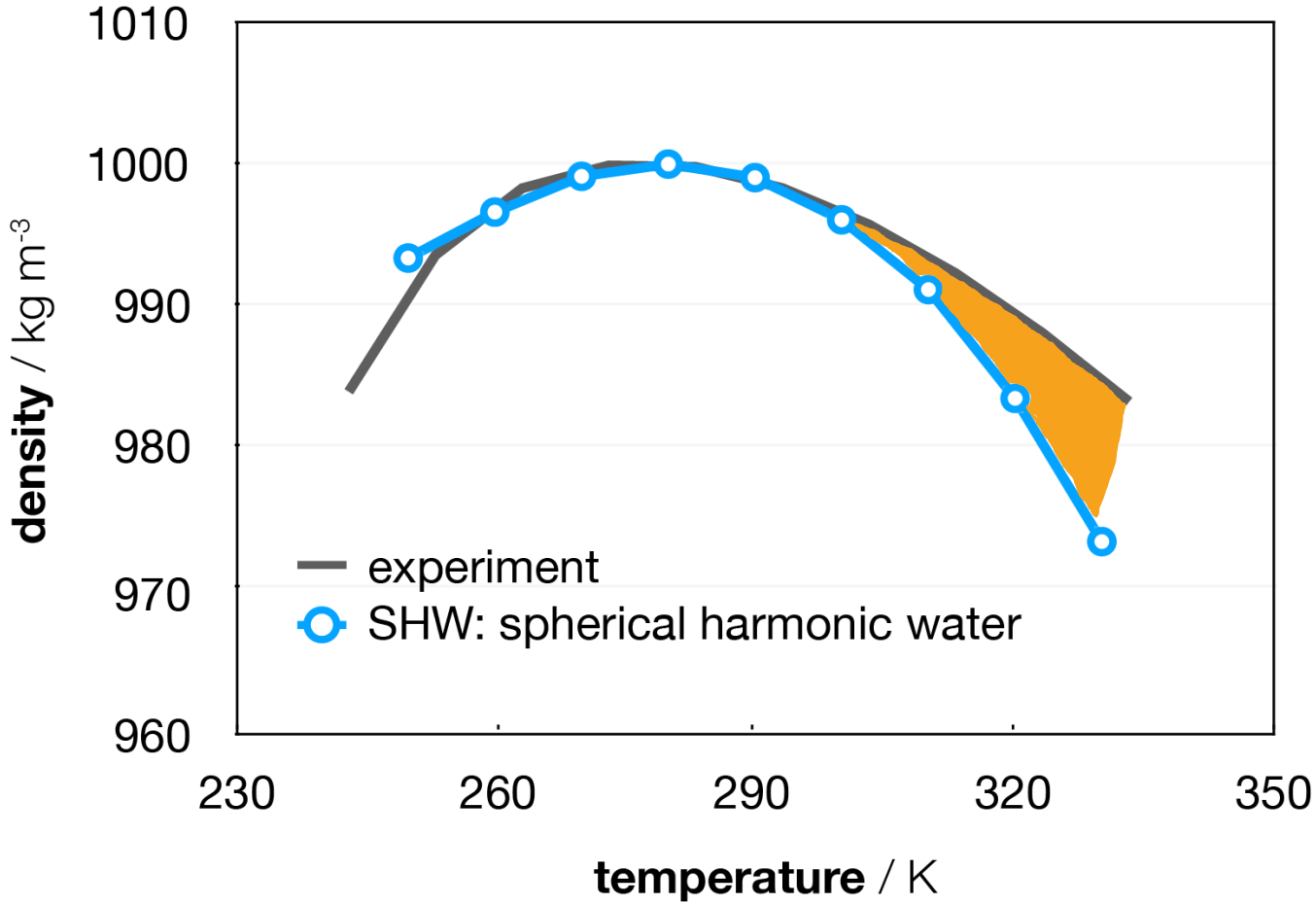

MODIFICATION

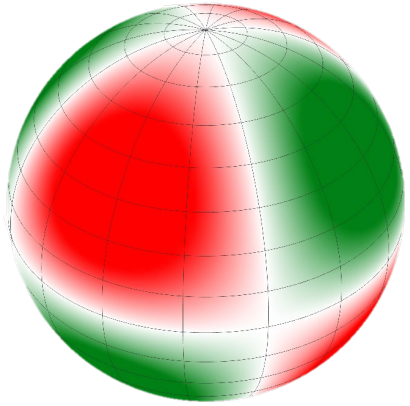

Manipulating the equation for V_{HB} can narrow the repulsive interactions

Repulsive red zones cause the water model to be overly structured

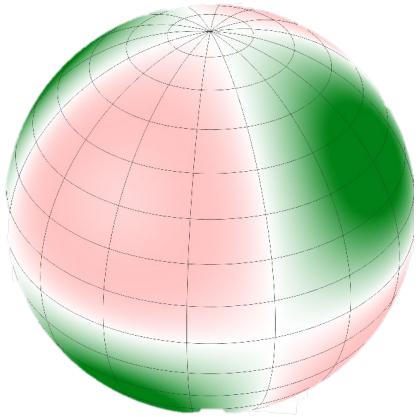

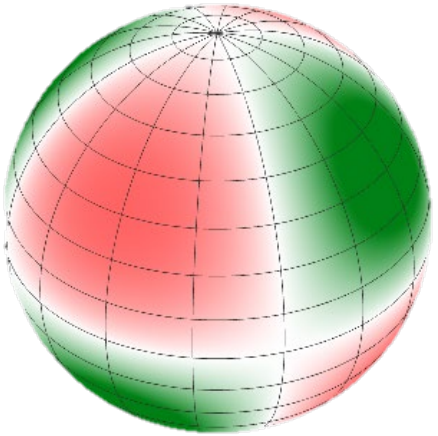

Trial Set A

$$V_{HB} = \frac{2}{3}V_{HB} - \frac{1}{3}{V_{HB}}^2$$

Trial Set B

$$V_{HB} = \frac{1}{2}V_{HB} - \frac{1}{2}{V_{HB}}^2$$

COMPUTATIONAL METHODS

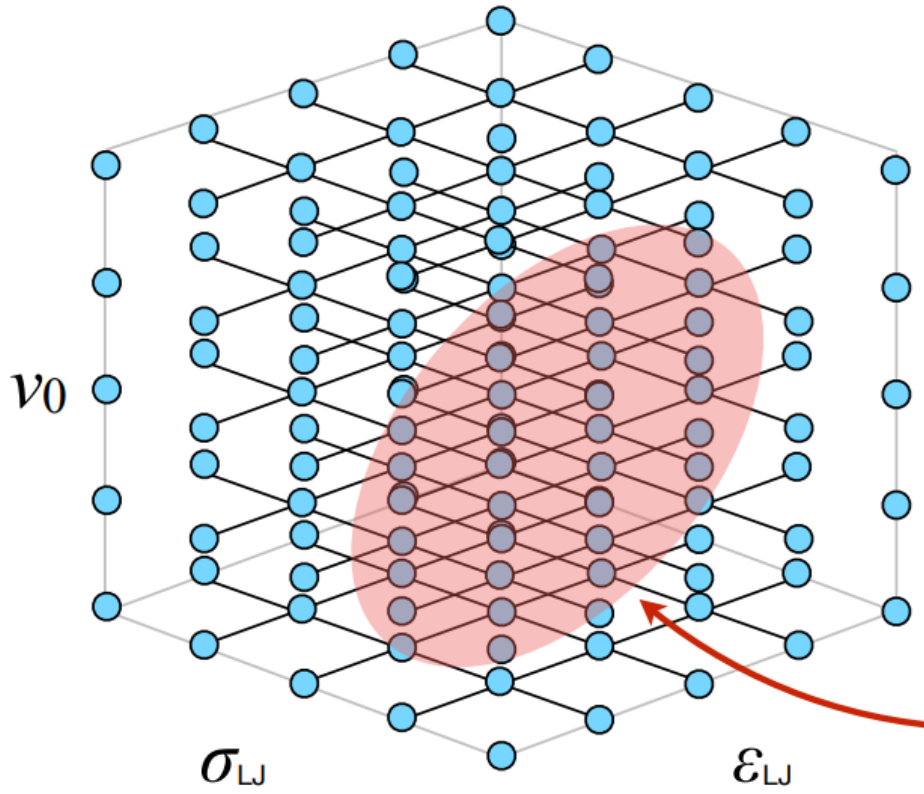

liquid
@ 298.15 K
& 1 atm

COMPUTATIONAL METHODS

1. **Scan across models in parameter space with new spherical harmonic function into OpenMD**
2. **Calculate RMSD for density and apparent diffusion**
3. **Simulate 50k best models at 273.15K and 310.15K**
4. **Simulate 100 best models at 240-360K**

MODEL PARAMETERS

Set 1: $V_{HB} = \frac{2}{3}V_{HB} - \frac{1}{3}{V_{HB}}^2$

Model	σ_{LJ}	ϵ_{LJ}	v_0
1	2.92	0.40	4.90
2	2.83	0.20	4.20

Set 2: $V_{HB} = \frac{1}{2}V_{HB} - \frac{1}{2}{V_{HB}}^2$

Model	σ_{LJ}	ϵ_{LJ}	v_0
1	2.74	0.32	4.40
2	2.74	0.30	4.30
3	2.79	0.44	4.60

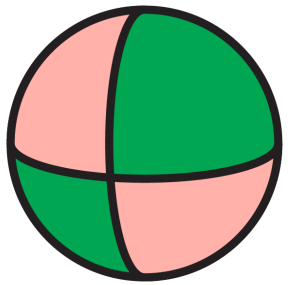

Model 1

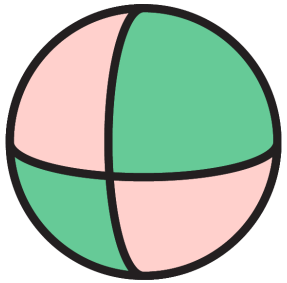

Model 2

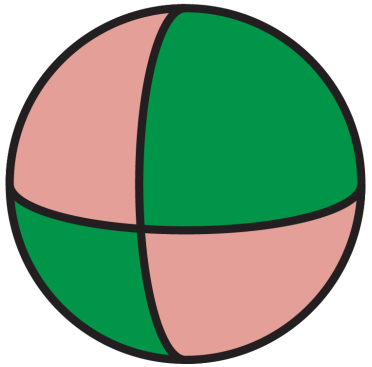

Model 3

SET 1 RESULTS

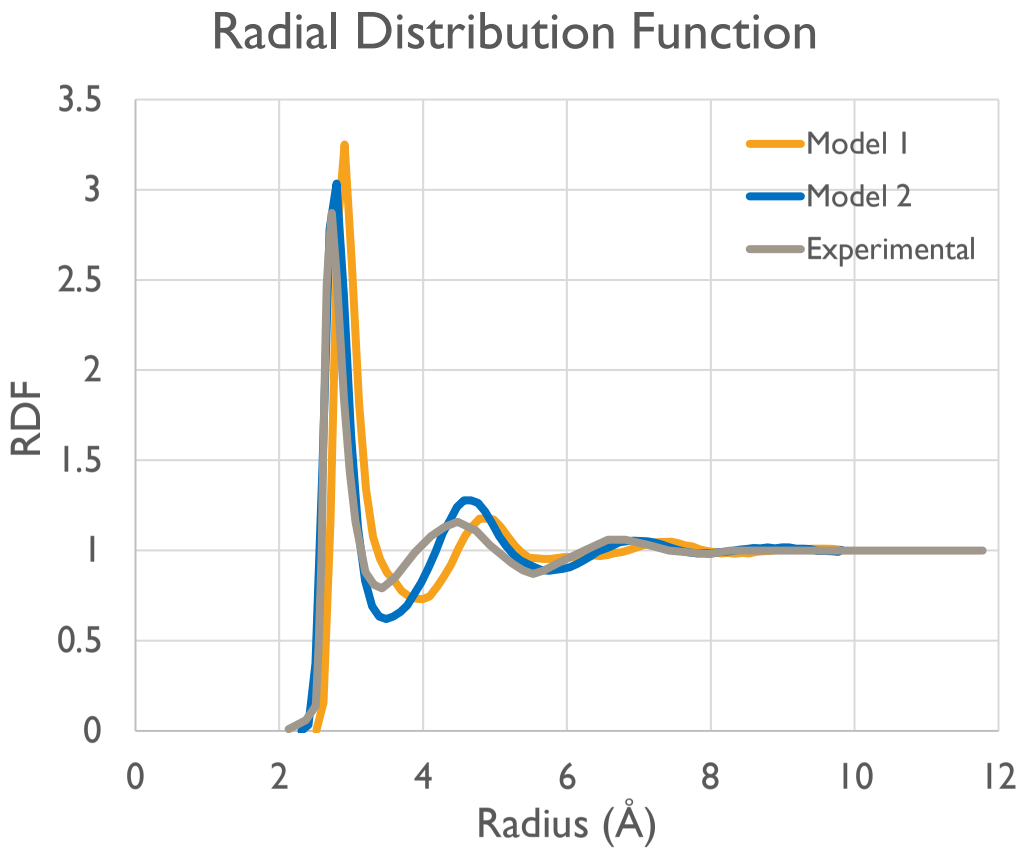

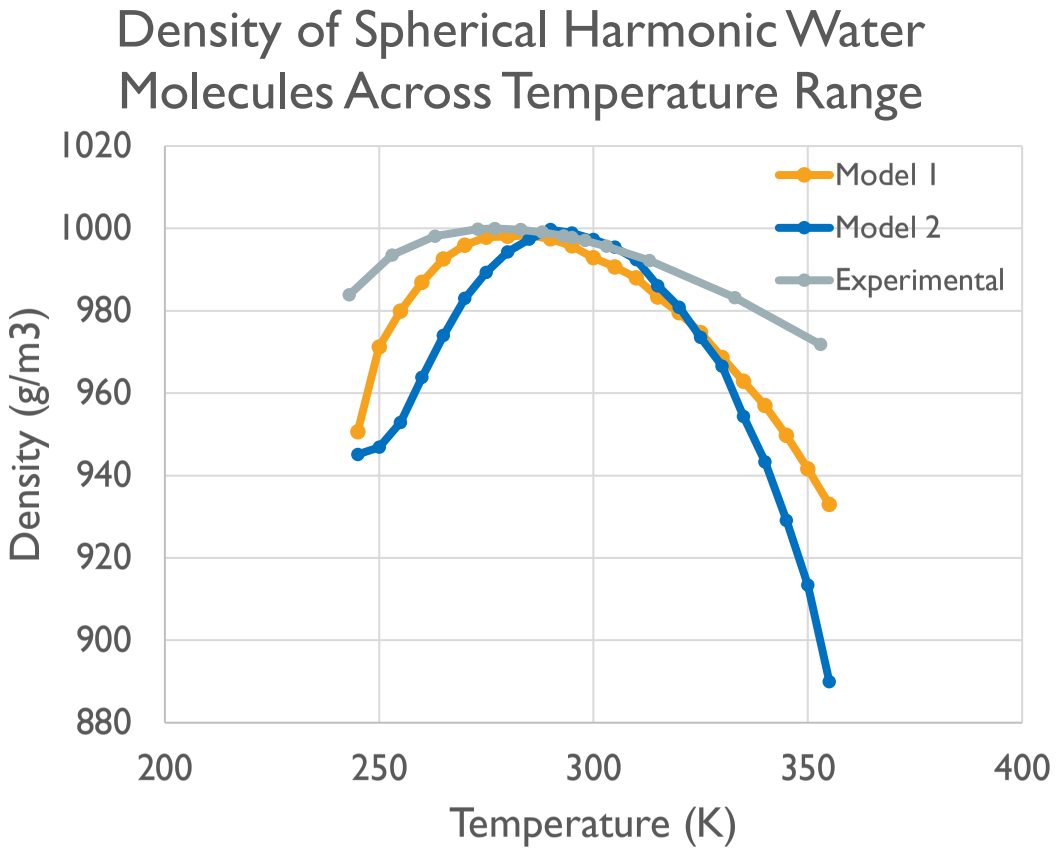

SET 2 RESULTS

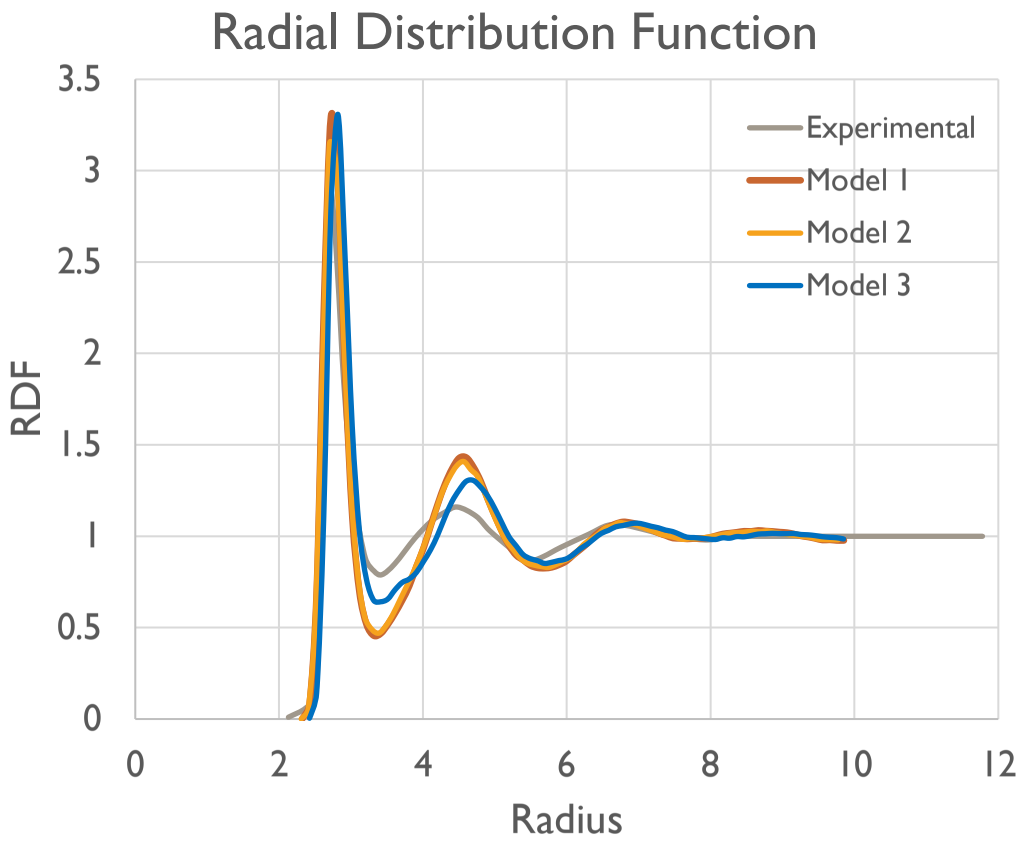

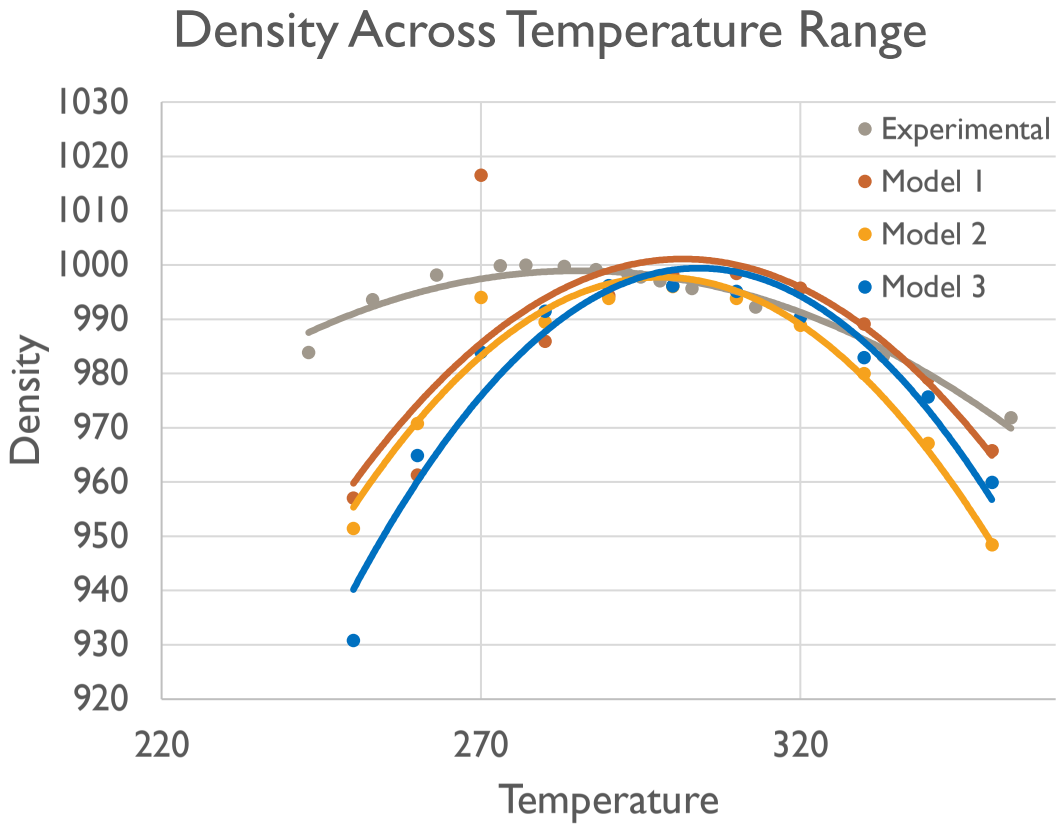

KEY POINTS

An optimized spherical harmonic equation approximates the structure of real water

Further analysis of models may yield better results

Spherical harmonic water is a good candidate for a more efficient water model

WHERE DO WE GO FROM HERE?

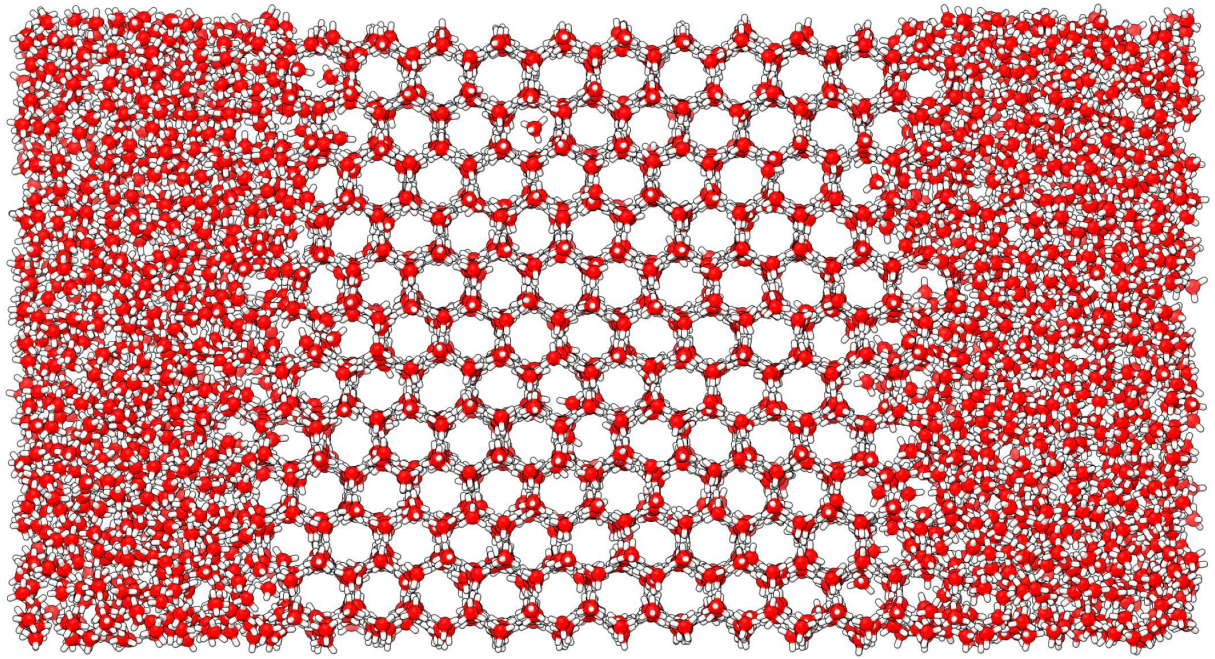

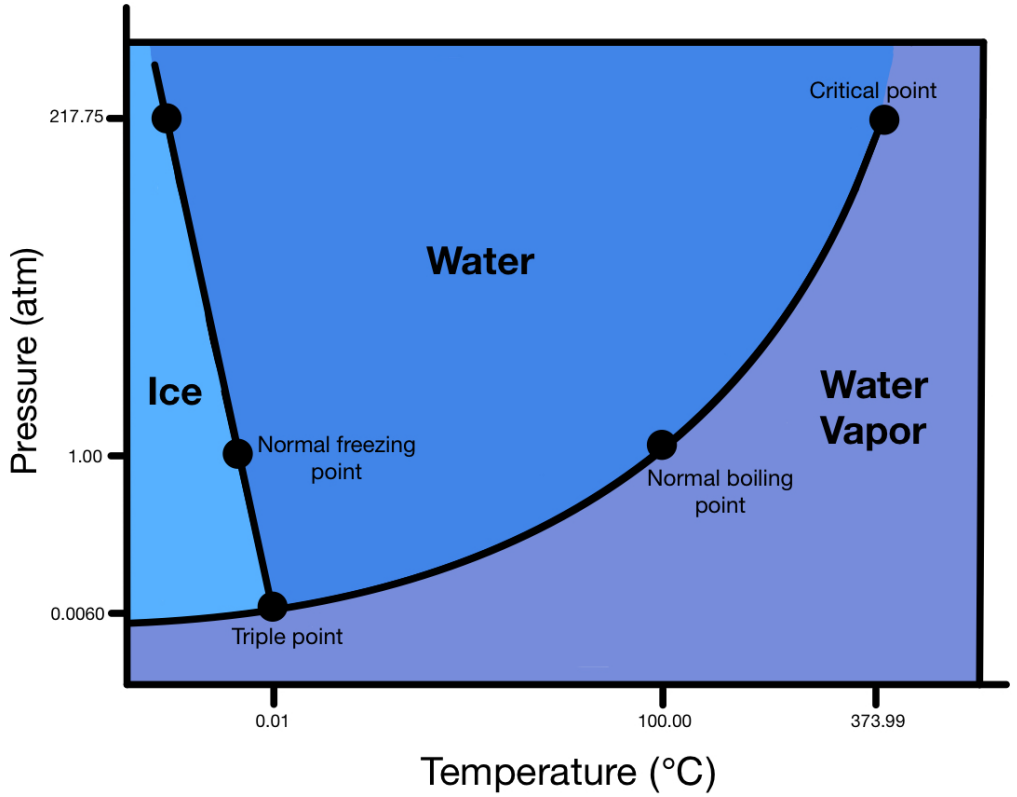

ACKNOWLEDGEMENTS

- Dr. Christopher Fennell, OSU Chemistry Department
- Dr. John and Heidi Niblack
- OSU HPCC funding from National Science Foundation MRI: OCI-1126330
- National Institute of Health: RM1 GM135136-01

REFERENCES

- Bratko, D., Blum, L., and Luzar, A., 1985. A simple model for the intermolecular potential of water. The Journal of chemical physics, 83:12, 6367-6370.
- Chandra, A., and Ichiye, T., 1999. Dynamical properties of the soft sticky dipole model of water: molecular dynamics simulations. The Journal of chemical physics, 111:6, 2701-2709.
- Izadi, D., and Onufriev, A., 2016. Accuracy limit of rigid 3-point water models. The Journal of chemical physics. 145(7): 074501.
- Price, S. L., Stone, A. J. and Alderton, M., 1984. Explicit formulae for the electrostatic energy, forces and torques between a pair of molecules of arbitrary symmetry. Molecular Physics, 52:4, 987 — 1001.

Economic Production of Hydrolytic Enzymes Pertinent to Biofuel Production from Overexpressed *Aspergillus nidulans* Transcription Factor and Recombinant Hydrolase Promoter

Andrew L. Thomas

Department of Microbiology and Molecular Genetics
Faculty Sponsor: Dr. Rolf A. Prade
Graduate Student Mentor: Rebekkah Friske-Pope

ABSTRACT

Biofuel is an incredible source of renewable energy, whose true potential is currently limited monetarily, in part through the cost to produce and transport hydrolytic enzymes. *Aspergillus nidulans* is one of the leading industrial fungi and used to produce enzymes needed to breakdown biomass. Production of hydrolytic enzymes is a costly process especially because it requires expensive carbon sources. In this work we modify the genetic makeup of *A. nidulans* in such a way that the resulting recombinant strains are enabled to use the cheap, almost free carbon source, Pentosan-Containing Pretreated Biomass liquors, to produce both cellulases and hemicellulases. Pentosan liquors are often discarded from biofuel refineries as waste products from the necessary pretreatment of lignin rich biomass. By overexpressing both cellulase and hemicellulase production at the expense of a ridiculously cheap carbon source, we can lower costs to produce hydrolytic enzymes, reducing the cost to manufacture biofuel from Lignocellulosic Biomass.

1. Introduction

Energy plays a critical role in the development of society and our future. The energy obtained from biomass is the fourth largest source of energy in the world, following only oil, natural gas, and coal (Wu et al., 2012). Lignocellulosic Biomass (LCB) used in the production of these biofuels contain cellulose - a 6 carbon sugar polymer -, hemicellulose - a 5 carbon sugar polymer -, and lignin - a complex aromatic biopolymer (Ballmann et al., 2019). *Aspergillus nidulans* among other industrial fungi are remarkably effective at producing hydrolytic enzymes to break down C5-sugar and C6-sugar polymers, except for

lignin; consequently, lignin must be removed through various biomass pretreatments (Reese, 1976, Gupta et al., 2016).

LCB pretreatment methods, including both physical and chemical processes, allow for the catabolism of lignin "rich" biomass, but also form a C5-sugar-rich liquor, known as Pentosan-Containing Pretreated Biomass liquors (PPTBs), through the partial breakdown of hemicellulose. Natively, the xylose contained in PPTBs could serve as an inducer, to produce hemicellulases (Ballmann et al., 2019). However, in the presence of these PPTBs, *A. nidulans* is incapable of producing the vast amount of cellulases it normally does (Ballmann et al., 2019). Should this barrier, established by the PPTBs blocking cellulase production, be overcome, the onsite production of hydrolytic enzymes required for biofuel production could be achieved, substantially reducing expenses pertaining to high-cost carbon inducers and transportation of enzymes to biorefineries.

Industrial strains of fungi are capable of producing up to 100g/L of protein secretions, with up to 60% being cellobiohydrolase I (CBHI) and 20% cellobiohydrolase II (CBHII) (Schuster and Schmoll, 2010). The ACE3 transcription factor (TF), regulates the production of these cellulases (Ballmann et al., 2019). Contrarily, the xylanase regulator 1 (XYR1) regulates the production of hemicellulases, such as xylanases but not cellulases (Klaubauf et al., 2014). The ACE3 and XYR1 transcription factors are induced by C6 or C5 sugar derivatives, respectively.

In this paper we aim to design a more economically efficient way for *Aspergillus nidulans* to induce the production of hydrolytic enzymes, specifically by utilizing a constitutively expressed XYR1 transcription factor controlling the production of CBH1 via the xynC promoter. This allows for the induction of both cellulases and hemicellulases from the xylose found in the waste product: PPTBs, s*ee Figure 1*.

2. Experimental Details

Chemicals and specialty chemicals

General chemicals, cellulosic and hemicellulosic substrates were purchased from the best source possible, Sigma Aldrich (St. Louis, MO) and Megazyme (Ireland, UK).

Genomic DNA Extraction to Gather Construct Pieces

10 colonies of A. nidulans were inoculated with 1*10^9 spores and grown at 37 ˚C for 3 days in a 1.1% mass/volume of glucose, Mandel's Liquid Media. Afterwards, the hyphae were transferred to a 1.5 mL Eppendorf tube using sterile tweezers. To each Eppendorf tube 1 mL of extraction solution – 8-parts nuclease free H20, 1-part EDTA with a final concentration of .05 M, and 1-part 1% SDS solution – was added. The following process was

completed 3 times: Freeze Eppendorf tube in -80 ˚C, heat tube in 42 ˚C heat block until hot, and then vortex to mix the solution. 1 µl from each sample was used as template DNA for each PCR reaction. To collect all fragments of DNA for our constructs, the required forward and reverse primers were used to amplify each piece of DNA.

Cleaning PCR Products and Gibson Assembly

To clean each PCR product, 3x the PCR volume of Sodium Iodide was added into a 1.5 mL Eppendorf tube, then the PCR product was added. To these tubes, 5 µl of glass-milk per 5 µg of DNA was added and suspended into solution. After waiting 5 minutes, the tubes were spun in a centrifuge for 5 seconds to pellet the glass-milk, the supernatant was then discarded, 500 µl of washing solution (Ethanol and Salts) was added, and the pellet was resuspended; this was repeated 3 times, with the 3rd cycle spinning for 30 seconds and no washing solution added. Each Eppendorf, containing only the pellet was placed onto a heating block at 42 ˚C for approximately 20 seconds, or until dry. Then 20 µl of nuclease free H20 was added to the tubes, the pellet was resuspended, pelleted in a centrifuge, and the supernatant pipetted off and saved. The Gibson Assembly® Protocol (E5510) from New England BioLabs was followed, stitching together our pieces to each other and the PUC19 plasmid vector.

Transformation into *E. coli* and Selection of Transformants

NEB 5-alpha Competent *E. coli* was purchased from New England BioLabs. Transformation of our construct into *E. coli* was performed through the Heat Shock method from the Gibson Assembly® Master Mix – Transformation Protocol from New England BioLabs. The solution of cells was plated onto 15 mL Lauria Agar plates containing ampicillin as a selection agent. Surviving colonies of *E. coli* were selected by touching an autoclaved pipet tip to the colony and were transferred to into 15 mL Falcon tubes containing 10 mL Lauria Broth with ampicillin. The tubes were then placed into an incubating thermal shaker at 37 ˚C at 300 rpm, and left to grow overnight. 1 µl of turbid (surviving) colonies were used as the template DNA for colony PCR using the following primers: 2 µl each of gpd_f and pyrG_r for construct 1, or 2 µl each of CPYROA_f and CBH1tr_r for construct 2.

Transformation into *A. nidulans* and Selection of Transformants

Formation of *A. nidulans* protoplasts and transformations were performed as according to Gruber et.al., except at 37 ˚C grown on PDA plates (Gruber et al., 1990). Additionally, transformants receiving construct 1 had the PDA supplemented with pyridoxine (PYRO) and para-amino benzoic acid (PABA), while transformants receiving construct 2 were supplemented with uracil and uridine, double transformants received only PABA. Our untransformed strain received PYRO.

Fungal Growth Conditions and Collection of Extracellular Protein from Media

Strains were grown in 10 mL petri dishes containing Mandel's Liquid Media with 1% mass/volume of glycerol, glucose, xylose, and xylan – additional supplements added to each set of strains were the same as in the selection of fungal transformants. To each petri dish, 1*10^9 transformed spores were inoculated and incubated at 37 ˚C, totaling 12 different experimental conditions and 4 different controls. At 24 hour increments up to 96 hours in total, 1 mL of media was removed from each petri dish and placed into a 1.5 mL Eppendorf, making sure to not take excess hyphae with the supernatant. The tubes were then spun in a centrifuge at 4000 rpm for 10 minutes and the supernatant was transferred to a clean 1.5 mL Eppendorf tube.

Determination of Enzyme Activities

We used beechwood hemicellulose as a substrate to measure the activity of xylanase, and used the release of reducing sugars that react with DNS (Miller, 1959) to measure the activity. To 230 µl of 50 mM ammonium acetate buffer pH 5, 20 µl of total extracellular protein extract was added, 60 µl of 5% (mass/volume) beechwood xylan added, and reactions were incubated for 5 min at 40 °C before we added 300 µL of DNS to the solution and boiled the solution for 5 minutes. Control reactions were conducted using blanks to determine the presence of reducing sugars in the starting mixture, and these reactions contained all the same reagents except that DNS was added prior to the addition of enzyme sample. To properly determine the amount of reducing sugar produced during the enzyme catalyzed reaction, the ABS540 nm of the control was removed from the enzyme reaction and resulting net gain in ABS540 nm converted into enzyme units µmol/min/µg protein.

Using *p*NPC, *p*-nitrophenyl β-d-cellobioside, (Sigma Aldrich, St. Louis MO) as a substrate, we measured CBH1 production through the measured release of *p*-nitrophenyl that absorbs at ABS415 nm on a TECAN microwell reader. To a solution of 30 µl of 4 mM *p*NPC and 290 µl of 50 mM ammonium acetate buffer, 40 µl of total extracellular protein extract was added and reactions incubated for 15 min at 45 °C prior to the addition of 30 µl of 1 M sodium carbonate. Control reactions only differed to normal reaction in one regard; 1 M sodium carbonate was added prior to the addition of enzyme sample. To properly determine the amount of *p*-nitrophenyl produced during the enzyme catalyzed reaction, the ABS415 nm of the control was removed from the enzyme reaction and the resulting net gain in ABS415 nm was converted into enzyme units µmol/min/µg protein.

3. Results

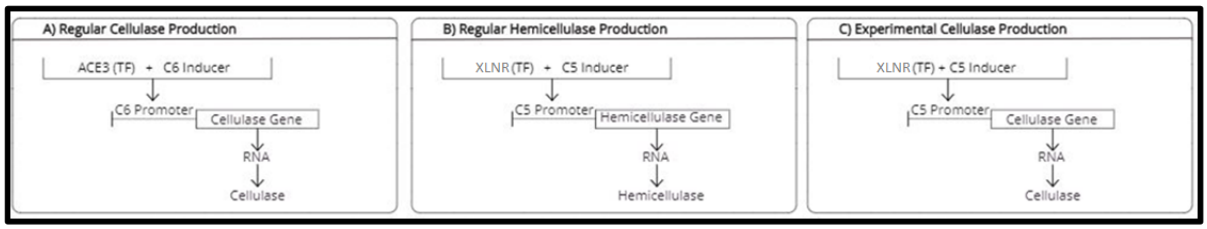

Figure 1) – **1A**) natural production of Cellulases using the ACE3 Transcription factor, a six-carbon sugar and the C6-Promoter; (**1B**) the natural production of Hemicellulase using the XYR1 transcription factor, a five-carbon sugar, and the C5 promoter; (**1C**) the experimental Cellulase production using the XYR1 transcription factor, a five-carbon sugar, and a C5-Promoter.

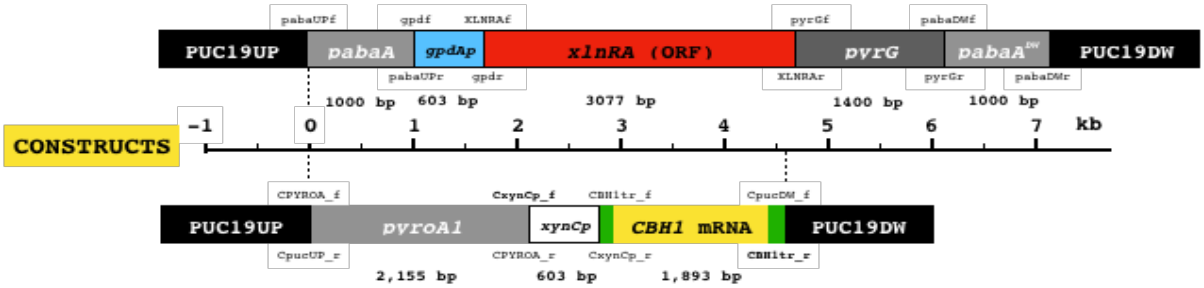

Figure 2) Shows the Gibson Assembly Technology (GAT) constructs created. **Construct 1**) – xlnR Transcription factor constitutive expression construct. Overexpression due to gpd promoter controlling synthesis of XLNR TF. Construct is placed into the Para-Aminobenzoic Acid (PABA) locus. **Construct 2**) – Xylanase C promoter controlling Cellulase gene transcription. Construct is placed into the Pyridoxine (PYRO) locus. **Both**) – constructs are initially inserted into the PUC19 plasmid, containing an ampicillin resistance gene.

Relevant Genotype

Strain	Overexpression	
	XlnR	CBH1 mRNA
APEX	----	----
XLN7	gpdp::XLNR	----
A7C115	----	xynCp::CBH1tr
XL7C418	gpdp::XLNR	xynCp::CBH1tr

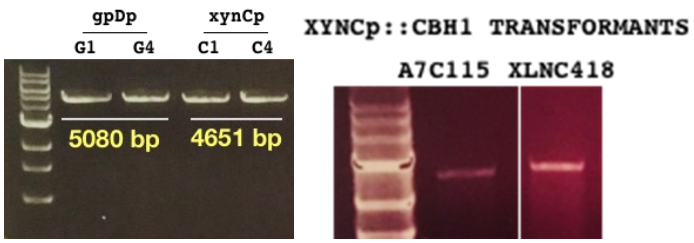

Figure 3) - Completed GAT products for both constructs: **(gpDP)** – PCR amplification of gpdAp_fwd :: pyrG_rev **(xynC)** – PCR amplification of pyroA1_fwd:: CBH1 mRNA_rev **(A7C115)** – C1 xynCp integrated into E. coli **(XLNC418)** – Double transformation of gpDP construct and xynCp construct

Main goals of this project included swapping the native promoter of the cellulase gene for a promoter which is activated by a 5-carbon sugar such as xylanase and respective transcription factor (TF); *figure 1* depicts the native production of cellulases and hemicellulases, as well as the experimental cellulase production. In addition to the swapping of promoters, the work presented here also aimed to overexpress the production of the XLNR TF – in conjunction with a 5-carbon sugar, this TF binds to the xynC promoter used in the second construct - using the constitutively expressed Glyceraldehyde 3-Phosphate Dehydrogenase promoter from glycolysis pathway, *see figures 1&2*. Four separate fungal transformants with differing genotypes were created using transformation methods described in the *A. nidulans* transformation section of the Experimental Details; APEX is considered to be the experimental control and received no transformation, XLN7 was transformed using construct 1 only, A7C115 only contained construct 2, while XLN7C418 contained a double transformation with both construct 1 and 2, *see figures 2 and 3*. Gel electrophoresis conformations of both Gibson Assembly constructs and fungal transformations of construct 2 can be visualized in *figure 3*.

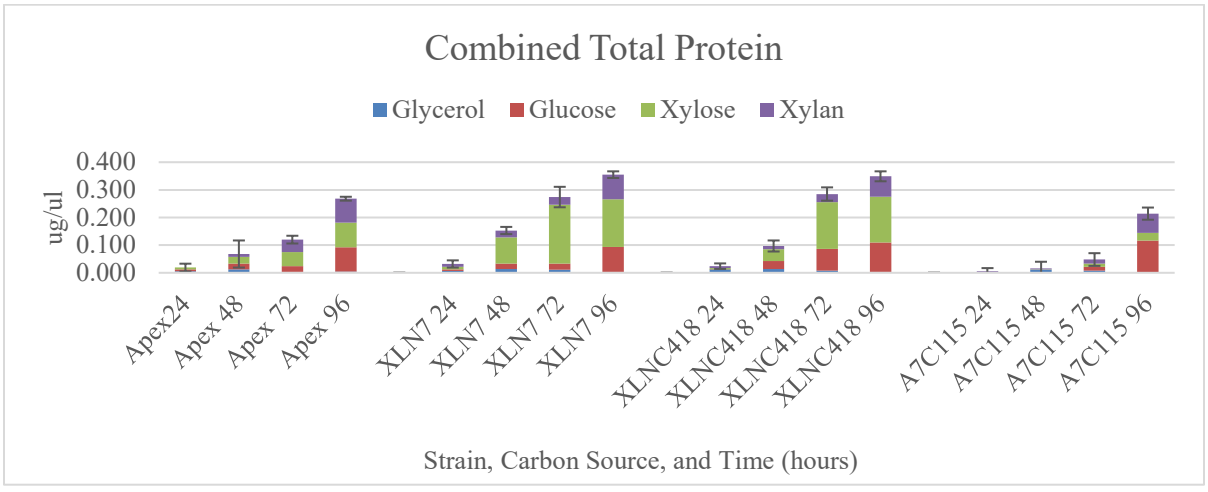

Figure 4) – Media protein concentrations taken from APEX, XLN7, XLNC418, and A7C115 grown in 1% mass/volume of Glycerol, Glucose, Xylose, and Xylan carbon sources at intervals of 24 hours. Error bars are additive within each column. <u>*NOTE*</u> – Same carbon source legend is used for *figures 4 - 7*.

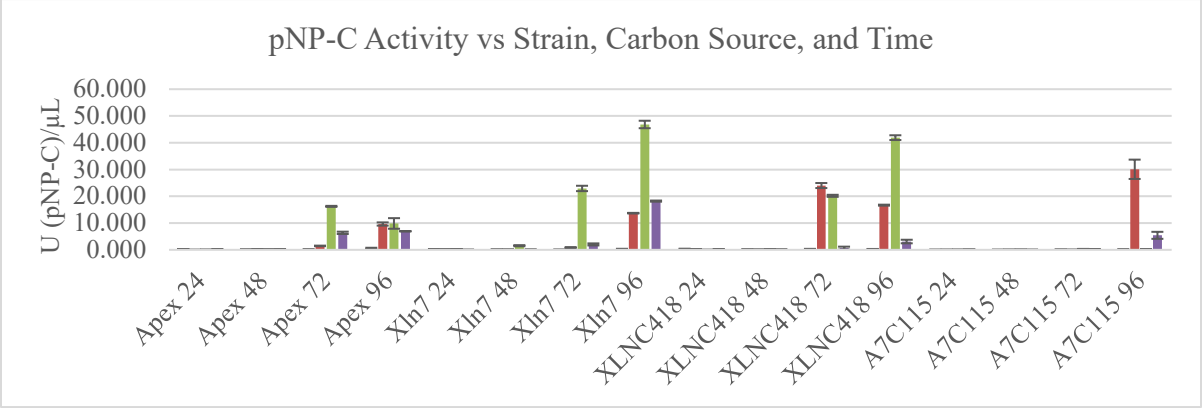

Figure 5) - APEX, XLN7, XLNC418, and A7C115 media protein activity measured in Units (µmol/min/µg)/µL. Absorbance at 415 nm were determined after 15 minutes incubation with pNP-C and converted to Units via a calibration curve.

Combining the media protein concentrations from all four carbon sources, showed increased concentrations from near zero levels at 24 hours to over 200 grams/liter by the 96-hour mark, *see figure 4*. Additional tests were conducted on the media protein to determine the activity level for both cellulases and hemicellulases from each of the four strains and carbon sources. *Figure 5* depicts a steady increase in cellulase activity over the 4-day trial from all four carbon sources and strains.

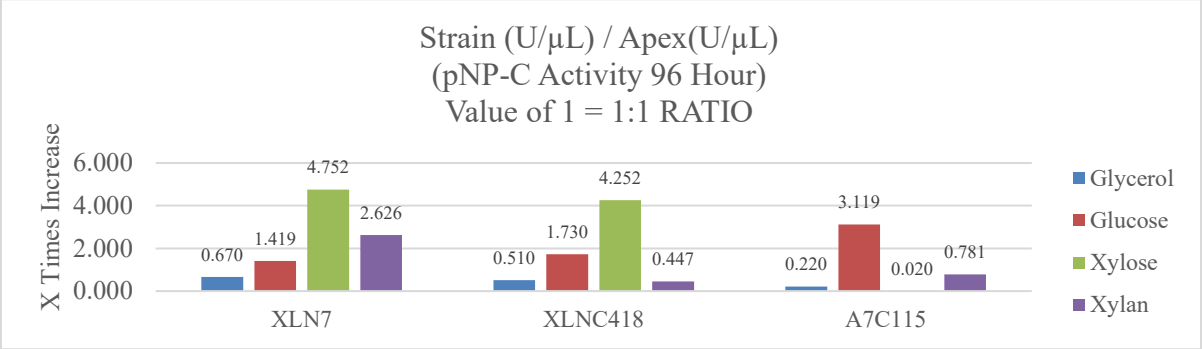

Figure 6) **–** Directly comparing APEX (unmodified) strain to XLN7, XLNC418, and A7C115 cellulase activity at 96 hours, achieved by taking the ratio of APEX U/µL to other strain U/µL from the 96-hour data.

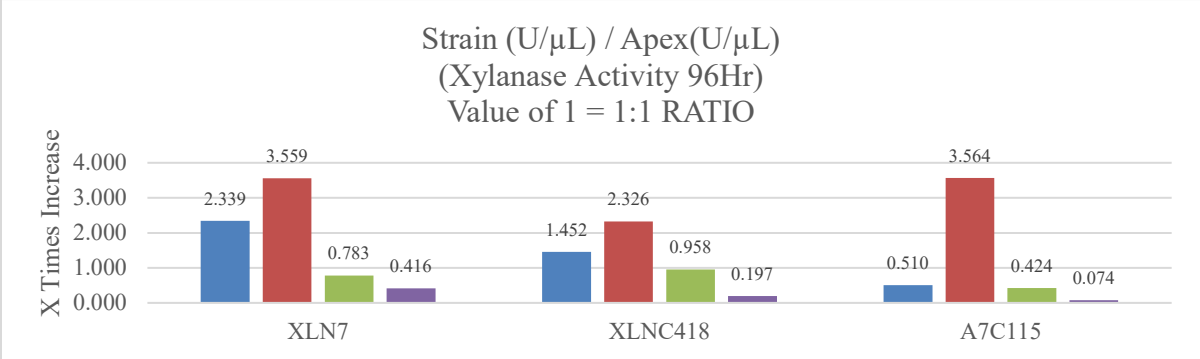

Figure 7) - Directly comparing APEX (unmodified) strain to XLN7, XLNC418, and A7C115 xylanase activity at 96 hours, achieved by taking the ratio of APEX U/µL to other strain U/µL from the 96-hour data. (Note: raw data not shown for brevity)

Figures 6 and *7* represent the ratio of activity in U/µL of experimental strains / Apex U/µL for cellulase and xylanase activity, respectively. There was 4.75 and 4.25 times increase in cellulase production from XLN7 and XLNC418, respectively, when grown on xylose carbon source, and a measured 3.11 times increase in cellulase production from A7C115 when grown on glucose, *see figure 6*. For the xylanase activity, all strains showed slight decrease in xylanase production when grown on xylose; XLN7, XLNC418, and A7C115 all had higher levels of xylanase activity than APEX when grown on glucose, *see figure 7*.

4. Discussion and Conclusions

The media of XLN7 and XLNC418, when compared to the protein concentrations of APEX, show a marked increase in production of hydrolytic enzymes. This is a desirable outcome. However, based on the theory of the overexpressed XLNR TF binding to our recombinant xynC promoter, XLNC418 – the fungal transformant receiving both construct 1 and 2 – was expected to show significantly more production of the cellulase enzyme compared to the strain XLN7, which received only construct 2. Leading theories as to why the production is lower, albeit comparable, between XLN7 and XLNC418 is human error and low sample sizes; thus far into the project only one 4-day trial of enzyme activities has been completed. Additionally, XLN7 is behaving as expected; when grown on xylose, a 5-carbon sugar, there is an increased level of cellulase production – specifically, 4.75 times as much as the control – and when grown on glucose, a 6-carbon sugar, there is an increased level of xylanase activity, likely due to the glucose activating the XLNR TF, via intermediates activating the GPD promoter found in construct 1. Similar reasoning can explain the increased levels of cellulase and xylanase production in strain XLNC418, however, expected results are to have construct 1 and 2 behaving in a synergistic manner. The data from A7C115 show a large jump between 72 and 96 hour reads in overall protein concentration

and cellulase and xylanase activities, casting doubt on the accuracy of the data collected for A7C115.

Additionally, we have yet to complete a trial using our experimental PPTB as a carbon source for our transformants. Initial attempts at using PPTBs proved difficult to concentrate the media protein extract due to the physical nature and relative grit composing the liquor. A concentrated protein extract would help eliminate experimental errors, providing us with more accurate data. Therefore, the next steps to be taken are to run the same 4-day enzyme assays using PPTBs as an additional carbon source and to determine a way to concentrate all the liquid media effectively.

5. Summary

In this work we have sought to alter the induction of transcription for cellulases and overexpress the transcription factor controlling the regulation of our desired hydrolytic enzymes. Constructs were formed using Gibson Assembly Technology, transformed into *E. coli* for validation of our insert, and purified in preparation for fungal transformations. We have created 3 separate strains of *Aspergillus nidulans* expressing construct 1, construct 2, and both constructs, and we have determined the protein levels and cellulase and xylanase activity in these constructs, comparing our transformants to unmodified strain. Further experiments still need to be conducted; most notably, the use of PPTBs as a carbon source.

6. Appendices

6a. Acknowledgements

I am deeply appreciative to Dr. and Mrs. Niblack for providing myself with the outstanding opportunity to conduct serious research as an undergraduate; not many students are as privileged as I have been, as both of you have allowed me to focus on this project without the need to focus on monetary struggles.

Thank you to Dr. Prade for having the patience to explain the protocols to me for the hundredth time and guiding me through this journey. Thank you to Bekkah Friske-Pope for letting me use your media and for struggling through research alongside one another. Thank you to Adam Soriano and Peyton Thompson for helping conduct this research. And one last thanks to everyone in our lab for seeking knowledge and understanding of such a fascinating branch of life that is fungi.

6b. Papers Published

Economic Biofuel Production from Recombinant *Trichoderma reesei* Genome (Thomas et al., 2020a)

Economic Biofuel Production from Recombinant *Trichoderma reesei* Genome (Thomas et al., 2020b)

Economic Biofuel Production from Overexpressed *Aspergillus nidulans*

Transcription Factor and Recombinant Hydrolase Promoter (Thomas et al., 2022)

6c. Literature Cited

BALLMANN, P., LIGHTFOOT, J., MÜLLER, M., DRÖGE, S. & PRADE, R. 2019. Redesigning the Aspergillus nidulans xylanase regulatory pathway to enhance cellulase production with xylose as the carbon and inducer source. *Microbial cell factories,* 18**,** 193.

GRUBER, F., VISSER, J., KUBICEK, C. & DE GRAAFF, L. 1990. The development of a heterologous transformation system for the cellulolytic fungus Trichoderma reesei based on a pyrG-negative mutant strain. *Current genetics,* 18**,** 71-76.

GUPTA, V. K., STEINDORFF, A. S., DE PAULA, R. G., SILVA-ROCHA, R., MACH-AIGNER, A. R., MACH, R. L. & SILVA, R. N. 2016. The post-genomic era of Trichoderma reesei: what's next? *Trends in Biotechnology,* 34**,** 970-982.

KLAUBAUF, S., NARANG, H. M., POST, H., ZHOU, M., BRUNNER, K., MACH-AIGNER, A. R., MACH, R. L., HECK, A. J., ALTELAAR, A. M. & DE VRIES, R. P. 2014. Similar is not the same: differences in the function of the (hemi-) cellulolytic regulator XlnR (Xlr1/Xyr1) in filamentous fungi. *Fungal Genetics and Biology,* 72**,** 73-81.

MILLER, G. L. 1959. Use of dinitrosalicylic acid reagent for determination of reducing sugar. *Analytical chemistry,* 31**,** 426-428.

REESE, E. History of the cellulase program at the US army Natick Development Center. Biotechnol. Bioeng. Symp.;(United States), 1976. Army Natick Development Center, MA.

SCHUSTER, A. & SCHMOLL, M. 2010. Biology and biotechnology of Trichoderma. *Applied microbiology and biotechnology,* 87**,** 787-799.

THOMAS, A. L., SORIANO, A. R., THOMPSON, P., FRISKE-POPE, R. & PRADE, R. A. Economic Biofuel Production from Overexpressed Aspergillus nidulans

Transcription Factor and Recombinant Hydrolase Promoter. Undergraduate Research Symposium, 2022 Oklahoma State University, Stillwater, Oklahoma.

THOMAS, A. L., SORIANO, D. G. & PRADE, R. A. 2020a. Economic Biofuel Production from Recombinant *Trichoderma reesei* Genome. *Research Reports From Life Science Freshman Research Scholars.*

THOMAS, A. L., SORIANO, D. G. & PRADE, R. A. Economic Biofuel Production from Recombinant *Trichoderma reesei* Genome. Annual Life Science Freshman Research Scholar Symposium, April 27, 2020 2020b Oklahoma State University.

WU, K.-T., TSAI, C.-J., CHEN, C.-S. & CHEN, H.-W. 2012. The characteristics of torrefied microalgae. *Applied energy,* 100**,** 52-57.

Economic Production of Hydrolytic Enzymes Pertinent to Biofuel Production from Overexpressed *Aspergillus nidulans* Transcription Factor and Recombinant Hydrolase Promoter

Andrew L. Thomas

Department of Microbiology and Molecular Genetics
Faculty Sponsor: Dr. Rolf A. Prade
Graduate Student Mentor: Rebekkah Friske-Pope

Why are Fungi Important?

What role do Fungi serve?

https://i0.wp.com/images-prod.healthline.com/hlcmsresource/images/AN_images/can-you-eat-moldy-bread-1296x728-feature.jpg?w=1155&h=1528

https://miro.medium.com/max/700/1*XEcSBHudnG9UulHJBPTQyA.jpeg

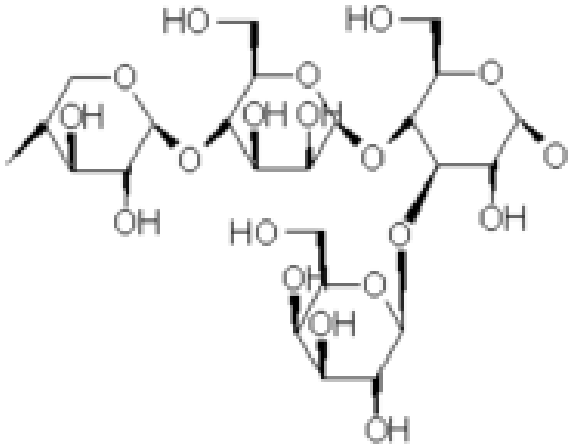

Hemicellulose

PPTBs

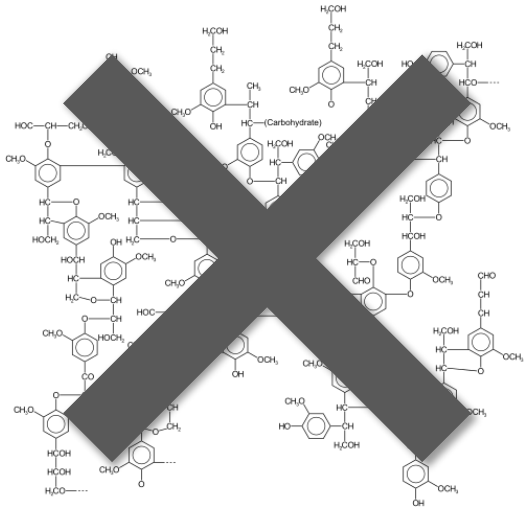

Lignin

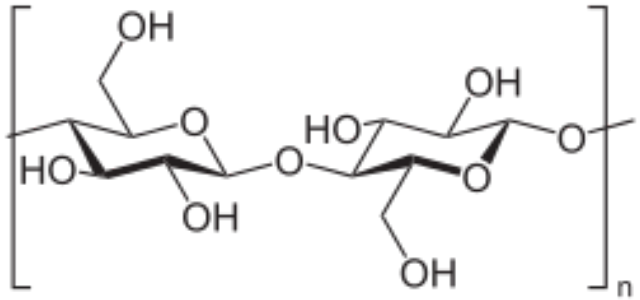

Cellulose

A Look Into ‘Woody’ Biomass

Crash Course in Molecular Biology: Transcription Factors and Inducers

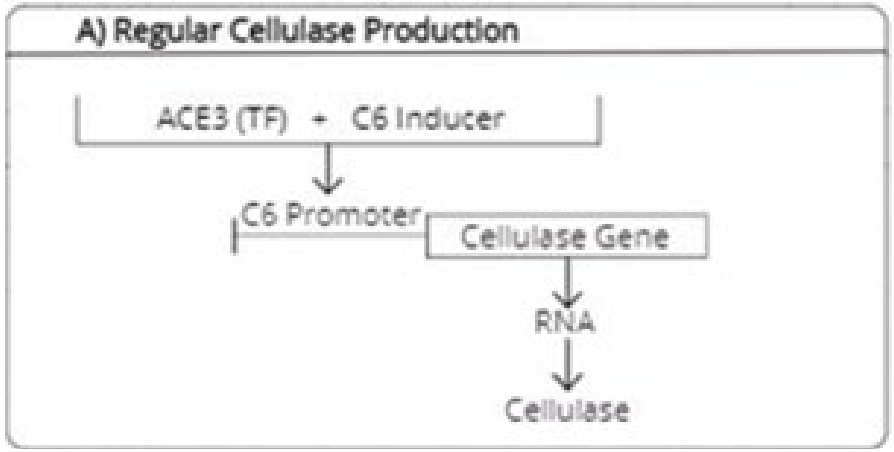

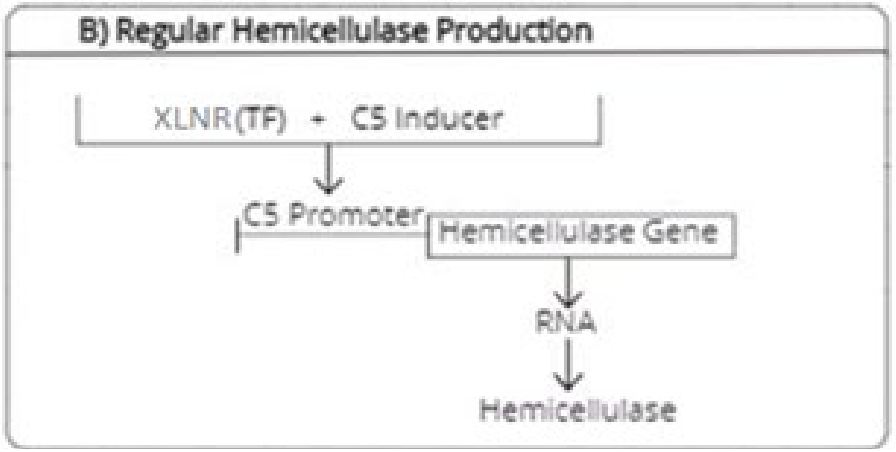

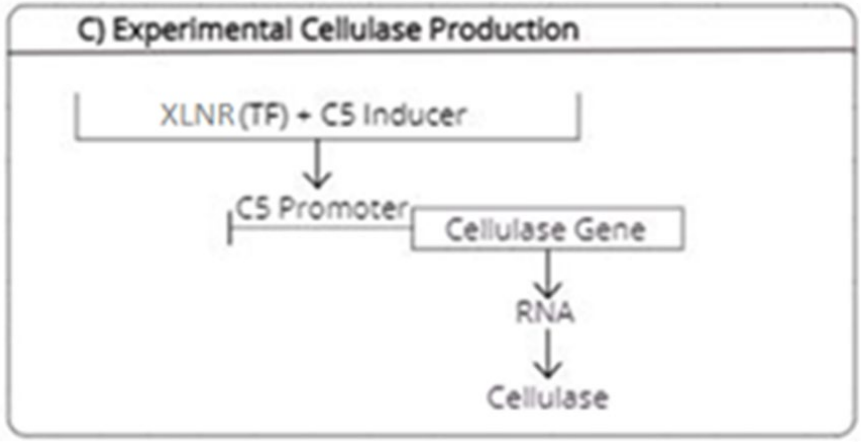

Genetic Constructs and Cloning

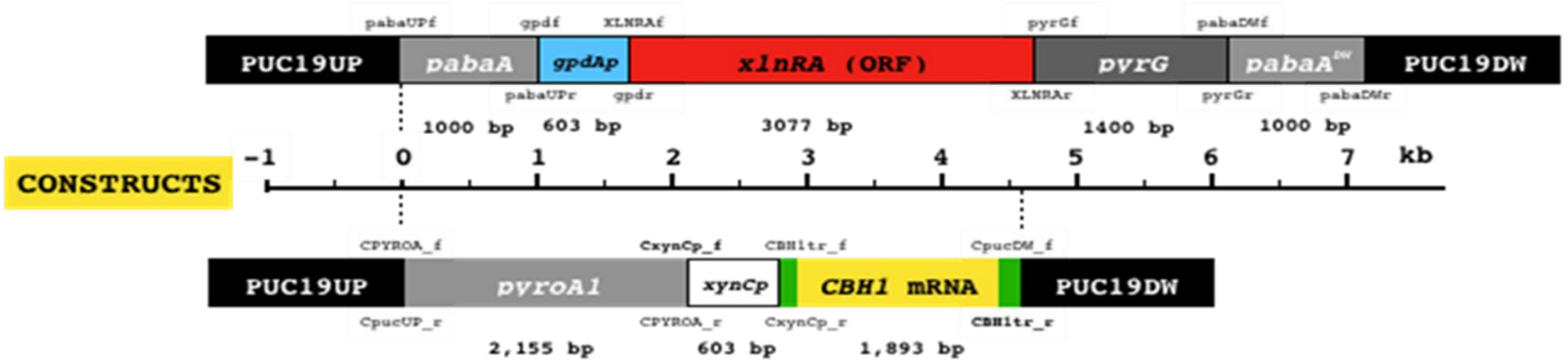

Relevant Genotype

Strain	Overexpression	
	XlnR	CBH1 mRNA
APEX	----	----
XLN7	gpdp::XLNR	----
A7C115	----	xynCp::CBH1tr
XL7C418	gpdp::XLNR	xynCp::CBH1tr

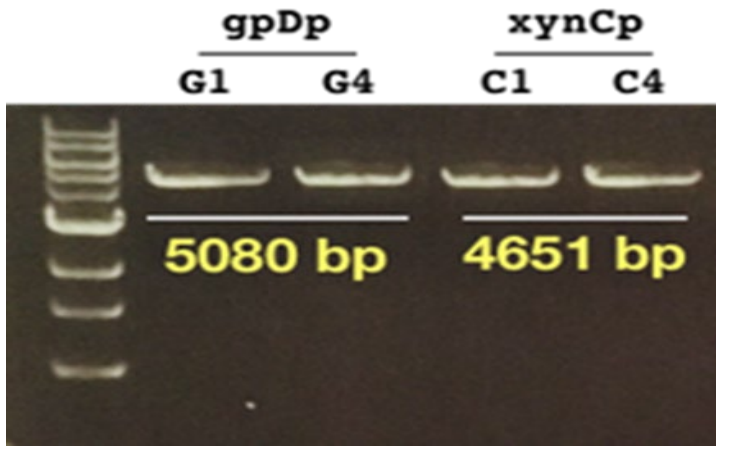

Bradford Assay for Total Protein Concentrations

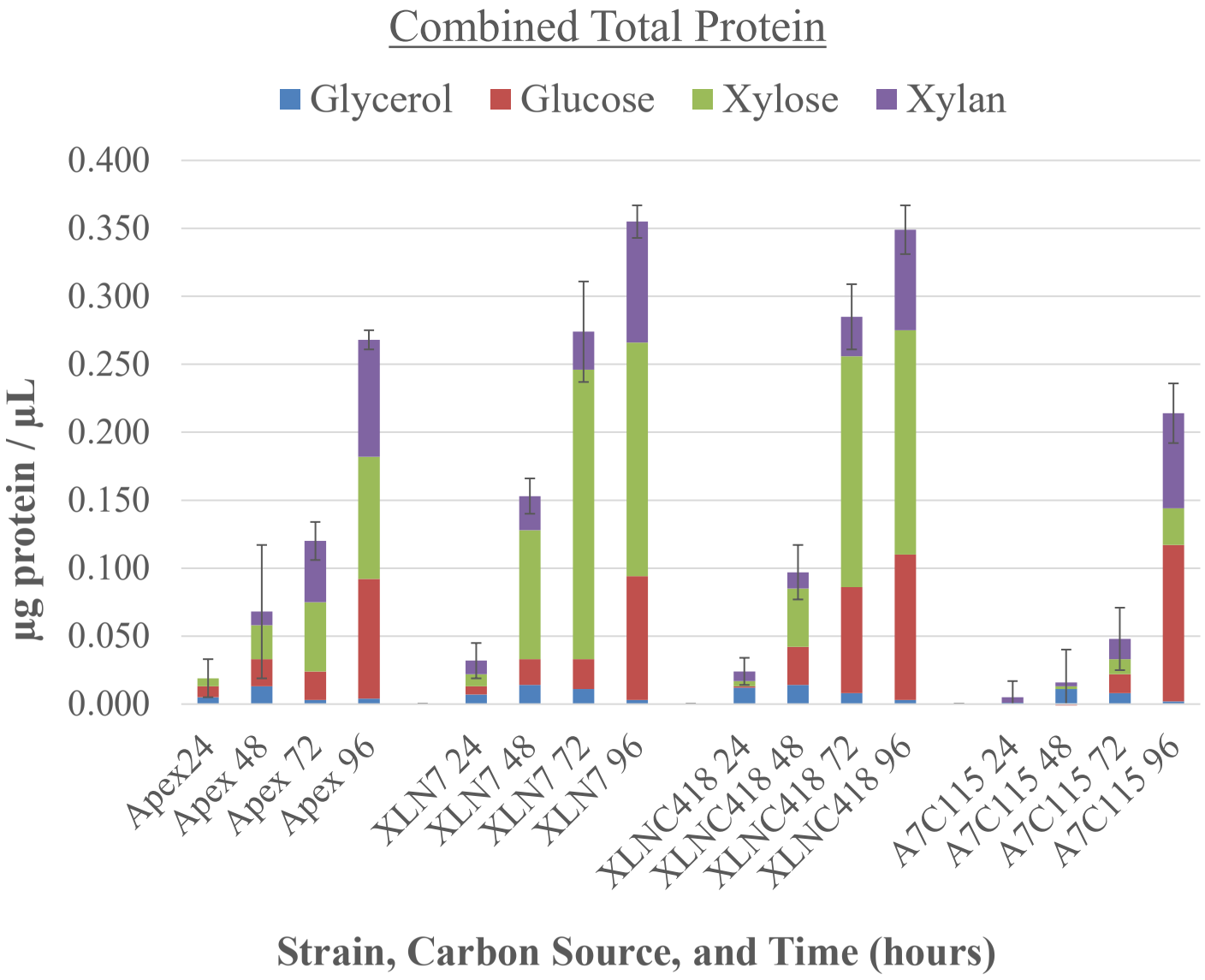

Relative Increase in Cellulase Activity Compared to Control (APEX)

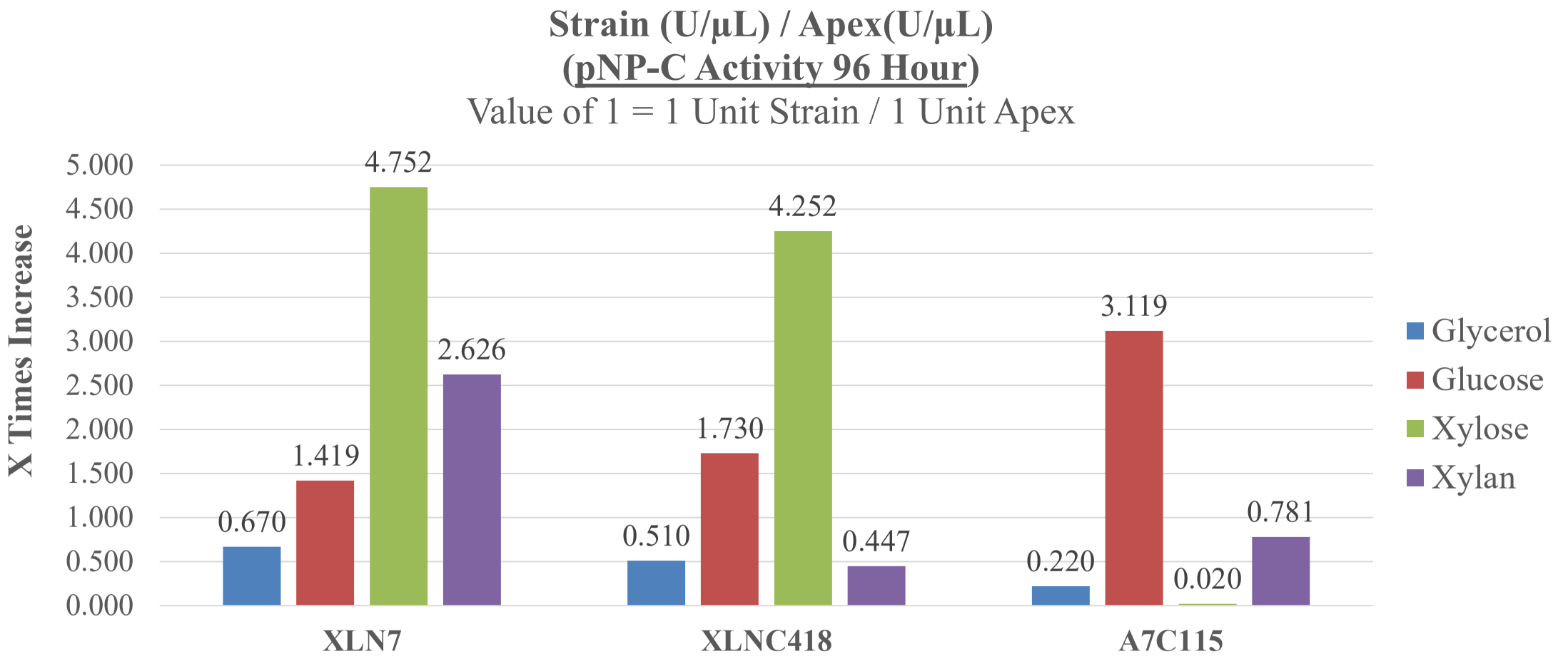

Relative Increase in Hemicellulase Activity Compared to Control (APEX)

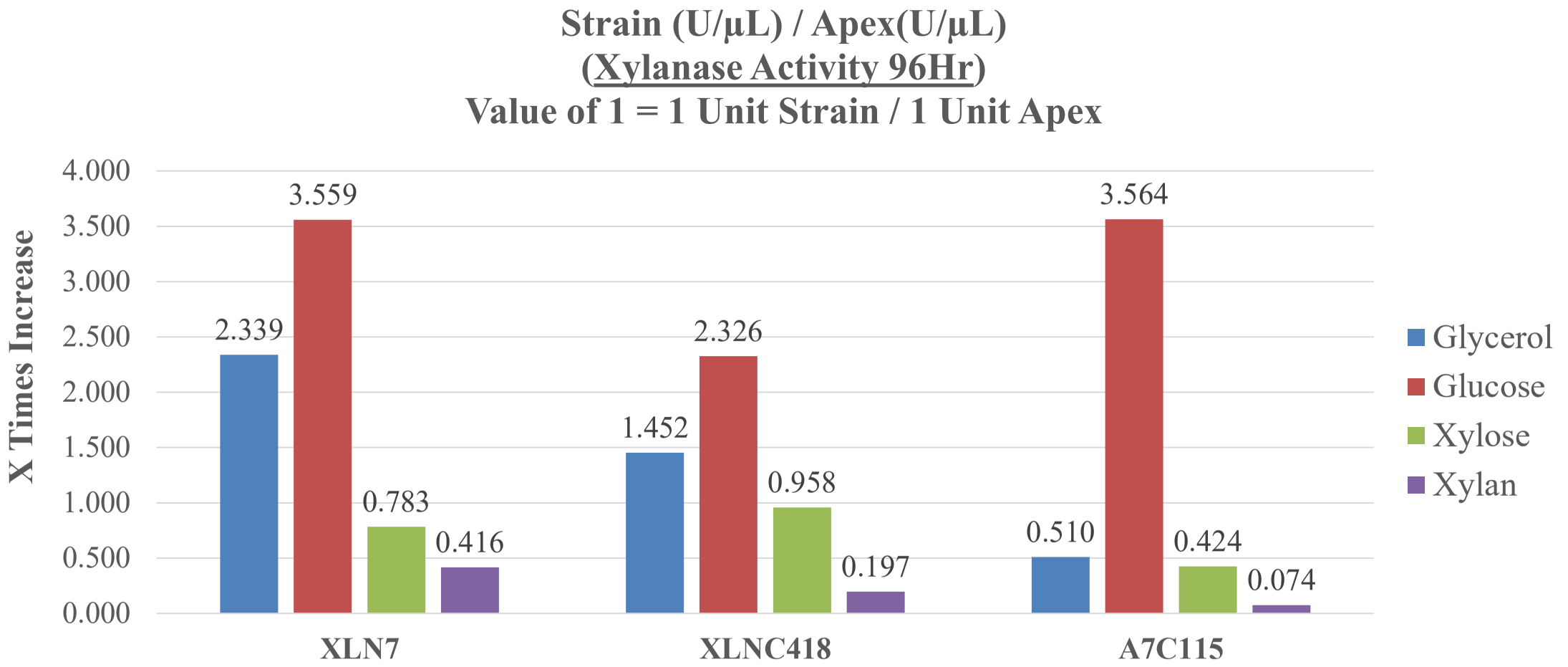

Summary

- Altered the Inducers of Transcription for Cellulases
  - Using xynC promoter in control of Cellulase Gene
- Over expressed the Xylanase Transcription Factor
  - This increases Native xylanase production and increases expression of modified Cellulase gene
- Increased the Protein Output
- Increased Enzyme Activity of Fungal Transformants

Thank You, Dr. and Mrs. Niblack!